THE UNIVERSITY *of* EDINBURGH

Crystal Structures and Phase Transitions of Bismuth-Tellurides Under High Pressure

Kenneth Freeman

Doctor of Philosophy
The University of Edinburgh
August 2019

Abstract

Bismuth-tellurides are binary compounds of bismuth (Bi) and tellurium (Te) which form an infinitely adaptive series, $(Bi_2)_m(Bi_2Te_3)_n$, within certain compositional limits. Members of this series exhibit a number of interesting and useful physical properties: they are among the most widely known thermoelectric materials and they have been shown to exhibit superconductivity and topological insulation. Many of these properties have been reported to be induced or enhanced by the application of high pressure. Despite this, the current understanding of the crystal structures of the $(Bi_2)_m(Bi_2Te_3)_n$ series under high pressure remains fragmentary. Knowledge of these crystal structures is the first necessary step towards further investigation of the properties of these materials through, for example, electronic structure calculations.

This thesis presents the analysis of high-pressure x-ray diffraction data collected for several members of the $(Bi_2)_m(Bi_2Te_3)_n$ series. Angle-dispersive x-ray powder diffraction experiments were performed at synchrotron facilities, utilising diamond-anvil pressure cells to generate pressures up to 26 GPa. Several structural phases of the $(Bi_2)_m(Bi_2Te_3)_n$ series are investigated in detail including a previously unreported complex host-guest structure that forms in several of the series members at high pressures. This is a similar structure to the host-guest phase of elemental bismuth (Bi-III) with a host framework enclosing linear guest chains which lie along the c-axis direction. The guest chains are found to be disordered along their lengths, contributing only diffuse features to the measured x-ray powder diffraction profiles. Along with this structural disorder, this structure is found to include chemical ordering with the guest chains composed primarily of bismuth

Other investigated phases include the layered structure found at ambient conditions, consisting of regular Bi_2 and Bi_2Te_3 blocks stacked along the *c*-axis. Where appropriate, Rietveld refinement of these structures found the block

compositions to differ from the idealised structure. For certain compositions, a four-dimensional modulated structure is the more appropriate description; le Bail fits were performed in these cases to provide the pressure-evolution of the lattice parameters and modulation vector.

All investigated samples were found to adopt high-symmetry cubic phases at the highest pressures investigated here. This, along with various similarities between the other pressure-induced phases, suggests a universal behaviour in the $(Bi_2)_m(Bi_2Te_3)_n$ series on pressurisation. Composition was found to have a significant influence on the behaviour under pressure and individual structures of bismuth-tellurides. This work represents the first systematic, high-pressure structural study of these materials and explores the pressure-behaviour of the series as a whole and as a function of composition. This provides a first necessary step towards an improved understanding of these materials and their properties at high pressures.

Lay Summary

A series of materials, the bismuth-tellurides, are composed of two elements, bismuth (Bi) and tellurium (Te) in different ratios. These materials exhibit a number of interesting and useful physical properties such as thermoelectricity (where they can be used to convert differences in temperature directly to electricity without the need for moving parts) and superconductivity (where they can conduct electricity with zero resistance). These properties have been found to be induced or enhanced when the materials are placed under high pressures. The first step to understanding these changes in their properties is to determine the structures of these materials at the atomic scale.

To do this, we have taken several different bismuth-tellurides and placed them under pressures tens of thousands of times higher than atmospheric pressure. This is achieved with the use of diamond anvil cells, which squeeze small samples between the flat tips of two diamonds. The high-pressure atomic structures of these materials were determined through x-ray diffraction, where intense x-rays are shone through the sample, producing a diffraction pattern that is measured as a two-dimensional image. This pattern is characteristic of the atomic structure of the material which produced it and can be used to determine how the atoms of the material are arranged in three-dimensional space.

We have measured several interesting atomic structures for different bismuth-telluride materials and have investigated how they change as a function of pressure. By studying materials with different Bi:Te ratios we have been able to systematically study the behaviour of the bismuth-tellurides under pressure, which will pave the way for future understanding of their physical properties and their enhancements under pressure.

Declaration

I declare that this thesis was composed by myself, that the work contained herein is my own except where explicitly stated otherwise in the text, and that this work has not been submitted for any other degree or professional qualification except as specified.

(*Kenneth Freeman, August 2019*)

Acknowledgements

I would like to thank my supervisor, Dr Ingo Loa, for his continued advice and guidance throughout this project. I've learned a lot about condensed matter physics and, admittedly, the use of the English language under his supervision. I'd like to thank my family and friends for their support, especially Rohana for keeping me going. Thanks also to the coffee shops of Leith for the same.

This work is based on a number of experiments performed before the start of this project, along with some during. I'd like to thank all those who participated in these and worked to gather the data on which this project is based: Dr Jan-Willem Bos, Dr Ruth Downie, Dr Rachel Husband, Dr Ciprian Pruteanu and Dr Ingo Loa, along with the beamline scientists who's support made these experiments possible, in particular, Dr Dominik Daisenberger, Dr Michael Hanfland, Dr Annette Kleppe and Dr Heribert Wilhelm. Thanks also to Dr Andreas Hermann for pointing out the diffuse features observed in lithium-boride.

I would like to acknowledge financial support from the Scottish Doctoral Training Centre in Condensed Matter Physics, allowing me to travel to many interesting conferences and schools.

Contents

Chapter 1

Introduction

Bismuth-telluride compounds have been of interest for a number of decades due mostly to their role in applied thermoelectric materials, Bi_2Te_3 being one of the most widely used thermoelectrics for applications near room temperature [1]. Bismuth-tellurides have also been reported to be superconductors [2–4] and topological insulators [5, 6], with potential for applications in spintronic devices. Many of these interesting and potentially useful physical properties are either induced or strongly influenced by pressure.

A number of studies have reported significant enhancement of these properties under high pressures (1–20 GPa, 10–200 kbar). For example, the thermoelectric efficiency of Bi_2Te_3 (and doped compounds thereof) has been reported to undergo significant enhancement at several GPa of pressure [7, 8]. Despite this, the current understanding of the high-pressure crystal structures remains fragmentary. A systematic study of the crystal structures and their behaviour under high pressures is a first necessary step before further work (such as electronic structure calculations) can be done in order to gain a better understanding of these properties under pressure. Furthermore, there are observed similarities in the structures adopted by bismuth-tellurides which make a systematic comparison of them crystallographically interesting.

To address this, high-pressure x-ray powder diffraction experiments have been performed on several members of the Bi-Te series. Pressures up to 26 GPa were produced with the use of Merrill-Bassett-type diamond anvil cells [9], where a small sample is compressed between the flat culets (tips) of two diamond anvils. The use of hard anvils and a small sample allows large pressures to be reached

with moderate force, due to *pressure=force/area*. Intense monochromatic x-rays provided by synchrotron sources were directed through the powdered samples, producing characteristic diffraction patterns. Analysis of these diffraction patterns allowed the crystal structures of the materials held at high pressures to be determined through Rietveld structure refinement [10] and le Bail fitting [11].

In this work we present the results of this analysis on Bi_xTe_{1-x} compositions spanning $0.44 \leq x \leq 0.70$. Several structural phases were studied in detail including the layered structure adopted by the Bi-Te series at ambient conditions. The compression of the constituent layers were determined as a function of pressure, illustrating the strong influence of composition on these structures. Several high-pressure structures were investigated, with all compositions adopting a fully site-disordered body-centred-cubic structure at the highest pressures reached here. Gentle thermal annealing has been shown to allow these cubic structures to partially chemically order [12] and a similar disorder-order transition is observed here in Bi_4Te_3 on pressure decrease.

The observed structural phases include a complex host-guest crystal structure, similar to those reported in a number of elements at high pressure including rubidium (Rb-IV [13]), potassium (K-III [14]) and elemental bismuth (Bi-III [15]). This structure is reported here in Bi-Te materials for the first time and is observed to include disorder within its guest component, in a manner similar to 'chain melting' - a phenomenon reported in Rb [16] and K [17, 18]. Along with this structural disorder, there is chemical ordering within the host-guest structure, with the guest component primarily comprised of bismuth. This is in contrast to the reported host-guest structures in Bi-Sb materials, which were found to be fully site-disordered alloys [19].

The layout of this thesis is as follows. Chapter 2 will provide an overview of the current understanding of the bismuth-telluride series under pressure. This literature review will start by summarising the interest in bismuth-tellurides and why they are worth studying. Then the $(Bi_2)_m(Bi_2Te_3)_n$ series and its structures at ambient conditions will be introduced, followed by a summary of the published structural studies under pressure. The complex host-guest structure type will be introduced and observations of disorder within these structures will be discussed. Finally, the physical properties of bismuth-tellurides under pressure will be summarised, illustrating the need for a better understanding of the high-pressure crystal structures.

Chapter 3 will then provide an overview of the experimental methods employed in this thesis, namely high-pressure x-ray powder diffraction at synchrotron facilities. This will be followed by a discussion of the theory of crystalline materials and x-ray diffraction. As the work in this thesis included the use of a custom Rietveld refinement code developed from the ground up, particular attention will be paid to how the intensities of diffracted x-rays are calculated from a structural model for comparison to real-world data. Finally the data analysis methods used will be discussed, including said refinement software.

Chapter 4 will provide a brief overview of the Bi-Te compositions investigated in this work, the experiments during which data were collected and a brief introduction to the observed structural phases. This chapter will serve as a reference, summarising the different samples and datasets that have been analysed in this work. The following chapters then introduce the main results and discussion of this thesis, one Bi-Te composition at a time.

Chapters 5–9 each detail the analysis of one Bi-Te composition, starting with Bi_2Te which exhibited most of the structural phases discussed in this work. Chapter 5 will introduce these structures in detail for the Bi_2Te composition and will present analysis and discussion one structural phase at a time. Chapters 6–9 will follow a similar format, presenting the results of analysis of Bi_7Te_3, Bi_4Te_3, BiTe and Bi_4Te_5.

Finally, Chapter 10 will then summarise the main results of this work, placing them in to the context of the Bi-Te series as a whole, and will suggest some future avenues for further study. The observed similarities and differences between different Bi-Te compositions will be discussed, along with observed trends as a function of composition.

Chapter 2

The Bi-Te Infinitely Adaptive Series Under Pressure

2.1 Introduction

This chapter presents a review of the high-pressure behaviour of bismuth-telluride compounds and their physical properties. First, the initial work on Bi-Te compounds will be discussed, the concept of the Bi-Te *infinitely adaptive series* will be introduced and the ambient-conditions structures of members of this series will be explored. The behaviour of these materials at high pressures will then be discussed, giving an overview of the work published to date. As will be discussed in this work, several members of the Bi-Te series adopt a complex semi-disordered *host-guest* structure at high pressures. The next section will introduce the host-guest structure and will discuss the phenomenon of 'chain melting', where the guest component of the structure exhibits structural disorder. The physical properties of Bi-Te compounds under pressure will then be discussed, and finally the current landscape of investigated (published) compositions and observations will be summarised.

2.2 Interest in Bismuth-Tellurides

Bi_2Te_3 is one of the most widely known thermoelectric materials. Thermoelectric materials have the ability to convert a temperature gradient into a difference in

electric potential and vice versa, and can be used to build thermoelectric modules which can generate electricity from waste heat or provide electronic solid-state refrigeration. Much of the interest in bismuth-telluride compounds stems from the fact that Bi_2Te_3 has become well-established as an efficient thermoelectric for applications around room temperature conditions and has been investigated in the interest of sensing, cooling of electronic components and harvesting of waste heat. Since the first observations of the thermoelectric (or 'Seebeck') effect in 1826 [20], interest in thermoelectrics for energy generation and refrigeration applications (by the converse 'Peltier' effect) has undergone peaks and troughs. Initial work focused on metals, which are poor thermoelectrics, and eventually turned to semiconductors after breakthroughs in the 1950's. It was during this shift to semiconducting materials that Bi_2Te_3 emerged as a promising and practical thermoelectric material [21].

The field again began to stagnate, while the contradictory nature of the ideal thermoelectric was determined (a high electrical conductivity coupled with a low thermal conductivity) and certain limitations in the investigated materials were reached. A recent renewed interest in thermoelectrics has arisen over the past 25 years due to several promising developments along with increased awareness of our environmental impact and the ongoing shift towards clean, renewable technologies. A new approach has seen complex crystal structures investigated as potentially efficient thermoelectric materials in an effort to fulfil the 'phonon-glass electron-crystal' concept, first introduced by Slack in 1995 [22]. This concept described the structure of an efficient thermoelectric as appearing glass-like to phonons, hindering their propagation through the material and hence maintaining a low thermal conductivity. At the same time this material would appear crystal-like to electrons, allowing them to pass through easily and exhibiting a high electrical conductivity. Nanostructural engineering has also been identified as a potentially valuable tool in the search for improved thermoelectrics [1]. Complexity within a thermoelectric material at a variety of length scales is able to disrupt the transfer of heat while maintaining electrical conductivity. This method has been applied and has produced significant improvements in efficiency in a number of systems.

Further to their thermoelectric properties, bismuth-tellurides have recently gained interest as topological insulators and as model spintronic materials. Pressure-induced superconductivity has also been reported in members of the Bi-Te series: in Bi_2Te_3 [23], and more recently in Bi_4Te_3 [3] and Bi_2Te [4].

Along with their interesting and potentially useful physical properties, bismuth-tellurides are also of interest crystallographically. These binary compounds form an infinitely adaptive series at ambient conditions and exhibit a number of pressure-induced phase transitions. Universal behaviours across the series, as well as differences between certain compositions suggest a rich range of atomic and electronic interactions in the structures induced by pressure.

2.3 The Bi-Te Infinitely Adaptive Series

Research has focused on Bi_2Te_3 and elemental Bi, which are end members of the homologous series $(Bi_2)_m(Bi_2Te_3)_n$. While some intermediate compositions have been studied, none has been investigated in detail. The CRC Handbook of Thermoelectrics, for example, describes the study of 'Bi_2Te_3 single crystals' with compositions between 50–70 % Te [22]. Work by Bos *et al.* in 2007 sought to rectify this by undertaking a systematic study of the $(Bi_2)_m(Bi_2Te_3)_n$ series at ambient conditions, determining the crystal structures and thermoelectric properties of nine members of the series spanning compositions containing 40–100 % Bi [24].

The proposed layered model for the ambient-conditions structures of members of the $(Bi_2)_m(Bi_2Te_3)_n$ series is well established [25, 26]. As illustrated in figure 10.2, this model describes structures comprised of five-layer Bi_2Te_3 and two-layer Bi_2 building blocks which are stacked along the crystallographic c-axis. These blocks are comprised of layers of a single atom type, in the order Bi-Bi for the Bi_2 block and Te-Bi-Te-Bi-Te for the Bi_2Te_3 block. Varying the number of these building blocks (i.e. m and n) allows this model to describe different Bi-Te compositions.

The number of layers per unit cell is a multiple of 3 so both rhombohedral and trigonal structures occur, with a rhombohedral structure if $(n + m)/2$ is even. This description provides 'idealised' models for the ambient-conditions phases (here referred to as *phase I*) and can provide estimated lattice parameters with a values typically around 4.4 Å and c values predicted by taking the c lattice parameters of Bi_2Te_3 and elemental Bi: c' and c'', respectively. The predicted phase-I c parameter is thus,

$$c_{predicted} = \frac{1}{3}\left[mc' + nc''\right]. \tag{2.1}$$

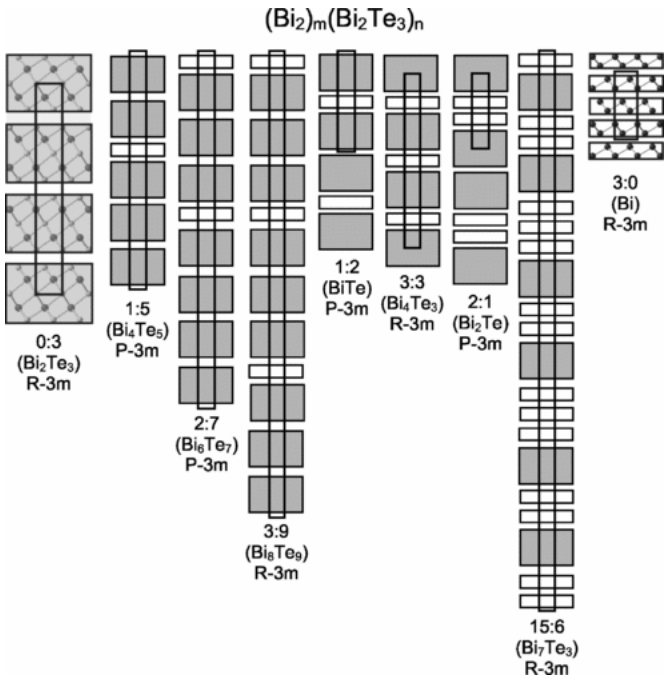

Figure 2.1 *Illustration of the ambient conditions crystal structure of members of the Bi-Te series (figure 1 from [24]). Grey rectangles represent Bi_2Te_3 blocks and white rectangles represent Bi_2 blocks. The end members include positions of the atoms within these blocks.*

The structures observed by Bos *et al.* support the characterisation of the series as an *infinitely adaptive series*. In such a series, small changes in composition result in stable compounds (no phase separation or solid solutions) which have distinct, well-ordered crystal structures [27]. These structures are made up by the stacking of regular blocks which can result in long periodicities (for example, Bi_4Te_3 which has a unit cell with c lattice parameter over 40 Å). More than one stacking sequence is possible, but the compounds exhibit only one; a feature typical of infinitely adaptive series [26].

Follow-up work by Bos *et al.* in 2012 more closely investigated the stability of these superlattice structures and found that the infinitely adaptive series spans a range of compositions between $0.44 \leq x \leq 0.70$ for Bi_xTe_{1-x}. Outwith this range the material decomposes in to a two-phase mixture [28].

In their 2007 work, Bos *et al.* recorded x-ray powder diffraction (XRPD) profiles and observed what appeared to be a smooth variation of the peaks in the diffraction profiles as a function of Bi content, suggesting a corresponding smooth variation of lattice parameters of the structures. This was in contrast to the predicted and refined c lattice parameters which showed 'wide and irregular' variation across the series. Similar observations have been made in

the $(Bi_2)_m(Bi_2Se_3)_n$ homologous series [29] and suggested that an alternative structural description might be more appropriate.

Such an alternative description considers an average structure that is modulated along the c-axis by a modulation vector of magnitude γ in a four-dimensional (4D) structure analysis. The modulation $\vec{q} = \gamma[001]^*$ is applied to a basic hexagonal subcell with approximate dimensions: $a \sim 4.4$ Å, $c \sim 6.0$ Å. Structures for which γ is a rational value can be equivalently described using the conventional 3D approach described above whereas compositions for which γ is irrational are incommensurately modulated.

2.4 Structural Studies Under Pressure

The constituent elements of this series, bismuth (Bi) and tellurium (Te), have themselves been studied in their elemental form as a function of pressure and found to adopt a number of different crystal structures.

Bismuth is a well studied element, with a phase diagram established in 1963 [30] that has remained largely unchanged. Some of the subtleties of its structures, in particular that of Bi-III, have only been revealed over the past few decades as experimental techniques and apparatus have improved for x-ray diffraction studies. At ambient temperature, bismuth adopts several structural phases on pressure increase labelled Bi-I, Bi-II and Bi-III [31]. The Bi-I phase found at ambient pressure has a rhombohedral structure, transforming to Bi-II, with a C-face-centred monoclinic structure, at around 2.55 GPa. This phase then transforms at around 2.70 GPa to Bi-III, a complex 'host-guest' structure, which will be described in more detail in a following section. The structure eventually becomes body-centred cubic at around 7.7 GPa in a fourth phase, Bi-V [32]. The phase labelled 'Bi-IV' describes a high pressure, high temperature phase of bismuth.

The determination of the crystal structure of elemental tellurium as a function of pressure has been a gradual process. As for bismuth, improvements in experimental techniques have allowed more of the subtleties of each structural phase to be uncovered. Work spanning from 1980 to 2004 describes the evolution of our understanding of the high pressure behaviour of tellurium [33–38]. The currently accepted [37] pressure-behaviour of Te describes an ambient-pressure

trigonal phase (Te-I) which transforms to a triclinic phase (Te-II) at around 4 GPa. On further pressure increase, Te adopts an incommensurately-modulated monoclinic structure (Te-III) at around 4.5 GPa. Finally, the structure becomes body-centred cubic (Te-V) above 29.2 GPa.

Bismuth-tellurides with compositions satisfying Bi_xTe_{1-x}, $0.44 \leq x \leq 0.70$, form an infinitely adaptive series of the form $(Bi_2)_m(Bi_2Te_3)_n$ at ambient conditions. There are a wide range of series members (compositions) that have been synthesised and studied at ambient conditions, however, only a few have been investigated under high pressures. What follows is a summary of the high-pressure structures of several series members, starting with the most widely studied composition, Bi_2Te_3. Often, especially in more recent work, high-pressure structural studies are complemented with measurements of physical properties motivated by the potential technological applications of these materials. A later section will provide a summary of the behaviour of these properties under high pressures; here we will focus on the crystal structures.

2.4.1 Bi_2Te_3

A comprehensive review of high-pressure studies of Bi_2Te_3 has been published by Manjón *et al.* in 2013 [39]. The structures and properties of Bi_2Te_3 have been investigated for well over half a century. Through the 1960–1980's, this work was focussed on determining the pressure-temperature phase diagram of the material, along with measurements of the electronic properties to determine the behaviour of the band gap and search for signs of superconductivity. More recently, high-pressure studies have been motivated by potential improvements to the thermoelectric efficiency and by the identification of Bi_2Te_3 as a 3D topological insulator.

The ambient-pressure layered structure of Bi_2Te_3 has been known for a long time [40–43]. As an end member of the $(Bi_2)_m(Bi_2Te_3)_n$ series, it consists only of Bi_2Te_3 blocks which are stacked along the c-axis. There are three blocks (and hence three formula units) per unit cell, with each block consisting of single-atom layers in the order Te-Bi-Te-Bi-Te, such that the gaps between the blocks are separations between Te atoms. The structure forms in the trigonal *R-3m* space group (number 166). The ambient-conditions structure has three atomic positions: Te at Wyckoff position 3*a* (atomic coordinates (0,0,0)), Te at Wyck. 6*c* (0, 0, 0.2097) and Bi at Wyck. 6*c* (0, 0, 0.4005). The reported lattice

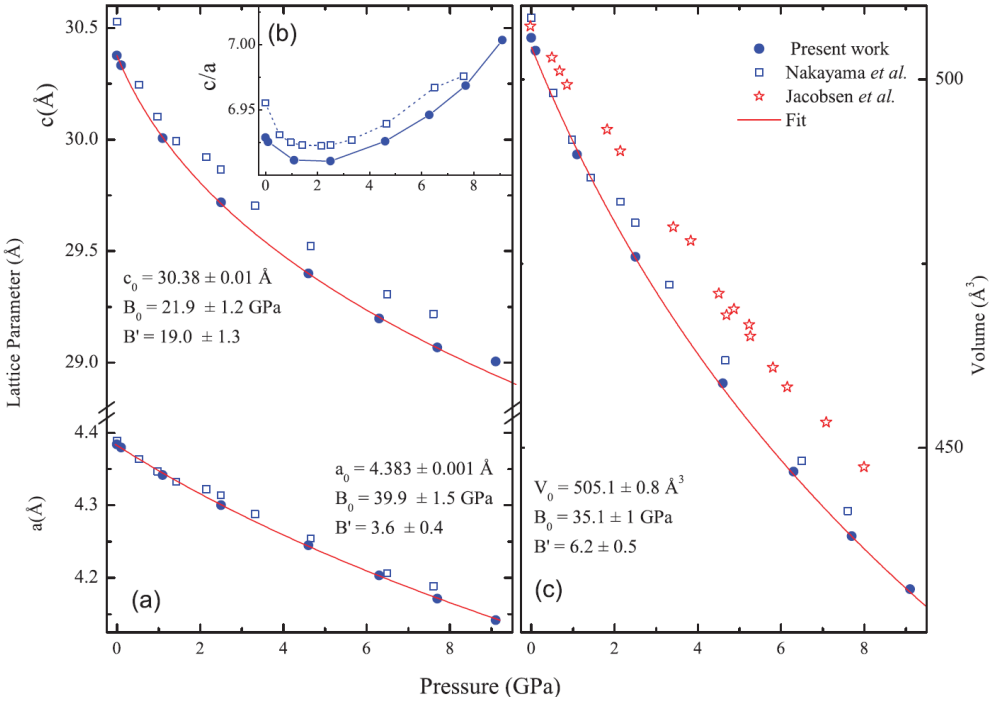

Figure 2.2 *Figure 2 from work by Polian et al. [47] showing reported lattice parameters for phase I of Bi_2Te_3. Reported data from Nakayama et al. [48] and Jacobsen et al. [49] are included for comparison. Note the significant discrepancies between the reported values.*

parameters are $a = 4.3950$ Å and $c = 30.4400$ Å giving a unit cell volume of $V_{UC} = 509.21$ Å^3 [43].

Studies of this phase under pressure have observed a structural anomaly at a few GPa. In 1972 Vereshchagin *et al.* reported a change in the pressure dependence of the ratio of the lattice parameters, c/a, within phase I and attributed this to an 'isostructural phase transition' [44]. In 1981, work on the isostructural Sb_2Te_3 compound observed anomalies in the pressure dependencies of the lattice parameters (a/a_0 and c/c_0) which they attributed to a change in the nature of the electronic interaction between the blocks [45]. This was later corroborated by a neutron diffraction and Raman scattering study [46] which observed a similar anomaly in Bi_2Te_3 and supported weak interaction between the constituent five-layer blocks. This structural anomaly is now well-established and is typically observed at pressures around 2–3 GPa; it is widely referred to in the literature as an '*electronic topological transition* (ETT)'. Figure 2.2 (b) illustrates the observed c/a ratio minimum, which is attributed to this ETT.

The structural anomaly labelled as an ETT is well-established and has been observed in a number of studies. This feature is also known as a Lifshitz

transition, after the work of Lifshitz in 1960 which described an 'electron transition' where changes in the Fermi surface topology occur [50]. This disruption of the Fermi surface can include the formation or closing off of 'neck' features, or the opening or closing of electron or hole pockets. Such a change in the shape of the Fermi surface can be induced by alloying or by the application of pressure. Such external factors that can change the electronic structure of the material are able to induce changes to the Fermi surface topology.

While the structural anomaly in Bi_2Te_3 has been described as an electronic topological transition, this is not accurate. An ETT is defined as a change in the topology of the Fermi surface which is defined only for metallic materials. Pure Bi_2Te_3 has been shown to be a narrow band-gap semiconductor [39] and, as such, has no Fermi surface. Furthermore, density functional theory (DFT) calculations which do not include any Fermi surface are able to reproduce the observed structural anomalies. This feature of Bi_2Te_3, currently described as an ETT, should instead be described as a structural anomaly.

The high-pressure crystal structures of Bi_2Te_3 took a significant amount of time to resolve. Initial high-pressure studies (discussed in [39]) had established that a structural phase transition occurs at around 8 GPa but this first high-pressure structure could not be resolved through neutron or x-ray diffraction studies. It was not until 2007 that a structure for this phase was proposed; Jacobsen *et al.* observed a phase transition between 7–10 GPa and indexed their synchrotron x-ray powder diffraction (XRPD) data for the high-pressure phase with an orthorhombic *I222* structure [49].

Similar work by Nakayama *et al.* performed high-pressure XRPD on Bi_2Te_3 up to 16 GPa [48]. They reported two structural phase transitions at around 8 GPa and 14 GPa. The structural phases were labelled as α (for the ambient-pressure layered structure), β for the first high-pressure phase above 8 GPa and γ for the second high-pressure phase, above 14 GPa. They report that they were unable to determine the structures of β- and γ-Bi_2Te_3, despite the high quality of their diffraction data.

The pressure range of structural studies of Bi_2Te_3 was extended by Einaga *et al.* in 2011 to 30 GPa [51]. They were the first to report an additional transition to a new structural phase labelled δ-Bi_2Te_3. They observed a transition to β-Bi_2Te_3 above 8.41 GPa and a transition to a mixed phase above 14.5 GPa. This mixed phase consisted of the β structure accompanied by small peaks from the

γ and (what was determined to be) the δ structures. This mixed phase persisted to 23.1 GPa and the sample transformed fully to the δ phase above 25.2 GPa. The structure of this newly observed high-pressure phase was identified as body-centred cubic (bcc).

The structural evolution of Bi_2Te_3 had thus been recorded to 30 GPa, but the β- and γ-Bi_2Te_3 structures were still to be solved. In the same year, Zhu *et al.* published a joint experimental and theoretical study which proposed structures for all three of the high-pressure phases observed. They performed synchrotron XRPD and analysed the resulting diffraction data using a *particle swarm optimisation* (PSO) algorithm as a crystal structure prediction tool [52].Using this method they proposed a layered monoclinic *C2/m* structure for the β-Bi_2Te_3 phase, a three-dimensional monoclinic *C2/c* structure for γ-Bi_2Te_3 and a compact monoclinic *C2/m* structure for δ-Bi_2Te_3.

The simplicity of the recorded δ-Bi_2Te_3 XRPD profiles is noted in the paper, where they refined the data from this phase using a bcc alloy structure. The misidentification of this structure as a compact monoclinic phase was due to the limitations of the PSO technique to effectively model atomic disorder within a structure. Indeed, the structure determined by the PSO technique does exhibit a bcc-like structural order. This illustrates the limitations of such a structure search tool; care must be taken to ensure the determined structures are sensible and appropriate, in order to avoid the misidentification of a disordered bcc structure as compact monoclinic *C2/m*.

These structures proposed by Zhu *et al.* provided good fits to their recorded XRPD data and have since been corroborated by Zhang *et al.* [53].

Recent Raman studies have indirectly supported the structures proposed by Zhu *et al.* for the β and γ phases. Within the pressure range of β-Bi_2Te_3, the Raman-active modes of the *C2/m* structure can be clearly followed [54–58]. At higher pressures, following individual Raman modes becomes difficult due to loss of intensity in the Raman spectra and a broadening of the peaks. However, within the pressure range of γ-Bi_2Te_3, more than 9 Raman-active modes can be observed, which could be consistent with the proposed *C2/c* structure which has 15 Raman-active modes. This observation does rule out an alternative (disordered *C2/m*) structure proposed by Zhao *et al.* which only has 3 Raman-active modes [59]. The bcc alloy structure is not predicted to be Raman-active, in agreement with the reported disappearance of the Raman signal above 20 GPa in Bi_2Te_3 [54].

2.4.2 Bi_4Te_3

The ambient-pressure structure of Bi_4Te_3 consists of three Bi_2Te_3 blocks and three Bi_2 blocks stacked alternately along the c-axis, in keeping with the structural trends of the $(Bi_2)_m(Bi_2Te_3)_n$ series (with $m = n = 3$) [24]. This structure is illustrated in schematic 'block' form in figure 2.1 on page 7.

The structural details at ambient conditions have been reported by Yamana *et al.* in 1979. They performed x-ray diffraction [60] and measured lattice parameters which corresponded with those measured 5 years previously by Ozawa & Shimazaki (reported to Yamana *et al.* in a private communication). Yamana *et al.* determined that the structure follows the established layered form [25] with *R-3m* symmetry, three formula units per unit cell and lattice parameters $a = 4.451(1)$ Å and $c = 41.888(5)$ Å.

The only published high-pressure study of Bi_4Te_3 was undertaken in 2011 by Jeffries *et al.* [3]. They performed synchrotron x-ray diffraction on powdered samples using diamond anvil cells, with neon as a pressure-transmitting medium and copper powder as a pressure marker. It is worth noting that neon can only sustain hydrostatic conditions up to around 10 GPa [61], while the experiment recorded data up to nearly 50 GPa.

Jeffries *et al.* report that measurements at low pressures agree with the established *R-3m* layered structure. On pressure increase, a phase transition was observed near 6.4 GPa, where peaks from another phase appeared in the diffraction profiles. These peaks can be indexed with a monoclinic *C2/m* structure with lattice parameters $a = 4.3110(34)$, $b = 4.6052(38)$ and $c = 6.2641(38)$ Å with $\beta = 110.22°$. They proposed a unit cell containing 4 atoms based on the presumption that the determined unit cell volume ($V_{UC} = 116.70$ Å^3) should be smaller than that of the previous phase. A unit cell containing 4 atoms results in a volume reduction of approximately 3% at the transition (whereas a 5-atom unit cell would result in a larger collapse of 22%). This results in a structure with the same space group and number of atoms as the high-pressure Bi-II phase [62]. As there are fewer than 7 atoms in the unit cell, this structure must be site disordered to maintain the composition Bi_4Te_3.

Around 11.5 GPa, the sample transforms to a mixed phase which persists to 16.5 GPa. Peaks from two new phases (referred to as 'phase III' and 'phase IV') appear alongside those of the previous phase. Jeffries *et al.* were unable to index

the phase III peaks but were able to identify phase IV as having a body-centred cubic structure. This bcc phase is the sole high-pressure phase above 16.5 GPa, with lattice parameter $a = 3.6702(2)$ Å at this pressure. The bcc structure is reported to be a fully site-disordered alloy with atomic sites having mixed occupancy in the ratio 4:3 Bi:Te, similar to that observed for other members of the series [12]. Jeffries *et al.* do not report any observations on pressure release.

2.4.3 Bi_2Te

At ambient conditions, Bi_2Te crystallises in a layered *P-3m* structure, as it is a member of the $(Bi_2)_m(Bi_2Te_3)_n$ series with $m = 2$ and $n = 1$ [24]. It consists of one Bi_2Te_3 block and two Bi_2 blocks, as illustrated in figure 2.1 on page 7. The structure of this ambient pressure phase was investigated in 2012 by Bos *et al.*, who performed Rietveld structure refinement on x-ray powder diffraction data [28]. The reported structure refinement yielded lattice parameters $a = 4.4688(1)$ Å and $c = 17.9216(4)$ Å.

The only work on the high-pressure structures of Bi_2Te is an XRPD study performed by Stillwell *et al.* published in 2016 [4]. They analysed powdered samples which were confirmed to be of the Bi_2Te composition through XRD characterisation; they report that the measured ambient-pressure lattice parameters were consistent with the work of Bos *et al.* [24]. A diamond anvil cell was used to investigate the high-pressure states up to 47 GPa, with copper powder as a pressure marker and neon pressure transmitting medium (it is noted that the neon can be considered hydrostatic only up to 10 GPa [61]). On pressure increase a new phase (referred to as 'phase II') begins to appear in the diffraction profiles around 5 GPa, alongside the 'phase I' structure from ambient pressure. These peaks are present in the diffraction profiles up to 17 GPa, for the most part alongside peaks from other phases, with only a 2 GPa pressure window where the sample fully adopts the 'phase II' structure. Stillwell *et al.* were unable to determine a structure for this phase that was consistent with the pressure-volume dependence of the previous and next phases.

The mixed 'I+II' phase persists to 9 GPa, where peaks from a third phase (denoted by Stillwell *et al.* as 'phase III') appear. The sample fully adopts the 'phase III' structure at 17 GPa and remains to 47 GPa, the highest pressure reached in this study. This phase was identified as a site-disordered bcc (*Im-3m*) structure, in agreement with recently published work [12]. The lattice parameter

of the bcc structure at 8.8 GPa was reported as $a = 3.747$ Å. No measurements of the sample on pressure release were reported.

2.5 Host-Guest Crystal Structures

In this thesis it is reported, for the first time, that members of the $(Bi_2)_m(Bi_2Te_3)_n$ series adopt a host-guest structure under high pressures. This complex structure (illustrated in figure 2.3) consists of two interpenetrating substructures — the *host* and the *guest*. The host forms a framework through which there are empty channels and in these channels sit linear chains of atoms, known as the guest. Host-guest structures of this type have been reported in a number of elements at high pressures [32] and in $Bi_{1-x}Sb_x$ alloys [19] (which exhibit similar structural behaviour to the Bi-Te series under high pressures).

The host-guest structure of bismuth (Bi-III, stable between 2.8–7.7 GPa) was first reported in 2000 by McMahon *et al.* in a combined powder and single-crystal (SC) x-ray diffraction study [15]. This resolved a long-standing uncertainty on the structure of Bi-III with several previous misidentifications of the structure. For example, a tetragonal structure had been found which explained the experimentally observed diffraction data well, but would lead to a volume increase at the Bi-II to Bi-III transition on increasing pressure [63]. A significant factor in the difficulty of determining this structure had been the lack of high-quality data; single crystal (SC) data in particular.

McMahon *et al.* were able to produce a SC sample by taking highly textured powder samples (consisting of several relatively large crystallites) and increasing the pressure until the sample transformed to the next high-pressure phase (Bi-V with a body-centred-cubic structure). On subsequent pressure release, the sample transformed back to the Bi-III phase and had mostly formed into a single crystallite. This valuable method of pressure-cycling to produce single-crystal samples at high pressures has been exploited in many of the studies of similar host-guest phases. Bi-III SC diffraction patterns were recorded, similar to that in figure 2.4a which shows an example from the host-guest phase of barium, Ba-IV. Two classes of reflections could be identified from the two sublattices (host & guest) and sheets of diffuse scattering due to some positional disorder in the guest were also observed (appearing as lines of diffuse intensity, as in figure 2.4a).

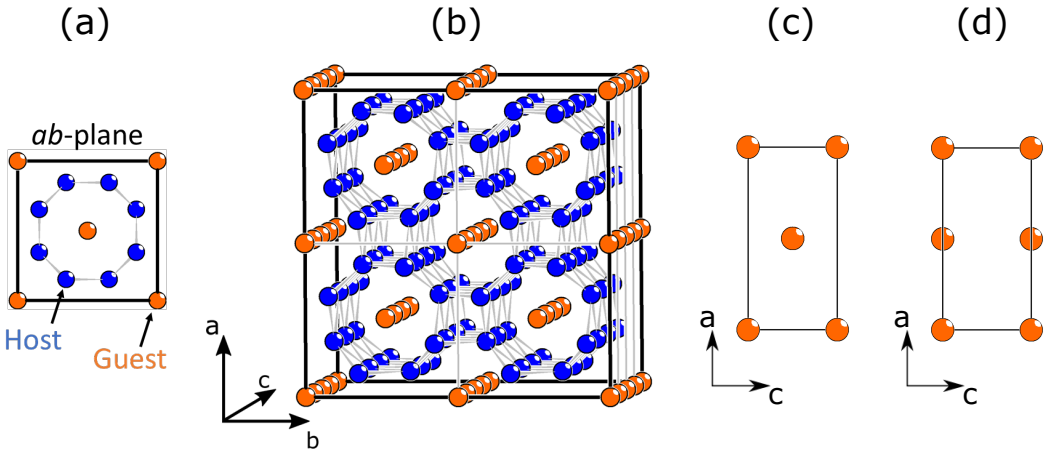

Figure 2.3 *Illustration of the host-guest composite structure found in several elements at high pressures. (a) Unit cell with host and guest components indicated. (b) Projected view of the host-guest structure with the channels formed by the host and the linear guest chains which lie within visible. Figures (c) and (d) illustrate different guest unit cells formed as a result of different relative positions of guest chains in adjacent channels.*

The Bi-III structure was determined to be of the composite *host-guest* type, similar to that previously reported in barium (Ba-IV) at high pressure [64]. The Bi-III structure is illustrated in figure 2.3. It consists of a tetragonal host with space group *I4/mcm* and one free atom at the Wyckoff *8h* position, such that there are 8 atoms in the host unit cell. The host forms a framework through which there are empty octagonal channels running along the direction of the *c*-axis; in these channels sit the atoms of the guest. In Bi-III the guest is also tetragonal with space group *I4/mmm* with atoms at the Wyckoff *2a* site, such that there are two atoms in the body-centred guest unit cell.

The host and guest have the same lattice parameters in the *ab*-plane, but have distinct lattice parameters in the direction of the *c*-axis (i.e. $a_H = b_H = a_G = b_G$ and $c_H \neq c_G$). In fact, the host and guest substructures of Bi-III are found to be incommensurate with one another, such that the ratio c_H/c_G is not a rational number and there are a non-integer number of guest unit cells per host unit cell. They report a c_H/c_G ratio of 1.309(1) at 6.8 GPa that is slightly pressure dependent and did not approach any commensurate (rational) value over the pressure range of the Bi-III phase.

Since its first observation in Ba-IV in 1999 [64], this host-guest composite

structure type with an 8-atom host has been observed in several other elements at high pressures including Sc [65], As [15, 66], Sr [67] and Sb [68]. A similar host-guest composite structure has been observed with the *I4/mcm* host atom placed instead at the *16k* Wyckoff position such that there are then 16 atoms in the host unit cell. This structure has been reported in the elements Rb [13], K [14] and Na [69]. All of these elements share the structural motifs of the *host-guest* structure: two interpenetrating substructures with a tetragonal host containing linear chains of guest atoms within channels which run along the *c*-axis. The linear chains of guest atoms in these systems have been reported to adopt a number of different structures and even undergo intra-phase transitions, where a structural transition occurs only in the guest substructure. Some of the reported guest structures are illustrated in figure 2.3.

The host-guest structure of Ba-IV provides a good example of the complexity that is possible within the guest component. Nelmes *et al.* [64] performed a combined powder and single-crystal (SC) x-ray diffraction study of the high-pressure phase IV above 12 GPa. Two distinct phases labelled 'IVa' and 'IVb' were identified, with a transition from IVa-IVb at 12.5(2) GPa. While both phases adopted the host-guest structures, each had a different guest substructure. Ba-IVa was determined to include several different guest substructures: a c-face centred tetragonal guest (denoted 'C'), and a set of c-face centred monoclinic structures related by 90° rotations around the *c*-axis (denoted 'M'). The relative proportions of these were found to differ in different measured samples.

The transition to Ba-IVb showed no change to the host or C-type guest structures, but the M-type guest was replaced by an orthorhombic structure denoted 'O', the details of which remain unresolved due to a decrease in SC sample quality at the IVa–IVb transition. A further host-guest phase of barium, Ba-IVc, was later investigated by Loa *et al.* and determined to have an extremely complex guest component [70]. The Ba-IVc structure can be described by a representative unit containing 768 atoms, with the guest substructure a complex tiling which shows patterning on the nanometre scale.

A 2004 study by Häussermann *et al.* sought to investigate the effect of alloying on the host-guest structure of $Bi_{1-x}Sb_x$ compounds, considering the fact that both elements adopt host-guest structures themselves (Bi-III and Sb-II) [19]. They measured x-ray powder diffraction data for several compositions of $Bi_{1-x}Sb_x$ and refined them using a 4D superspace method, taking into account expected modulations in the host-guest structure. This was combined with computational

total energy calculations. While their results were somewhat obscured by phase separation occurring in the measured samples, they were able to conclude that neither composition nor pressure had a significant effect on the incommensurate structure of the host-guest phase. Also, their results support the conclusion that there is no chemical ordering within the structures, with all atomic sites occupied by a stoichiometric mix of Bi and Sb.

Clearly a wide variety of host-guest structures exists, with changes in the guest resulting in intra-phase transitions which can include complex guest substructures. Further complexity is added through observations of disorder within the guest component, which will be discussed in the following section.

2.5.1 Guest Chain Disorder and 'Chain Melting'

The example of Ba-IV becomes more complex when the observed guest disorder is considered. Nelmes *et al.* report that while the monoclinic M-type guest of Ba-IVa is well-ordered and crystalline, the tetragonal C-type includes large atomic displacement parameters along the c-axis direction. This is related to a positional disordering of the guest chains along their lengths, where guest chains in different channels are shifted randomly along the c-axis direction, reducing correlation between chains in adjacent channels. This *inter*-chain disorder gives rise to a sharp fall-off in intensity for the C-type guest reflections as a function of l-index. They observed sheets of diffuse scattering perpendicular to the c-axis direction in their single-crystal diffraction patterns (figure 2.4a), attributed to this disorder in the majority C-type guest.

These diffuse features, due to a degree of disorder in the guest component, appear to be a common feature in host-guest x-ray diffraction patterns. Lines of diffuse scattering with $l_{Guest} \neq 0$ have also been observed in Bi-III [15] and Sr-V [67].

It has been suggested that the guest disorder in these structures (Ba-IV, Sr-V and Bi-III) is a result of the incomplete formation of the host-guest phase, rather than an intrinsic feature of the structure. In Ba-IV, for example, the diffuse features were observed to weaken on repeated pressure-cycling through the intraphase (Ba-IVa – Ba-IVb) transition at around 12.5 GPa. This reduction in the diffuse intensity suggests that the structure is moving toward a fully-ordered structure, which must be the true equilibrium state. This is supported by the fact that higher-order (i.e. $l_{Guest} > 1$) sheets of diffuse scattering are readily visible

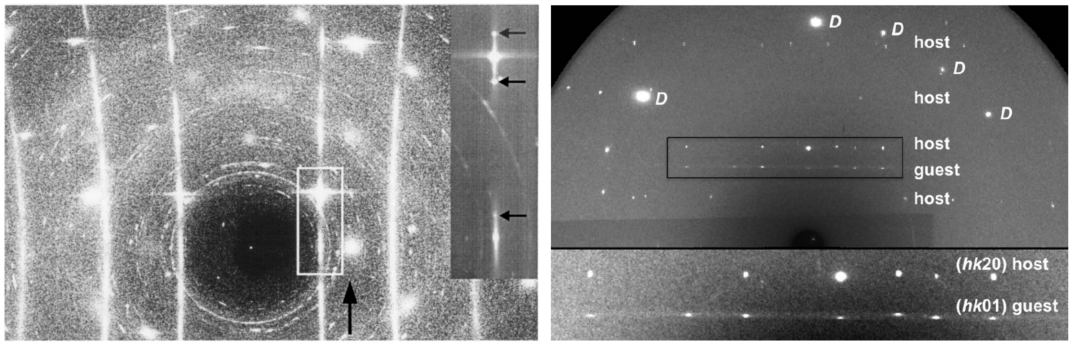

(a) Ba-IV at 12.1 GPa (b) K-III at 20.3 GPa

Figure 2.4 *Examples of room-temperature single-crystal x-ray diffraction patterns from the host-guest phases of (a) barium [64], and (b) potassium [17]. (a) shows the $l \neq 0$ sheets of diffuse scattering from the guest as vertical lines. Powder rings are from contaminant and reflections from the M-type guest are indicated with arrows, next to the stronger C-type reflections. (b) indicates the host and guest reflections, along with those from the diamond anvils (D).*

in the single-crystal and pseudo-single-crystal diffraction patterns, as illustrated in figure 2.4a. This indicates that the guest chains remain well-ordered along their lengths, such that there is no significant *intra*-chain disorder. Furthermore, high temperature studies of Ba-IV to 700 K and Bi-III to 450 K (the maximum temperature that can be reached while remaining in the Bi-III phase) have shown no evidence of induced intra-chain disorder [16].

Distinct from this is the process referred to as '*chain melting*', where the guest is observed to reversibly become disordered due to changes in external conditions such as temperature or pressure. In this process, the guest is found to lose both inter- and intra-chain order and exhibits the properties of a one-dimensional (1D) liquid-like state - hence, 'chain melting'. This process was first investigated in Rb-IV in 2004 and has since been established and closely studied in K-III as well. Recent observations suggest that chain melting may also occur in scandium (Sc) [71] and sodium (Na) [17, 69].

The active process of chain melting was investigated in detail by McMahon and Nelmes in the high-pressure host-guest phase of rubidium, Rb-IV [16]. On pressure increase, the transition from Rb-III to Rb-IV starts at 16.6 GPa, with the sample fully transforming to Rb-IV at 17.2 GPa where it is stable up to around 20 GPa. On pressure decrease from the host-guest phase, slight sample hysteresis allows Rb-IV to exist down to 16.2 GPa, below which the transition back to phase III starts. In their previous work on Rb-IV [13], they observed the guest

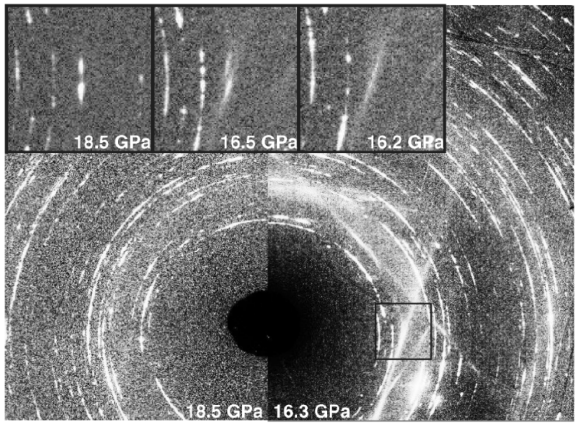

Figure 2.5 *Figure 2 from [16] illustrating the broadening of the guest reflections below 16.7 GPa with the associated diffuse scattering. The insets focus on the (1001) guest reflections. Both reflections are from different single crystallites, with the lower reflection much more intense.*

reflections to rapidly broaden on pressure decrease below 16.7 GPa with only the strongest (1001) guest reflection visible at 16.2 GPa. As the guest peaks broaden, they observed sheets of diffuse scattering developing and increasing in intensity. This process is reversible, with the diffuse scattering reducing on pressure increase and vanishing at 16.7 GPa.

Clearly, with the pressure range of interest so small (between around 16.7–16.2 GPa) and so close to a phase transition that would lose the Rb-IV single crystal (below 16.2 GPa) this work required very careful pressure alterations. They were successful in measuring SC diffraction patterns at room temperature in approximately 0.1 GPa steps, providing a good level of detail on the observed transition in the guest. Above 16.7 GPa they observed diffraction from a sample consisting of several well-crystallised single crystallites, resulting in overlapping yet separable SC diffraction patterns. On reducing the pressure below this point, the diffraction spots associated with the guest substructure were observed to broaden (with no change in the host reflections). This broadening occurred in the *ab* plane i.e. perpendicular to the direction of the guest chain length, as illustrated in figure 2.5.

Two sheets of diffuse scattering can be seen in the right main panel of figure 2.5 as diffuse lines of intensity; these stem from two differently orientated crystallites within the sample. Each sheet is reported to be somewhat structured, with most

of the diffuse intensity centred at the position of the guest reflection and falling off in intensity with distance from this point. This is an extreme broadening of the guest peaks, attributed to a loss of correlation between guest chains in different channels — a loss of inter-chain order. However, the remaining structure within the diffuse scattering is an indication that some inter-chain order still remains, as a complete loss of inter-chain order would result in uniform sheets of diffuse intensity. The fact that only the first order sheet of diffuse scattering ($l_{Guest} = 1$) is visible signifies a loss of order within each guest chain.

It is by this loss of *intra*-chain order that the process of chain melting is distinct from the inter-chain guest disorder reported in Ba-IV, Sr-V and Bi-III which has been associated with incomplete formation of a fully ordered host-guest structure. In chain melting the guest has lost both inter- and intra-chain order, allowing it to be described as a '1D ordered liquid' [16, 72] and the guest chains can be said to have truly melted in the direction of the c-axis.

Recent work in 2015 investigated a similar transition in the host-guest phase of potassium, K-III [17]. In this work the transition could be studied as a function of temperature and pressure up to 47 GPa and 750 K. At room temperature K-III is stable between 19–54 GPa in two forms, K-IIIa and K-IIIb, both of which have a 16-atom host. K-IIIa features a tetragonal C-face centred guest structure and K-IIIb has an orthorhombic A-face centred guest structure. On pressure increase the K-IIIa phase transforms to K-IIIb at 30 GPa, then the sample transforms back to K-IIIa at 40 GPa; these transitions are reversible on pressure decrease [73].

McBride *et al.* had previously observed K-III to undergo an order-disorder transition within its guest component, similar to Rb-IV, between 350–420 K at 21 GPa [74]. The reversibility of this transition, along with the distances from pressure or temperature induced phase transitions indicated that K-III presented an opportunity to investigate this chain melting phenomenon in detail. To do so, a high quality single crystal of K-III was produced at 20.3 GPa through melting and high-temperature annealing. This SC sample was analysed in detail using synchrotron x-ray diffraction over a temperature range of 295–345 K.

The effect on the diffraction pattern is illustrated in figure 2.6 where the chain melting process can be followed clearly. Initially, the SC diffraction peaks can be identified as host reflections (sharp spots) and guest reflections, which are broadened in the *ab*-plane. As the temperature is increased these guest peaks broaden further and form sheets of diffuse scattering, as observed in Rb-

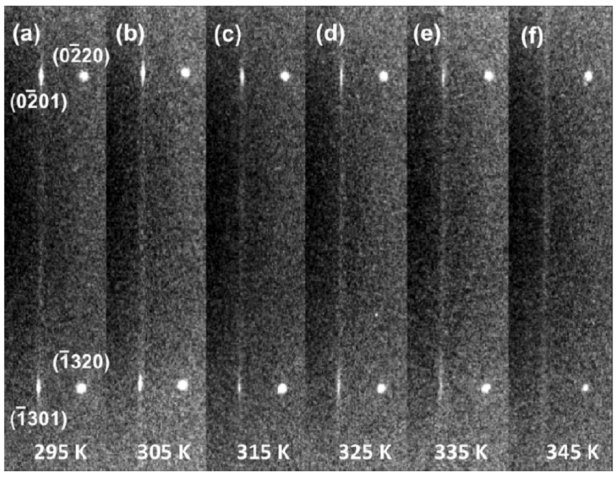

Figure 2.6 *Figure 3 from [17] illustrating the temperature-induced guest chain melting in the K-III host-guest structure. The host reflections are sharp spots, while the guest reflections are broadened in the ab-plane. This broadening increases with temperature until the guest contributes only a uniform sheet of diffuse intensity to the diffraction pattern.*

IV. Unlike in Rb-IV, where the chain melting process is 'interrupted' by the transition back to Rb-III at 16.2 GPa, here the process can be followed fully. The gradual transition of the guest peaks is evident; from broadened SC reflections, to 'disc-like' sheets of diffuse scattering (with intensity peaked around the guest reflections), and finally to uniform sheets of diffuse scattering, as inter-chain ordering is lost entirely. As in Rb-IV, large anisotropic atomic displacement factors are found for the guest atoms along the length of the chains as a precursor to chain melting. Also in concurrence with observations in Rb-IV, only the first-order sheet of diffuse scattering is visible (figure 2.4b) suggesting that there is significant intra-chain disorder in the chain-melted K-III structure as well as Rb-IV.

To investigate chain melting at higher pressures required the use of poly-crystalline and pseudo-single-crystal samples, as high-quality single crystals were difficult to grow at elevated pressures. In these cases the chain melting transition could be identified from the disappearance of Bragg scattering from these powder-like samples. These results were consistent with the chain melting temperature determined from the SC sample at 20 GPa. Recent work has studied this chain melting process with the use of atomistic simulations of the potassium structure, finding no long-ranged order between chains in adjacent channels or along the

lengths of individual chains [18].

Similar behaviour has been widely studied in the $Hg_{3-\delta}AsF_6$ compound, which adopts a different host-guest structure. In $Hg_{3-\delta}AsF_6$ the linear guest chains (comprised fully of Hg) lie in channels which run through the host framework (comprised of AsF_6) in two perpendicular directions. At room temperature, these guest chains are fully disordered to the extent that they can be classified as an 'ordered 1D liquid' [72]. The study of this compound has informed many of the studies of the elemental host-guest systems and the disorder of the guest components within them.

2.6 Bi-Te Compounds – Physical Properties Under Pressure

Bi-Te compounds have been investigated under pressure mainly in an effort to find new pressure-induced phases which have interesting physical properties. A number of the properties which make bismuth-tellurides so interesting are found to be greatly affected by pressure, either being induced in a high-pressure phase or becoming enhanced or degraded by the application of pressure. This section introduces some of the key properties that motivate high-pressure research into bismuth-tellurides and the effect that pressure has on these properties.

2.6.1 Thermoelectricity

The bismuth-tellurides are probably best known for their thermoelectric properties, with Bi_2Te_3 one of the most widely recognised efficient thermoelectric materials for applications near room temperature. The thermoelectric effect describes the ability of a material to generate a voltage difference from an applied thermal gradient, or vice versa. In a simple interpretation of this – the Seebeck effect – the mean free path of free charge carriers within the material is dependent on the temperature of the material. If a thermal gradient exists across the material, the mean free paths of charge carriers at one end will be longer than those at the other end, resulting in a difference in density of free charge carriers in the material. This establishes a voltage difference parallel to the thermal gradient (or anti-parallel, depending on material properties). This effect can be utilised

to build thermoelectric modules from pairs of thermoelectric materials which can generate electricity from heat without the need for moving parts. This effect can also work in reverse, producing a temperature gradient from an applied voltage in what is known as the Peltier effect. This means that thermoelectric modules can also operate in reverse and be used for cooling or heating applications (Peltier coolers are a common application of these materials and are particularly useful for cooling of electronic components).

Unfortunately, current thermoelectric materials are quite inefficient, limiting their use to niche applications. An efficient thermoelectric must balance a set of competing material properties; it must have a high electrical conductivity, while also having a low thermal conductivity to maintain the temperature gradient across it. The search for efficient thermoelectrics employs a wide range of techniques including doping of materials, nanostructuring and the search for complex crystal structures. Part of this has included studies of materials under high pressures, where novel, complex structures can occur, and the effect of pressure on the electronic structure of a material may produce improvements in thermoelectric efficiency.

Such improvements have been reported previously. In 2007, Ovsyannikov *et al.* reported significant improvement of the thermoelectric properties of PbTe-based compounds under 2–3 GPa of pressure [75]. Soon after, the same group reported a pressure-induced (up to ten-fold) improvement in the thermoelectric power factor (defined $\alpha^2\sigma$ where α is the Seebeck coefficient, the ratio of the voltage developed to the temperature gradient, and σ is the electrical conductivity) of pure and indium-doped Bi_2Te_3 [7]. Since then, the group has continued work on high-pressure effects in thermoelectrics, including Bi_2Te_3-based compounds alloyed with antimony — again with significant improvements to the thermoelectric properties under 2–4 GPa of pressure [8].

While this work does seem encouraging, with titles referring to 'colossal' and 'giant' improvement of thermoelectric properties, the results must be carefully considered. There is no doubt that the work represents a promising avenue for the development of thermoelectric materials and each example shows clear dependence of thermoelectric properties on pressure, with potential improvements attainable at a few GPa, but the quoted quantitative enhancements may not be reliable for two reasons.

Firstly, measurement of TE properties is notoriously difficult and can suffer

from large errors and inconsistencies [76]. The second reason for caution lies in the reproducibility of results. While the complexity of thermoelectric property measurement at high pressure makes independent verification of high-pressure measurements less likely, several other groups have published results that do not corroborate these high-pressure improvements. Work by Jacobsen *et al.* in 2012 [77] and Ibarra-Hernandez *et al.* in 2014 [78] fail to confirm the results of Ovsyannikov *et al.* Both examples did find pressure dependence but found the thermoelectric feasibility of the materials to worsen with increasing pressure.

Jacobsen *et al.* performed electronic transport measurements on samples of Bi_2Te_3, Sb_2Te_3 and $BiSbTe_3$ up to 10 GPa. They found interesting structure in the pressure dependence of the thermoelectric figure of merit of Bi_2Te_3 where it was found to drop, then recover its ambient pressure value at around 2 GPa, in agreement with the expected 'electronic topological transition' which has since been established [39]. The overall trend, however, was for the figure of merit to drop substantially (by around 90%) between ambient pressure and 10 GPa. Ibarra-Hernandez *et al.* performed density functional theory calculations on p-type Bi_2Te_3 up to 5 GPa. They found an overall decrease in the thermopower, S, with an anomaly at around 2 GPa indicative of an 'electronic topological transition'. As such, they found the thermoelectric efficiency of the material to reduce with applied pressure.

The authors suggest that differences in samples used may account for the disagreement with the results of Ovsyannikov *et al.* Jacobsen *et al.* worked with powdered n-type samples, whereas Ovsyannikov *et al.* investigated single crystals of p-type [7]. The *ab initio* simulations by Ibarra-Hernandez *et al.* disagreed with both other works to some extent, suggesting that the results of Jacobsen may be subject to preferred orientation effects in their powders.

2.6.2 Superconductivity

Pressure-induced superconductivity in Bi_2Te_3 has been well established [2] and investigated through physical measurements and calculations. Electrical resistance measurements of Bi_2Te_3 at high pressures were performed by Einaga *et al.* in 2010 in order to build on previous work. They observed the onset of superconductivity at 9 GPa, with the sample starting in the first high-pressure phase (Bi_2Te_3-II) at room temperature, before the temperature was reduced. The behaviour of the superconductivity was found to change above 11 GPa which was

attributed to the gradual ingrowth of the next high-pressure phase (Bi_2Te_3-III). Earlier work by Zhang *et al.* reported superconductivity in Bi_2Te_3 between 3–6 GPa, while in the same structural phase (Bi_2Te_3-II). The ambient-pressure phase is semiconducting and not found to exhibit superconductivity [79].

High-pressure superconductivity has also been investigated in other members of the $(Bi_2)_m(Bi_2Te_3)_n$ series, providing some of the few structural studies of other Bi-Te compositions under high pressures. Jeffries *et al.* investigated Bi_4Te_3 in 2011 [3] and Stillwell *et al.* investigated Bi_2Te in 2016 [4]. Both studies performed electronic transport measurements using an eight-probe designer diamond anvil cell (DAC) with steatite pressure-transmitting medium and supplemented these with x-ray diffraction structural studies using a standard DAC and neon pressure-transmitting medium. It should be noted that while neon can be considered hydrostatic up to ∼10- GPa [61], steatite is a solid and can support substantial pressure gradients. As such, some discrepancies between the transition pressures reported in the electronic and structural studies may be expected.

Bi_4Te_3 transforms from its ambient-pressure layered $R3\bar{m}$ structure to a monoclinic *C2/m* structure near 6 GPa at room temperature; the onset of superconductivity was reported to occur within this high-pressure phase at 8.2 GPa with a low critical temperature of $T_c = 2.1\ K$. It should be noted, however, that high-pressure low-temperature structure measurements were not performed and this conclusion is based on the room-temperature structural behaviour of Bi_4Te_3. On further pressure increase, T_c increases and reaches 3.7 K at 12.8 GPa. A discontinuous increase in T_c occurs around 13 GPa, concurrent with the growth of the body-centred cubic (bcc) phase in the sample. This bcc phase includes a new superconducting state with T_c enhanced by a factor of two, reaching a maximum value of $T_c = 8.4\ K$ at 16.2 GPa near where the sample fully adopts the bcc structure (16.5 GPa). At higher pressures, T_c decreases to 4.1 K at 42.5 GPa (the maximum pressure attained in this study).

The onset of superconductivity in Bi_2Te occurs at 11.5 GPa while the sample is in a mixed phase of the first high-pressure phase (Bi_2Te-II, structure unresolved in this work) and the second-high-pressure phase (Bi_2Te-III, with the body-centred cubic structure). However, Bi_2Te did not fully enter the superconducting state at this pressure due to the limitations of the experiment ($T_{min} = 1.8\ K$), but extrapolation of the resistivity to lower temperatures indicated a broad transition to the superconducting state with $T_c \approx 2.1\ K$. The critical temperature increases as the pressure is increased to 12.9 GPa, at which point two distinct T_c values are

identified, each associated with the individual structures in the mixed phase (II + III). The superconductivity associated with the bcc phase is reported to dominate the transition, with only a single critical temperature present at 14.5 GPa, which has a value of $T_c = 8.6\ K$, the maximum T_c recorded in this work. The critical temperature decreases on further pressure increase, down to a value of 4.9 K at the maximum pressure attained, 32 GPa.

2.6.3 Topological Insulators

Topological insulators (TIs) display both electrically insulating and conducting properties. In the bulk of the material they are insulators, but at the surface of the material there exist certain 'topologically protected' states that are conducting. These states allow the transport of electrons but the direction of this transport is spin-dependent due to strong spin-orbit coupling, with up spins moving in one direction and down spins moving in another. This directionality greatly reduces the amount of heat produced as current passes through these states and leads to efficient transport of electrons. The fact that the direction is spin-dependent is a valuable property for potential applications in spintronics.

These conducting states exist as one-dimensional edge states for two-dimensional (2D) topological insulators, and as two-dimensional surface states for 3D TI's. These states are protected against changes of topology, such that changes in the material's shape and dimensions have no effect on these states or their ability to transport electrons. These properties make TI's of interest in practical applications such as in quantum computing, or as a means to study exotic states such as Majorana fermions.

In 2007 Bi_2Te_3 was predicted as having topological insulation properties [5]. This was soon experimentally confirmed by Chen *et al.* in 2009, using angle-resolved photoemission spectroscopy (ARPES) [6]. Their widely-cited work established Bi_2Te_3 as a model example of a 3D topological insulator, leading to much scientific interest in this compound.

Bilayers of elemental bismuth have been shown to exhibit TI behaviour in a combined study including scanning tunneling microscopy and spectroscopy, ARPES, and density functional theory band-structure calculations. Yang *et al.* resolved the one-dimensional edge states in a single Bi bilayer, indicative of its behaviour as a two-dimensional topological insulator [80]. The fact that both

components of phase I of the Bi-Te series (Bi_2 bilayers and five-layer Bi_2Te_3 blocks) exhibit topological insulator properties suggests that the other members are likely to exhibit TI behaviour [81].

Other than the end members, the Bi-Te series has not been well-studied in terms of topological insulation, particularly under pressure. However, recent work has suggested that topological insulation may be a common feature of phase I of the Bi-Te series at ambient conditions. Eschbach *et al.* have reported BiTe to exhibit three-dimensional TI properties [82] and band structure calculations by Saito *et al.* have predicted that Bi_4Te_3 also exhibits TI properties.

2.7 Conclusion

The infinitely adaptive $(Bi_2)_m(Bi_2Te_3)_n$ series spans a wide range of compositions and describes compounds which share many structural and physical properties. It is these similarities, along with the observed differences, that make this series so interesting. Common structural behaviour under pressure can allow for the effect of composition to be studied directly, with series members adopting a number of crystallographically interesting structures. Bismuth-tellurides also exhibit a variety of properties that are of interest to fundamental condensed matter research and have potential for practical applications. The application of pressure has been reported to affect these properties, likely through changes to the structures of these materials.

Despite this, the current understanding of the high-pressure crystal structures is fragmentary. Most structural studies have focused on the end members, Bi and Bi_2Te_3, with only a few high-pressure studies of other compositions (Bi_4Te_3 and Bi_2Te). The work presented in this thesis seeks to expand the understanding of these materials under pressure through analysis of the crystal structures and investigating the similarities and differences as a function of composition.

The next chapter will introduce the experimental methods used in this work and the underlying theory of x-ray diffraction. Following that, the compositions and structural phases investigated here will be summarised in what will be a short reference chapter. The results of our high-pressure studies and analysis will then be detailed one composition at a time, before these results are discussed in the context of the series as a whole.

Chapter 3

Theory & Method

3.1 Introduction

One method that is employed to determine the crystal structure of materials is x-ray diffraction. The work in this thesis is primarily based on data gathered during high-pressure *x-ray powder diffraction* (XRPD) experiments. The typical workflow of an XRPD experiment is illustrated in figure 3.1. Intense monochromatic x-rays are directed through a powdered sample that is held at high pressure. The sample diffracts the x-rays in a way that is characteristic of its structure at the atomic scale, producing a diffraction pattern that is recorded as an image on a detector. This image is then processed to produce a diffraction profile of diffracted x-ray intensity as a function of diffraction angle; the positions and intensities of peaks in this profile can be analysed to determine the crystal structure of the material.

This analysis includes *structure refinement*, where a model structure (the 'best guess' at the true structure of the material) is used to simulate an XRPD profile. This simulated profile is compared to the profile measured in the experiment and the structural parameters of the model are varied in such a way as to reduce the difference between the two profiles. When good agreement has been achieved, the resulting *refined* structural parameters of the model represent the best understanding of the material's structure that is achievable from the measured data. Of course, this is a simplified description, and care must be taken by the analyst to ensure that the resulting structural model is physically sensible

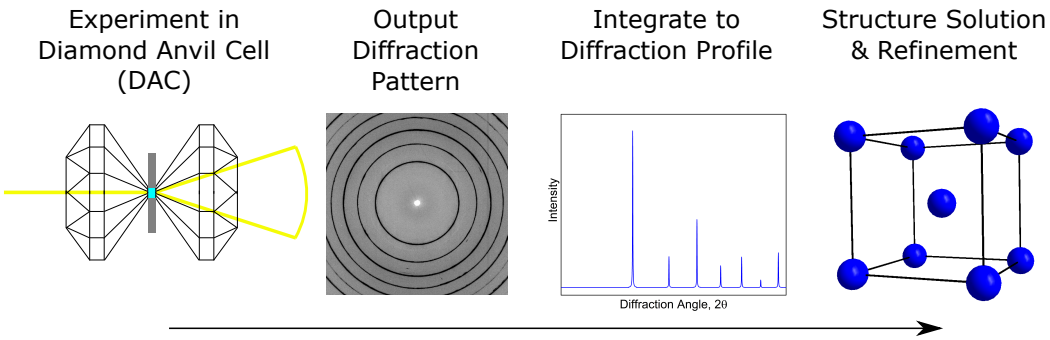

Figure 3.1 *Illustration of the typical process of a high-pressure x-ray powder diffraction experiment.*

and appropriate given the wider details of the experiment and the material investigated.

This work on the bismuth-telluride series includes the XRPD analysis of a complex *host-guest* structure, the analysis of which warranted the use of a custom Rietveld refinement program, written in Python. What follows in this chapter is an overview of the theoretical background to the XRPD technique, describing the physical principles that must be understood in order to develop a refinement program. We must understand what is meant by a 'crystal' and how x-rays are diffracted by crystals and how we can start from a model of a crystal structure and simulate an XRPD profile from the underlying physical principles. All while taking the physical and practical limitations of the experiment into account.

3.2 High-Pressure Experiment Methods

Pressure is now widely and regularly employed as a valuable tool in the study of condensed matter physics. The application of pressure increases the density of materials, typically forcing atoms closer together resulting in dramatic changes to the electronic and atomic structures of materials. This, in turn, can result in the adoption of surprisingly complex structures and the exhibition of new physical properties.

The generation of high pressures for experiments initially relied on bulky pieces of apparatus such as hydraulic presses which could apply large forces to relatively large ($\sim 10\ \mathrm{mm}^3$) samples. Further static compression to above ~ 10 GPa is based on the principle: *pressure = force/area*. By reducing the size of the sample we can produce larger pressures, up to the point where the limiting factor becomes

the hardness of the materials used in construction of the pressure-generating device. A valuable asset to high-pressure research is the *Diamond Anvil Cell* (DAC) which compresses a sample between two diamond anvils. This design has certain incidental benefits such as the fact that the diamond anvils are transparent to a wide spectrum of light, providing 'windows' to the sample under pressure. However, the inherently small size of the sample poses certain challenges such as how to obtain a measurable signal-to-noise ratio in an x-ray diffraction experiment (as a small sample results is less diffracted intensity than a larger sample).

This problem can be addressed by the use of *synchrotron* x-ray sources, which produce intense and highly-focused beams of x-rays that can provide ample signal from the small samples used in high-pressure DAC experiments. Synchrotrons are also able to produce a well-focussed beam — an important feature that allows the x-rays to be directed only on to the small sample, while avoiding the surrounding components of the DAC. The development of such experimental tools and techniques, along with the methods of data analysis have largely kept pace with one another, making high-pressure condensed matter physics a field where experiment, theory and technology are constantly developing in parallel.

3.2.1 The Diamond Anvil Cell

The Diamond Anvil Cell (DAC), illustrated in figure 3.2, consists of two opposed diamond anvils, typically around 3mm in diameter, with flat tips. The flat tips of the diamonds, or *culets*, are typically several hundreds of microns in diameter. The flat culets enclose a cylindrical hole drilled in a gasket made of thin metal foil (on the order of 100μm, typically pre-indented with the diamond anvils to 30–50μm). The diameter of the hole is smaller than the size of the diamond culets, typically around a third of the size. The flat faces of the diamond culets and the cylindrical hole in the gasket form a *sample chamber* into which the sample, a *pressure-transmitting medium* (PTM) and a pressure marker (here, a ruby sphere) are placed.

Large pressures are produced in the sample chamber as the diamond anvils are forced together, requiring only moderate force due to the small size of the sample chamber. There are several different designs of DAC built with different considerations in mind. The diamond anvil cells used in this work are based on the Merrill-Bassett design [9]. The diamond anvils are mounted to backing plates and are held in a metal housing. The metal housing includes three Allen

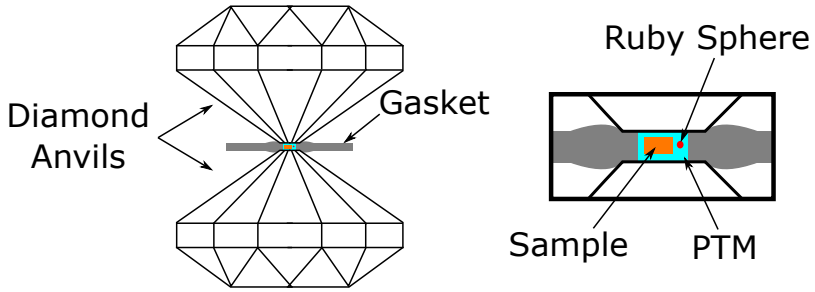

Figure 3.2 *Illustration of a Diamond Anvil Cell (DAC) with enlarged view of sample chamber and key components indicated, including the pressure-transmitting medium (PTM). The cell housing, anvil backing plates and screws have been omitted from this diagram.*

screws and three guide pins which ensure the two plates that form the metal housing (and, hence, the anvils) are aligned. The Allen screws are then tightened carefully by hand, evenly as possible to avoid the diamond culets becoming non-parallel and forcing the sample to one side of the sample chamber. An alternative method of varying the pressure makes use of an external gas membrane, which is attached to the DAC and holds the two halves of the DAC together, without the need for Allen screws. This membrane is filled with gas which causes it to expand and force the diamond anvils together; release of gas from the membrane allows the anvils to separate. This method has the advantage of allowing the DAC to remain mounted to the experimental apparatus, without the need for removal and manual tightening of Allen screws.

The DAC is a valuable tool for performing experiments at high pressures. In an x-ray diffraction experiment the incident x-ray beam is directed on to the sample through one of the diamonds and the diffracted x-rays exit through the second diamond. The Merrill-Bassett-type DAC [9] is small enough to be mounted on most goniometer heads found at synchrotron beamlines, although the construction of the DAC does limit the available range of reciprocal space that can be probed due to the limited opening angle through the sample chamber. It is vital to ensure that the cell is properly aligned in the x-ray beam to avoid clipping of any of the DAC components which will produce unwanted diffraction in the measured 2D diffraction image.

The DAC must be carefully prepared before an experiment with the quality of the *cell loading* potentially affecting the pressure ranges attainable and the quality of the collected data. The disassembled DAC is first cleaned, with particular attention paid to the diamond culets. The thin metal foil forming the gasket is

then *pre-indented* by closing and tightening the DAC with the metal foil between the diamond culets. A hole is then drilled in the centre of this pre-indented region, typically with the use of a spark-erosion device. The size of this hole and the thickness to which the foil is pre-indented define the size of the sample chamber, as discussed in the following section.

The diamond culets are again cleaned and the now fully-formed gasket aligned and placed between the diamonds. Typically the edges of the gasket are secured to the DAC body with some adhesive to keep it stable during loading, with care taken to keep the sample chamber and area around it free of any adhesive. The sample is then prepared (cut to size) and placed in the sample chamber by means of a fine needle, along with any other items such as a ruby sphere for pressure measurement. The chamber is then filled with the pressure-transmitting medium (PTM) and the DAC is closed, taking care to correctly align the two diamond anvils.

All stages of DAC loading require close attention to detail. Any contaminants introduced to the sample chamber will appear in measurements. Common sources of such contamination include dirt washed in to the chamber when the PTM is introduced, unclean diamond culets, unclean gasket hole and (potentially) small pieces of steel shaved off from the needle used in sample placement.

Choice of Gasket Material & Dimensions

The size of the sample chamber is a trade-off between the stability of the chamber (and hence the highest pressures achievable) and the size of sample that can fit into the chamber. A well-loaded DAC will make good use of the chamber volume, while leaving some space around the sample to allow for some hole collapse. As the sample chamber is compressed, the gasket will become thinner and the hole will reduce in size. It is important that none of the contents of the sample chamber is allowed to come into direct contact with both diamond culets; this would bridge directly between the diamonds, causing non-hydrostatic stress in the bridged material and also increasing the likelihood of damaging the diamonds.

The choice of gasket material is dictated by the pressure range being investigated. Inexpensive steel gaskets are used for lower pressures of several GPa, and more expensive tungsten gaskets used for pressures above 10 GPa.

Choice of Pressure-Transmitting Medium

A diamond anvil cell produces pressure by applying a force on the sample chamber in one direction, with the sample contained radially by the gasket. This may result in inhomogeneous compression which can result in the broadening of measured diffraction peaks and systematic *hkl*-dependent shifts in the peak positions. In order to study materials under isotropic, or *hydrostatic*, compression requires the use of a *pressure-transmitting medium* (PTM). The PTM is ideally an inert material that produces little to no x-ray diffraction so as to not interfere with the measurement of diffraction from the sample. The PTM takes the uniaxial stress applied to the sample chamber by the anvils and transfers it to all sides of the sample, resulting in hydrostatic conditions.

Different materials behave differently when utilised as a pressure-transmitting medium with the choice of PTM used in an experiment depending on several factors. These include considerations of how the PTM might react chemically with the sample under investigation, with care taken to use an inert PTM that will not affect the sample. Certain practical considerations are also considered such as availability and cost of the PTM, as well as the complexity of the DAC loading process. Use of liquid helium or nitrogen as a PTM necessitates handling cryogenic liquids and complicates the DAC loading process, whereas use of a PTM that is liquid at ambient conditions allows a much simpler loading.

Above all, the most important consideration is the maximum pressure that is to be reached during the experiment, as the PTM has a significant effect on the pressure range that can be achieved under hydrostatic conditions. Under increasing pressure a liquid PTM will eventually solidify; as solids can support pressure gradients, this leads to non-hydrostatic conditions within the sample chamber. As such, each PTM will have a hydrostatic limit — a pressure above which the PTM is no longer able to produce acceptably hydrostatic conditions. Several common PTM's have liquid-solid transitions that occur at pressures within commonly explored ranges, such as methanol-ethanol (typically a 4:1 mix) at 10.5 GPa and nitrogen at around 10 GPa. Despite becoming solid, these can be considered as producing acceptably hydrostatic conditions up to around 8 GPa and 10 GPa, respectively. The use of liquid helium as a PTM provides hydrostatic conditions up to the highest pressures reached in this work ($\sim$ 25 GPa), despite solidifying at around 12 GPa. Measurement and evaluation of the hydrostatic limits of several pressure-transmitting mediums, including those used in this work,

has been previously reported [61]. Most of the experiments described in this work made use of liquid helium as a pressure-transmitting medium.

3.2.2 Pressure Measurement

In this work we used the ruby fluorescence technique, first described in 1972 [83], to determine the pressure inside the sample chamber of the DAC. Ruby (Al_2O_3 doped with a small amount of Cr^{3+}) fluoresces strongly due to electronic transitions in the Cr ions, with two lines at $R_1 = 692.86$ nm and $R_2 = 694.25$ nm at ambient temperature and pressure. The positions of these lines are pressure-dependent, allowing the shift in the observed wavelength of either line (usually R_1) relative to a reading taken at ambient pressure to be used for pressure measurement according to equation 3.1, where A and B are constants, $\Delta\lambda$ is the wavelength shift, and λ_0 is the wavelength of the R_1 line at ambient pressure.

$$P = \frac{A}{B}\left(\left[1 + \frac{\Delta\lambda}{\lambda_0}\right]^B - 1\right) \tag{3.1}$$

The calibration used in this work is that of Mao *et al.* [84] which is valid at room temperature and at pressures up to 80 GPa. This calibration uses constants $A = 19.04$ Mbar and $B = 7.665$. The value of λ_0 was measured at ambient pressure from the ruby spheres loaded with each sample. In the earlier days of this technique ruby flakes were placed in the sample chamber. Now, with the availability of synthetic ruby, a typical DAC is loaded with several ruby spheres of 5-10 μm diameter.

The intensities and positions of the ruby fluorescence lines are sensitive to temperature, making the technique impractical above 550 K [85]. As all data in this work was collected at ambient temperature, these limitations are not an issue.

3.2.3 Synchrotrons

Investigating materials through x-ray diffraction at high pressures often necessitates the use of small samples. A drawback of this is the reduction in diffracting power as the size of the sample is reduced, such that the small samples found

in diamond anvil cell (DAC) experiments offer only very weak x-ray diffraction. To obtain measurable diffraction we require a very intense x-ray source, one that is able to produce monochromatic x-rays for use in x-ray diffraction. As well as intensity we importantly require the x-ray beam to be well-focused to a beam diameter that allows us to direct it through the opening of the DAC and on to the sample, while avoiding the gasket of the DAC. Such an x-ray source exists in *synchrotrons*, the development of which has been a crucial component to the field of high-pressure science. The working principle of a synchrotron is that accelerating charges emit radiation, so by causing the relativistic electrons stored in the synchrotron ring to accelerate they can generate intense x-rays for a variety of scientific applications.

Synchrotrons were first developed in the 1950s as particle accelerators. Charged particles accelerated to relativistic speeds were maintained in an approximately circular path around the ring of a synchrotron by so-called 'bending magnets'. It was found that as the beam of particles was bent by these magnets they emitted intense electromagnetic radiation. This radiation (which was, in effect, a mere by-product of the particle collision apparatus) was recognised as useful and experiments using this intense light were performed parasitically at these 'first-generation' synchrotrons.

As the scientific potential of synchrotron radiation was realised in the 1960s, 'second-generation' synchrotrons began to be constructed purely as intense light sources. The first dedicated synchrotron light source was built at Daresbury, UK in 1980 and now many such facilities exist across the world.

The function of a synchrotron can be described starting with a source of electrons (the charged particles to be accelerated). This is typically done with thermionic emission, which produces bunches of electrons that are accelerated to energies on the order of 100 keV. These electrons are then passed to a linear accelerator (*linac*) where they are accelerated to relativistic velocities with an energy on the order of 100 MeV. The now-relativistic bunches of electrons are then injected into a booster synchrotron which accelerates them to energies of several GeV.

The *booster* is itself a miniature synchrotron where the electrons follow an approximately circular path around an enclosure held under vacuum. This 'track' is a series of connected straight sections, with *bending magnets* at the intersections which correct the trajectory of the electron bunches. The electrons are accelerated in the straight sections by means of a radio-frequency voltage source.

The electron bunches are then injected into the much larger *storage ring* which is similarly formed of a number of straight sections held under vacuum to minimise air scattering, with strong bending magnets at the intersections which keep the electron *beam* in its closed path around the ring. The action of the bending magnets on the beam produces synchrotron light over a wide spectrum tangentially to the plane of the electron beam; such radiation is useful for spectroscopy experiments. While bending magnets ensure the course of the electrons at the intersections, the straight sections also contain focusing magnets that maintain the cross-sectional shape of the beam and radio frequency cavities ensure the energy of the beam does not drop too far as it loses energy in the form of radiation.

Additional components, known as *insertion devices*, are housed in the straight sections and are characteristic of 'third-generation' synchrotrons. These insertion devices further stimulate the electrons in the beam, producing far more intense radiation. There are two main types of insertion devices: *wigglers* and *undulators*. Both types consist of arrays of magnets of alternating polarity which produce a magnetic field perpendicular to the trajectory of the electrons.

A wiggler in its simplest form consists of three magnets; the outer two of opposite polarity to the central magnet. The first magnet typically bends the electron beam in the 'wrong direction' (opposite to the curvature of the synchrotron), the second magnet over-compensates for this, then the third magnet corrects the course of the beam. The second magnet is typically a superconducting magnet that is much stronger than the other two which allows for very tight radius of curvature and hence the production of intense, 'hard' (high-energy) x-rays.

An undulator consists of a number of periodically-spaced low-field magnets that cause the beam to 'undulate' with many small changes in path. X-rays are produced through the alternating accelerations of the electrons, with the x-rays produced at consecutive bends overlapping and interfering. Tuning of this interference by altering the setup of the undulator allows intense peaks of emitted x-rays at particular wavelengths to be selected.

All data in this work were collected at two synchrotron facilities: the European Synchrotron Radiation Facility (ESRF) in Grenoble, France, and Diamond Light Source (DLS) in Oxfordshire, UK.

3.3 Crystals

3.3.1 Theory of Periodic Structures

A periodic crystal is an arrangement of atoms or molecules that exhibits long-range order. An ideal crystal can be described using an infinite array of regularly spaced points that extends in three dimensions. These are known as lattice points and they define the Bravais, or direct, lattice. To each of these lattice points, a basis can be added. A basis is a group of atoms or molecules that, when applied to the lattice points, produces the full crystal structure. As the lattice is regularly spaced in three dimensions it has translational symmetry and can be described by three translation vectors: $\vec{a_1}, \vec{a_2}, \vec{a_3}$. This symmetry is described by:

$$\vec{R'} = \vec{R} + u_1\vec{a_1} + u_2\vec{a_2} + u_3\vec{a_3}, \tag{3.2}$$

where u_1, u_2 and u_3 are integers and the crystal is identical when viewed from every equivalent point, $\vec{R'}$.

The translation vectors describing the lattice form a parallelepiped which is a repeat unit or 'building block' of the crystal. This is often chosen as the unit cell, in which case it is described as a primitive unit cell as it contains a single lattice point. Unlike the lattice, which is an intrinsic property of the crystal structure, the choice of unit cell is arbitrary so that a larger cell may be chosen for convenience depending on symmetry present in the overall structure. A unit cell chosen such that it contains several lattice points is known as centred. The unit cell is described by six parameters: a, b, c, α, β and γ, which denote the magnitudes of the three vectors forming the cell and the angles between them — this is illustrated in figure 3.3. These are known interchangeably as lattice parameters or unit cell parameters. The volume of the unit cell is given by: $\vec{a} \cdot \vec{b} \times \vec{c}$.

Crystal structures tend to display symmetries other than their inherent translational symmetry such as inversion points, rotation axes and reflection planes. Such symmetries impose restrictions on the unit cell parameters that can be used to describe the crystal. There are 32 classes of symmetry applicable to three-dimensional crystals, resulting in 14 fundamental lattice types which are described by the restrictions placed on their unit cell parameters. These 14

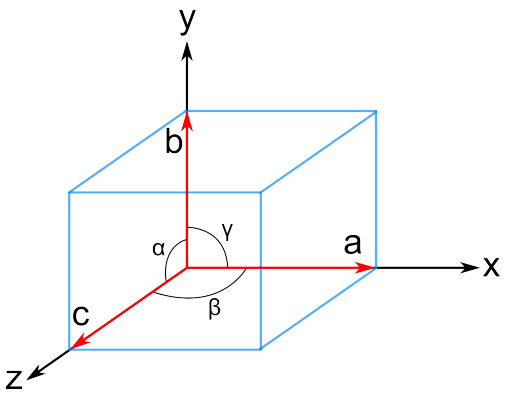

Figure 3.3 *Simple illustration of a unit cell, with the lattice parameters, a, b & c, and angles between them, α, β & γ, shown.*

'Bravais Lattices' include the triclinic lattice (where a, b, c, α, β and γ are all independent) along with 13 special lattice types where restrictions are imposed.

As a point in a particular unit cell is equivalent to that same point in any other unit cell, combinations of translation and other symmetry operations are permissible. The point group symmetry elements that are present in one unit cell are simultaneously present in all other unit cells throughout the crystal. There are a finite number of ways to consistently combine the point group symmetry elements with the translational symmetries of the crystal. Combination of these elements described the complete symmetry of the crystal structure and is known as the space group. There are 230 possible space groups and they are tabulated in the International Tables for Crystallography, Volume A [86].

Symmetry elements can relate atoms within the unit cell to one another, as such the smallest unique portion of the structure can be smaller than the unit cell. This portion is known as the asymmetric unit and it generates all atoms in the unit cell when the symmetry operations of the space group are applied to it. The position of an atom within the unit cell is described as shown in equation 3.3 using fractional coordinates x_j, y_j and z_j which describe the position of the j-th atom in terms of the unit cell dimensions. Atoms in a unit cell occupy the Wyckoff positions associated with the crystal space group. These describe the unique positions available in the unit cell, from which all others are produced by symmetry. These positions are labelled by a letter, assigned in order, preceded by a number that is the multiplicity of the position e.g. *1a* for the general position (x, y, z) or *4c* etc. for other special positions.

$$\vec{r_j} = x_j\vec{a} + y_j\vec{b} + z_j\vec{c} \tag{3.3}$$

The atomic sites in a unit cell need not be fully occupied by one atom type. As the unit cell describes essentially an average of the overall structure, atomic sites can be partially vacant or partially occupied by one or more atom types. This is described by the site occupation factor (SOF) that ranges from 0 for an unoccupied site to 1 for a fully occupied site. Mixed sites often have the condition that the site occupation factors of the different atom types sharing the site must sum to 1 for a mixed but fully occupied site.

A crystal also has an associated reciprocal lattice, described with three vectors: $\vec{a^*}$, $\vec{b^*}$ and $\vec{c^*}$ that are related to the direct lattice by the set of equations 3.4. Points on the reciprocal lattice are described by the reciprocal lattice vector $\vec{G}_{hkl}$, where h, k and l are integers.

$$\begin{aligned} \vec{a^*} &= 2\pi \frac{\vec{b} \times \vec{c}}{\vec{a} \cdot \vec{b} \times \vec{c}} \\ \vec{b^*} &= 2\pi \frac{\vec{c} \times \vec{a}}{\vec{a} \cdot \vec{b} \times \vec{c}} \\ \vec{c^*} &= 2\pi \frac{\vec{a} \times \vec{b}}{\vec{a} \cdot \vec{b} \times \vec{c}} \end{aligned} \tag{3.4}$$

$$\vec{G}_{hkl} = h\vec{a} + k\vec{b} + l\vec{c} \tag{3.5}$$

3.3.2 Disordered and Aperiodic Crystals

A periodic crystalline material consists of atoms that are regularly-spaced in three dimensions. However, a solid material need not be crystalline — a *glass* is essentially the opposite of a crystal, where the atoms are randomly placed in three dimensions (subject to bond length constraints) and there is no long-range ordering of the atoms. There exists a wide range of possibilities between the extremes of a perfect crystal (ordered) and a perfect glass (disordered) where a crystalline material can include a degree of disorder. Indeed, this is the case in most (real) physical materials. Disorder may be present through irregularities of the atom types (substitutional disorder) or through offsets in the positions of atoms from their periodic positions (structural disorder).

Structural disorder can be either static or dynamic. Static disorder occurs when

the positions of atoms are not identical in all unit cells, leading to difficulties in describing the structure using one 'averaged' unit cell. Dynamic disorder is due to the thermal motion of atoms in the structure; this occurs on a much shorter timescale than a typical diffraction experiment and so the experimental data gives a time-averaged picture of the structure.

Static structural disorder is the most pertinent to this project and will be discussed further in terms of the composite 'host-guest' structure investigated here. Substitutional disorder is somewhat accounted for through the refined site occupation factors (allowing multiple atoms types to share the same position) and dynamic disorder through the 'atomic displacement factors' that will be introduced in the following section.

3.4 X-ray Diffraction

The technique of x-ray diffraction was first demonstrated by Max von Laue in 1912 [87] shining (relatively recently discovered) x-rays though a copper sulphate crystal and observing a diffraction pattern on a photographic plate. For this, he was awarded the 1914 Nobel Prize in Physics. The field of x-ray crystallography developed rapidly from then, with the advent of computerised techniques later in the century making the investigation and solution of extremely complex structures possible.

In an x-ray diffraction experiment, x-rays are shone through a sample and the intensities of diffracted x-rays are measured as a function of either x-ray energy or diffraction angle. Early x-ray diffraction experiments used 'white' x-ray beams with a number of different superimposed wavelengths in energy-dispersive experiments. This made full use of the comparatively low intensity achievable with early x-ray sources. As more intense sources became available, in particular synchrotron sources, angle-dispersive x-ray diffraction experiments using monochromatic x-rays became more practical.

The x-rays are diffracted through their interaction with the electron density within the sample. As areas of high electron density can be identified as the positions of atoms, x-ray diffraction can be used to determine the atomic structure of materials. In order to resolve an image of the structure from an x-ray diffraction pattern, the diffracted x-rays would need to be re-combined taking into account

their amplitudes and relative phases. Unfortunately, while the amplitudes are proportional to the measured intensities, the phase information is lost leading to the central challenge of x-ray crystallography: the phase problem.

In the case of single-crystal diffraction, the diffraction pattern is essentially an image of the reciprocal lattice, which is, in turn, the Fourier transform of the image of the crystal lattice. If it were possible to directly recombine the pattern of scattered radiation to obtain an image of the lattice, this would be a Fourier transform of the scattering pattern, returning to the original object and leaving us with an image of the crystal structure.

Crystal structures act as three-dimensional diffraction gratings for x-rays, producing a diffraction pattern characteristic of the structure where interference between the diffracted x-rays produce high, measurable intensities only in certain directions. The positions of points observed in the scattering pattern relate to the symmetry and size of the unit cell, while the relative intensities of these points relate to the positions and types of atoms within the unit cell. It is the job of the crystallographer to circumvent the phase problem by determining a suitable and physically sensible model for the positions of atoms within the unit cell.

3.4.1 Theory of X-ray Diffraction

This section will present the relevant theory of x-ray diffraction by following Kittel [88], Warren [89] and the textbook of the Durham School on X-ray Crystallography [90]. We will build up from the scattering due to a single electron to the scattering conditions for a crystalline sample. We will then go on to present the calculation of the intensities of diffracted x-rays and show how theory links the measured intensities to structural properties and how accurate simulations can be developed using this theory. The expressions introduced here are used in the bespoke crystal structure refinement code developed for this project and the origin of the different corrections and refinable parameters will be discussed.

Scattering by an Atom

X-rays are electromagnetic waves with orthogonal oscillating electric and magnetic fields, both perpendicular to the direction of travel. X-rays are scattered through interaction with the electron cloud of an atom (rather than with the

atomic nucleus, as is the case for neutron diffraction). The electric component of the wave interacts with the electrons, causing them to accelerate and become a source of radiation of the same wavelength; this is the scattered radiation. An electron in isolation would scatter x-rays in all directions with equal intensity except for a polarisation factor which is a function of diffraction angle (this will be described in detail in section 3.4.2).

As the wavelength of x-rays is on the same scale as an atom, interference can occur between x-rays scattered from different parts of an atom's electron cloud. This results in a drop-off in scattered intensity with increasing diffraction angle, as described by the atomic form factor.

Scattering by a Crystal

The translational symmetry of periodic crystals gives rise to x-ray diffraction; a regular spacing of objects separated by a distance comparable to the wavelength of the incident radiation will act as a diffraction grating. This process of diffraction by a large number of arranged atoms results in measurable diffracted intensity which contains some information about the crystal.

Bragg's Law

The Bragg formalism considers x-ray diffraction in terms of interference between x-rays scattered from planes of atoms within a crystal, as illustrated schematically in figure 3.4. While this model is not as physically rigorous as the Laue formalism (discussed later), it offers an intuitive way of understanding the process of diffraction and is more convenient in many applications. Both formalisms give equivalent results. In the Bragg formalism, sets of planes are denoted by three Miller indices h, k and l which describe how a plane intersects the three axes of the unit cell: $\vec{a}$, $\vec{b}$ and $\vec{c}$. Any particular set of planes is denoted by (hkl) and intersects the lattice axes at $\frac{\vec{a}}{h}$, $\frac{\vec{b}}{k}$ and $\frac{\vec{c}}{l}$.

The Bragg formalism asserts that each plane of atoms reflects specularly but only certain diffraction angles, where the x-rays scattered from numerous layers interfere constructively, will result in a strong detectable reflection. Considering the geometry of incident x-rays scattering from planes of atoms in a crystal leads

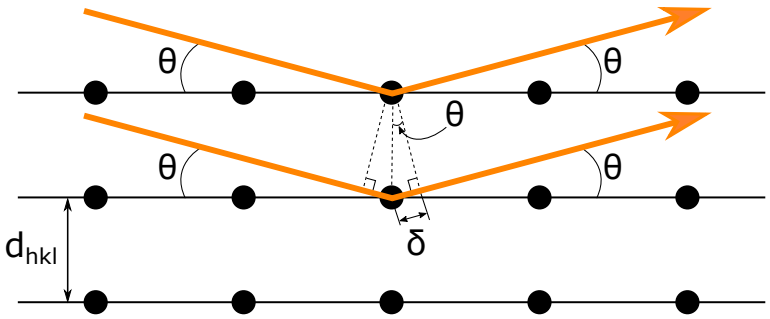

Figure 3.4 *Illustration of x-ray diffraction geometry in relation to Bragg's Law. Planes of atoms are illustrated with the distance between the planes, d_{hkl}, indicated. Incoming x-rays (orange arrows) are specularly reflected by the planes at an angle, θ, with the diffraction angle defined as 2θ. The path length between the illustrated upper and lower x-ray paths is 2δ.*

to Bragg's law, satisfied for wavelengths $\lambda \leq 2d_{hkl}$, which is given by:

$$2d_{hkl} \sin\theta = n\lambda, \tag{3.6}$$

where d_{hkl} is the inter-planar spacing (or 'd-spacing') of planes defined by the indices (hkl), θ is half of the diffraction angle and n describes the scattering order. Note that equation 3.6 depends only on the periodicity of the lattice, not on the contents of the unit cell.

Laue Equations

The Laue formalism offers an alternative, more mathematically sound, description of diffraction. It considers the reciprocal lattice and the wavevectors of the x-rays in reciprocal space.

Consider an incident wave described by its wavevector, $\vec{k}$, scattered by the sample such that the scattered wave has a wavevector, $\vec{k'}$. The scattering vector is then defined as:

$$\Delta\vec{k} = \vec{k'} - \vec{k}. \tag{3.7}$$

The x-ray is scattered by the electron density, $n(\vec{r})$, in a volume element, dV. The amplitude of the scattered wave is proportional to the integral, over the sample,

of the electron density multiplied by the phase factor. This gives an expression for the scattering amplitude:

$$F = \int dV n(\vec{r}) \exp[-i(\Delta\vec{k} \cdot \vec{r})]. \tag{3.8}$$

Due to the crystalline nature of the sample, the electron density is periodic such that $n(\vec{r})$ is invariant under any crystal translation vector, $\vec{T}$. We can expand the periodic electron density, $n(\vec{r})$, as a 3D Fourier series and take the Fourier components of the periodic electron density, $n_{\vec{G}}$, in terms of reciprocal lattice vectors, $\vec{G}$, as shown in equation 3.9.

$$n(\vec{r}) = \sum_{\vec{G}} n_{\vec{G}} \exp(i\vec{G} \cdot \vec{r}) \tag{3.9}$$

Substituting these Fourier components in place of $n(\vec{r})$ we arrive at:

$$F = \sum_{\vec{G}} \int dV n_{\vec{G}} \exp[i(\vec{G} - \Delta\vec{k}) \cdot \vec{r}]. \tag{3.10}$$

We can see that the argument of the exponent vanishes when the scattering vector is equal to a reciprocal lattice vector to give $F = Vn_G$. The value of F is negligibly small for scattering vectors significantly different from any reciprocal lattice vector, hence the diffraction condition is that the scattering vector is equal to a reciprocal lattice vector.

This diffraction condition can be expressed by the Laue equations 3.11, obtained by taking the scalar product of each of the crystal lattice vectors ($\vec{a}$, $\vec{b}$ and $\vec{c}$) with the expression $\Delta\vec{k} = \vec{G}$, using the definition of $\vec{G}$, equation 3.5. They provide a simple geometrical representation which illustrates the condition which must be satisfied for diffraction to occur. Namely, each expression tells us that the scattering vector, $\Delta\vec{k}$, lies on a cone about the direction of each lattice vector.

$$\vec{a} \cdot \Delta\vec{k} = 2\pi h; \qquad \vec{b} \cdot \Delta\vec{k} = 2\pi k; \qquad \vec{c} \cdot \Delta\vec{k} = 2\pi l \tag{3.11}$$

3.4.2 Intensities of Diffracted X-rays

When the diffraction condition is met, equation 3.8 can be written, for a crystal of N cells, as:

$$F_{\vec{G}} = N \int_{cell} dV n(\vec{r}) \exp[-i\vec{G} \cdot \vec{r}] = NS_{\vec{G}}, \tag{3.12}$$

where $S_{\vec{G}}$ is the structure factor, defined as an integral over a single cell. In order to obtain an expression that integrates over all atoms in one unit cell, we must consider the electron density $n(\vec{r})$ as a superposition of the contributions from each atom, j, in the cell. This contribution is defined as $n_j(\vec{r}-\vec{r_j})$ with the vector from the origin to the centre of atom j given by $\vec{r_j}$. Defining $\vec{\rho} = \vec{r} - \vec{r_j}$, we can write the structure factor as:

$$S_{\vec{G}} = \sum_j \exp(-i\vec{G} \cdot \vec{r_j}) \int dV n_j(\vec{\rho}) \exp(-i\vec{G} \cdot \vec{\rho}). \tag{3.13}$$

The atomic scattering factor (described in detail later) can be defined, integrated over all space, as:

$$f_j = \int dV n_j(\vec{\rho}) \exp(-i\vec{G} \cdot \vec{\rho}). \tag{3.14}$$

As will become important when simulating x-ray powder diffraction profiles, it should be noted that the atomic scattering factor is a function of the diffraction angle. As $G = 4\pi\frac{\sin\theta}{\lambda}$ and therefore $f_j \equiv f_j(\vec{G}) \equiv f_j(\frac{\sin\theta}{\lambda})$. An expression for the structure factor of the basis can then be written as:

$$S_{\vec{G}} = \sum_j f_j \exp(-i\vec{G} \cdot \vec{r_j}). \tag{3.15}$$

Applying the expressions for the position of an atom within the unit cell and the reciprocal lattice vector in terms of the Miller indices (equations 3.3 and 3.5, respectively) to $S_{\vec{G}}$ gives the structure factor for a particular reflection, F_{hkl},

denoted by the set of Miller indices (hkl), as,

$$F_{hkl} = \sum_j f_j \exp[2\pi i(hx_j + ky_j + lz_j)] \tag{3.16}$$

This expression, known as the structure factor, describes the phase and amplitude of x-rays scattered by the (hkl) plane, taking into account the positions and types of atoms in the crystal structure. However, this expression assumes the atoms to be completely stationary within the structure; thermal motion of the atoms must be considered separately. As the atoms move, their surrounding electron clouds are spread out and hence have different scattering characteristics from those assumed in the atomic scattering factor. This is described by the atomic displacement factor, $ADF_{2\theta}$, which is applied to the geometric structure factor.

The intensity of scattered x-rays is proportional to the modulus squared of the structure factor. In order to calculate the intensity of diffracted x-rays from a particular structure (as required during analysis by Rietveld refinement), we must include several prefactors and corrections to the calculated intensity to account for different physical processes. The generalised expression for calculated intensities is shown in equation 3.17 and is the expression used in the Rietveld refinement program used in this work for analysis of the host-guest structure. Existing refinement software (e.g. Jana2006 [91]) utilises a similar expression.

$$I_{hkl} = m_{hkl} \times LPF_{2\theta} \times |ADF_{2\theta} \times F_{hkl}|^2 \tag{3.17}$$

This expression includes the multiplicity, m_{hkl}, which accounts for the number of equivalent orientations of lattice planes that contribute to a given reflection in an x-ray powder diffraction experiment. There is also the Lorentz-polarisation factor, $LPF_{2\theta}$, which corrects the calculated intensities based on the geometry of the experiment and accounts for the anisotropic scattering of polarised x-rays by electrons.

Atomic Scattering Factor

The atomic scattering factor (ASF), also known as the atomic form factor, describes the ratio of the amplitude of radiation scattered by an atom, to that of radiation scattered by a single electron. Interference effects must be considered

as x-rays scattered by different parts of the same electron cloud destructively interfere, resulting in a reduction of the amplitude of scattered x-rays with increasing diffraction angles. In the forward direction, where $\vec{G} = 0$, the value of f_j reduces to Z, the number of atomic electrons.

The ASF is implemented in this project following equation 6.1.1.15 in the International Tables of Crystallography [92]:

$$f\left(\frac{\sin\theta}{\lambda}\right) = c + \sum_{i=1}^{4} a_i \exp\left(\frac{-b_i \sin^2\theta}{\lambda^2}\right), \tag{3.18}$$

where $f(\sin\theta/\lambda)$ is the ASF and the (constant) scattering parameters are given by a_i, b_i and c, which are tabulated for all elements in the International Tables of Crystallography.

This expression is an expansion which approximates the ASF as described by x-ray scattering theory [93] and has been shown to closely fit the atomic scattering curves over a range of values, $0 < \frac{\sin\theta}{\lambda} < 2.0$ Å^{-1} [92]. For an x-ray wavelength of 0.4 Å, this suggests that equation 3.18 is valid for diffraction angles up to $2\theta \approx 106°$, far beyond the typical range (1–30°) considered in a high-pressure XRPD experiment.

Atomic Displacement Factor

The atomic displacement factor (ADF) describes the change in intensity of scattered x-rays, resulting from the movement of the atoms in the structure about their equilibrium positions. A higher temperature will result in larger deviations of the atoms from their equilibrium positions as they have more thermal energy. This movement results in a 'smearing' of each atom's electron cloud, changing the scattering properties of the atom as described by the atomic scattering factor. As the electron cloud becomes more diffuse, the scattering power of the atom reduces.

The expression used in this work to describe the atomic displacement factor is the Debye-Waller isotropic temperature factor; a first approximation to the thermal motion of atoms in a crystal [94]. It is implemented here by equation 3.19, where θ is half the diffraction angle, λ is the x-ray wavelength in Å and U_{iso} is the isotropic thermal parameter, units Å^2, which describes the square of the average

amplitude of thermal vibrations.

$$ADF = \exp\left[\frac{-8\pi^2 U_{iso}\sin^2\theta}{\lambda^2}\right] \tag{3.19}$$

Lorentz-Polarisation Factor

The Lorentz-Polarisation Factor (LPF) is a combined expression describing both polarisation and Lorentz corrections to the intensity of scattered x-rays for a linearly polarised incident beam of x-rays. The LPF is implemented in this work as a single expression, as given by equation 3.20.

$$LPF = \frac{1}{\sin\theta\sin 2\theta} \tag{3.20}$$

The effect of the polarisation of the incident radiation is described by the numerator of equation 3.20. In this work it is set equal to one, as shown in equation 3.20, such that no polarisation correction is applied. This is because the program Fit2D [95, 96], used to process the diffraction pattern images in to XRPD profiles, already accounted for polarisation effects at that stage. The LPF as shown above is the expression used in the custom Rietveld refinement code used to refine the host-guest structures. When existing refinement programs were used, the settings were adjusted to take into account the fact that polarisation had already been accounted for.

Nevertheless, the expressions for polarisation correction will be discussed for completeness. The amplitude of scattered x-rays is known to be proportional to $\sin\gamma$, where γ is the angle between the direction of the scattered x-rays and the polarisation vector.

For linearly polarised x-rays there are two extreme cases to consider, these are illustrated in figure 3.5 where the diffraction angle, 2θ, lies in the x-y plane. In figure 3.5 (a), the incident x-rays are polarised in the x direction. In this case the x-rays are scattered in the plane in which they are polarised, and so $\gamma = (\pi/2) - 2\theta$. As the intensity of scattered radiation is proportional to the amplitude squared, this results in the polarisation factor: $[\sin((\pi/2) - 2\theta)]^2 = \cos^2 2\theta$. In figure. 3.5 (b), the polarisation is perpendicular to the plane of scattering and so $\gamma = \pi/2$ leading to no reduction in amplitude (as $\sin(\pi/2) = 1$). For unpolarised

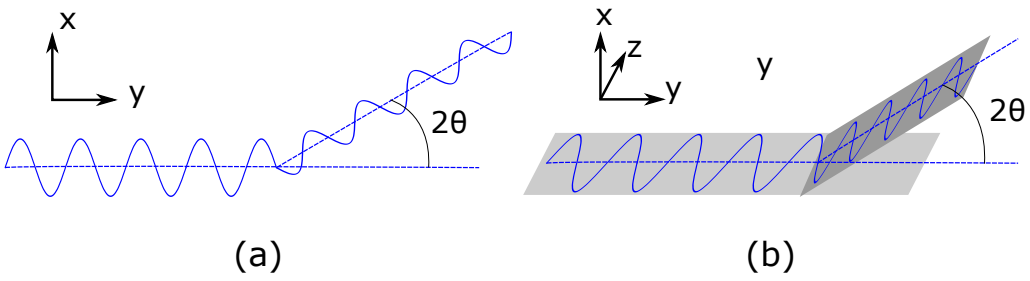

Figure 3.5 *Illustration showing the two extreme cases considered in the Lorentz-polarisation factor. The diffraction angle, 2θ, lies in the x-y plane.*

x-rays, the radiation can be thought of as having two equal components of these extremes. As such the polarisation factor for an unpolarised beam is : $(1 + \cos^2 2\theta)/2$.

The denominator of equation 3.20 denotes the Lorentz correction which is comprised of two corrections: one for the probability of crystallites in a powder sample contributing to that particular diffraction event, and a term describing the geometry of a cone of diffracted x-rays being intercepted by a flat detector. Bragg's Law (equation 3.6) gives precise diffraction angles at which a given reflection can occur. In reality there is a small, but finite, range of angles over which a crystal can contribute to a given Bragg reflection. A powder sample contains many tiny crystallites; the likelihood of crystallites having planes suitable for contributing to a given Bragg reflection has been shown [97] to be proportional to $1/\sin\theta$, where θ is half the diffraction angle, 2θ.

The Lorentz factor has been derived in several ways by taking the geometry of the experimental setup into account [98]. As scattered intensity in XRPD is spread over a cone of half-apex angle 2θ, then the intensity observed by a 2-dimensional image plate detector a distance, R, from the sample is spread over a circle of circumference $2\pi R \sin 2\theta$. The constant terms can be discarded as it is only the relative intensities of peaks in a single profile that are being investigated. Combining this with the probability term gives the denominator of equation 3.20.

Multiplicity

Unique to powder diffraction crystallography is the multiplicity factor, m_{hkl}, in the calculation of the intensity. Unlike single crystal diffraction, equivalent reflections (that is, reflections with different Miller indices hkl but the same d-

spacing) cannot be separately resolved in an XRPD experiment. All equivalent reflections exactly overlap in the 2D diffraction image and so contribute intensity to the same peak in the 1D diffraction profile. The multiplicity factor allows for more efficient calculation as just one intensity is calculated for a given set of equivalent reflections, which is then multiplied by this factor.

3.5 Data Analysis

3.5.1 X-ray Powder Diffraction Patterns

When studying materials at high pressures, single-crystal samples often suffer due the the induced changes of pressure, either lessening in quality or deteriorating to such an extent that single-crystal analysis becomes impossible. This, along with the technical difficulties of growing single crystals of certain materials, means that powdered samples are often used in high-pressure experiments. An ideal powder consists of a large number of randomly oriented crystallites, each acting as a small single crystal.

The diffraction pattern produced by a single crystal is essentially an image of the reciprocal lattice. It produces sharp spots of diffracted intensity, with each spot representing a unique reflection. These spots change position as the sample is rotated or moved. In an x-ray powder diffraction (XRPD) experiment, diffraction of the x-ray beam through the powder results in a characteristic pattern of Debye-Scherrer rings. These are concentric circles of diffracted intensity which are centred on the direct beam position and result from the combined diffraction from all crystallites that happen to be orientated in such a way as to satisfy the diffraction condition. For a given d-spacing and angle which together satisfy the diffraction condition (i.e. Bragg's Law), a number of crystallites within the sample may be able to satisfy that condition. These will produce a cone of diffracted intensity with semi-vertex angle of 2θ, the diffraction angle. This cone is intercepted by a flat detector which records a Debye-Scherrer ring, with the radius of the ring proportional to the diffraction angle of that particular reflection.

A result of this process we lack the full view of the reciprocal space lattice that is produced by single-crystal diffraction and can only see the d-spacings in an XRPD experiment. The aforementioned multiplicity factor describes the overlap of equivalent reflections in a powder. In a single crystal such reflections

are distinct, appearing as separate spots in the diffraction pattern. This allows for unambiguous indexing of these reflections (assignment of Miller indices) and consistency checks on the intensities of equivalent reflections.

An example XRPD pattern is shown in figure 3.6. The Debye-Scherrer powder rings are clearly visible with varying intensities (higher measured intensity corresponds to darker shading in the image) and positions relative to the beam centre (at the centre of the image). An ideal powder would produce smooth, continuous rings which exhibit no visible texture (variations in intensity/shading within the same ring) but measured patterns often include some texture. This can arise due to a number of causes but is typically due to the non-ideal nature of the measured sample, where grains of different sizes and orientations will exist within the powder.

The data analysed in this work were collected during several different experiments at different beamlines. As such, the x-ray diffraction patterns were recorded using several different detectors. At the ESRF the detector used was a Mar555 area detector which converts incident x-rays directly into an electrical signal by means of a thin film of selenium. At Diamond Light Source a Perkin Elmer 1621 detector was used — a scintillation device which uses a thin-film amorphous-silicon photon detector.

3.5.2 Image Masking & Integration with Fit2D

The recorded two-dimensional (2D) diffraction patterns were converted in to 1D diffraction profiles of integrated x-ray intensity as a function of diffraction angle (or, equivalently, d-spacing). This *integration* was performed using the program Fit2D [96, 99]. The first step in an x-ray diffraction experiment is to measure a reference sample in order to accurately determine the geometry of the experimental setup. In this work, standardised powder samples of silicon (Si) and lanthanum hexaboride (LaB_6) were used for calibration. Using these reference samples, along with the specifications of the detector (such as pixel size), Fit2D can be used to refine the experimental geometry; namely, the position of the beam centre on the image, the tilt of the detector, the sample-detector distance and the x-ray wavelength. Fit2D can then be used to produce diffraction profiles of integrated intensity as a function of diffraction angle from the measured two-dimensional images.

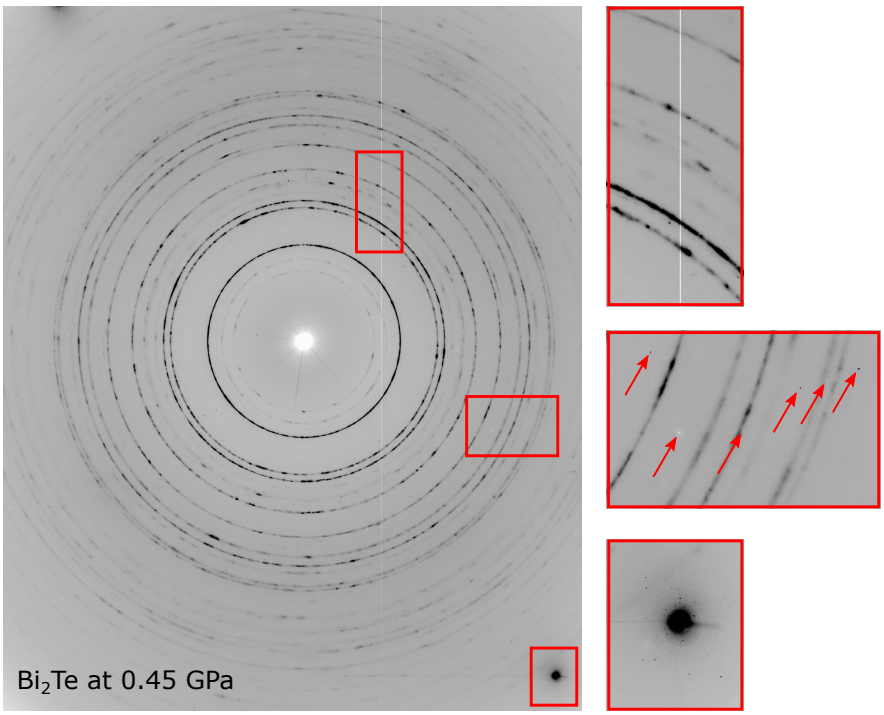

Figure 3.6 *An example XRPD image, recorded at 0.45 GPa. Common masked features are indicated including a detector line defect, individual saturated or 'dead' pixels, and a strong single-crystal reflection from the diamond anvils.*

An additional step in this integration is *masking*, where the 2D diffraction image can be inspected for signs of contaminants or artefacts. Features that are erroneous or not from the sample can be manually masked in the image, allowing Fit2D to omit these masked areas from the integration process. Several examples of commonly masked features are illustrated in figure 3.6. These include faulty detector pixels and non-sample diffraction, such as the intense single-crystal diamond reflection highlighted in figure 3.6. Once the measured diffraction image has been suitably masked, Fit2D is then used to integrate the image, producing a diffraction profile which can be used for further analysis. This process was followed for all x-ray diffraction profiles analysed in this work.

Some additional processing after this integration was required for the diffraction images measured with the Perkin Elmer detector. It was found that there were slight discrepancies between the calculated and simulated peak positions when analysing the calibration samples (Si and LaB_6). These discrepancies were attributed to a slight non-uniformity in the pixel size of the Perkin Elmer detector caused by inhomogeneous thermal expansion of the pixels. This caused a slight skewing of the diffraction angle, 2Θ. This was addressed using a script which

corrected the integrated 2Θ values such that they were in agreement with the expected reference values [100]. This correction was applied to all data collected with the Perkin Elmer detector, resulting in subtle changes to the diffraction profiles.

Determining Uncertainties on the Integrated Intensities

This work makes use of code developed by I. Loa to calculate statistical uncertainties on the integrated XRPD intensities. Standard XRPD profile refinement software weights the points in the profile according to simple counting statistics. Jana2006, for example, weights points in the refinement based on 'standard uncertainties of profile intensities' through the equation:

$$w_i = \frac{1}{\sigma^2[y_i(obs)]}, \tag{3.21}$$

where $y_i(obs)$ is each measured intensity in the profile [91]. Such a weighting scheme does not account for the large number of individual pixels that contribute to a single data point in an XRPD profile, nor does it account for the significant texture often seen in the measured Debye-Sherrer rings in high-pressure XRPD data.

In this work, the use of statistical errors on the intensities which are based on the measured data have resulted in more consistent Rietveld refinements. This is achieved by determining uncertainties on the intensities and, hence, statistical weights that are based on the texture in the measured data. This method makes use of the 'cake integration' feature of Fit2D which transforms the image of Debye-Scherrer rings to a plot of stripes against radial distance — effectively unwrapping the rings and laying them out straight, producing an image where the rows correspond to azimuthal angles and the columns to radial distances. This output is then analysed by a python script which determines the standard error on the mean of the intensity at each radial bin according to the equations:

$$\sigma_m = \frac{\sigma}{\sqrt{n}} \tag{3.22}$$

$$\sigma^2 = \frac{1}{n-1}(I_i - \bar{I})^2, \tag{3.23}$$

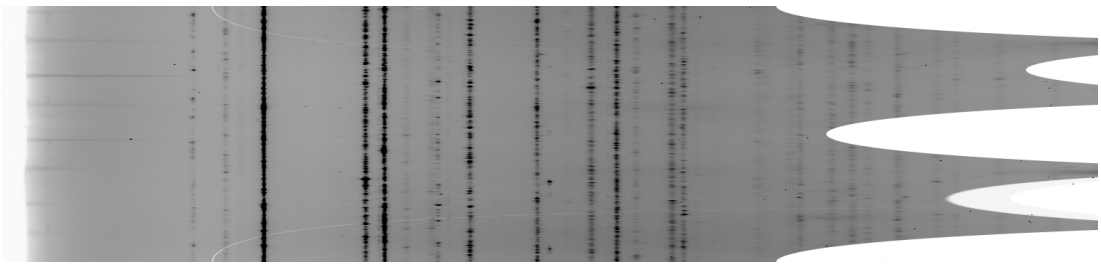

Figure 3.7 *Example of a Fit2D cake integration (Bi_2Te at 0.45 GPa) where the concentric Debye-Scherrer rings have been transformed to straight lines. Rows in this image correspond to azimuthal angle and columns correspond to radial distance. The texture (variation in measured intensity) along each vertical diffraction line can be seen.*

where n is the number of intensity values and σ^2 is the unbiased estimate of the variance of the sample. The so-determined variances are then used a weights (equation 3.21) in the fitting process.

3.5.3 Structure Solution and Refinement

Once the measured diffraction image has been processed and integrated to produce a diffraction profile, the solution of the crystal structure can begin. When starting from an unknown structure, the measured d-spacings are used to determine potential crystal types and unit cell dimensions that can account for the observed d-spacings in a process called *indexing*. Profile indexing is a process by which Miller indices (hkl) are assigned to the recorded peaks in a way that allows any systematic absences in the profile (i.e. certain combinations of Miller indices that are not observed in a profile) to be identified and used to suggest a possible crystal structure. Indexing software, for example the software suite *CRYSFIRE* [101], uses these absences to determine the lattice centring and other symmetry elements of structures that could produce the recorded diffraction profile. Where necessary in this work, indexing was performed using *Dicvol06* [102] and *Treor90* [103]. However, the majority of structure discussed in this work were previously known or simple to identify.

The resulting d-spacings were then analysed with the use of the software suite *CRYSFIRE* [101] which provides a single interface to utilise several indexing programs including *Dicvol06* [102] and *Treor90* [103].

The unit cell dimensions (a, b, c, α, β and γ) can be determined directly from the diffraction profile by means of a le Bail fit [11]. This method models the

entire diffraction pattern based on the unit cell dimensions, peak shapes and a background function. The le Bail fit does not include any information on the positions of the atoms within the unit cell and, as such, cannot be used to simulate the intensities of the peaks. Instead, the le Bail method fits the intensities arbitrarily.

In order to refine a full structural model based on the measured intensities (as well as the measured peak positions), requires calculation of the structure factors as described in section 3.4.2. Such a full-profile refinement method was developed through the 1960s by several individuals based at the Reactor Centre Netherlands: B. Loopstra, B. van Laar and H. Rietveld. This method developed from existing attempts to extract the contributions of multiple, overlapping peaks in neutron powder diffraction profiles but with the additional aspect of describing the profile as a whole, using the combined contributions from peaks with widths which vary as a function of diffraction angle. This method is now widely referred to as *Rietveld Refinement* [10, 104].

In Rietveld refinement the full structural model is used to calculate the intensities of reflections and these are combined with peak shape functions to create a full diffraction profile. This allows full refinement of a structural model including atom positions and site occupation factors. The refinement program Jana2006 [91] was used for analysis of all data in this work, with the exception of the host-guest structures which will be discussed subsequently. Refinement in Jana2006 uses least squares to minimise the residual between the observed and simulated profiles, with the residual function defined as:

$$S = \sum_i w_i |I_{io} - I_{is}|^2 \tag{3.24}$$

where w_i is the weight, I_{io} is the observed intensity at point i and I_{is} is the simulated intensity at point i [105]. The goodness-of-fit is characterised by the 'R-value', shown in equation 3.25, where a lower R-value is indicative of a better agreement between observed and simulated profiles.

$$R_{wp}^2 = \frac{\sum_i w_i (I_{io} - I_{ic})^2}{\sum_i w_i I_{io}^2} \tag{3.25}$$

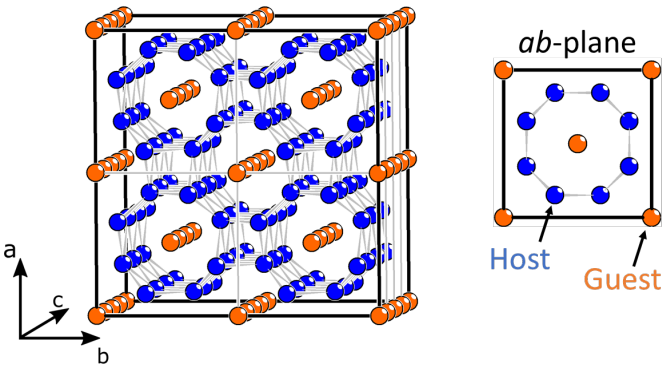

Figure 3.8 *Illustration of the host-guest composite structure. The host (blue) forms a framework through which run octagonal channels along the c-axis. The guest (orange) forms linear chains of atoms sitting within these channels.*

3.5.4 Custom Host-Guest Structure Refinement Code

As will be discussed in the following chapters, several members of the Bi-Te series adopt complex *host-guest* structures at high pressures. Refinement of these structures was not feasible using existing software and so a Rietveld refinement program was developed from the ground up in order to analyse these structures. The initial development of this program formed the basis of the author's Masters (MPhys) Project, with significant improvements made to the software during the course of this PhD work. In order to understand the function of this software, the host-guest structures found in the Bi-Te series must be introduced in brief; the host-guest structure will be fully introduced in section 5.2.

The host-guest structure is similar to that of Bi-III [15] and is illustrated in figure 3.8. The structure consists of two interpenetrating substructures: the host (illustrated in blue) forms a framework which encloses octagonal channels running along the *c*-axis; the guest (orange) forms linear chains of atoms sitting within these channels. In Bi-III the host and guest substructures are incommensurate along the *c*-axis direction. Unlike in Bi-III, the Bi-Te compounds are comprised of two distinct atom types, leading to the possibility of chemical ordering within the structure. Furthermore, it is found that the guest substructure in the Bi-Te compounds is actually only semi-ordered — it appears to be structurally disordered along the length of the chains (along the *c*-axis). These structural complexities necessitated the use of a custom refinement program, in order to give a greater level of control over the refinement.

The refinement software considers the different contributions to the diffraction

profile. The diffraction pattern associated with a compound crystal is a superposition of the diffraction patterns of the two substructures, along with satellite reflections that are a result of the structural modulations imposed on each substructure by the other [106]. The compound host-guest structure can be described in a four-dimensional (4D) superspace, using four Miller indices: (hkl_Hl_G). As the substructures are commensurate in the a-b plane they can be described by the same h and k Miler indices, but require two distinct indices related to the host and guest substructures along the c-axis direction (l_H and l_G, respectively). The reflections of the host-guest structure (indexed by (hkl_Hl_G)) can then be split into four groups:

Common	$(hk00)$	reflections common to both substructures
Host	(hkl_H0)	reflections unique to the host substructure
Guest	$(hk0l_G)$	reflections unique to the guest substructure
Satellite	(hkl_Hl_G)	reflections due to interactions between substructures.

There are no signs of satellite, (hkl_Hl_G), reflections in any of our measured Bi-Te host-guest data and these are not considered by the refinement software. The software therefore considers three sets of reflections: those uniquely due to the *host* substructure, those uniquely due to the *guest* substructure, and reflections which are *common* to both substructures. The software calculates the structure factors for reflections from each group separately and combines all contributions with the same Pseudo-Voigt peak shape function to produce a full diffraction profile. The structure factors of the *host* and *guest* reflections are calculated using only the structural details of the relevant substructure. The calculation of the *common* structure factors takes the details of both substructures into account.

The refinement software is able to refine a number of structural parameters including atomic site occupation factors, lattice parameters and pseudo-Voigt peak shapes. The code was developed systematically, first through the simulation of simple structures, building up to the complex host-guest Bi-III structure. The simulations were validated throughout by comparison with results from established software such as PowderCell 2.4 [107].

The refinement function of the software follows the standard Rietveld refinement technique [10] as implemented in GSAS [108]. It minimises the residual function (equation 3.26) via the least-squares Levenberg-Marquardt technique, as

implemented in the *lmfit* Python package [109]. The residual is squared by *lmfit*, such that the actual functions minimised are equivalent, despite the difference between equations 3.24 and 3.26. This residual (equation 3.26) is the absolute value of the difference between the measured, I_{Obs}, and simulated, I_{Sim}, intensities of diffracted x-rays, weighted by the uncertainty in the measured intensity, δI.

$$M_w = \frac{1}{\delta I}|I_{Obs.} - I_{Sim.}| \tag{3.26}$$

The goodness-of-fit is characterised by the 'weighted R-value' given by equation 3.27, with lower values typically indicating a better fit to the data.

$$R_{wp} = \sqrt{\frac{\sum M_w^2}{\sum \frac{1}{\delta I^2} I_{Obs.}^2}} \tag{3.27}$$

Chapter 4

Compositions Investigated

This section will provide a brief summary of the Bi-Te compositions investigated including details of specific samples and datasets, along with a short overview of the structural phases observed. This section is intended for reference only and full details of the structures investigated in this work will be provided in the following chapters, one composition at a time.

The bismuth-telluride compositions investigated in this work are summarised in table 4.1. A total of five different Bi-Te compounds were studied with compositions containing between 44% and 70% Bi. These span the stability range of bismuth-telluride compounds at ambient conditions as reported by Bos *et al.* [28]. Stable Bi-Te compounds can be synthesised for compositions containing between 44–70% Bi, with other compositions decomposing into multiple phases. As such the Bi-Te *infinitely adaptive series* is defined at ambient conditions only between those limits, with the end members — Bi_2Te_3 and Bi — the exceptions to these compositional phase stability limits.

Composition:	Bi_4Te_5	BiTe	Bi_4Te_3	Bi_2Te	Bi_7Te_3
% Bi Content:	44.4	50	57.1	66.7	70

Table 4.1 *Summary of compositions investigated in this work.*

4.1 Summary of Experiments

The work presented in this thesis is based on data collected over several experiments spread over a period of several years. The author was directly involved in experiment EE12996, with the other experiments performed by those listed in the acknowledgements. These experiments are summarised in table 4.2, with experimental details provided in the following chapters where relevant to the analysis. All experiments performed high-pressure x-ray diffraction on powdered samples of Bi-Te compounds at synchrotron facilities. The samples were rocked by ±3–5° during exposure in order to improve powder averaging.

Merrill-Bassett-type diamond anvil cells [9] were used for generation of high-pressures and various pressure-transmitting media were employed to ensure hydrostatic conditions within the sample chamber. Pressure was measured primarily by the ruby fluorescence method [83], except in cases where failure of the ruby measurement system necessitated the use of other internal standards. Details of sample preparation and measurement are included where appropriate in the following chapters.

Experiment	Date	Facility	X-ray Wavelength (Å)
EE8105	Oct. 2012	DLS	0.415301
hs4718	Feb. 2013	ESRF	0.415051
hc1335	Jul. 2014	ESRF	0.415352
EE12996	Feb. 2016	DLS	0.415666

Table 4.2 *Summary of experiments performed at Diamond Light Source (DLS), UK, and the European Synchrotron Radiation Facility (ESRF), France.*

4.2 Summary of Samples

The samples analysed in this work are summarised in table 4.3 which includes a label for each sample. These details and sample labels will be included where necessary in the following chapters and are listed here for reference. The pressure ranges over which each sample was measured are included. Some samples included pressure-cycling (repeated increase and decrease of applied pressure) as well as thermal annealing. These details will be provided in the following chapters.

All samples investigated in this work were powders. While single-crystal x-ray diffraction would provide a greater degree of information on the structures of these materials, single-crystals of Bi-Te compounds were not attainable at the high pressures considered here. While single crystals of Bi-Te compounds have been produced and investigated at ambient conditions (e.g. [28]), such samples have not been investigated at high pressures. This is primarily due to the difficulties posed by growth of such single-crystal samples, along with the fact that these samples do not typically survive the structural phase transitions induced by pressure. As such, investigation of high-quality powder samples was performed and is presented in this work.

Label	Sample	Experiment	Pressure Range (GPa)	PTM
MB-V3	Bi_2Te	EE8105	4.52 – 25.0	He
MB-V6	Bi_2Te	EE8105	0.91 – 9.47	m/e
hs21a	Bi_2Te	hs4718	0.45 – 17.01	He
hs21b	Bi_2Te	hs4718	10.20 – 20.19	N
hc73	Bi_7Te_3	hc1335	0.94 – 25.90	He
EE73	Bi_7Te_3	EE12996	2.40 – 26.43	He
EE43	Bi_4Te_3	EE8105	2.98 – 14.47	He
hc43	Bi_4Te_3	hc1335	1.57 – 18.93	He
EE43b	Bi_4Te_3	EE12996	1.37 – 16.79	He
BiTe	BiTe	EE8105	2.5 – 21.9	He
Bi_4Te_5	Bi_4Te_5	hs4718	2.81 – 21.2	He

Table 4.3 *Summary of samples investigated under high pressures including pressure range (P_{min}–P_{max}) over which each sample was studied. All samples held within diamond anvil cells with tungsten (W) gaskets and liquid pressure transmitting medium (PTM). m/e: mix of methanol and ethanol.*

4.3 Observed Structural Phases

What follows is a short introduction to the pressure-induced phases discussed in this thesis and their crystal structures. The phases are referred to by labels I – V which reflect the order in which they are typically encountered on pressure increase. As will be discussed in the following chapters, composition has a

significant influence on the behaviour of Bi-Te compounds under pressure. Not all Bi-Te compositions exhibit all of the following structural phases and the order in which the phases occur under pressure does vary.

All Bi-Te compositions adopt the *phase-I* structure at ambient conditions and ultimately end up in *phase-V* at the highest pressures attained in this work. Otherwise, each composition will adopt some or all of the following phases.

Phase I layered structure as found at ambient conditions, comprised of Bi_2 and Bi_2Te_3 blocks stacked along the *c*-axis [24].

Phase II observed in all compositions studied here. Appears similar to first high-pressure phase of Bi_2Te_3, proposed in the literature as having a monoclinic *C2/m* structure [110]. However, several observations in this work suggest that a more appropriate structural model may exist.

Phase III only observed briefly on pressure increase as a minority phase in certain compositions. Due to the small number of recorded peaks from this phase, unambiguous determination of the structure was not feasible in this work.

Phase IV semi-disordered variant of the well-known host-guest structures that exist in several elements at high pressures [64]. Consists of two interpenetrating substructures: a host framework with octagonal channels within which sit linear chains of atoms known as the guest. We observe that in the Bi-Te compounds the guest chains are uncorrelated along their lengths in a situation similar to 'chain melting' that has been reported elsewhere.

Phase V cubic structure, typically a fully site-disordered body-centred cubic alloy with atomic sites occupied by a stoichiometric mix of Bi and Te. In some compositions this phase is found to also adopt an ordered variant with a B2, CsCl-type structure after pressure-cycling. Such ordering has been reported elsewhere as resulting from gentle thermal annealing [12].

Chapter 5

Bi_2Te

The results of the analysis and refinement of x-ray powder diffraction (XRPD) data obtained from the composition Bi_2Te will be presented in this chapter. This particular composition exhibited all of the structural phases that will be discussed in this thesis. Therefore, the analysis of Bi_2Te will be discussed here in detail and the following chapters will then present corresponding results from the other bismuth-telluride compositions investigated. All refinement results will then be compared across the different compositions in chapter 10.

The results within each chapter will be presented one crystal structure (or 'phase') at a time. The observed structural phases and typical pressure behaviour across the series have been introduced in chapter 4. Here we will proceed not in pressure order, but will begin with the most complex phase on which most time was spent — the host-guest phase.

5.1 Bi_2Te Experiment Summary

The composition Bi_2Te was first investigated at beamline I15 of the Diamond Light Source in October of 2012 (experiment EE8105). The use of a Perkin-Elmer x-ray detector for recording of the diffraction patterns required extra processing of the integrated diffraction data in order to correct the diffraction angles (see section 3.5.1). Part of this involves correction of the x-ray wavelength; the wavelength used for analysis of all EE8105 diffraction data was $\lambda_{EE8105} = 0.415301$ Å.

This investigation recorded diffraction data from three samples of powdered Bi_2Te, all taken from a single powdered sample. Each sample was held in a Merrill-Basset-type diamond anvil cell (DAC) denoted by a label ('*MB-...*'). One sample was loaded in to '*MB-π1*' with no added pressure transmitting medium (PTM) or pressure calibrant; this sample was recorded only at ambient pressure, with the DAC used simply as a sample holder.

A second sample was loaded in to '*MB-V3*' with liquid helium as a pressure-transmitting medium. This sample was taken up in pressure from 4.5 GPa to a maximum of 25 GPa, where the cell was annealed at 100°C for 2 hours while the sample was in the cubic phase. The diffraction pattern was then measured after annealing, by which time the pressure had dropped substantially to 15 GPa.

The third sample was held in '*MB-V6*' with a methanol/ethanol mixture as a PTM. It should be noted that the methanol/ethanol mixture used can only be considered hydrostatic up to around 10 GPa [61]. However, this sample was investigated only between 1–10 GPa, focussing on the earlier high-pressure phases.

Further data on Bi_2Te was collected in February of 2013 at beamline ID09 of the European Synchrotron Radiation Facility (ESRF) during experiment hs4718. The wavelength of synchrotron radiation used was $\lambda_{hs4718} = 0.415051$ Å. In the present work, datasets from two hs4718 samples have been analysed. The first dataset (denoted '*hs21a*') is from a sample loaded with helium pressure transmitting medium. Due to the gasket hole becoming unstable at 17 GPa, this sample did not reach the pressure required to fully transform to the high-pressure cubic phase and was reduced back down in pressure from a maximum value of 17 GPa. The second dataset (denoted '*hs21b*') was recorded starting from around 10 GPa in order to focus on the transition to the cubic phase, reaching a maximum pressure of 20.2 GPa. This sample was loaded with nitrogen as the pressure transmitting medium.

All measurements of Bi_2Te samples utilised tungsten (W) gaskets and pressures were measured via ruby spheres placed in the sample chamber and the ruby fluorescence technique [83].

Powder diffraction profiles from each of the observed phases are shown in figure 5.1. The selected profiles show as little overlap of different phases as is possible, with most recorded data including diffraction peaks from several phases at once. The pair of dashed lines indicate the two most intense peaks of the host-guest phase which are weakly present in all of the phase-II profiles. The

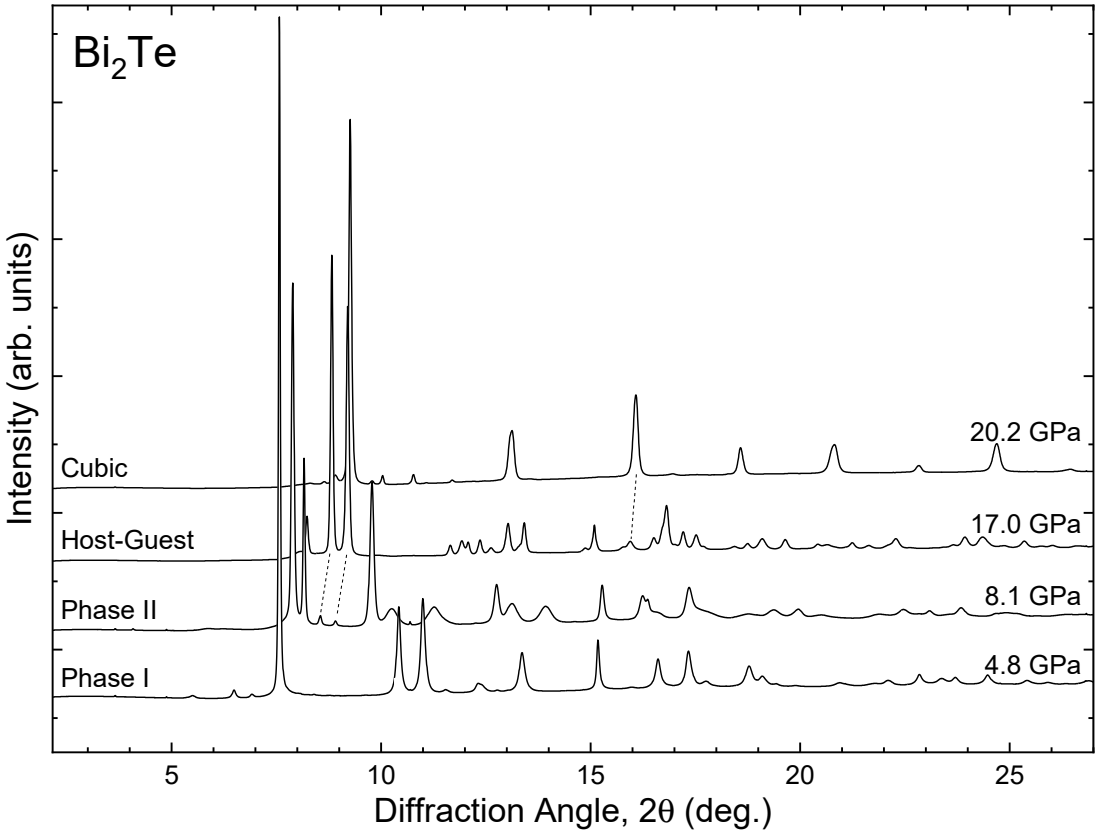

Figure 5.1 *Powder diffraction profiles of Bi_2Te illustrating the observed structural phases on initial pressure increase. All profiles from the hs21a sample, except that of the cubic phase, where weak peaks from the solidified nitrogen pressure-transmitting medium used with sample hs21b can be seen.*

single dashed line near 16° in the main panel indicates a peak from the cubic phase which can be readily identified in many of the host-guest profiles. These structural transitions are reversible on pressure decrease, but with some sample hysteresis such that the transition pressures and stability ranges are different.

The phases observed in this work on Bi_2Te are summarised in figure 5.2 which illustrates the pressures at which peaks from each phase could be clearly identified in the diffraction profiles. Each coloured band represents a different phase and the solid black dots indicate the pressures at which XRPD patterns were recorded. It should be noted that these observations are limited by the pressures at which our measurements were made and the maximum pressure attained. For example, the maximum pressure attained in this work, 25 GPa, does not necessarily represent an upper bound for the stability range of the cubic phase. The cubic phase is expected to persist to higher pressures; this is indicated in the pressure summary plot by the dashed lines at the high-pressure edge of the cubic-phase bands.

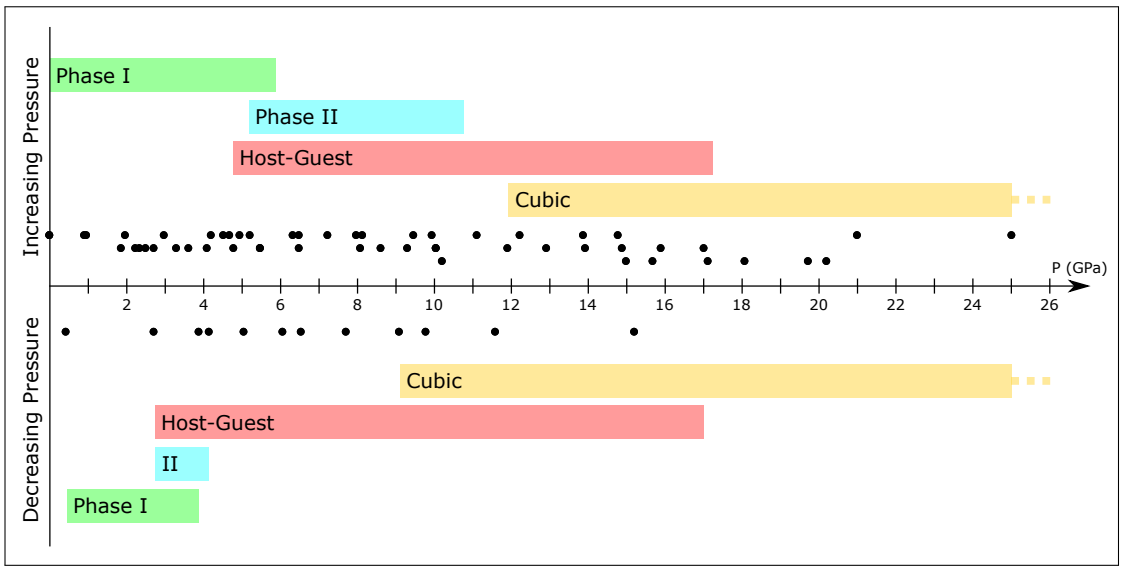

Figure 5.2 *Summary of observed phases for Bi_2Te. Illustrates pressure ranges as determined by visibility of clearly identifiable peaks in the powder diffraction profiles. Dashed lines at ends of coloured rectangles indicate expected phase stability outwith the range of our observations. Black circles represent the pressures at which diffraction images were recorded on pressure increase (EE1805 - top, hs21a - middle, hs21b - bottom) and decrease (hs21a only).*

5.2 Phase IV: Host-Guest

5.2.1 Semi-disordered Host-Guest Structure

On initial pressure increase, Bi_2Te was observed to transform from phase I (with the ambient-pressure layered structure), to phase II and then to the host-guest phase before finally reaching the cubic phase. The transitions overlapped significantly and clearly identifiable peaks from minority phases were present in most of the profiles.

The peaks from the two strongest host-guest reflections were visible from around 5.5 GPa while the majority of the sample was in phase I. These peaks grew in intensity as the pressure was increased and phase II became the majority phase, with the host-guest phase becoming dominant at around 10 GPa; the start of this process can be seen in the phase-II profile in figure 5.1.

Analysis of the high-pressure profiles, which were later revealed to belong to the host-guest phase, was performed following standard techniques for structure determination. First, the positions of peaks in the diffraction profile were recorded

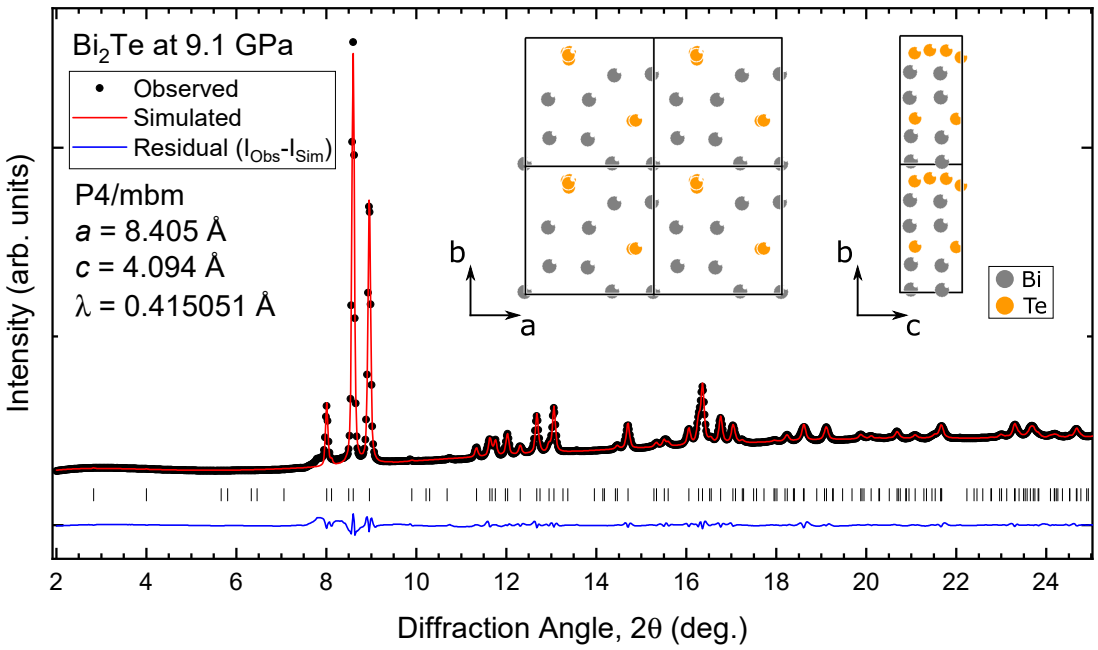

Figure 5.3 *Le Bail fit of diffraction profile of Bi_2Te at 9.1 GPa, using structure with tetragonal unit cell and P4/mbm space group. Inset: result of placing atoms using Superflip [111] with tellurium atoms shown in orange and bismuth atoms in grey. Similarities to the host-guest structure of Bi-III can be seen.*

using Fit2D [95, 96] to give a list of diffraction angles and corresponding *d*-spacings for the observed peaks. These measured peak positions were than used to index the diffraction profile, determining an appropriate unit cell to describe all of the observed peaks. This was done with the use of standard indexing software.

Indexing of the profile yielded a tetragonal unit cell which was then used as a basis to perform a le Bail fit to the measured profile using the refinement software Jana2006 [91]. Such a le Bail fit of a diffraction profile of Bi_2Te at 9.1 GPa is shown in figure 5.3. The agreement between the simulated and observed profiles is very good, with the tetragonal unit cell able to account for all observed peaks. In this le Bail fit, the unit cell dimensions are refined from the positions of the peaks, while the intensities are set arbitrarily in order to achieve the best fit possible using pseudo-Voigt peak shapes.

The structure solution software Superflip [111], as implemented in Jana2006, was then used to place atoms within the unit cell and produce a full structural model. The resulting structure solution is shown in the inset of figure 5.3. The resulting structure includes tellurium atoms which are placed in very close proximity to one another in approximately linear chains which lie along the *c*-axis. The closest

of these Te atoms exhibit extremely short separations, only 1.055 Å apart, indicating some issue with the structure proposed by Superflip. As can be seen in figure 5.3, the structure shares structural motifs with the incommensurate host-guest structure observed in elemental bismuth at high pressures, Bi-III [15]. Here, the bismuth atoms appear to form a framework which includes wide channels running along the *c*-axis, and approximately linear chains of tellurium atoms occupy these channels.

The bunching up of the tellurium atoms in the structure proposed by Superflip suggests that it is struggling to describe the structure with an integer number of atoms in the unit cell. This is similar to the first determination of the incommensurate host-guest structure of rubidium, Rb-IV, previously reported by Schwarz *et al.* [112]. In Rb-IV, initial structure solution produced guest atoms that were extremely close together. Refinement of the site occupancies of these 'guest' atoms revealed a structure with a non-integer number of atoms per unit cell, leading to the identification of the Rb-IV structure as an incommensurate host-guest structure.

It appears that the host-guest structure is, in fact, the more appropriate structure for describing this phase of Bi_2Te.

The Bi-III structure (illustrated in figure 5.4) can be described as two interpenetrating substructures known as the *host* and the *guest*. The host has space group $I4/mcm$ (#140) and a single atom at the $8h$ Wyckoff position (with coordinates $(x, x+\frac{1}{2}, 0)$) giving one free atomic positional parameter, x, and 8 atoms per unit cell. The tetragonal host has equal lattice parameters along the *a*-axis and *b*-axis directions ($a_H = b_H$) and a dimension along the *c*-axis denoted here as c_H.

The guest substructure is also tetragonal, with the same unit cell dimensions as the host in the *a* and *b* directions ($a_H = b_H = a_G = b_G$) but an independent dimension along the *c*-axis, which will be denoted as c_G. In Bi-III, the host and guest substructures are incommensurate along the *c*-axis, such that the ratio $\frac{c_H}{c_G}$ is irrational.

As described in section 3.5.4, x-ray diffraction by the host-guest structure can be modelled by considering the Miller indices of reflections in a 4D superspace, using the same h and k indices for both substructures and a distinct l index for each. Reflections due to the host-guest structure can then be divided in to four

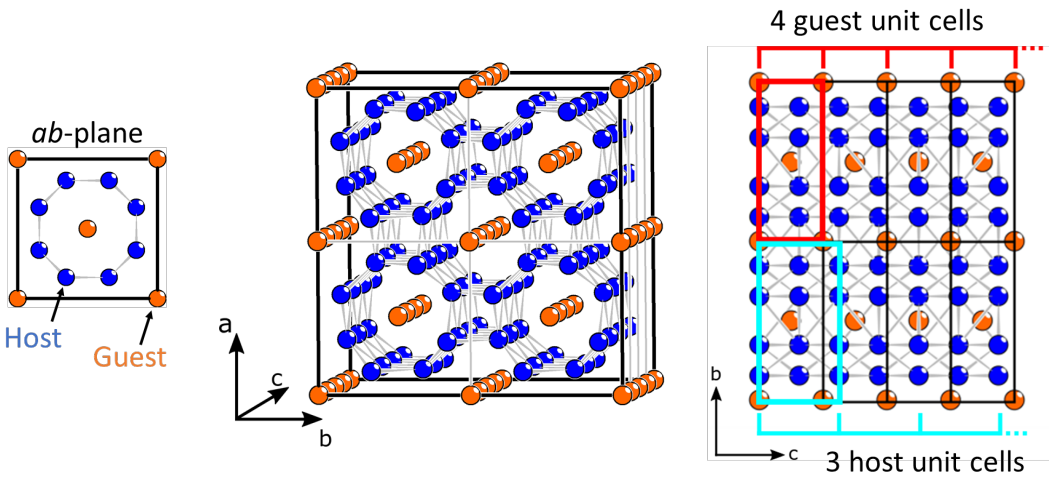

Figure 5.4 *Illustration of the host-guest structure using a commensurate approximation. Left: a single unit cell indicating the host and guest components. Centre: parallel projection view of the host-guest composite structure illustrating the channels formed by the host and the linear guest chains sitting within them. Right: view of structure in bc-plane. Commensurate approximation shown here has 4 guest unit cells per 3 host unit cells i.e.* $c_{Host}/c_{Guest} = 4/3$. *The incommensurate host-guest structure discussed here has a irrational value of* c_{Host}/c_{Guest}.

classes:

Common	$(hk00)$	reflections common to both substructures
Host	(hkl_H0)	reflections unique to the host substructure
Guest	$(hk0l_G)$	reflections unique to the guest substructure
Satellite	(hkl_Hl_G)	reflections due to interactions between substructures.

Applying the structural model of Bi-III to our measured Bi_2Te profiles provides an excellent fit to the observed *host* and *common* peaks, but no peaks associated with *guest* or *satellite* reflections are observed (see figure 5.5).

The lack of satellite reflections suggests that there is no significant structural modulation caused by interactions between the two substructures, and so the three-dimensional structural model of two interpenetrating substructures is a valid method of analysis. The lack of visible *guest* peaks suggests that the guest substructure is not well ordered along the *c*-axis. As such, the guest substructure only contributes sharp intensity to the profile through its contribution to the

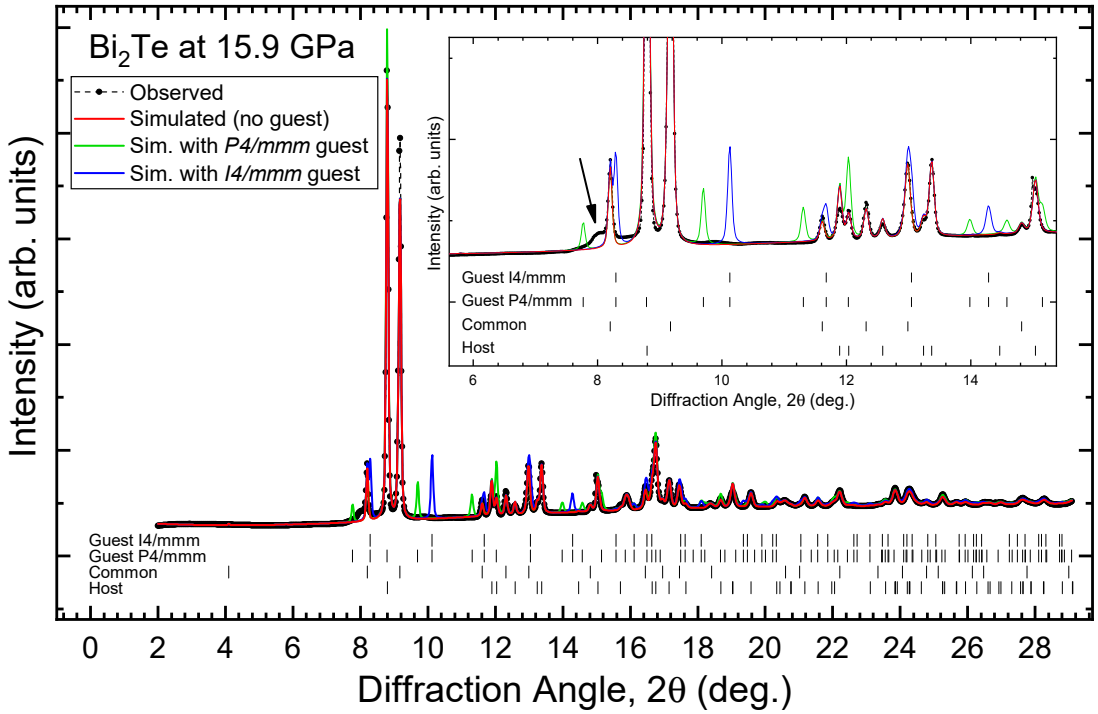

Figure 5.5 *Powder diffraction profile of Bi_2Te at 15.9 GPa on initial pressure increase, compared to simulated host-guest profiles with two different guest substructures. The profile without any guest-only peaks clearly describes the observed profile best — it appears there are no sharp guest peaks in the measured profile. Inset: closer view with a diffuse 'edge' diffraction feature indicated.*

common peaks, and the *guest* reflections must only contribute diffuse intensity to the diffraction profile. The lack of sharp *guest* peaks poses a problem, as the only information on the guest unit cell c-lattice parameter (c_G) is contained in the *guest* contribution to the XRPD profile, which does not appear to take the form of sharp reflections.

While the lack of *guest* peaks is unambiguous in most integrated host-guest profiles, several included a pair of clear peaks, one either side of the host-guest main pair, as illustrated in figure 5.6. The proximity of these observed peaks to expected guest reflection positions warranted closer inspection. Attempts to index these peaks using either the face-centred (*P4/mmm*) or body-centred (*I4/mmm*) tetragonal guest substructures were unsuccessful, as were attempts to index the peaks using a monoclinic guest as has been reported in other host-guest structures [113].

By following these extra peaks through the pressure range from the lower pressure structure (phase II), they can be identified as residual phase-II peaks. These same

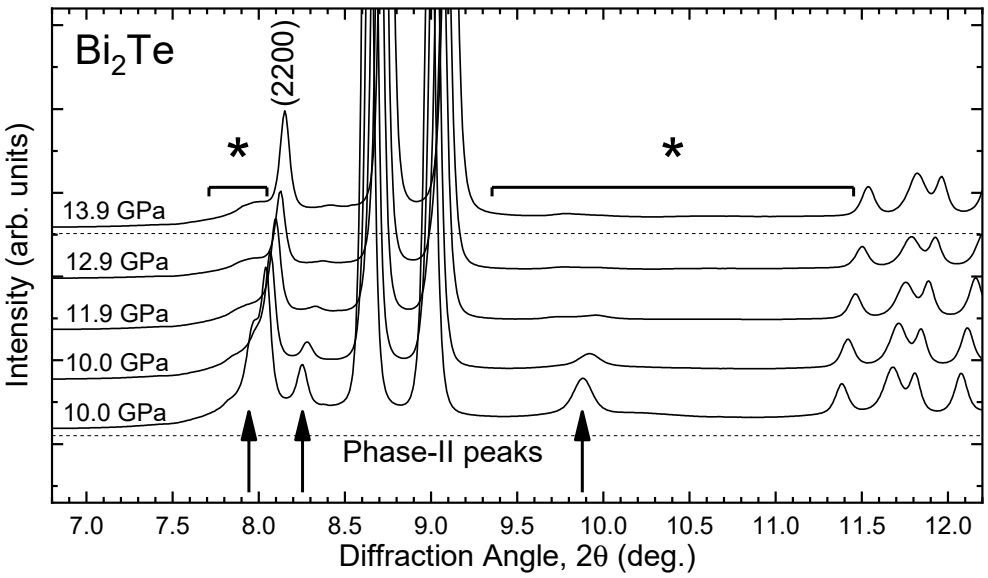

Figure 5.6 *The extra peaks observed in the host-guest phase are indicated. While these were initially suspected to be due to a fully ordered guest, they were later confirmed to be from phase II of the sample. Asterisks indicate observed diffuse diffraction features. Dashed horizontal lines are guides to the eye.*

peaks also appear on pressure decrease, as the sample transforms from the host-guest structure to that of phase II. With the lack of sharp *guest* peaks confirmed, the profiles could be checked for diffuse features which may provide information about the *guest* contribution.

Diffuse features are indeed visible in the host-guest diffraction profiles as illustrated in the inset of figure 5.5 and in figure 5.6. These diffuse features consist of an 'edge' feature — a visible rise or shoulder on the lower-angle edge of the *common* (2200) reflection, typically below 8°. This edge feature leads to an area of raised flat intensity at higher diffraction angles which spans several degrees. These diffuse features are observed in the host-guest phases of all bismuth telluride compositions studied in this work. There are some transitional profiles where peaks from the previous phase somewhat obscure these features (such as in the lower-pressure profiles in figure 5.6).

Host-guest structures with disordered guest components have been reported previously, such as in rubidium (Rb-IV) [16], where the peaks corresponding to guest reflections reversibly undergo significant broadening on reduction of the applied hydrostatic pressure in a process described as 'chain melting' (section 2.5.1 presents a review of published literature on this). This process is attributed to a reduction in the guest-guest correlation length parallel to the

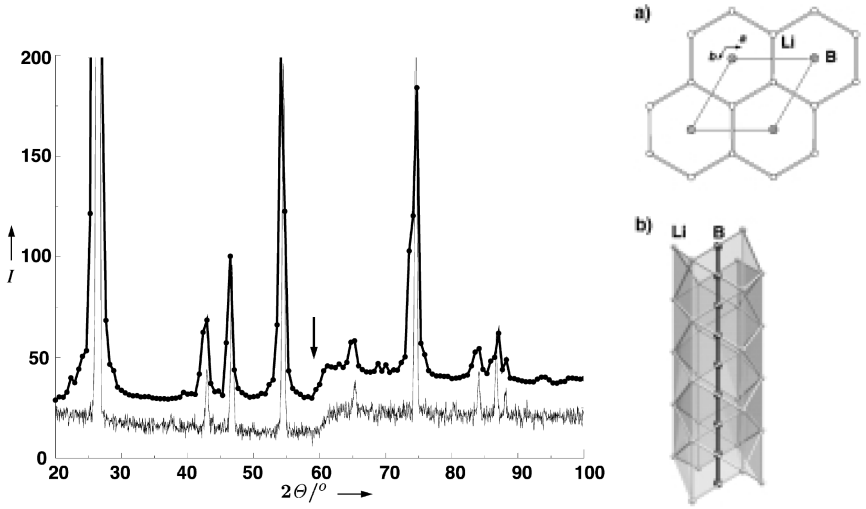

Figure 5.7 *Figure 1 from [114] showing neutron powder diffraction data for LiB_x (lower curve) along with a simulated profile (upper curve). The arrow indicates the 'step-like' diffuse scattering feature that was used to estimate the average atom-atom distance along the guest chains. Insets (a) and (b) illustrate the host-guest structure of LiB_x.*

ab plane. The complete lack of sharp guest peaks in the Bi_2Te diffraction profiles observed here suggest a guest system with chains in adjacent channels which are essentially entirely uncoordinated.

Diffuse features similar to those observed here were reported before in a combined x-ray and neutron powder diffraction study of lithium-boride (LiB_x) by Wörle *et al.* [114]. LiB_x adopts a host-guest structure similar to that considered here, with linear chains of boron atoms running along the *c*-axis that are confined within hexagonal channels in the lithium host structure. The structure is illustrated in the inset of figure 5.7, which shows neutron powder diffraction data with a clear diffuse edge feature (this feature was also reported in the same work to be observable in XRPD data, albeit less clearly). Wörle *et al.* used the position of the edge feature to determine the average distance between boron atoms along the length of the disordered chains by converting the position of the edge (in terms of diffraction angle) to a *d*-spacing.

This phenomenon has been described previously in work Chen *et al.*, published in 1982 [115]. In their paper, 'X-ray scattering by one-dimensional chains: Powder diffraction', they develop a model of the diffuse intensity resulting from disordered 1D chains in an x-ray powder diffraction experiment. Their work aimed to reduce the need for large, high-quality single crystals when studying materials which include disordered 1D chains, such as the widely studied compound: $Hg_{3-\delta}AsF_6$.

They develop a model of disordered 1D chains and find a characteristic diffuse contribution to the diffracted intensity of a 'steplike leading edge and very slow falloff at higher q' (magnitude of diffraction vector), in agreement with the features observed here. This model is then compared with experimental measurements of $Hg_{3-\delta}AsF_6$ and is found to reproduce the observed diffraction features very well.

It was therefore promising that information on the Bi_2Te guest substructure could be obtained from the observed diffuse edge feature.

5.2.2 Diffuse Scattering — Guest Disorder

Simulations using the Bi-III structure and a single atom type were performed to model the effect of varying degrees of structural disorder on the XRPD profile. This was done in order to confirm that disorder in the guest chains could lead to the observed diffuse features, and to determine a method for extracting a value for the guest periodicity and inter-atomic spacing along the chains, c_G.

Supercells were produced consisting of 25×25 host-guest unit cells stacked in the a and b directions, with 3 host and 4 guest unit cells along the c direction (providing a commensurate approximation to the Bi-III structure, with $c_H/c_G = 4/3$). Atomic positions were defined in Python code with a total of 15,000 host and 5,000 guest atoms.

The program initially sets up a host unit cell by defining atomic positions given host-guest unit cell parameters and the position of the free atom, x. This is then extended in three dimensions to create the host component of the supercell. The code then sets up an ordered guest supercell of 25×25 unit cells stacked in the ab plane, and one unit cell deep in the c direction.

Disorder is introduced by iterating through all guest unit cells and displacing each of the two guest atoms within the unit cell along the c axis. The atoms are displaced randomly according to a Gaussian distribution defined by a width, σ, which represents the amount of disorder present in the system. This process is repeated several times and this semi-disordered guest supercell is extended in the c direction and combined with the host supercell to produce the full host-guest supercell (with disordered guest component).

The structure factors of reflections resulting from this supercell can then be

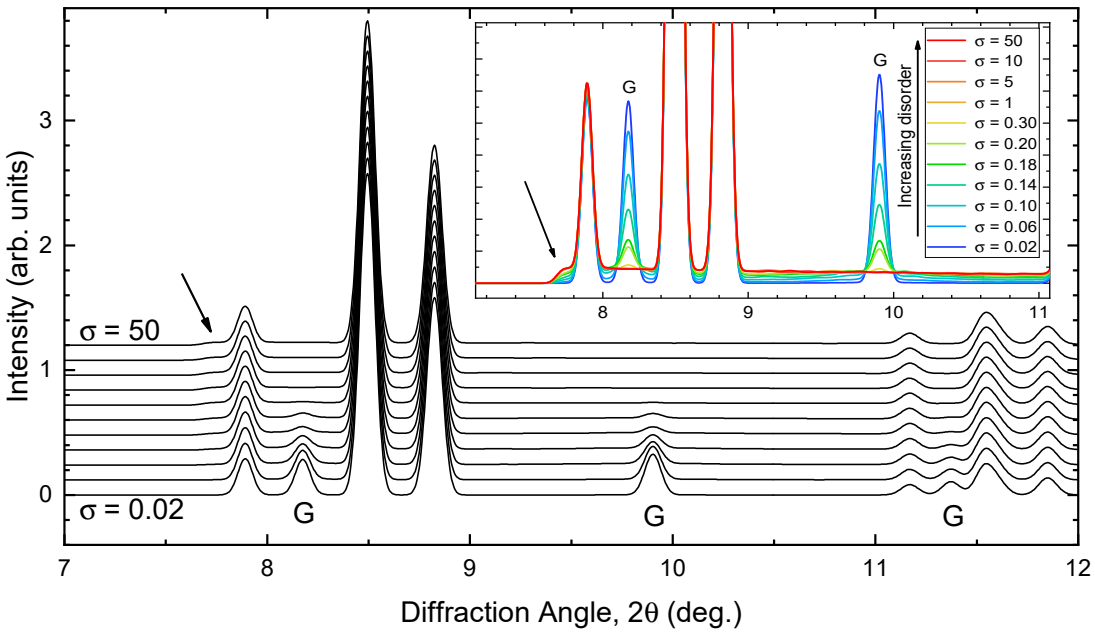

Figure 5.8 *Simulated XRPD profiles resulting from 20,000 atom semi-disordered host-guest supercells with σ reflecting the degree of disorder in the guest. The main panel illustrates the weakening of the indicated 'guest-only' peaks (G) as the guest becomes increasingly disordered. The inset shows the same profiles, illustrating the appearance of the diffuse features at 7.7° and between 9–11° .*

calculated as in the host-guest refinement program (section 3.5.4). An XRPD profile can then be simulated by calculating the intensities of reflections, applying peak shapes and combining to form a continuous XRPD profile given experimental parameters.

The effect of disorder imposed on the guest structure (through σ) on the simulated powder diffraction profiles is illustrated in figure 5.8 which shows profiles with different degrees of disorder present in the guest system. The main panel shows the gradual decrease in intensity of the *guest* reflections as the amount of disorder is increased. As these guest peaks (G) disappear, diffuse features similar to those observed in the measured Bi_2Te host-guest diffraction profiles appear. This is made clearer in the inset, which shows the same diffraction profiles. The diffuse edge feature is indicated below 8° and the raised area of flat intensity can be seen between 9–11°. This confirms that the observed diffuse diffraction features are due to disorder within the guest system. This behaviour corresponds with that reported by Wörle *et al.* in a follow-up to their initial LiB_x study, where the step in the background present in neutron diffraction data obtained at 200 K resolves into peaks from sharp Bragg reflections at lower temperatures [116].

Now that the source of the diffuse features has been confirmed, the observed features can be analysed to obtain information about the structure of the guest component. Wörle *et al.* used the position of the edge feature to determine the periodicity of the guest chains in LiB_x [114] — before doing the same it is prudent to investigate the shape of the edge feature and determine exactly which point on this feature should be measured.

In the simulations of powder diffraction profiles from the host-guest supercells, each contribution to the XRPD profile is calculated separately; as such, the contribution of the guest system to the profile can be plotted alone. Figure 5.9 shows the guest contributions to simulated XRPD profiles where the guest has been fully disordered (with $\sigma = 50$).

Figure 5.9a shows the effect of varying the size of the guest unit cell along the c-axis (c_G). Sharp peak shapes were applied here to make the onset of diffracted intensity clear. The position of the edge feature varies with c_G and lies at a diffraction angle that is equivalent to a d-spacing equal to c_G. As such, the position of this edge corresponds to the average distance between atoms of the linear guest chains, in agreement with the analysis presented by Wörle *et al.* Figure 5.9b illustrates the effect of varying the peak width used in the simulation of the diffraction profile, while keeping the value of c_G fixed. As the feature broadens, the point at the half-maximum of the edge feature remains fixed — this is the point that must be measured to determine the average atom-atom distance along the guest chains (i.e. c_G).

Fitting Diffuse Features to Determine c_{Guest}

To determine the value for c_{Guest} from the diffuse edge feature, a fitting routine was written using python which uses the measured profile and the simulated host-guest profile from an initial Rietveld refinement. This initial Rietveld fit was done using our custom refinement program which included only the *host* and *common* reflections, excluding any contribution to the profile from the *guest* reflections. Excluding the *guest* contribution allows the structural model of the host to be refined using the observed *host* and *common* reflections. These initial refinements included an estimated value of c_G, based on published c_H/c_G ratios determined for the high-pressure host-guest phases of bismuth and antimony [32].

The diffuse feature fitting routine defines a function to represent the edge

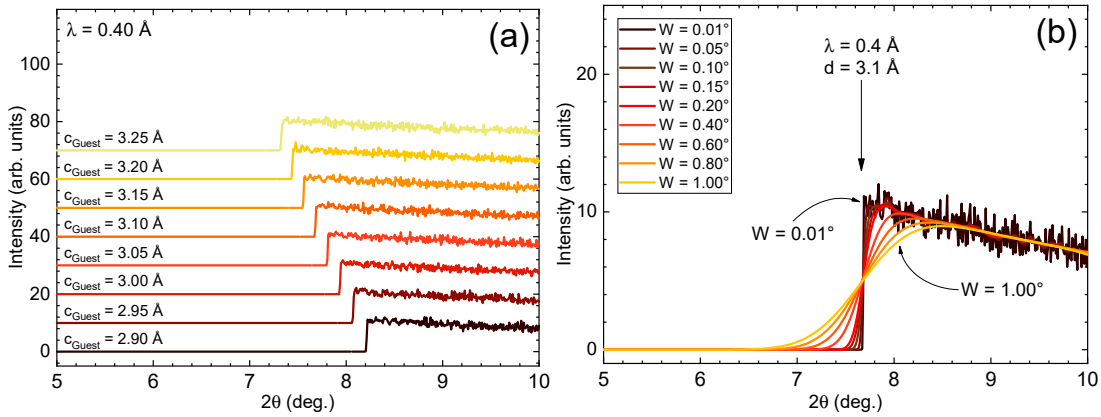

Figure 5.9 *Simulated XRPD profiles of the disordered guest substructure using a 20,000 atom supercell of the host-guest structure. These profiles are simulations of the intensity contributed to the XRPD profiles by the disordered guest substructure and show the effects of varying (a) the guest lattice parameter and (b) the peak width applied to each reflection in this profile.*

feature and adds this function to the simulated host-guest profile from the initial refinement. The residual defined in equation 5.1 between the observed and simulated (refinement + diffuse feature function) profiles is then minimised using the same *lmfit* Python package [109] as in the Rietveld refinement program. The full host-guest simulated profile from the initial refinement remains fixed and only the parameters of the function describing the diffuse feature are varied.

$$y_{obs} - (y_{sim} + y_{diffuse}) \tag{5.1}$$

An example of the output from this code is shown in figure 5.10, illustrating the diffuse feature function, the simulated profile from initial refinements, the sum of these and the observed profile. Clearly the addition of the diffuse feature function to the simulated profile greatly improves the fit. Also indicated (with a solid vertical line) is the diffraction angle which corresponds to a d-spacing equal to the average atom-atom distance along the guest chains, i.e. c_{Guest}. Dashed lines indicate the uncertainty on this value.

The diffuse feature is modelled using a piecewise function, equation 5.2, which consists of a hyperbolic tangent step function, which changes to a linear decrease at a diffraction angle, x_0 (as illustrated in figure 5.10). The tanh component effectively models the edge of the diffuse feature, while the linear decrease gives the code some flexibility in the minimisation. This decrease is typically sharp and

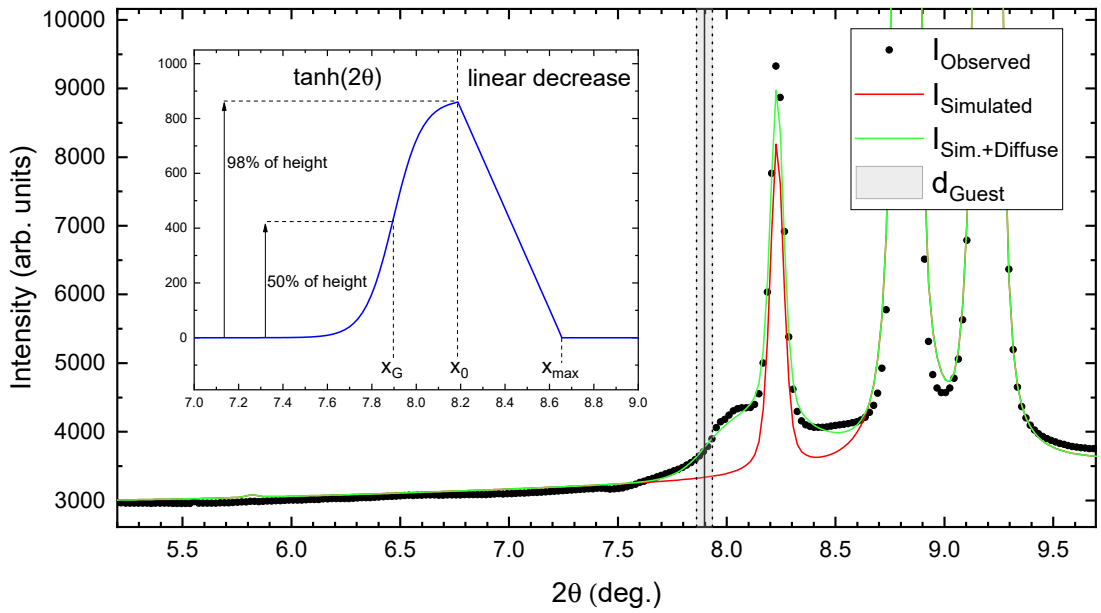

Figure 5.10 *Example showing fitting of diffuse edge feature. The vertical line indicates the determined diffraction angle which corresponds to a d-spacing equal to the atom-atom distance along the guest chains. Inset shows the function used to fit the diffuse feature. Profile is of Bi_2Te at 17 GPa.*

this portion of the function is unimportant; we are only interested in the position of the edge.

$$I(x) = \begin{cases} A\tanh\left[B(x - x_G)\right] + \frac{height}{2} & \text{if } x < x_0 \\ m(x - x_0) + height \times 0.98 \times 0.5 + \frac{height}{2} & \text{if } x_0 \leq x < x_{max} \\ 0 & \text{if } x \geq x_{max} \end{cases} \tag{5.2}$$

The function $\tanh(x)$ is centred at $x = 0$ and asymptotically approaches +1 (-1) in the positive (negative) x direction. Here the position of x_0 is defined as the point at which the tanh function has reached 98% of its maximal value. There are 4 refined parameters in the fitting of the diffuse feature:

x_G	The diffraction angle about which the tanh function is centred, corresponding to the guest atom-atom distance.
xmax	The angle at which the diffuse feature function should return to zero, not contributing to the XRPD profile above that diffraction angle.
height	This describes the height (intensity) of the step feature.

width This describes the width of the step feature.

The uncertainties on the refined values are provided by *lmfit*. The average atom-atom distance along the guest chains (i.e. c_{Guest}) can then be calculated from Bragg's law using the wavelength of the incident x-rays, λ, by:

$$c_{Guest} = \frac{\lambda}{2\sin\left(\frac{xG}{2}\right)} \tag{5.3}$$

with the uncertainty determined from the percentage uncertainty in x_G.

5.2.3 Bi_2Te Host-Guest Rietveld Refinements

The Bi_2Te host-guest diffraction profiles were produced by integrating the measured 2D diffraction images as described in section 3.5.1, and uncertainties on the integrated profile intensities were estimated as described in section 3.5.2. Use of these uncertainties produced more stable and consistent refinements when compared to 'unweighted' refinements. Rietveld refinements were performed using a custom Rietveld refinement program which allowed for the semi-disordered host-guest structure to be refined, taking into account the lack of refinable guest peaks. The function of this code is described in section 3.5.4. The goodness-of-fit of the simulated (refined) powder diffraction profile is indicated by the weighted R-value, R_{wp}, with lower values typically indicating a better quality of fit.

An example refinement of the Bi_2Te host-guest structure is shown in figure 5.11. The positions of the *host*, *common* and *guest* reflections are indicated using tick marks beneath the diffraction profile. Note that, while they are indicated, the *guest* reflections are not included in the refinement and contribute no intensity to the simulated diffraction profile. The inset illustrates the diffuse diffraction features that are not captured by the simulated profile (however, the raised flat intensity between 9–11° is accounted for by the background function).

A total of 20 XRPD profiles from three different samples were used to refine the host-guest structure of Bi_2Te between pressures of 4.1–18.1 GPa: 6 on pressure increase and 9 on subsequent pressure decrease for sample *hs21a*; 4 on pressure increase for *hs21b*; and 1 profile on pressure increase from experiment EE8105. A number of these profiles contained peaks from the cubic phase of Bi_2Te which were included in the refinements as a separate phase. No other Bi_2Te phases

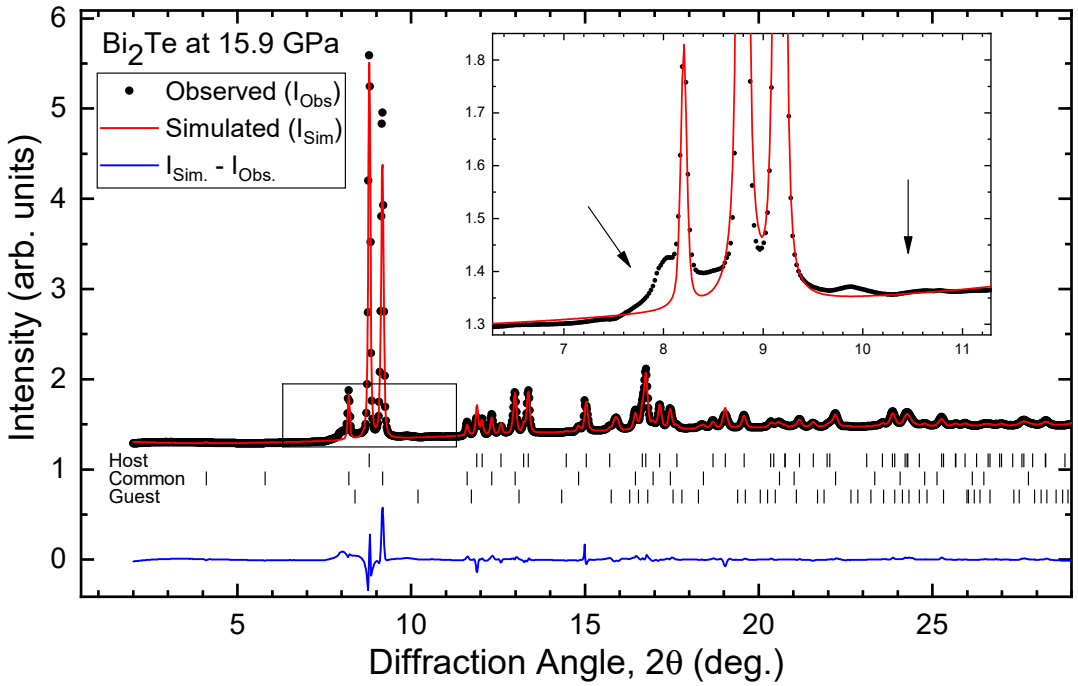

Figure 5.11 *Refined host-guest profile of Bi_2Te at 15.9 GPa on initial pressure increase. Inset indicates diffuse features from the semi-disordered guest; flat intensity between 9-11° is accounted for by the background but the edge feature at 8° is missed by the refinement.*

were included in these refinements, with only a few peaks from the lower-pressure phases visible in the low-pressure host-guest profiles.

In order to achieve consistent and stable refinements, the isotropic atomic displacement parameters ('U_{iso}') for the bismuth and tellurium atoms had to be set at a fixed value. This parameter (units Å^2) describes the random, thermal motion of the atoms in the structure and controls the resulting fall-off in diffraction intensity with increasing diffraction angle that is observed in XRPD data. Particularly unstable refinements would lead to refined U_{iso} values that were unphysically small or negative. Therefore, all atomic displacement parameters were fixed at a value of $U_{iso} = 0.015$ Å^2, based on reported values for bismuth and tellurium atoms in Bi-Te compounds at ambient pressure [28, 117–119] and initial refinement results.

Several refinements were performed with atomic displacement parameters fixed at $U_{iso} = 0.01$ Å^2 and $U_{iso} = 0.02$ Å^2 to test the effect on the other refined parameter values. Typical changes to refined parameters were negligible (<1%); the largest change was to the refined site occupation factor, which refined to a value around 2% larger with the larger of the two U_{iso} values. This is an absolute

difference on the order of 0.02 — well within the associated SOF uncertainties.

The structural parameters included in the refinement are: the host lattice parameters (a_H and c_H); the host *8h* atomic position (x); the guest bismuth site occupation factor (SOF); three pseudo-Voigt peak shape parameters (U, W and n); a scaling factor; and a background function (fifth-order Chebyshev polynomial). Where appropriate, peaks from the cubic phase are also refined as a separate phase using a single lattice parameter, three pseudo-Voigt peak shape parameters and a scaling factor. In such refinements the atomic displacement ('U_{iso}') parameter is also fixed.

The refined lattice parameters are summarised in figure 5.12. Across the 20 profiles analysed, the refined structural parameters show a smooth decrease with increasing pressure that is consistent across all samples and increasing/decreasing pressure runs. Figure 5.12 also shows the unit cell volume of the host-guest phase which can be fitted with the Murnaghan equation of state, resulting in fitted values of $V_0 = 335.0(12)$ Å^3, $B_0 = 42(2)$ GPa and $B' = 4.6(2)$. The volume per atom (taking into account the non-integer number of atoms in the host-guest unit cell) is also shown. The refined atomic volumes from the host-guest phase lie between the values of the preceding and subsequent structural phases, supporting the host-guest structure as an acceptable model.

The common lattice parameter of the host and guest, a_H (perpendicular to the chains), and the host lattice parameter, c_H (along the chain direction), could be obtained directly from Rietveld refinement of the measured profiles. The guest lattice parameter, c_G, however, had to be determined separately from the location of the edge feature. As such, these c_G values were then included in the host-guest refinements as a fixed parameter. The ratio of c-lattice parameters between the host and guest substructures, c_H/c_G, is shown in figure 5.13. It appears to start close to the commensurate value of $c_H/c_G = 4/3$ at lower pressures, with a very slight pressure dependence similar to that reported in the host-guest structures of bismuth and antimony: Bi-III and Sb-II [32].

There is one free atomic position within the structure, with the rest defined by symmetry. This is refined through the parameter x, which describes the position of the atom at the host *8h* Wyckoff site as a fraction of the unit cell dimension. The pressure dependence of x is shown in figure 5.13 (b) where it can be seen to decrease slightly with increasing pressure. The data point from experiment EE8105 appears to be a slight outlier here, but still agrees within uncertainty

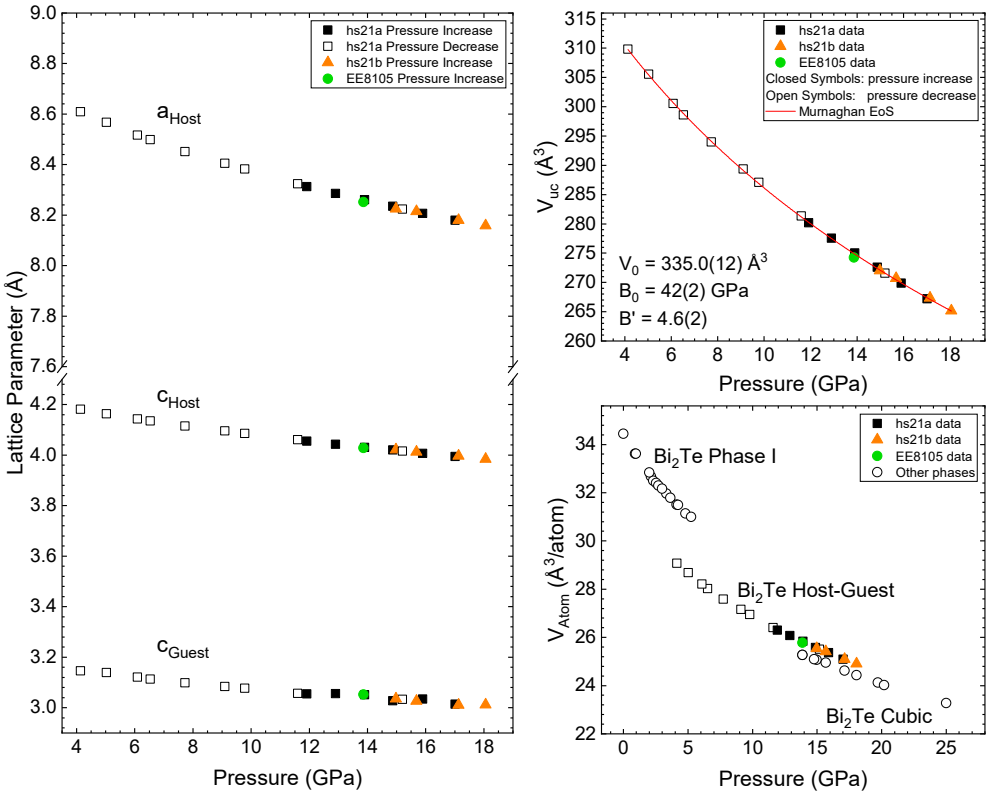

Figure 5.12 *Refined lattice parameters of the host-guest phase of Bi_2Te. Combined results using two samples (hs21a & hs21b). The variation of lattice parameters with pressure is consistent across both experiments and pressure runs. Uncertainties for all lattice parameters were less than the symbol size and are not included here.*

with the other data. Such discrepancy between different experiments is found in other compositions and will be discussed later.

The chemical occupation of atomic sites is refined through a single parameter — the guest bismuth site occupation factor (SOF) which describes the occupancy of the guest substructure. A value of 1 indicates guest chains that are fully occupied by bismuth, a value of 0 indicates guest chains fully occupied by tellurium, and intermediate values indicate a mixed Bi/Te occupancy. All atomic sites are assumed to be fully occupied (i.e. no vacancies) with the occupancy of the host *8h* site constrained by maintaining overall Bi_2Te stoichiometry. The calculated occupation factors for the host take into account the non-integer number of atoms in the host-guest unit cell, due to the incommensurate c_{Host} and c_{Guest} lattice parameters.

Refinement of the host-guest phase reveals partial ordering in the structure.

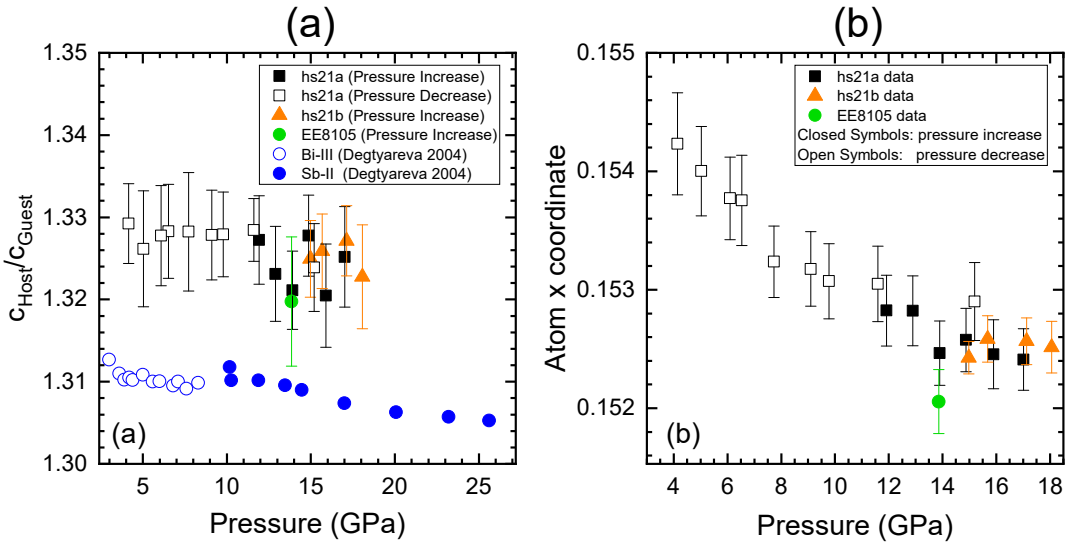

Figure 5.13 *(a) Ratio of lattice c parameters in host-guest Bi_2Te with linear fit compared to published work on Bi and Sb host-guest phases. (b) Refined free atomic position parameter, x, in host-guest phase of Bi_2Te.*

The refined SOF (figure 5.14 (a)) indicates that the material is not a fully site-disordered alloy. Instead, the guest consists of around 85% bismuth — significantly more than would be expected in a fully site-disordered Bi_2Te alloy (67% Bi).

The refined SOF values for sample *hs21a* appear stable across the pressure range, with a change in value on the decreasing pressure run. This sample was reduced in pressure after the gasket hole became unstable at 17 GPa, which was accompanied by a sudden drop in pressure (∼2 GPa). This seems to have caused a change in the structure, with an increase in the amount of bismuth present in the guest substructure. The refined values from the other samples show much more variation, spanning a range of SOF values across those observed for *hs21a*. The agreement of the SOF values is encouraging, while the differences between the samples is not surprising given the different rates of pressurisation experienced by each (*hs21a* and the sample from EE8105 were slowly pressurised, whereas *hs21b* was pressurised more quickly to reach the cubic phase).

Interestingly, the pressure dependence of the site occupation factors appears to be somewhat reflected in the ratio of host lattice parameters as illustrated in figure 5.14 (b). There are no correlations greater than 0.1 reported in the host-guest refinements between the bismuth site occupation factor and host lattice parameters. The refinement at 15 GPa appears to be an outlier in both the site

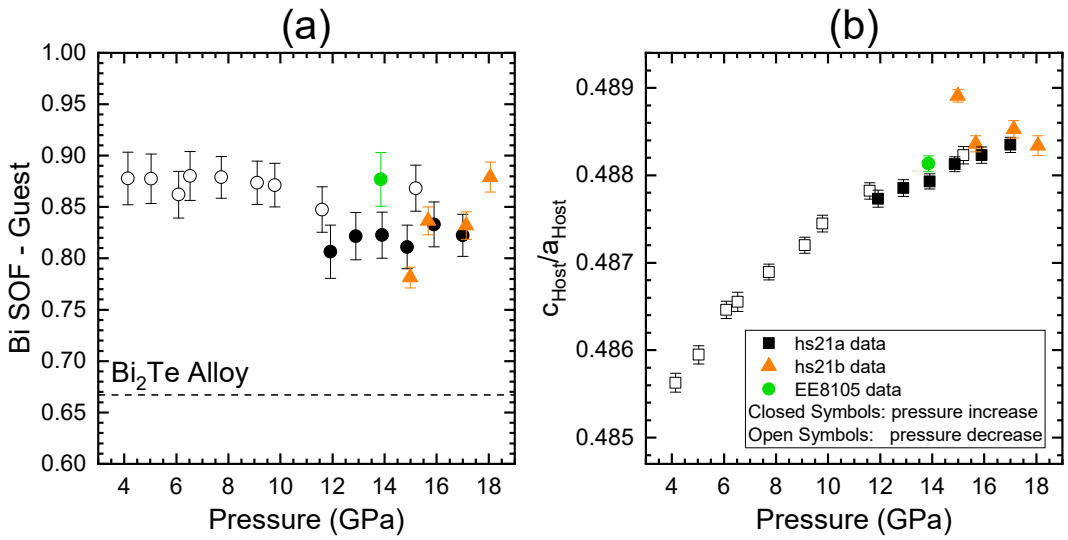

Figure 5.14 *Refined site occupation factor (a value of 1 here represents a guest substructure fully occupied by Bi). This was the only free SOF parameter; the others determined by maintaining overall Bi_2Te stoichiometry. There is variation in the refined values but the refinements support the existence of a bismuth-rich guest. Ratio of the refined Bi_2Te host lattice parameters. Note that the spread of data points appears similar to that of the site occupation factors.*

occupation factors and, more clearly, in the ratio of host lattice parameters.

Conclusion

In this section high-pressure x-ray powder diffraction data of Bi_2Te have been analysed, revealing that Bi_2Te adopts a complex host-guest structure similar to that of bismuth (Bi-III). The host-guest structure of Bi_2Te features a semi-disordered guest component, with the guest chains disordered along their lengths. This was evidenced by the lack of sharp *guest* diffraction peaks in the measured profiles. Instead, the *guest* reflections contribute only diffuse intensity to the diffraction profile, which takes the form of a step-like 'edge' feature around 8° followed by a raised area of flat intensity to higher diffraction angles.

The lack of sharp *guest* peaks would have prevented full determination of the structure (in particular the guest lattice parameter, c_{Guest}) but the position of the diffuse edge feature could be used to determine the guest lattice parameter. This was done with a separate fitting routine and the resulting guest lattice parameter then included in Rietveld refinement of the host-guest structure as a fixed parameter.

Structural refinements of the host-guest phase were performed using data from three experiments. The refined structural parameters showed good consistency across all experiments and increasing/decreasing pressure runs. The ratio of host and guest lattice parameters (c_{Host}/c_{Guest}) was found to exhibit a similar behaviour to those previously published for the host-guest structures of bismuth (Bi-III) and antimony (Sb-II), with a very slight decrease over the pressure range. This c-ratio remains at a value close to 1.326; this is near to the commensurate value of 4/3.

Refinement of the atomic site occupation factors reveals that the host-guest structure is partially chemically ordered, with the guest chains consisting of approximately 85% bismuth. This is significantly higher than would be expected for a fully site-disordered structure, where all atomic sites would be occupied by an average of 67% Bi and 33% Te. This ordering is interesting as materials which exhibit this structure at high pressures are elements or appear to be fully site-disordered alloys [19].

The next section will deal with the layered structure found at ambient conditions, referred to here as *phase I* of Bi_2Te.

5.3 Phase I: Ambient-Conditions Structure

At ambient conditions, phase I of Bi_2Te adopts a layered structure following the structural trends of the $(Bi_2)_m(Bi_2Te_3)_n$ series [24], consisting of two Bi_2 blocks and a single Bi_2Te_3 block stacked along the c-axis. The structure can be described by the $P\bar{3}m1$ space group with three formula units per unit cell. There are 5 atomic sites: one at (0,0,0) and the other four with (x, y) coordinates fixed by symmetry and free z parameters. Here we refer to these atoms by atom numbers (1-5) and z-coordinates (z_1-z_5) as illustrated in figure 5.15.

The structure can be described in terms of the thicknesses ('t') of the two-atom Bi_2 and five-atom Bi_2Te_3 blocks and the distances ('d') between them as illustrated in figure 5.15. Calculation of these values is based on the following equations, where c is the c-axis lattice parameter and z_i are the z-coordinates of the atomic

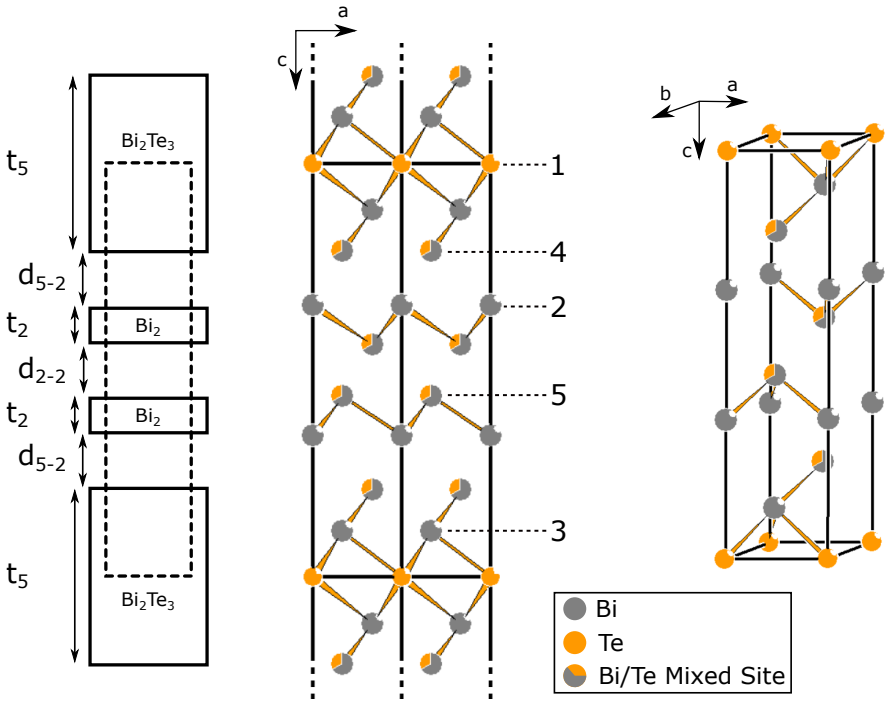

Figure 5.15 *Phase I of Bi_2Te. Left: schematic diagram showing the stacking of 2 two-atom and 1 five-atom layers which forms the idealised structure, with inter-layer distances ('d') and layer thicknesses ('t') indicated. Centre: ac-plane view of structure showing two full unit cells and four portions of unit cells, with atomic site labels indicated. Right: projected view of a single unit cell of the structure.*

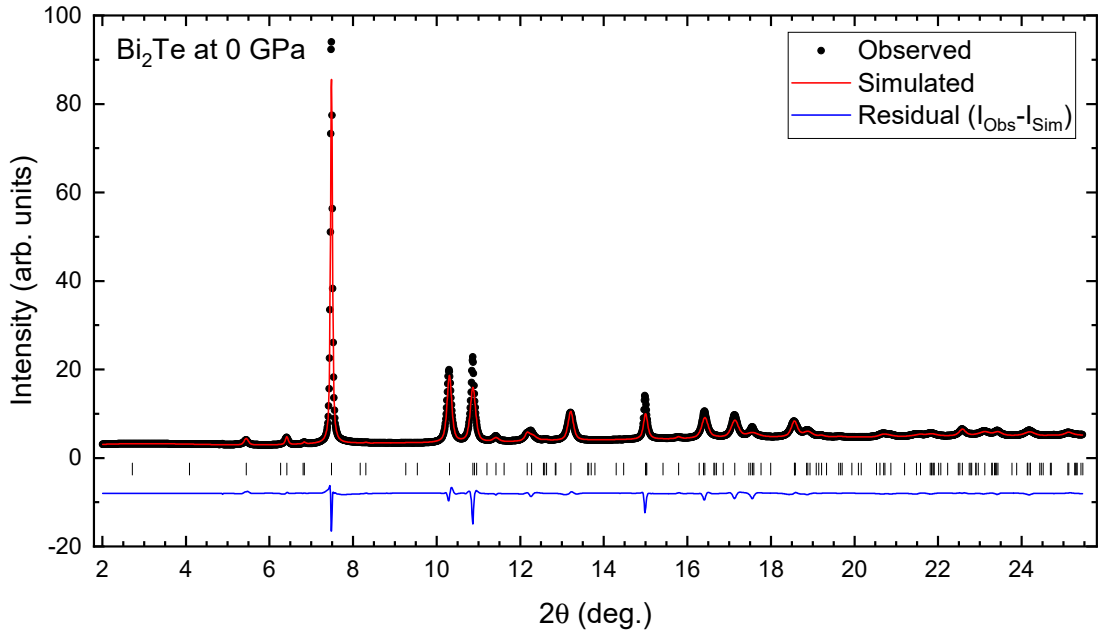

Figure 5.16 *Rietveld refinement of a Bi_2Te x-ray powder diffraction profile at ambient pressure, while in phase I. The refinement describes the observed profile well, with an R-value of $wR_p = 0.89\%$.*

positions:

$$t_5 = 2cz_4 \tag{5.4}$$

$$t_2 = c[(1 - z_5) - z_2] \tag{5.5}$$

$$d_{5-2} = c[z_2 - z_4] \tag{5.6}$$

$$d_{2-2} = c[z_5 - (1 - z_5)] \tag{5.7}$$

A single XRPD image recorded at ambient pressure was available from experiment EE8105 at Diamond Light Source in 2012. The image is a 300s exposure of powdered Bi_2Te (sample *MB-π1*) with the sample rotated by $\pm 5°$ during the exposure to achieve better powder averaging. The image was integrated using Fit2D and uncertainties on the integrated intensities were estimated (see section 3.5.2). The resulting XRPD profile was then analysed using the Rietveld refinement software Jana2006 [91]. The refinement of this profile using the final structural model is shown in figure 5.16

The ambient-pressure structure of Bi_2Te has previously been determined and refined by Bos *et al.* [28]. The structural parameters determined by Bos *et*

al. were used as a starting point for refinement of the ambient pressure profile. Refinements in Jana2006 can be characterised by their weighted R-value, wR_p, in order to compare the quality of different fits, with lower R-values generally indicating better fits [10]. Refinement with atomic parameters (site occupation factors (SOF), isotropic atomic displacement parameters (U_{iso}) and atomic positions) fixed at the values determined by Bos *et al.* produced a good fit with $wR_p = 1.14\%$.

While this initial fit was reasonable, there were clear discrepancies in the peak intensities and widths. This was most pronounced for the most intense peak in the profile, corresponding predominantly to the (103) reflection, along with a negligible contribution from the $(1\bar{1}3)$ reflection. Improvement of the fit required inclusion of the effects of anisotropic strain broadening, whereby profile peaks can have differing widths based on the Miller indices of the reflection corresponding to that peak. This can result from structural defects like stacking faults and is not unexpected in this layered structure. In fact, signifiant broadening of x-ray diffraction peaks has been reported in some Bi-Te compositions at ambient conditions and is suspected to be a result of stacking irregularities [28]. Anisotropic strain broadening is modelled in Jana2006 through the 'tensor method' developed by P. W. Stephens in 1999 [120].

Inclusion of anisotropic strain broadening required the addition of 4 free parameters to the refinement: 3 independent parameters in the anisotropic strain tensor, and '*Zeta*', which determines the proportion of Gaussian and Lorentzian components in the Pseudo-Voigt peak shapes used here. The profile was refined first without anisotropic strain broadening to determine starting values of the other peak shape parameters, GW and LY. These values were comparable to the instrumental broadening as determined through refinement of a profile from a reference sample of silicon, recorded during the same experiment. Alternating the refinement of the anisotropic strain broadening parameters with the peak shape parameters fixed, and vice versa, allowed the refinement to converge to an improved fit.

The anisotropic strain broadening parameters refined to sensible values, comparable to those reported as examples by Stephens. Inclusion of this correction improved the R-value from $wR_p = 1.14\%$ to $wR_p = 0.93\%$ (an 18% reduction), along with providing a visually improved fit to the profile. The other structural parameters could then be refined, starting from the values reported by Bos *et al.*.

Full refinement of the atomic parameters resulted in small improvements in wR_p but led to unphysical values in the refined parameters. The atomic displacement parameters (U_{iso}), which have units of Å^2, would often refine to at least one negative value. Fixing that displacement parameter would allow another to become negative or approach zero. Refining all atomic parameters also resulted in several site occupation factors which refined to significantly negative values (e.g. the tellurium site occupation factor of Atom 2: -15.3(3)%).

In order to successfully refine the profile, the atomic displacement parameters (U_{iso}) were fixed at the values published by Bos *et al.* (see table 5.1). This had negligible effect on the refined atomic positions (z_2–z_5) which remained the same within uncertainty, with the exception of z_4 where fixing the U_{iso} values increased its value by 0.7%, comparable to its refined uncertainty of 0.4%.

The refined profile fits well to the measured profile, as shown in figure 5.16. The R-value of this refinement is $wR_p = 0.89\%$. The refined atomic parameters are summarised in table 5.1.

Atom	**x**	**y**	**z**	**Bi SOF**	U_{iso} **(Å^2)**	
1	0	0	0	-0.02(8)	0.025	
2	0	0	0.3418(10)	1.03(4)	0.020	
3	1/3	2/3	0.8836(15)	0.97(3)	0.021	this work
4	1/3	2/3	0.2113(9)	0.29(8)	0.011	
5	1/3	2/3	0.5627(10)	0.72(10)	0.016	
Te2	0	0	0	-0.01(2)	0.025(4)	
Bi1	0	0	0.3383(3)	0.98(2)	0.020(2)	
Bi3	1/3	2/3	0.8880(4)	1.00	0.021(1)	Bos *et al.* [28]
(Te/Bi)1	1/3	2/3	0.2113(4)	0.33(2)	0.011(2)	
(Bi/Te)2	1/3	2/3	0.5681(3)	0.67(2)	0.016(2)	

Table 5.1 *Comparison of published Bi_2Te-I ambient pressure parameters [28], bottom, to refinement results from measured XRPD data, top. Note that the thermal parameters are fixed in our refinement. Published lattice constants are a=4.4688(1)Å, c=17.9216(4)Å, and refined lattice constants are a=4.4693(2)Å, c=17.8808(17)Å.*

The refined lattice parameters are slightly different from those reported by Bos *et al.* [28], as are the atomic positions with the exception of z_4. Such slight disagreement is not surprising given the different natures of the measured Bi_2Te samples in both cases: here, a small powdered sample held within a diamond anvil cell, and the bulk sample held within a vacuum-sealed quartz tube investigated

by Bos *et al.*. The quality of diffraction data obtained from such samples also varies considerably, with our small sample much more susceptible to the effects of powder texture.

The refined site occupation factors agree within uncertainty with those previously reported, indicating some transfer of atoms between the layers and a slight departure from the idealised structure where Bi_2 and Bi_2Te_3 blocks are stacked along the *c*-axis (figure 5.15). Atoms 4 and 5, which are fully occupied by tellurium and bismuth (respectively) in the idealised structure, are instead occupied by both atom types in the ratio 2:1, with the majority atom type the same as their idealised type.

Phase I was observed in our high-pressure XRPD data (experiments EE8105 and hs4718) up to a pressure of 6.5 GPa and was the only phase present up to around 5 GPa, above which peaks from the phase-II and host-guest structures were also visible. Measured diffraction images were again processed to produce profiles of diffraction angle vs. integrated intensity, along with estimated intensity uncertainties. These profiles were then refined using Jana2006.

6 profiles from the EE8105 experiment were analysed using Rietveld refinement, with an additional profile analysed with a le Bail fit (providing only lattice parameters and not any information on the atoms within the unit cell). These profiles span a pressure range from 0.9–5.2 GPa and were collected on increasing pressure. A total of 8 profiles were refined from data recorded during the hs4718 experiment, at increasing pressures from 2.1–4.8 GPa. In all exposures, the sample was rocked $\pm 3^\circ$ during exposure to improve powder averaging; all are 10s exposures, except the profile at 2.14 GPa, which appears to be only 1s. Initial refinements of profiles across the pressure range were found to be unstable, particularly in the refined atomic site occupation factors (SOFs) and isotropic thermal parameters, with the latter often refining to unphysically small or negative values as for the ambient-pressure refinement.

In order to achieve consistent and stable fits, the thermal parameters and SOFs were fixed for all Bi_2Te high-pressure phase-I refinements at the values published by Bos *et al.* (see table 5.1).

The results of the Bi_2Te phase I refinements are summarised in figures 5.17 – 5.19. The refined lattice parameters are shown in figure 5.17; they exhibit a smooth reduction with increasing pressure. The lattice parameters reported by Bos *et al.* are included for comparison. Clearly the *c* lattice parameter shows the greater

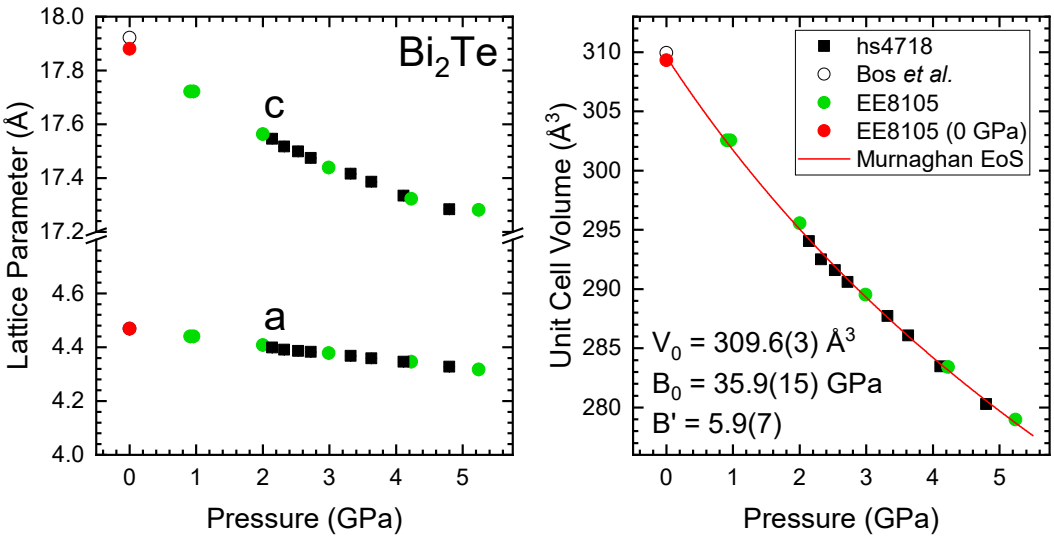

Figure 5.17 *Refined lattice parameters and unit cell volume of the Bi_2Te phase I structure. The unit cell volume is fitted with the Murnaghan equation of state [121]. Uncertainties are smaller than the symbol size and have been omitted for clarity. The lattice parameters are plotted to the same vertical scale, illustrating the higher rate of compression along the c-axis.*

difference from the published value, even when taking into account the relative magnitudes of a and c. The relative differences between the published and refined values are small: +0.01% for a and -0.2% for c, using (1 − published/refined).

The unit cell volume can be fitted using the Murnaghan equation of state [121] giving a fitted unit cell volume at zero applied pressure, $V_0 = 309.6(3)$ Å^3 and a bulk modulus value of $B_0 = 35.9(15)$ GPa with a first derivative of $B' = 5.9(7)$. The fitted value of V_0 agrees well with the previously published [28] and refined (in this work) ambient-pressure unit cell volumes of 309.95(2) and 309.31(4) Å^3, respectively.

Figure 5.18 summarises the refined atomic positions (z coordinates) with all data plotted to the same scale. The positions of atoms 2 & 3 appear to remain fixed over the pressure range (0–5 GPa), the z-coordinate of atom 4 gradually increases (from around 0.21–0.22) and that of atom 5 shows a slight decrease. The layer thicknesses and separations calculated from these atomic positions are plotted in figure 5.19; they show layer thicknesses that remain approximately constant and inter-layer distances that reduce gradually over the pressure range. As expected, the weaker Van der Waals bonding between the Bi_2 and Bi_2Te_3 layers provides less resistance to compression than the mixed covalent-ionic bonds within the layers.

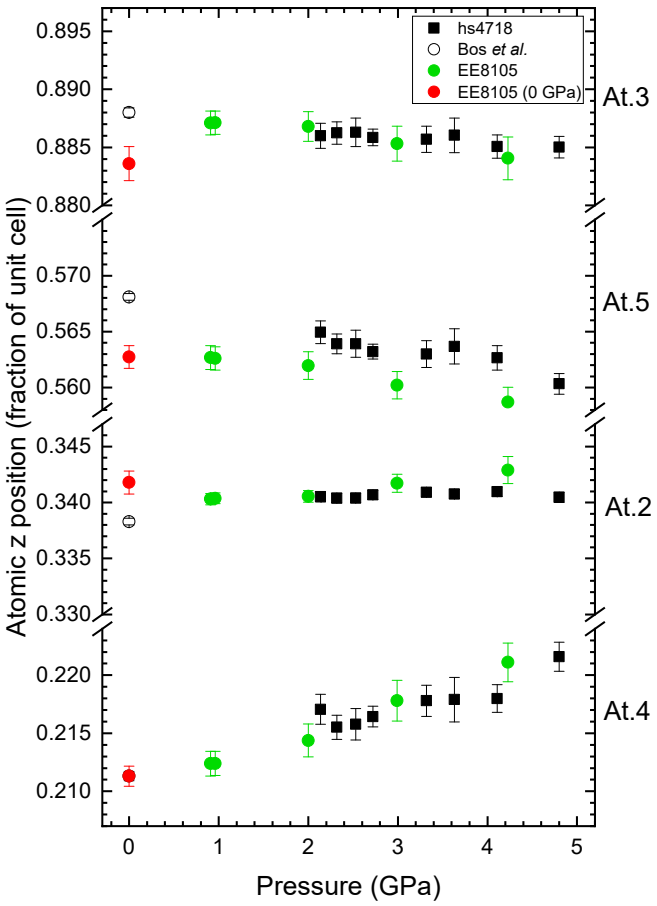

Figure 5.18 *Refined atomic positions in phase I of Bi_2Te. All data plotted to same y-axis scale with error bars included; the refined coordinates of atom 2 have significantly smaller uncertainties than the others, similar to the size of the symbols.*

The results from the two experiments agree qualitatively, but show slight discrepancies in the actual values. This is most noticeable in the z-coordinate of atom 5, where the hs4718 data is offset from the data from EE8105. As the distance between the two-atom layers in the structure is defined as $d_{2-2} = c[z_5 - (1 - z_5)]$, this discrepancy in z_5 leads to a significant difference in d_{2-2}. The d_{2-2} values from both experiments straddle the values for d_{5-2}, the distance between the two-atom and five-atom layers, suggesting that these differences are, on average, quite similar.

As detailed in chapter 2, it has been established that Bi_2Te_3 exhibits a structural anomaly within the stability range of phase I. This anomaly has been described in the literature as an 'isostructural transition' or more widely as an 'electronic topological transition' ('ETT') and is reported to occur at pressures of a few GPa. This anomaly does not result in any discontinuous change of the crystal

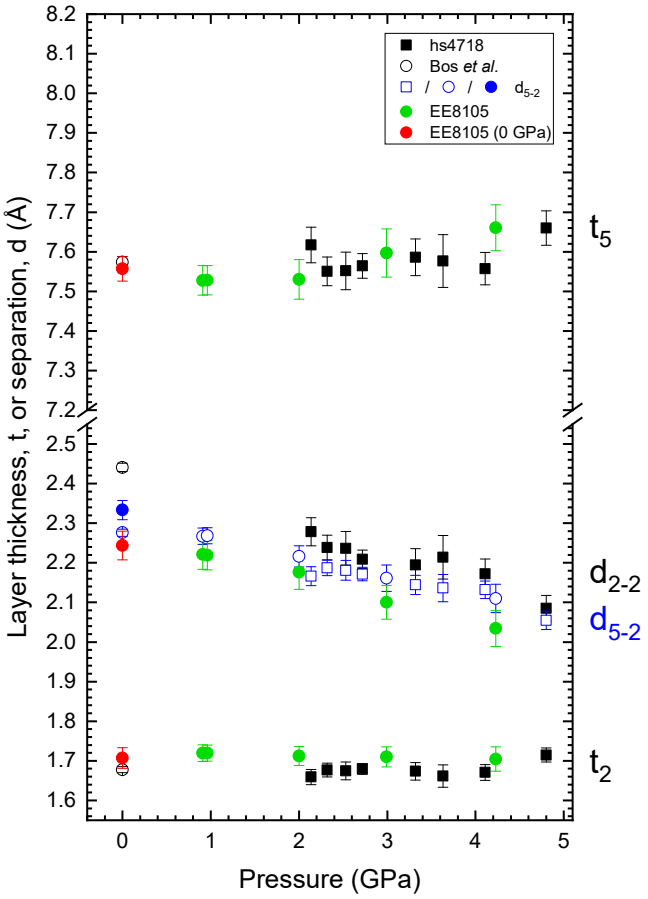

Figure 5.19 *Thicknesses and separations of the constituent 5-atom Bi_2Te_3 and 2-atom Bi_2 layers of Bi_2Te phase-I, as illustrated in figure 5.15 and defined in equations 5.4-5.7. The same y-axis scale is used on both sides of the axis break.*

structure or atomic positions and has been predicted and evidenced through a variety of methods including band-structure calculations [122] and anomalies in compressibility in structural studies [47, 48]. Due to the similarities in the phase I crystal structures between Bi_2Te_3 and Bi_2Te and evidence of universal behaviours across the $(Bi_2)_m$ $(Bi_2Te_3)_n$ series [3, 4, 12, 24], it might be expected that Bi_2Te also shows such structural anomalies at relatively low pressures.

Indeed, the ratio of lattice parameters, (c/a), exhibits a minimum at around 3 GPa, as can be seen in figure 5.20a. There is a systematic offset between the data collected during experiments EE8105 and hs4718, with both datasets appearing to exhibit a minimum around 3 GPa. This feature in the pressure dependence of the (c/a) ratio has been previously used as an indication of the presence of an isostructural transition in phase I of Bi_2Te_3. Work by Nakayama *et al.* reports a similar (c/a) pressure dependence [48] and a later study by Polian *et*

al. also found a minimum in the (c/a) ratio as a function of pressure [47], in agreement with Nakayama *et al.* Figure 2 of that study [47] compares the (c/a) ratios reported in the two studies which show a systematic offset between the results of Nakayama and Polian *et al.* This is similar to the offset observed in this work on Bi_2Te. Here there is a relative difference of about 0.1% and the offset in the reported Bi_2Te_3 data is around 0.3%.

An alternative analysis of the refined structural parameters, reported by Polian *et al.* in their work on Bi_2Te_3 [47], makes use of a linearised version of the Birch-Murnaghan equation of state. By utilising the refined unit cell volume as a function of pressure, this method indicates structural anomalies by a change in the linear behaviour of the linearised equation of state. They use this method to obtain a clearer estimate of the pressure at which this anomaly occurs. To determine whether this method could be of use for the Bi_2Te refinements performed here, this method was applied to the hs4718 dataset.

The Birch-Murnaghan equation of state (equation 5.8) relates the pressure to the bulk modulus, B_0, its derivative with respect to pressure, B', and X [123]:

$$P = \frac{3}{2}B_0X^5(X^2-1)\Big[1+\frac{3}{4}(B'-4)(X^2-1)\Big], \tag{5.8}$$

where $X = \left(\frac{V_0}{V}\right)^{\frac{1}{3}}$, V is the unit cell volume and V_0 is the unit cell volume at ambient pressure.

The Eulerian strain can be defined as:

$$f_E = \frac{1}{2}(X^2-1) \tag{5.9}$$

By rearranging (5.9) for X and substituting into (5.8), a linear form in terms of f_E can be obtained:

$$H = \frac{3}{2}B_0(B'-4)f_E + B_0, \tag{5.10}$$

where we have defined a reduced pressure, H, by:

$$H = \frac{P}{3f_E(2f_E+1)^{\frac{5}{2}}} \tag{5.11}$$

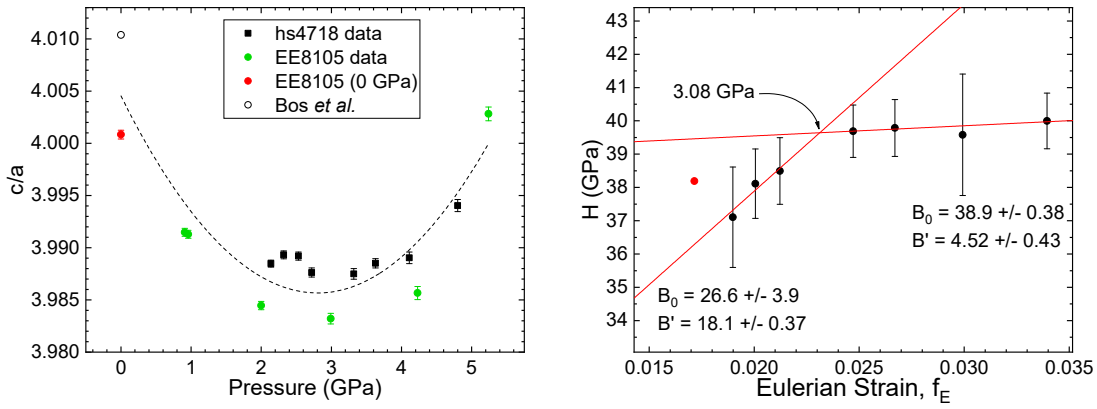

Figure 5.20 *Left: Bi_2Te ratio of lattice parameters. The proposed pressure at which the iso-structural transition occurs is indicated. Dashed line is guide to the eye. Right: Following analysis performed in [47] the Eulerian strain, f_E, is plotted against the reduced pressure, H. The intersection of two linear fits in the regions before and after the transition gives an estimate of the transition pressure.*

Figure 5.20b shows H plotted as a function of f_E using the measured pressures and refined unit cell volumes. In such a plot, a 'normal' structure which has no changes in its behaviour under pressure would appear as a single linear trend in the data. In our Bi_2Te data, there appears to be a change in the linear behaviour, similar to the reported analysis of Bi_2Te_3 [47]. Taking linear fits of the data on either side of this change and determining the point of intersection, gives a Eulerian strain (f_E) which corresponds to a pressure of 3.08 GPa. This agrees well with the observed minimum in the (c/a) ratio data.

However, estimating the uncertainty on this value through standard error propagation reveals a huge uncertainty in this value of ± 1.95 GPa. While Polian *et al.* obtain a reasonably precise estimate of the pressure at which the structural anomaly occurs, the Bi_2Te data does not have the range to provide a similar result. As such, this method can be applied here to produce an alternative visualisation of the structural anomaly, but is unable to determine a more precise pressure than simple visual inspection of the (c/a) ratio data. A similar conclusion was reached by Manjón *et al.* in work on Bi_2Se_3, which adopts the same ambient-pressure structure as Bi_2Te_3. They found that this analysis suffered from 'very large errors ... even for very good data obtained using monochromatic x-rays from synchrotron sources' and concluded that this method is 'not accurate enough to discuss the occurrence of the pressure-induced ETT' [39].

Conclusion

In this section the layered structure of phase I of Bi_2Te was investigated under pressures up to 5 GPa. A single x-ray powder diffraction profile measured at ambient conditions was available for refinement and direct comparison to a previously reported refinement by Bos *et al.* [28]. This profile was refined using structural models consisting of fixed, idealised Bi_2 and Bi_2Te_3 layers, and with the exchange of atoms between the layers included. Exchange of atoms between the layers was found, in agreement with the work of Bos *et al.*

Slight discrepancies between the reported and refined lattice parameters were found, with relative differences of 0.01% and 0.2% for the a and c lattice parameters, respectively. Such slight differences may be due to the differing nature of the powder samples considered in each case; here a small sample held within a diamond anvil cell, and a bulk sample vacuum-sealed in a quartz tube in the published study.

High-pressure phase-I profiles were analysed up to around 5 GPa. Rietveld refinements yielded lattice parameters and atomic coordinates for the structure, allowing the pressure behaviour of the constituent layers to be observed. On increasing pressure, the thicknesses of the two-atom (t_2) and five-atom (t_5) layers are found to increase slightly, by around 1%, over the pressure range. Meanwhile the distances between the layers (d_{2-2} and d_{5-2}) both decrease by around 13%. The subtle increase in layer thicknesses as the pressure is increased suggests a strengthening of the inter-layer interactions as the layers are brought closer together and the structure approaches a phase transition. Refinements of the high-pressure data were performed with atomic site occupation factors fixed at the same values determined at ambient pressure, in agreement with Bos *et al.*

The refined data was obtained in two separate experiments; the refined structural parameters show good agreement across both, but with a systematic difference between the values of the inter-layer distance, d_{2-2}, of approximately 5%. Both datasets appear to share similar values of the inter-layer distance d_{5-2}, with one dataset having a slightly larger d_{2-2} separation than d_{5-2} separation. This is reversed for the other dataset, suggesting some variability in the inter-layer distances.

The ratio of lattice parameters (c/a) was found to exhibit a minimum as a function of pressure. A systematic offset was observed between the data collected during

different experiments, but with both datasets exhibiting the same minimum near 3 GPa. This behaviour is similar to that of Bi_2Te_3 which also exhibits a minimum in the c/a ratio as a function of pressure (see section 2.4.1). This structural feature has been attributed to an 'electronic topological transition' in the literature and an analysis method used by Polian *et al.* [47] was used in an attempt to better resolve this structural anomaly. However, the method suffers from large uncertainties even with good data and, as such, did not provide any improvement in the analysis.

On increasing pressure, Bi_2Te transforms from phase I to the (unidentified) phase-II structure, then to the host-guest phase. The next section in this chapter will consider phase II.

5.4 Phase II: Unidentified Structure

The first high-pressure phase of Bi_2Te, referred to here as *phase II*, appears both on initial pressure increase and pressure release. It emerges from phase I at around 5.5 GPa, becoming the dominant phase at around 8.5 GPa and remaining visible in the diffraction profiles up to 13 GPa. Phase II overlaps briefly with phase I and significantly with the host-guest phase, the most intense peaks from which are visible in the phase-II diffraction profiles. Once the Bi_2Te sample has been pressurised up to the higher-pressure phases (host-guest and cubic), the sample adopts the same structural phases on pressure release. Phase II appears between around 4 GPa and 2.7 GPa on pressure release, before the sample returns to the phase-I structure.

The diffraction profiles of phase II across all compositions are very similar, suggesting a common phase-II structure in the Bi-Te series. Figure 5.21 shows an example of an x-ray diffraction profile from phase II of Bi_2Te showing the typical form of three sharp, intense diffraction peaks near 8° and 10° along with several broad peaks, seen here at around 10.5°, 11.5° and 14°. Figure 5.21 also includes a profile measured from Bi_2Te_3; there is a strong similarity between the two profiles, suggesting that both compositions have closely related structures in this phase.

The Bi_2Te_3 profile shows the first high-pressure phase of Bi_2Te_3, referred to in the literature as β-Bi_2Te_3. As discussed in section 2.4.1, the structure of

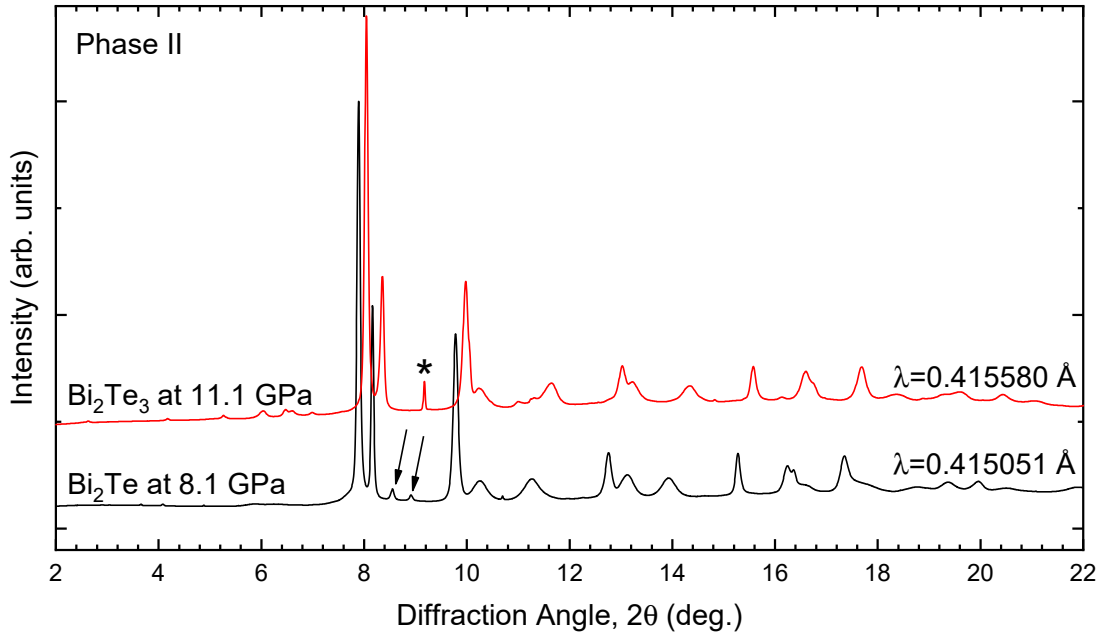

Figure 5.21 *Comparison of x-ray powder diffraction profiles from the first high-pressure phase ('phase II') of Bi_2Te (bottom) and Bi_2Te_3 (top) illustrating the close resemblance between them. Indicated in the profiles are peaks from the Bi_2Te host-guest phase (↓) and a peak due to the solidified nitrogen pressure-transmitting medium used in the measurement of Bi_2Te_3 (*).*

this phase of Bi_2Te_3 has been proposed as a monoclinic *C2/m* structure [110]. However, observations based on our data suggest that this may not be the most appropriate structural description of phase II and a better model may be attainable. Unfortunately, in this work we were unable to determine the structure of phase II and are restricted here to merely report that: i) all investigated Bi-Te compounds appear to adopt the same first high-pressure phase, *phase II*, and ii) these phases appear to share similar structures which are closely related to β-Bi_2Te_3.

The attempts at closer investigation of phase II, along with observations pertaining to the appropriateness of the *C2/m* structure are described in section 10.3.

5.5 Phase V: Cubic Structure

The final phase observed in Bi_2Te at the highest pressures investigated in this work (up to 25 GPa) is referred to as the *cubic phase*. On initial pressure increase,

the diffraction profiles of Bi_2Te include peaks from a body-centred cubic (bcc) structure which appear while the majority of the sample is in the host-guest phase. As the sample transitions out of the host-guest phase it adopts a fully site-disordered bcc alloy structure, where the atomic site of the structure is occupied by a stoichiometric mix of Bi and Te (2:1, Bi:Te). This bcc structure persists on subsequent pressure decrease, with peaks due to this structure visible after the sample has transformed to the host-guest phase. However, during experiment EE8105 the sample was annealed at 100°C for two hours while in the cubic phase. After annealing, the sample was observed to have partially ordered, adopting a variant of the CsCl structure, as reported by Loa *et al.* [12].

All investigated samples of Bi_2Te showed evidence of the presence of a bcc structure over a reasonably wide pressure range. Sample *hs21a*, which did not fully transform to the bcc structure, included peaks from this cubic phase in profiles from 11.9 GPa on pressure increase and down to 9.10 GPa on pressure decrease, while still in the host-guest phase. Sample *hs21b* focused on the cubic phase and was measured at pressures from 15.0–20.2 GPa. Peaks from the cubic phase were visible in all recorded *hs21b* profiles, with the sample fully adopting the bcc structure at 19.7 GPa. Data obtained from experiment EE8105 includes only three profiles where the cubic phase is present: one at 14 GPa while the majority of the sample is in the host-guest phase, and two others where the sample has adopted the cubic phase, at 25 GPa and 15 GPa.

The transition from the host-guest to cubic phase is illustrated in figure 5.22, which shows powder diffraction profiles from sample *hs21b*. A structural phase transition in the nitrogen pressure transmitting medium, which has solidified at these high pressures, can also be observed (δ^*-N_2 to ϵ-N_2 [100, 124]). Due to the significant overlap with the host-guest phase, the lattice parameter of the cubic phase was included in the host-guest refinements, allowing the structures of both phases to be refined simultaneously. The most clear peak from the cubic phase present in the host-guest profiles appears around 16°, as can be seen in figure 5.22, which shows the growth of the cubic phase on pressure increase from 15–20 GPa.

Clean diffraction profiles of the cubic phase (once the sample had transformed from the host-guest phase) were refined using Jana2006 [91]. An example refinement is shown in figure 5.23. Clearly, the bcc structure provides a good fit to the measured diffraction profile, while some weak peaks are left unaccounted for (these being residual peaks from the preceding host-guest phase and peaks due to the solidified nitrogen pressure transmitting medium).

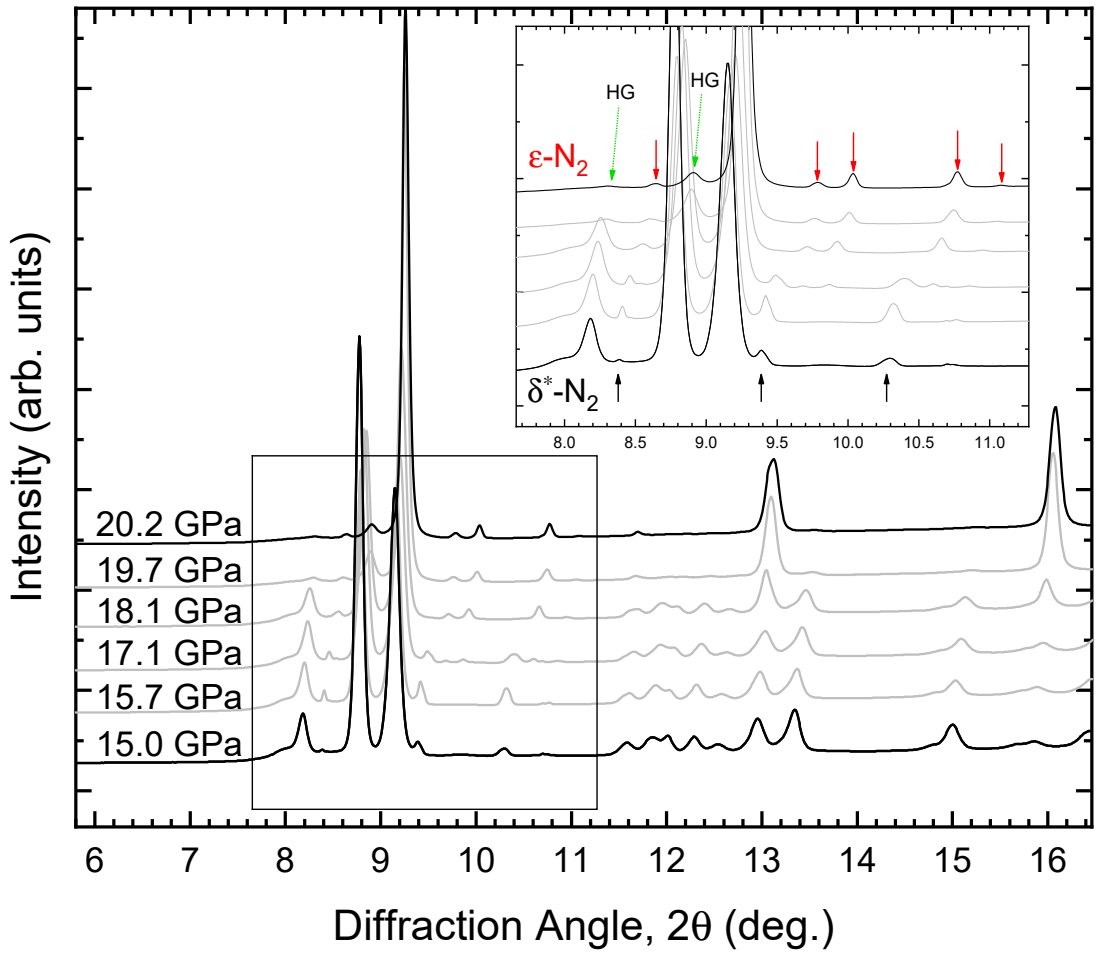

Figure 5.22 *Powder diffraction patterns of Bi_2Te showing a transition from the host-guest to the cubic phase on pressure increase. Inset illustrates the peaks from nitrogen pressure-transmitting medium and residual host-guest peaks in the highest-pressure profile.*

The inset of figure 5.23 indicates the calculated position of the (100) reflection, near 6.5°. This reflection is forbidden in the fully site-disordered bcc structure, but would be present if any atomic ordering existed within the cubic structure, as has been reported previously in several bismuth-telluride compounds at high pressures [12]. There is no evidence of any diffracted intensity at this position, confirming that the cubic phase of Bi_2Te adopts a fully site disordered bcc structure.

After annealing, however, the cubic phase does partially order. In experiment EE8105 a sample of Bi_2Te was taken up in pressure to 25 GPa, where it assumes the site-disordered bcc structure of the cubic phase. This sample was then annealed at 100°C for two hours, during which time the pressure dropped to 15 GPa. On subsequent measurement, the sample was found to have partially

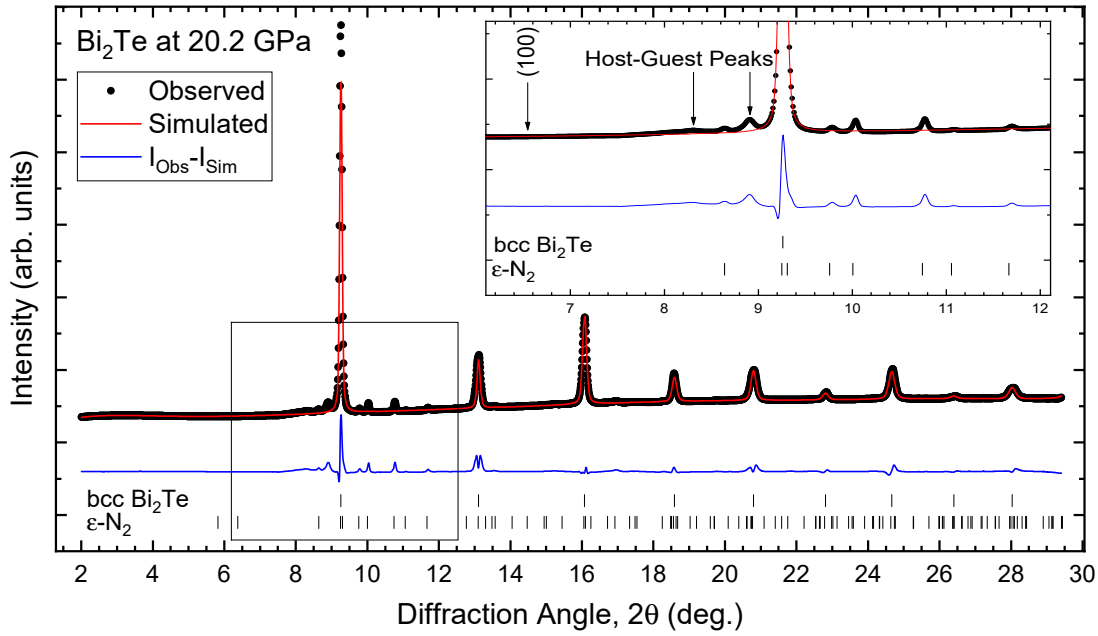

Figure 5.23 *X-ray powder diffraction profile of Bi_2Te at 20.2 GPa where the sample is in the cubic phase. The indicated sharp, weak peaks are due to the nitrogen pressure transmitting medium, which has solidified in to the ϵ -N_2 structure.*

ordered, adopting a variant of the CsCl structure in which the two atomic sites have mixed Bi/Te occupancy. This profile (along with other, similar profiles from other compositions) was refined by I. Loa and the result reported in a recent paper [12]. The sample of Bi_2Te was found to adopt a structure with Bi:Te ratios of 90:10(2) and 41:59(2) for the two atomic sites. A small amount of bismuth (around 6%) was found to have precipitated from the sample, appearing as shoulders on the lower-angle edges of the cubic-Bi_2Te peaks.

The refined cubic lattice parameter of Bi_2Te is shown in figure 5.24, exhibiting a smooth decrease with increasing pressure and showing consistency across the two samples and increasing/decreasing pressure runs. Figure 5.24 also shows the unit cell volume as a function of pressure, to which the Murnaghan equation of state [121] has been fitted resulting in values of the unit cell volume at zero applied pressure, bulk modulus and first derivative of the bulk modulus of $V_0 = 61.6(5)$ Å^3, $B_0 = 42(4)$ GPa and $B' = 4.8(2)$, respectively.

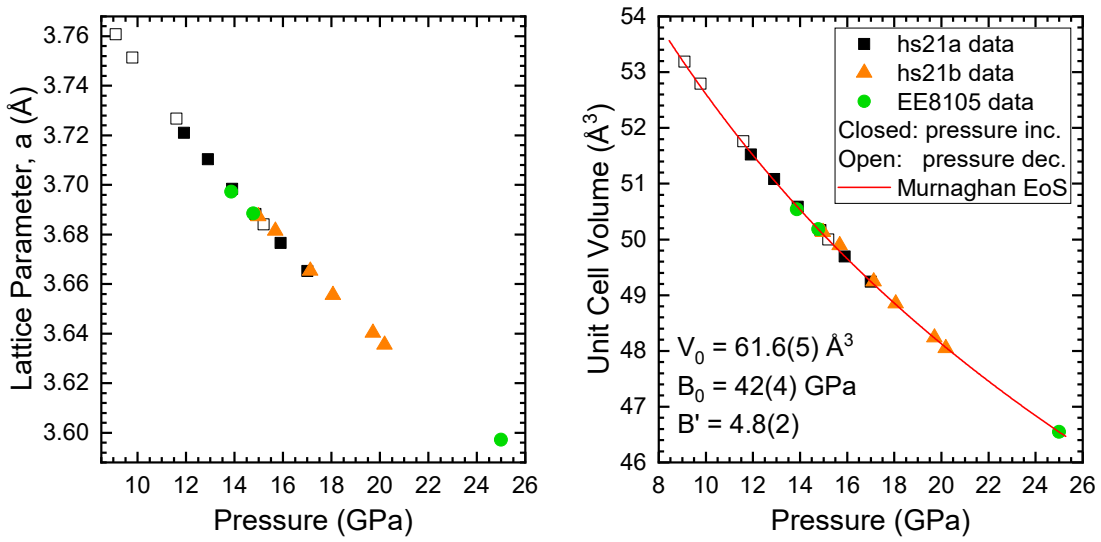

Figure 5.24 *Refined lattice parameter of cubic Bi_2Te phase, with unit cell volume fitted with the Murnaghan equation of state. Note that closed (solid) symbols correspond to data collected on pressure increase, while open symbols denote data collected on pressure decrease.*

5.6 Phases on Pressure Decrease

Only sample *hs21a* was recorded on pressure decrease, from the host-guest phase at 17 GPa. Bi_2Te remains purely in the host-guest phase down to 4.1 GPa, where peaks from phase II appear. This mixed phase (majority host-guest) persists down to 2.7 GPa, after which the pressure was reduced to 0.5 GPa where the XRPD profile shows the sample to have fully adopted the ambient-pressure layered structure (phase I) once again. The sample recovered to ambient pressure shows a clean diffraction profile indicating phase I with no evidence of other structural phases present. These transitions are illustrated in the waterfall plot shown in figure 5.25.

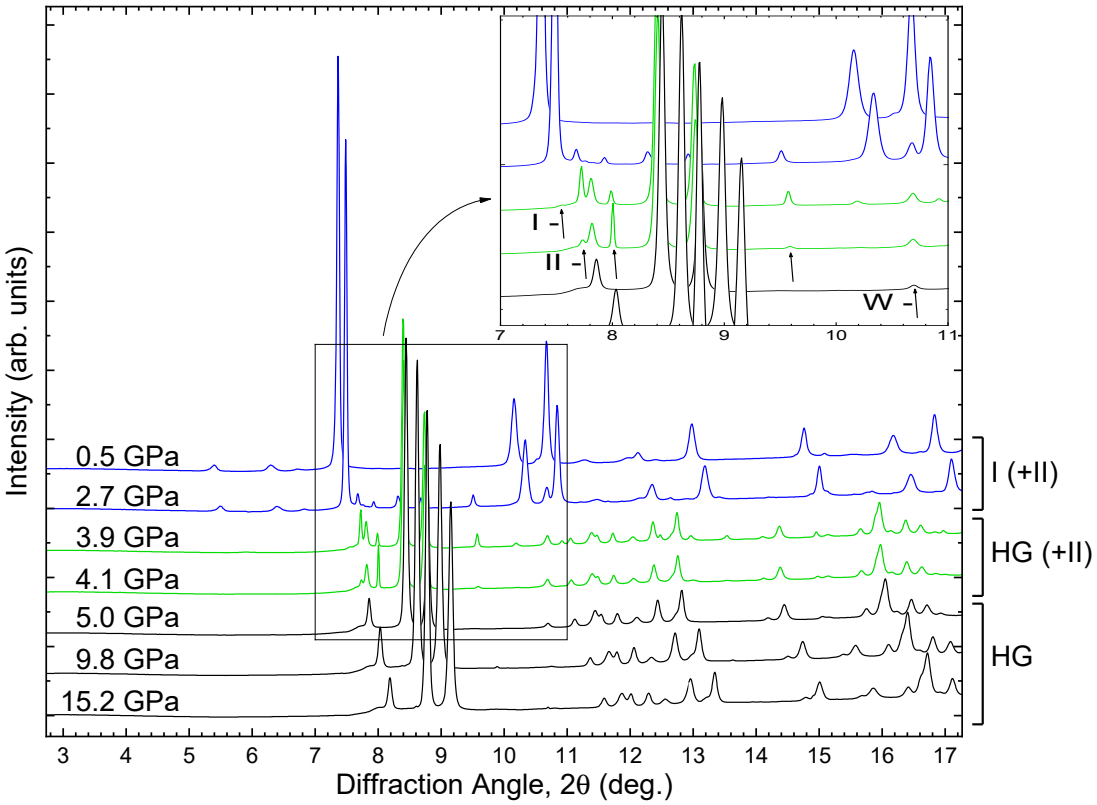

Figure 5.25 *Powder diffraction profiles of Bi_2Te on pressure decrease illustrating the transition from the host-guest (HG) phase. Inset: detail showing emergence of low-pressure phases ('I' and 'II') and a peak from hitting the tungsten gasket ('W').*

Chapter 6

Bi_7Te_3

Bi_7Te_3, comprised of 70% bismuth, is close in composition to Bi_2Te and is the most bismuth-rich member of the Bi-Te series investigated here. It lies at the extreme of the stability region of the $(Bi_2)_m(Bi_2Te_3)_n$ series, with Bi_xTe_{1-x} compositions of $x > 0.70$ decomposing into multiple phases and only compositions with $0.44 \leq x \leq 0.70$ stable as a single phase at ambient conditions [28]. As such it is the most bismuth-rich stable member of the series except for the end member — pure bismuth.

This chapter will present the results of XRPD experiments on Bi_7Te_3 and the analysis of the data collected. It appears that members of the Bi-Te series share a number of structural phases and behaviours under pressure. Being close in composition to Bi_2Te, Bi_7Te_3 may be expected to behave similarly under pressure. Indeed, this is found to be the case. Now that the details of the main structural phases have been introduced in the previous chapter, this chapter can proceed to discuss the observed phases in the order in which they appear on initial pressure increase.

This chapter will describe the layered structure of phase I of Bi_7Te_3 and introduce the alternative description of this structure as a incommensurately-modulated structure in four dimensions. This is in contrast to phase I of Bi_2Te which can be fully described in three dimensions. The chapter will then proceed with a description of phase II, which appears to be a similar phase to that described in the previous chapter. The host-guest phase will then be described, and the same analysis of this semi-disordered structure will be performed as in the previous chapter. Finally, the cubic phase of Bi_7Te_3 will be discussed before the

observations made on pressure reduction are presented.

6.1 Bi_7Te_3 Experiment Summary

In this work, Bi_7Te_3 was investigated in two synchrotron experiments: hc1335 at the ESRF (July 2014) and EE12996 at Diamond Light Source (February 2016). Both made use of powdered samples held within Merrill-Bassett diamond anvil cells with tungsten (W) gaskets and helium (He) as a pressure-transmitting medium.

Diffraction patterns of the sample from the first experiment (denoted here by '*hc73*') were measured at pressures between 0.9–25.9 GPa using x-rays with wavelength $\lambda_{hc1335} = 0.415352$ Å. Due to a failure of the beamline ruby system, alternate x-ray exposures were taken with the beam directed through a portion of the gasket in order to determine the internal cell pressure by fitting the observed position of W diffraction peaks to the equation of state.

Experiment EE12996 investigated a sample (denoted here by '*EE73*') at pressures between 2.4–26.4 GPa. This experiment made use of a Perkin-Elmer detector and the wavelength of x-rays used in the data analysis was $\lambda_{EE12996} = 0.415666$ Å, taking the correction for the detector into account. This later experiment sought to investigate several 'peaks of interest' which had been previously observed at the lower pressure range of the host-guest phase. These peaks appear at positions close to expected guest reflections and were considered to be a sign of an ordering of the guest substructure. As discussed for Bi_2Te (see page 71), these peaks are actually from phase II which overlaps slightly with the host-guest phase. To investigate the effect of pressure-cycling and annealing on these peaks, sample *EE73* was taken initially up in pressure to the cubic phase, then the pressure was reduced until the sample transformed to the host-guest phase. From here, the pressure was again increased and the sample was annealed, while in the host-guest phase, at 100°C for 20 hours.

Powder diffraction profiles from each of the observed phases of Bi_7Te_3 are shown in figure 6.1. The inset illustrates the overlap between the host-guest phase and phase II, with the most intense host-guest peaks indicated by dashed lines. Also indicated are peaks due to the 'contaminant' that was identified as elemental bismuth present in the sample chamber. As this bismuth may have precipitated

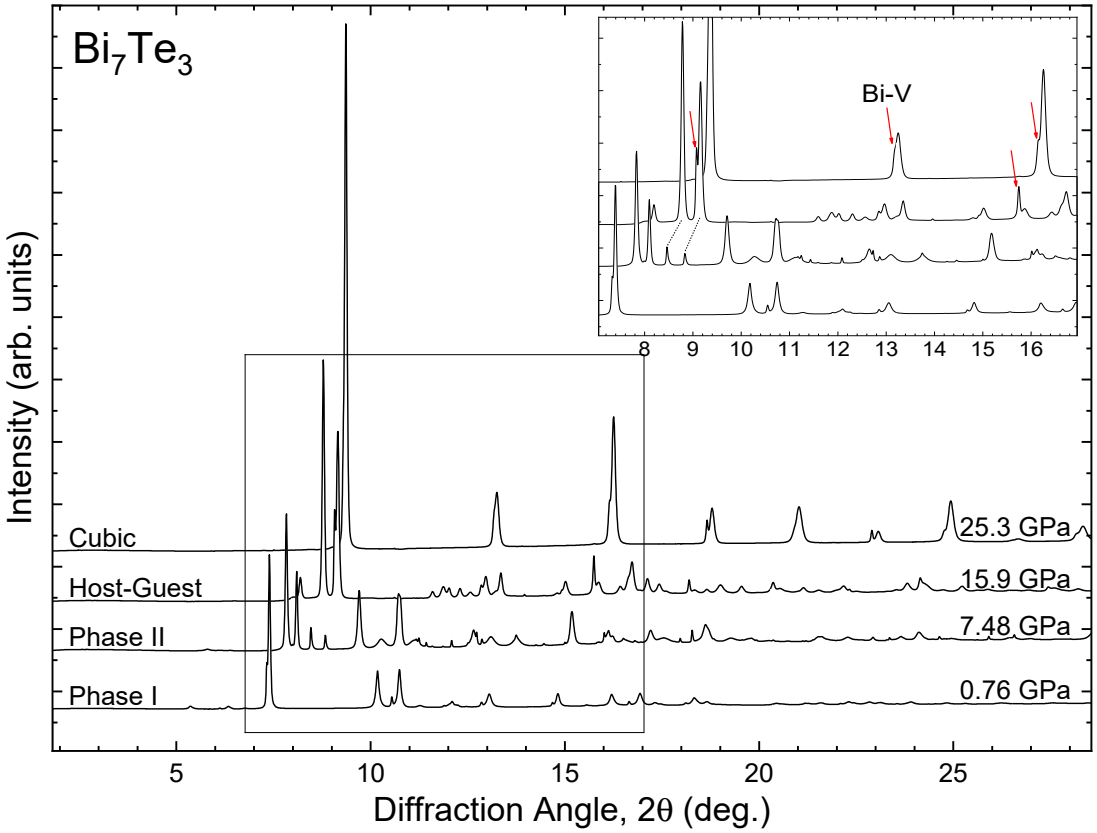

Figure 6.1 *Powder diffraction profiles of Bi_7Te_3 illustrating the observed phases on initial pressure increase. All profiles are from experiment hc1335. Inset shows the 'contaminant' peaks that have been identified as from elemental bismuth.*

out of the Bi_7Te_3 sample, the actual composition of the Bi-Te material studied here may include less than 70% bismuth. The composition will continue to be referred to as Bi_7Te_3 in this work. This elemental bismuth contaminant phase is most clearly seen at pressures where the bismuth adopts the body-centred-cubic structure of Bi-V [125]; peaks from this phase are indicted by red arrows and can be seen in the profiles from the Bi_7Te_3 host-guest and cubic phases.

Bismuth undergoes several phase transitions over the pressure range considered here from an As-type *hR2* structure, Bi-I [126], at ambient conditions to Bi-II with the *mC4* structure at around 2.6 GPa [32]. This is then quickly followed by a transition to the host-guest phase of bismuth, Bi-III, at around 2.7 GPa [15]. Finally, bismuth adopts a body-centred cubic structure, Bi-V, above 7.7 GPa [125].

The phases observed in this work on Bi_7Te_3 are summarised in figure 6.2. Each coloured band represents a different phase and the solid black dots indicate the

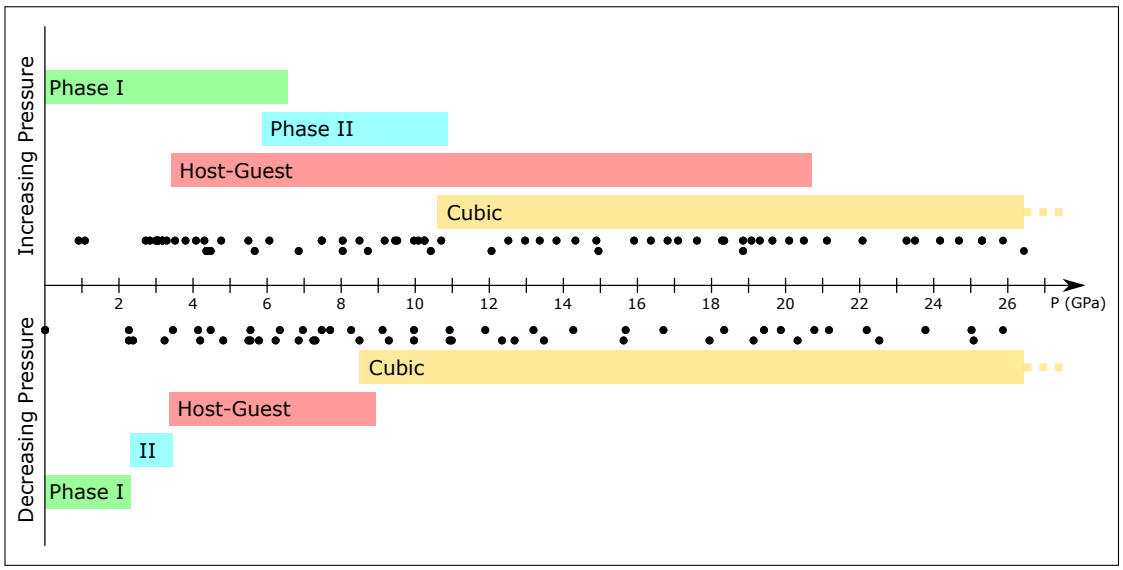

Figure 6.2 *Observed phases of Bi_7Te_3, with pressure ranges determined by visibility of peaks in the powder diffraction profiles. Where necessary, these pressures were averaged across observations from both experiments. Black circles represent pressures at which data were recorded (upper rows of dots: experiment hc1335 at ESRF, lower rows: EE12996 at Diamond Light Source). Here, the upper limit to the cubic phase is determined by the maximum pressure attained in our experiments and is not the upper bound for stability of the cubic phase, this is represented by the dashed line.*

pressures at which XRPD patterns were recorded. The pressure ranges of the observed phases are based on the visibility of peaks in the powder diffraction profiles and the ends of these ranges have been averaged between experiments where appropriate. The highest pressure attained in this work on Bi_7Te_3, 26.4 GPa, does not represent an upper limit to the stability of the cubic phase, as denoted by the dashed lines at the end of the yellow band representing the cubic phase.

Due to the presence of elemental bismuth in the diffraction profiles, the actual pressure-range of the host-guest phase cannot be determined as peaks due to the most intense pair of Bi-III reflections appear at the same diffraction angles as those of the Bi_7Te_3 host-guest phase would. As such, the host-guest pressure ranges shown in figure 6.2 are over-estimated. The fact that the lower bound is at approximately 2.7 GPa on both pressure increase and decrease suggests that these low-pressure host-guest peaks are in fact from the Bi-III structure, which is stable above 2.7 GPa. The Bi_7Te_3 host-guest phase transitions most likely occur close to the phase-II transitions, as is the case in Bi_2Te (see figure 5.2 on page 67).

6.2 Phase I: Ambient Conditions Structure

In the standard three-dimensional description of the ambient-conditions structures of the $(Bi_2)_m(Bi_2Te_3)_n$ series, Bi_7Te_3 has one of the largest unit cells. It is comprised of 15 Bi_2 blocks and 6 Bi_2Te_3 blocks, stacked along the c axis with Bi_2Te_3 blocks alternately interspersed with groups of two and three Bi_2 blocks [24] (illustrated in figure 10.2 on page 191). This results in a large unit cell ($a \sim 4.4$ Å, $c \sim 120$ Å) containing 60 atoms.

This description has since been determined to be an approximation to the true structure which is better described using a modulated subcell, based on the four-dimensional (4D) modulated structures described by Lind and Lidin for the analogous Bi-Se series [29]. This model describes structure reflections in terms of four Miller indices, $(hklm)$, with m describing *satellite* reflections which are due to the modulation present in the structure. This improved structural model of Bi_7Te_3 has been discussed by Bos *et al.*, where they describe the ambient-conditions structures of the entire $(Bi_2)_m(Bi_2Te_3)_n$ series [24]. The structural parameters of the composition Bi_7Te_3 were reported by Bos *et al.* as determined by le Bail fits to x-ray powder diffraction data.

The 4D model consists of a smaller unit cell ($a \sim 4.4$ Å and $c \sim 6.0$ Å) that is modulated along the c axis according to the modulation vector, $\vec{q} = \gamma[001]^*$. Lind and Lidin show that these structures can include complex modulations, and determination of the full structural details requires high-quality single crystal data. This is not feasible with the data available in this work and, therefore, the analysis presented here is limited to the lattice constants and modulation vectors of the phase-I structure.

Only diffraction patterns recorded at high pressure were available for analysis of the phase-I structure of Bi_7Te_3, so no direct comparison could be made to the lattice constants and modulation vector values reported by Bos *et al.* at ambient conditions. These published ambient-pressure values are: $a = 4.4721(2)$ Å, $c = 5.9707(3)$ Å and $\gamma = 1.3424(2)$ [24].

Diffraction profiles showing phase I of Bi_7Te_3 were recorded across two experiments: hc1335 and EE12996. Measured diffraction patterns were processed using Fit2D [95, 96] resulting in profiles of integrated intensity as a function of diffraction angle. These profiles were then analysed using the refinement software

Jana2006 [91].

A total of 17 profiles are available for analysis, with 13 profiles from experiment hc1335 and 4 from EE12996. Both experiments included ruby spheres loaded in to the sample chamber for pressure measurement via the ruby fluorescence technique [83]. Due to a failure of the ruby system during experiment hc1335, alternate exposures were recorded with the sample purposely offset so that the x-ray beam would pass through the tungsten (W) gasket. The position of the measured tungsten diffraction rings would then be used to estimate the sample pressure from the tungsten equation of state. However, this method is subject to large systematic errors as the pressure conditions within the gasket are not equivalent to those within the sample chamber. As such, pressures determined from the gasket are unreliable.

Initial analysis of the diffraction data using le Bail fits with the 4D modulated structural model gave widely scattered results for the hc1335 data; this was determined to be due to the unreliable pressures determined from the gasket. Fortunately, there are reasonably clear peaks in the recorded Bi_7Te_3 diffraction profiles due to elemental bismuth, which is present as a contaminant. The low-pressure structure of bismuth (Bi-I [126]) was included in the le Bail fits and the Bi-I unit cell parameters determined from the fit were then compared to the bismuth equation of state, as determined by fitting the Murnaghan equation of state [121] to Bi-I data reported by Degtyareva *et al.* [32]. Using this bismuth contaminant as a pressure calibrant, sensible values were determined.

This is illustrated in figure 6.3, which shows the refined Bi-I atomic volumes (volume per atom) plotted using the pressures determined from the tungsten gasket. The bismuth atomic volume values are spread irregularly, rather than forming a smooth decreasing curve as would be expected. This indicates the unreliability of the pressures as determined from the tungsten gasket. The hc1335 pressures were therefore determined by matching the measured Bi-I data to the bismuth equation of state fitted to the data shown in figure 6.3.

6.2.1 Bi_7Te_3 4D le Bail Fits

All 17 available phase-I profiles were analysed by means of le Bail fitting, with the pressures for the hc1335 data determined from the bismuth contaminant. As the le Bail fits do not consider the intensities of the peaks in the measured diffraction

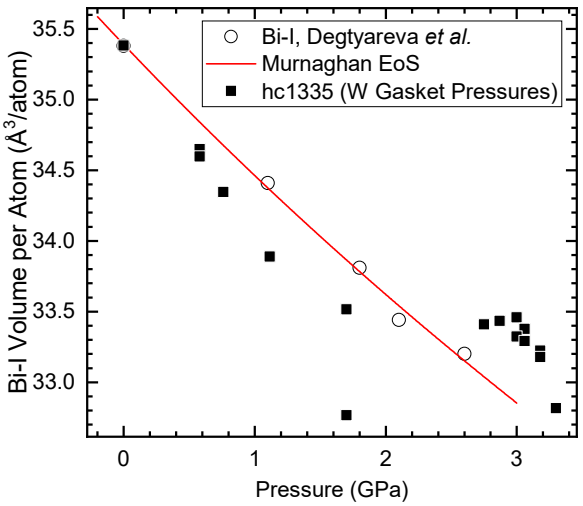

Figure 6.3 *Volume per atom for elemental bismuth (Bi-I) reported by Degtyareva et al. [32] and fitted with a Murnaghan equation of state [121]. Also plotted are the measured values in our hc1335 data, with pressures determined from the W gasket. The clear and varied discrepancies between the hc1335 data and that of Degtyareva et al. show the unreliability of the pressures estimated from the gasket.*

profiles, only the lattice constants, a & c, and the magnitude of the modulation vector, γ, were determined by the fitting. The fits also included a Chebyschev polynomial background function and utilised pseudo-Voigt peak shapes with the widths defined by the anisotropic strain broadening tensor, as used in the phase-I refinements of other Bi-Te compositions.

An example le Bail fit to a diffraction profile recorded at 1.6 GPa is shown in figure 6.4. The model includes first order satellite reflections ($m \neq 0$) which are shown in green. The profile is well fitted with an R-value of $Rw_p = 1.93\%$. The refined lattice parameters, unit cell volume and ratio of the lattice parameters are shown in figure 6.5. The refined values are largely consistent across both experiments and appear to agree well with the ambient-pressure structure data reported by Bos *et al.* The volume data is fitted using the Murnaghan equation of state [121] resulting in fitted values of unit cell volume at zero applied pressure, $V_0 = 103.37(9)$ Å^3, bulk modulus at zero pressure, $B_0 = 38.0(15)$ GPa, and first derivative, $B_0' = 4.7(8)$. The fitted volume, V_0, is in good agreement with the published volume at ambient pressure, $V_{Bos} = 103.41(1)$ Å^3 [24].

Bi_7Te_3 exhibits a structural anomaly similar to the other members of the series — a minimum in the ratio of the refined lattice parameters (c/a) around 2.4–2.8 GPa, as illustrated in figure 6.5. This minimum can be seen in data from

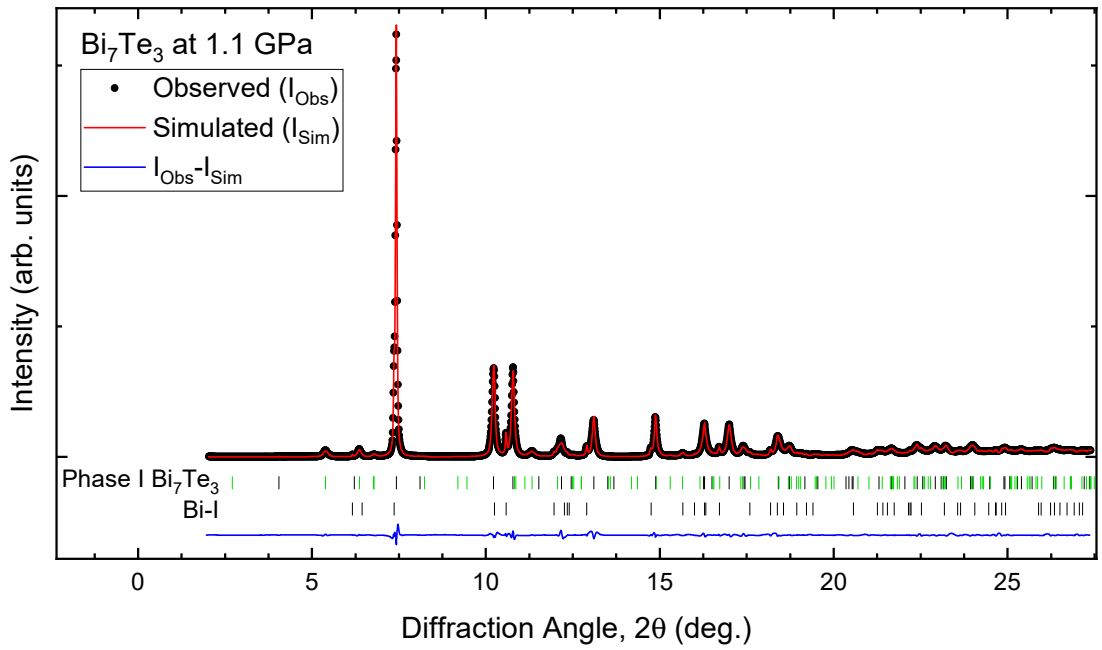

Figure 6.4 *Example le Bail fit of phase I of Bi_7Te_3 recorded at 1.6 GPa during experiment hc1335 (background subtracted). Rw_p = 1.93%. Fit includes both phase I of Bi_7Te_3 and the bismuth contaminant, Bi-I. Satellite ($m \neq 0$) reflections shown in green.*

both experiments, despite the lack of consistent coverage at that pressure range. The c/a values of the two datasets are systematically offset, as has been seen in the other Bi-Te compositions, while still exhibiting the same pressure behaviour. The value reported by Bos *et al.* fits well with this trend.

The refined modulation vector magnitude, γ, is shown in figure 6.6. The first data point agrees well with that of Bos *et al.*, but the rest of the data refine to values around 1.30. There is significant scatter in the data near 2.4 GPa, where the minimum in the c/a ratio is observed. This may be indicative of some anomaly in the modulation vector at this pressure, linked to the observed structural anomaly, but may also be due to under-estimated uncertainties on the refined values. Unfortunately, no firm conclusion can be reached from this data. Note that the highest pressure data point represents a refinement in which the value was fixed, this was due to peaks from the next phase interfering with the fit and resulting values of γ which gave poorly-fitted satellite peaks. The value was fixed such that the (0001) reflection, near 5.5° was correctly fitted.

These results further support the evidence of a common structural anomaly present within the pressure range of phase I, indicated by the minimum in the c/a ratio. The refined lattice parameters and unit cell volume (that is, volume of

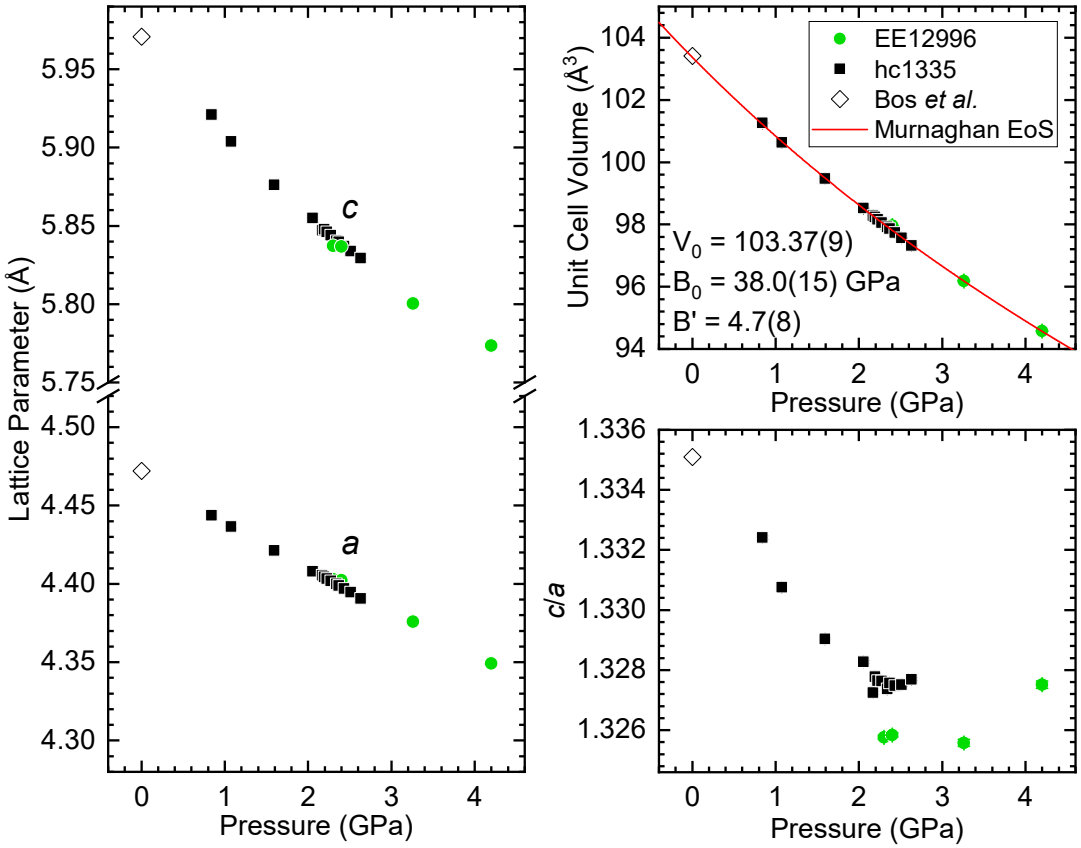

Figure 6.5 *Refined lattice parameters, unit cell volume and lattice parameter ratio for phase I of Bi_7Te_3. Unit cell volume data is fitted with a Murnaghan equation of state [121]. Values reported by Bos et al. included for comparison [24].*

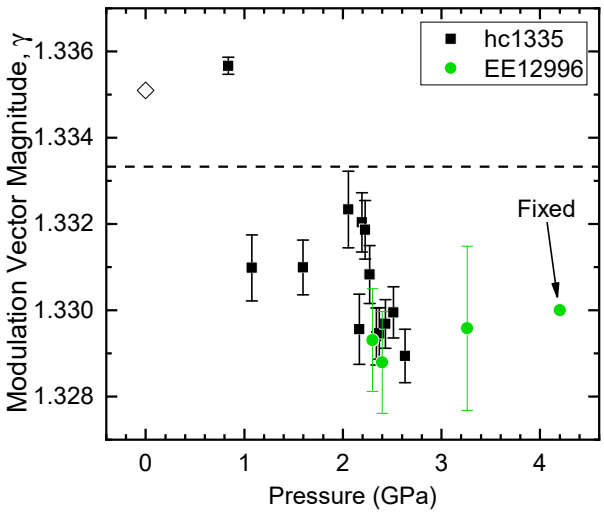

Figure 6.6 *Refined modulation vector magnitude, γ, for phase I of Bi_7Te_3. Values reported by Bos et al. included for comparison [24]. Dashed line indicates the commensurate value, 4/3.*

the average cell in the 4D description) are in good agreement with those reported by Bos *et al.* at ambient pressure. The magnitude of the modulation vector, however, does not appear to show a clear pressure behaviour.

6.3 Phase II: Unidentified Structure

On pressure increase, the diffraction profiles of Bi_7Te_3 show peaks belonging to phase II at around 6 GPa. Phase II overlaps slightly with phase I and persists up to a pressure of around 11 GPa. As illustrated in figure 6.7, the diffraction profile of phase II is similar to that of other Bi-Te compositions and to the first high-pressure phase of Bi_2Te_3. The tick marks in the figure indicate additional peaks in the phase-II Bi_7Te_3 profile which belong to elemental bismuth present as a contaminant. At this pressure bismuth adopts the host-guest structure, Bi-III [15]. Also indicated with arrows are strong peaks due to the Bi_7Te_3 host-guest phase, along with a peak (*) due to the nitrogen pressure-transmitting medium used in the Bi_2Te_3 measurement.

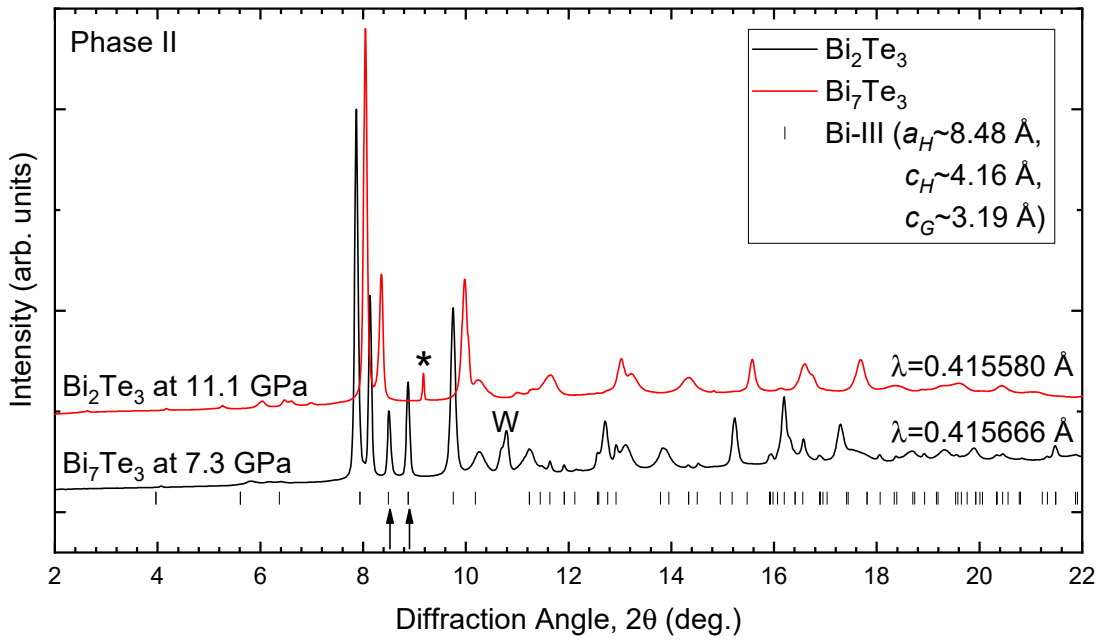

Figure 6.7 *X-ray powder diffraction profiles of Bi_7Te_3 (bottom) and Bi_2Te_3 (top) illustrating the similarity between both phases. The Bi_7Te_3 profile includes peaks from the next structural phase (↑), an asymmetric peak due to the x-ray beam clipping the tungsten gasket (W) as well was weak peaks due to a Bi-III contaminant (indicated by tick marks). The Bi_2Te_3 profile includes a peak (*) due to the solidified nitrogen pressure-transmitting medium.*

6.4 Phase IV: Host-Guest

After initially adopting the phase-I structure at low pressures, Bi_7Te_3 transforms to phase II on pressure increase, followed by the host-guest phase. Further pressure increase causes Bi_7Te_3 to transform to the cubic phase. On subsequent pressure decrease, the sample transforms from the cubic phase back to the host-guest phase. This section details the host-guest phase of Bi_7Te_3, as seen on both pressure increase and decrease.

As previously discussed, there is an elemental bismuth contaminant present in the Bi_7Te_3 samples. Over the pressure range investigated in this work, Bi undergoes several phase transitions. Two of these phases are observed within the pressure range of the host-guest phase of Bi_7Te_3: Bi-III — the host-guest phase of elemental bismuth, and Bi-V — which has the body-centred cubic (bcc) structure. The transition from Bi-III to Bi-V is expected at 7.7 GPa [31, 32]. This transition can be seen in the recorded Bi_7Te_3 host-guest diffraction profiles, as illustrated in figure 6.8.

Figure 6.8 shows recorded diffraction profiles on initial pressure increase, with the majority of the Bi_7Te_3 sample in the host-guest phase. The profile at 10.0 GPa includes clear peaks from Bi-III at 9.9° and 13.9°, along with several peaks in the 11.5–12.5° range. These peaks can all be seen to decrease in intensity as the pressure is increased, with all Bi-III peaks absent in the profile at 12.5 GPa (note there are fewer visible peaks in the 11.5–12.5° range in the 12.5 GPa profile, compared to at 10 GPa). As the Bi-III peaks diminish, sharp peaks due to Bi-V can be seen to grow in intensity as the pressure is increased. Peaks from the next Bi_7Te_3 phase (the cubic phase) can also be seen to slowly increase in intensity at diffraction angles $\sim 0.2°$ greater than those of Bi-V.

The bismuth contaminant is taken into account in all refinements of the host-guest Bi_7Te_3 phase, which were performed using the custom Rietveld refinement code described in section 3.5.4. All recorded diffraction images were integrated to produce diffraction profiles and uncertainties on the integrated intensities were estimated as detailed in section 3.5.2. A total of 49 diffraction profiles were available for analysis of the host-guest phase, with 29 profiles from experiment hc1335 and 20 from EE12996. The profiles from hc1335 span a pressure range from 12.5–21 GPa on initial pressure increase, then 9.1–4.2 GPa on subsequent decrease from the cubic phase. It should be noted that, due to a failure of the

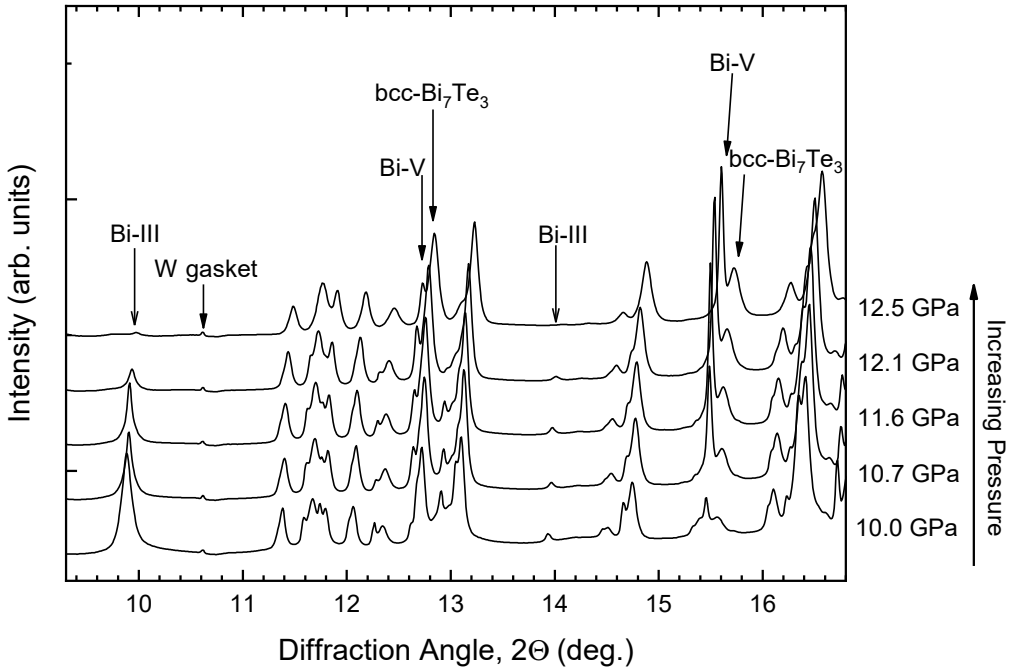

Figure 6.8 *X-ray powder diffraction profiles recorded for Bi_7Te_3 on initial pressure increase. The Bi_7Te_3 sample is in the host-guest phase throughout, while transitions in the minority phases can be seen as indicated.*

ruby fluorescence system, the pressures recorded on initial pressure increase in experiment hc1335 were estimated using the tungsten gasket, as detailed in the phase-I section. As such, these pressures are considered less reliable than those determined from ruby fluorescence (hc1335 on pressure decrease, and all E12996 data). This has no significant effect on the results, except in the case of fitting of the equation of state.

Experiment EE12996 included some pressure cycling and annealing of the sample. Profiles corresponding to the host-guest phase span the range 12.4–20.3 GPa during initial pressurisation, then from 8.7–6.9 GPa on decrease from the cubic phase. The sample was then annealed at 100°C for 20 hours and measured again on pressure reduction from 5.7–4.4 GPa, then on a second pressurisation up to 12.7 GPa.

An example refinement of the host-guest phase is shown in figure 6.9. The refinement is of a profile measured at 15.9 GPa and includes the host-guest structure of Bi_7Te_3, along with an additional two bcc structures: Bi-V and the

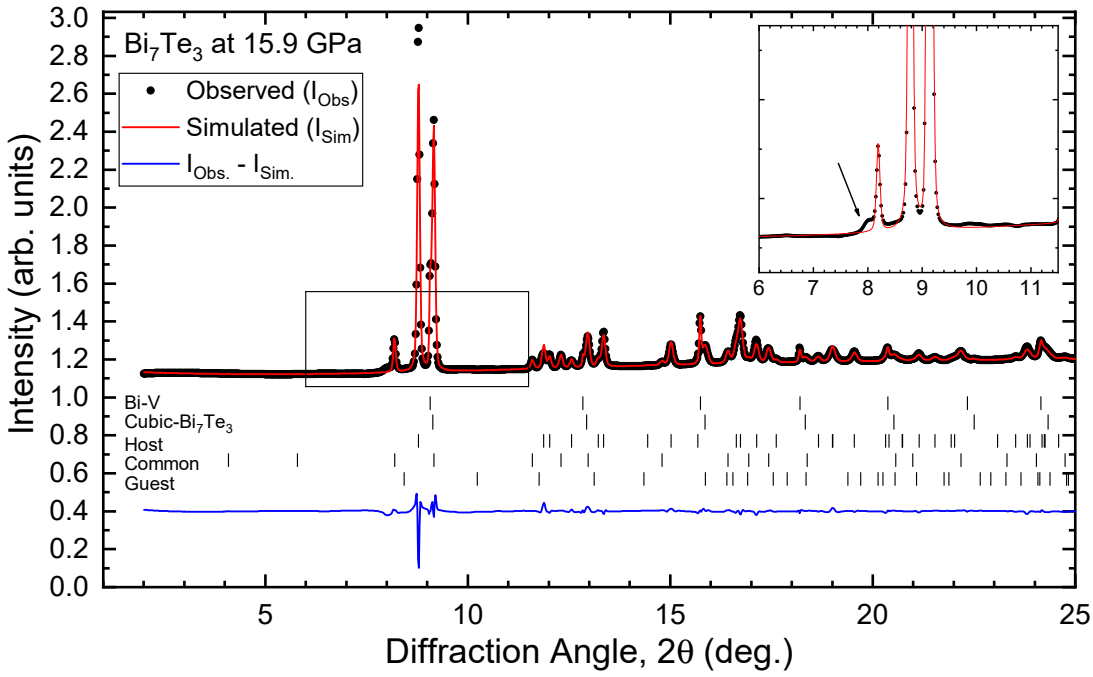

Figure 6.9 *Rietveld refinement of the host-guest phase of Bi_7Te_3, $wR_p = 1.6\%$. Inset shows the edge feature resulting from the diffuse intensity contribution from the disordered guest substructure.*

cubic phase of Bi_7Te_3. The bcc structure of Bi-V has a slightly larger lattice parameter than that of Bi_7Te_3 and so produces diffraction peaks that appear at slightly lower diffraction angles than those of cubic-Bi_7Te_3. The observed profile is well fitted, with a resulting R-value of $wR_p = 1.6\%$. The relatively large discrepancies in the main peak intensities are a result of the weighting scheme used in the refinements, with weights corresponding to uncertainties determined from the texture in the integrated diffraction pattern. This allows the refinement to prioritise accurately fitting the intensity of peaks which correspond to good-quality powder-like diffraction rings. The diffraction rings corresponding to the main peaks were somewhat textured, resulting in larger uncertainties in the integrated intensities.

As in all host-guest phases observed in this work, the *guest* reflections contribute no sharp peaks to the diffraction pattern; the *guest* reflections are indicated in figure 6.9 only for reference and contribute no intensity to the simulated profile. As in Bi_2Te, there are visible diffuse features arising from the disordered guest component. The 'edge' feature (where there is a visible rise in the 'background' intensity) can be clearly seen and can be fitted to determine an estimate of the guest lattice parameter along the c-axis direction. This edge feature is indicated in the inset of figure 6.9 and c_{Guest} values were determined for Bi_7Te_3 as they

were in Bi_2Te, as described in section 5.2.2. These estimated c_{Guest} values were then included in the Rietveld refinements as a fixed parameter.

The fitted c_{Guest} values are included in figure 6.10, which shows the refined lattice parameters, unit cell volume and c-ratio (c_{Host}/c_{Guest}) as a function of pressure. The host lattice parameters have uncertainties that are on the same scale as the symbol size, whereas the c_{Guest} values fitted from the edge feature have significantly larger uncertainties. The uncertainties on the c_{Guest} result in large uncertainties in the c_{Host}/c_{Guest} ratio, which shows some variance in the refined data, but well within the estimated uncertainties. At higher pressures the value appears to remain constant, close to the commensurate value of 4/3.

The refined unit cell volume data from experiment EE12996 is fitted using a Murnaghan equation of state [121], resulting in fitted unit cell volume at zero applied pressure, $V_0 = 337(2)$ Å^3, bulk modulus at zero pressure, $B_0 = 41.2(35)$ GPa, and first derivative of this bulk modulus, $B_0' = 4.6(3)$. During experiment hc1335 there was a failure of the ruby fluorescence system, requiring pressures on initial pressure increase to be estimated from the tungsten gasket. As such, these pressures are less reliable than those determined from ruby fluorescence in experiment EE12996.

Figure 6.11 shows the refined atomic coordinate, x, and the ratio of the host lattice parameters, a_{Host}/c_{Host}. On pressure increase the values of x (figure 6.11 (a)) determined from the EE12996 and hc1335 data are in excellent agreement, showing a gradual decrease in value with increasing pressure. On subsequent pressure decrease from the cubic phase, the EE12996 data appear to follow the same trend, whereas the data from hc1335 are systematically offset to slightly smaller values. This pressure reduction includes the annealing of the sample in experiment EE12996 between 6.9–5.7 GPa, which does not appear to have a significant effect on the atomic coordinate. A second pressure increase was applied in experiment EE12996 and the data from this second pressure increase follow the same trend as the other EE12996 data. All atomic coordinate data show the same trend towards slightly lower values of x at higher pressures, with only a slight decrease in value ($\sim 2\%$) over the entire pressure range.

The refined host lattice parameter ratio, a_{Host}/c_{Host}, is shown in figure 6.11 (b). It appears to be the only value that is clearly affected by the annealing of the sample in experiment EE12996 and also shows sensitivity to pressure cycling. Data from both experiments are in close agreement on initial pressure increase

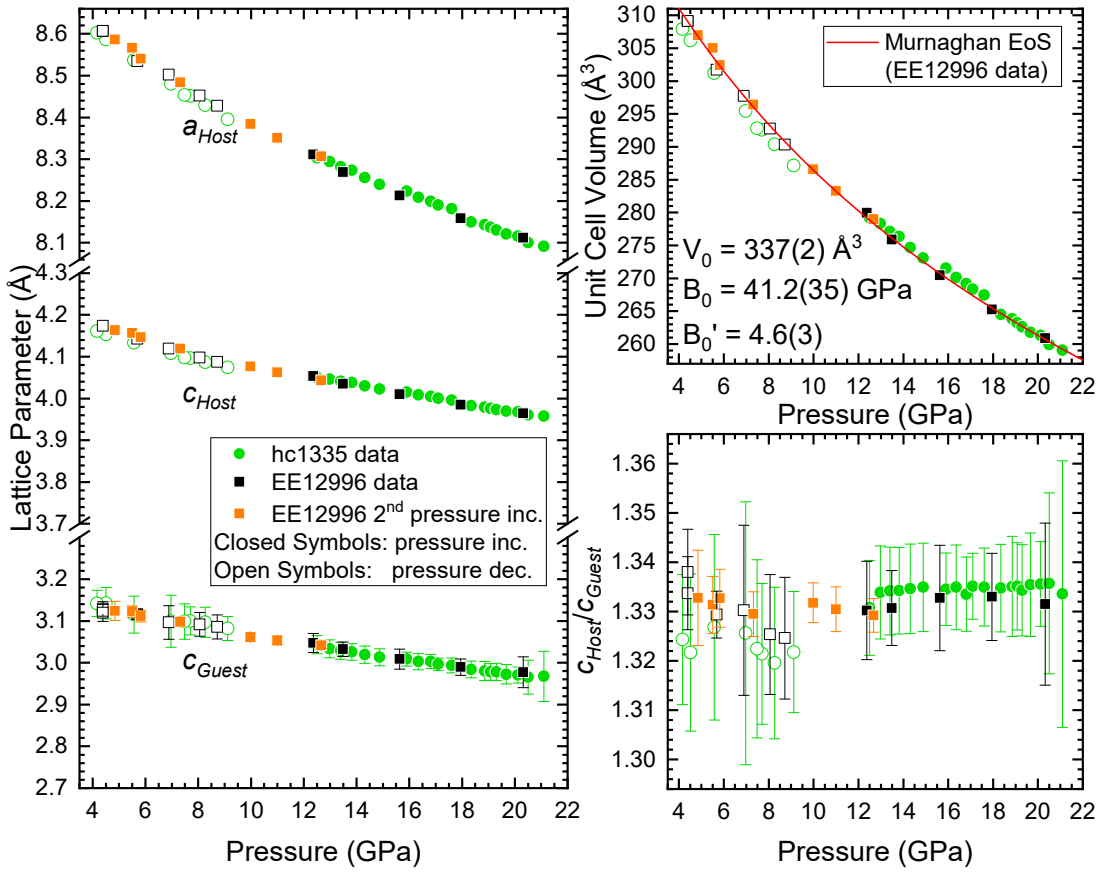

Figure 6.10 *Refined lattice parameters, unit cell volume and ratio of c lattice parameters for the host-guest phase of Bi_7Te_3. The unit cell volume data from experiment EE12996 is fitted using the Murnaghan equation of state [121].*

and subsequent decrease, until the EE12996 sample is annealed (between 6.9–5.7 GPa, on pressure decrease) . At that point (indicated in the figure by a dashed line), the ratio drops slightly and the data show the same pressure-behaviour but with a systematic offset. This is true also on the subsequent pressurisation of the now-annealed EE12996 sample.

Interestingly the annealing appears to have no effect on the refined site occupation factor, as shown in figure 6.12. The refined values before and after annealing (at 6.9 GPa and 5.7 GPa, respectively) are the same within uncertainty and in keeping with the overall pressure behaviour. The refined SOF values show no clear pressure trend and remain at a value of around 0.8, still higher than would be expected for a fully site-disordered Bi_7Te_3 alloy (0.7). This is in contrast to Bi_4Te_3 and Bi_2Te, with the former showing significant changes in the SOF on pressure cycling and annealing (see chapter 7), and the latter exhibiting an increase in Bi occupancy on pressure release from the cubic phase.

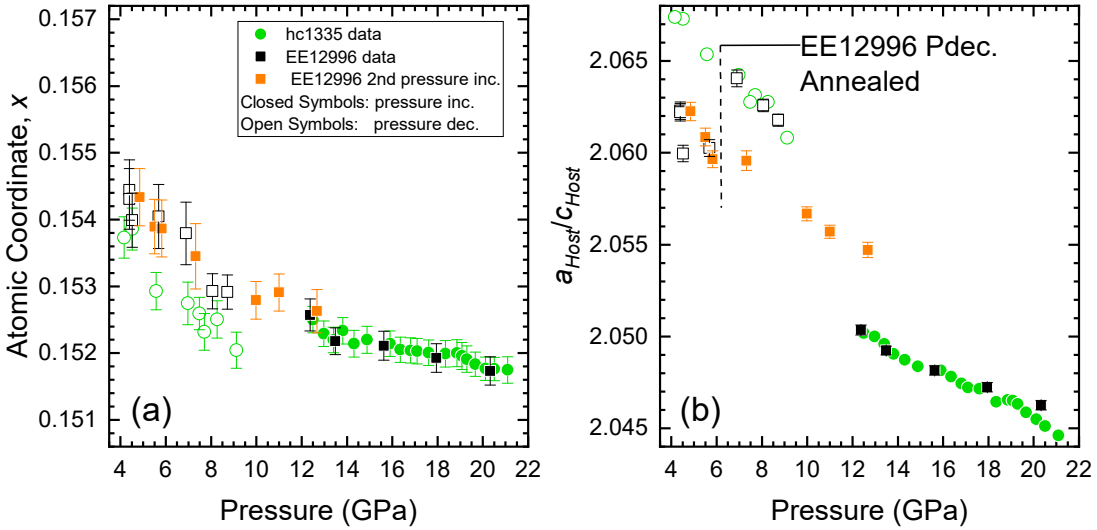

Figure 6.11 *(a) Ratio of refined host lattice parameters, and (b) atom position, x, for the host-guest phase of Bi_7Te_3. Note that the sample in experiment EE12996 was annealed on pressure decrease between 6.8 GPa and 5.8 GPa.*

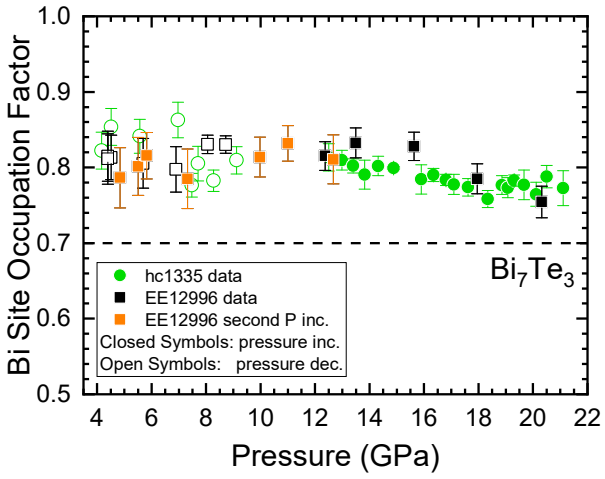

Figure 6.12 *Refined guest bismuth site occupation factor of the host-guest phase of Bi_7Te_3. The dashed line shows the expected value for a fully site-disordered structure (0.7).*

Conclusion

In this section, the host-guest phase of Bi_7Te_3 has been investigated between 4–22 GPa. The diffuse 'edge' feature was used to determine the guest lattice parameter, c_{Guest}, from the diffraction profile. This value was then included as a fixed parameter in Rietveld structure refinements, which yielded structural parameters as a function of pressure.

The analysed data were collected over two experiments and the refined structural

parameters show good agreement between both datasets. Data collected during experiment EE12996 included pressure cycling (initial pressure increase to cubic phase, followed by decrease back to host-guest phase then one further increase, while remaining in the host-guest phase) and annealing of the sample at 100°C for 20 hours (on pressure decrease, between 6.9–5.7 GPa). The pressure cycling and annealing was found to have a significant effect only on the ratio of host lattice parameters, a_{Host}/c_{Host}. Surprisingly there was no visible effect on the refined site occupation factors, with the guest chains consisting of approximately 80% Bi throughout the pressure range.

On pressure increase, the host-guest phase of Bi_7Te_3 transforms to the cubic phase, which will be discussed in the next section.

6.5 Phase V: Cubic Structure

Diffraction profiles of the cubic phase of Bi_7Te_3 were analysed by Rietveld refinement using Jana2006. The bcc structure of Bi-V (present as a contaminant) was included as a separate phase in these refinements. As illustrated in figure 6.13, the refinements resulted in good fits to the observed profiles with both sample and contaminant well described. The cubic phase of Bi_7Te_3 adopts the fully site-disordered body-centred cubic (bcc) structure, with no evidence of any chemical ordering in the diffraction profiles (i.e. no cubic (001) or (111) peaks present which would indicate an ordered B2, CsCl-type structure).

A total of 25 profiles were available for refinement spanning a pressure range of approximately 10–27 GPa. Data were collected during two separate experiments, hc1335 and EE12996. As discussed previously, the pressures for the hc1335 data on initial pressure increase are unreliable due to being determined from diffraction peaks from the gasket. Rietveld refinement of the high-pressure cubic profiles resulted in good fits; the refined unit cell volumes are plotted in figure 6.15. There is a slight offset visible in the refined unit cell volumes between the hc1335 data collected on initial pressure increase (pressures determined from gasket) and

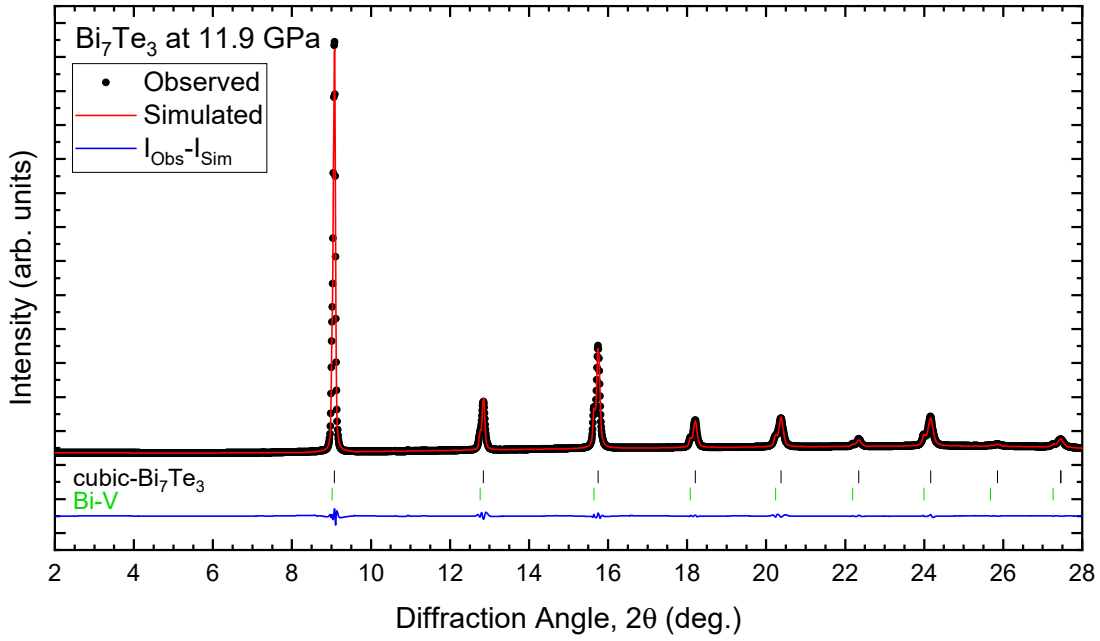

Figure 6.13 *Rietveld refinement of the cubic phase of Bi_7Te_3 at 11.9 GPa, $wR_p = 3.54\%$. Peaks due to the bismuth contaminant (bcc structure Bi-V) can be seen on lower-angle edges of the main sample peaks.*

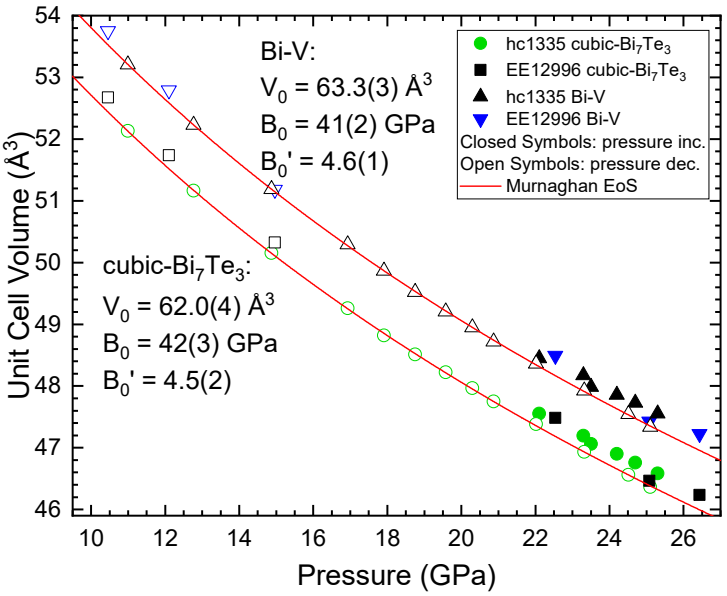

Figure 6.14 *Refined unit cell volume of the Bi_7Te_3 cubic phase and body-centred-cubic bismuth (Bi-V). The hc1335 (decreasing pressure) volume data has been fitted using the Murnaghan equation of state [121].*

on subsequent pressure decrease (pressures determined by ruby fluorescence). A similar offset is apparent between the hc1335 and EE12996 data, suggesting some difference in the two samples.

To determine an expression for the equation of state of cubic-Bi_7Te_3, the hc1335 data collected on pressure decrease was selected as most reliable. This Bi_7Te_3 unit cell volume data was fitted using a Murnaghan equation of state [121], as shown in figure 6.15, resulting in fitted unit cell volume at zero applied pressure, $V_0 = 62.0(4)$ Å^3, bulk modulus, $B_0 = 42(3)$ GPa, and first derivative of bulk modulus, $B' = 4.5(2)$.

The elemental bismuth contaminant was also refined, and the unit cell volumes of Bi-V were determined as a function of pressure. This Bi-V data (hc1335 pressure decrease) was also fitted using a Murnaghan equation of state resulting in fitted unit cell volume at zero applied pressure, ${}_{Bi}V_0 = 63.3(3)$ Å^3, bulk modulus, ${}_{Bi}B_0 = 41(2)$ GPa, and first derivative of bulk modulus, ${}_{Bi}B_0' = 4.6(1)$.

The data collected during experiment EE12996 gives similar values when fitted with a Murnaghan equation of state: $V_0 \approx 62$ Å^3, $B_0 \approx 41$ GPa, and $B' \approx 4.5$ for cubic-Bi_7Te_3; ${}_{Bi}V_0 \approx 65$ Å^3, ${}_{Bi}B_0 \approx 34$ GPa, and ${}_{Bi}B_0' \approx 5$ for Bi-V.

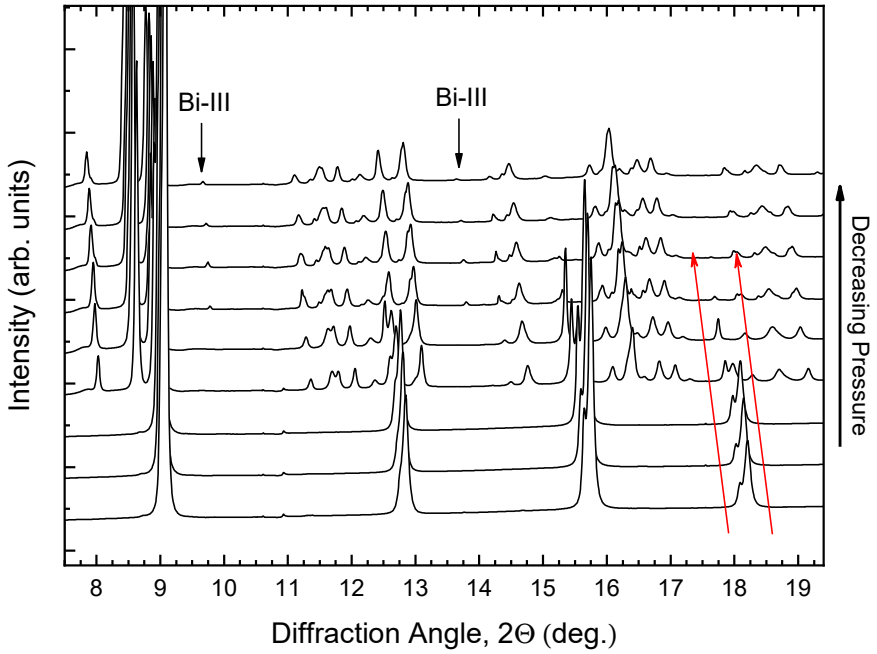

Figure 6.15 *Observed x-ray powder diffraction profiles of Bi_7Te_3 on decreasing pressure from the cubic phase. As the sample transforms from the cubic to the host-guest phase, the elemental bismuth can be seen to transform from Bi-V to Bi-III. Several cubic-Bi_7Te_3 and Bi-V peaks overlap with the host-guest phase, as indicated by the red arrows.*

6.6 Phases on Pressure Decrease

On pressure release, Bi_7Te_3 exhibits the same structural phases as observed on initial pressurisation. First, the cubic phase transforms to the host-guest phase. This transition is illustrated in figure 6.15 which shows the overlap between the two phases. The red arrows indicate a cubic-Bi_7Te_3 and a Bi-V peak that reduce in intensity as the pressure is decreased. The higher angle Bi_7Te_3 peak can be seen to disappear first as the sample adopts the host-guest structure. The lower-angle Bi-V peak remains visible to lower pressures, disappearing as peaks from the Bi-III phase appear.

On further reduction in pressure, the Bi_7Te_3 sample adopts the phase-II structure before finally returning to the phase-I layered structure.

Chapter 7

Bi_4Te_3

Bi_4Te_3, containing approximately 57% bismuth, lies in the middle of the phase stability region of the $(Bi_2)_m(Bi_2Te_3)_n$ series [28] and is unique among the bismuth-telluride compositions investigated here. While it goes through similar high-pressure phases to those described so far, it adopts the host-guest structure only on decompression from the high-pressure cubic phase.

This change in behaviour clearly indicates the strong influence that composition has on Bi-Te compounds. This chapter will present the analysis of Bi_4Te_3 in the order in which the structural phases were encountered on initial pressure increase and subsequent pressure release. First, the layered phase-I structure of Bi_4Te_3 is analysed using a full 3D structural model, allowing the compression of the constituent blocks to e investigated. Bi_4Te_3 exhibits similar behaviour to the compositions discussed so far, including the structural anomaly within the pressure range of phase I.

The next phase of Bi_4Te_3, phase II, is then discussed; adopting a similar structure to the other series members. A unique feature of this composition is that it includes a few peaks from an additional minority phase, *phase III*, that appear on pressure increase around where the majority of the sample transforms from phase II to the cubic phase. While the structure of this phase could not be determined, potential explanations are discussed.

The cubic phase is then discussed, including the observation of chemical ordering within the cubic structure as the pressure is decreased. Finally, the host-guest phase of Bi_4Te_3 is encountered on pressure reduction. Analysis of this phase is

presented, with the results from Bi_2Te and Bi_7Te_3 providing a means to estimate the periodicity of the guest lattice, due to the lack of clear diffuse features in this composition. During these experiments, the host-guest phase of Bi_4Te_3 was pressure cycled resulting in interesting shifts in the host-guest structure. The order of observed Bi_4Te_3 structural phases is therefore *phase I* $\rightarrow$ *phase II* $\rightarrow$ *cubic* on initial pressure increase, and then *cubic* $\rightarrow$ *host-guest* $\rightarrow$ *phase II* $\rightarrow$ *phase I* on subsequent pressure release.

7.1 Bi_4Te_3 Experiment Summary

The composition Bi_4Te_3 was investigated in three synchrotron experiments: EE8105 at Diamond Light Source (October 2012), hc1335 at the ESRF (July 2014) and EE12996 at Diamond Light Source (February 2016). Several samples were studied in these experiments and are denoted here by the labels *EE43*, *hc43* and *EE43b*, respectively. All samples were of powdered Bi_4Te_3 held in Merrill-Basset-type diamond anvil cells (DACs) using tungsten (W) gaskets and with helium (He) as a pressure-transmitting medium. In all experiments, pressure was varied by means of an external gas membrane attached to the cell and the internal pressure was measured using the ruby fluorescence technique [83].

The phases observed in this work on Bi_4Te_3 are summarised in figure 7.1. Each of the coloured bands represents the pressure range over which peaks from a particular phase were clearly visible in the powder diffraction profiles during initial pressure increase (top) and subsequent decrease (bottom). The ends of the ranges have been determined by averaging the observations from all experiments. The highest pressure reached in this work on Bi_4Te_3, 18.1 GPa, does not represent an upper limit to the stability range of the cubic phase.

Sample *EE43* was investigated in the earliest experiment, EE8105. Diffraction data were recorded up to 14.5 GPa in approximately 1 GPa steps, and then on subsequent pressure release down to ambient pressure. Sample *hc43* was investigated at the ESRF using x-rays of wavelength $\lambda_{hc1335} = 0.415352$ Å. Diffraction data were recorded on pressure increase from ambient pressure up to a maximum of 18.9 GPa in approximately 1 GPa steps, and then on subsequent pressure release back to ambient conditions. Sample *EE43b* was investigated during the second experiment at Diamond, EE12996. This experiment aimed to follow up on the observation of what was presumed to be a structural transition

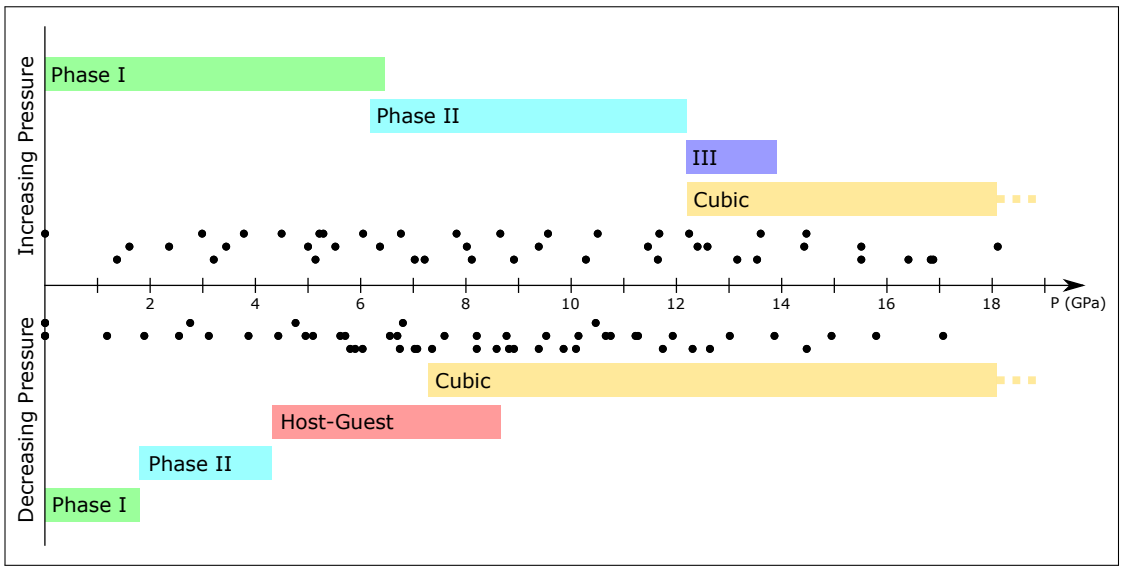

Figure 7.1 *Summary of observed phases for Bi_4Te_3. Illustrates pressure ranges as determined by visibility of clearly identifiable peaks in the powder diffraction profiles. Dashed lines at ends of coloured rectangles indicate expected phase stability outwith the range of our observations. Black circles represent the pressures at which diffraction images were recorded (upper row of circles: experiment EE8105, middle row: hc1335, lower row: EE12996).*

within the Bi_4Te_3 host-guest phase, based on the observation of some additional peaks in the host-guest profiles at the lower end of the pressure range. This presumed transition was investigated by means of thermal annealing and pressure cycling, but has since been determined to be an overlap of phase II and the host-guest phase (see page 71 for details). Sample *EE43b* was taken up to a maximum pressure of 16.8 GPa in steps of approximately 1 GPa. On subsequent pressure release, the sample was annealed at 100°C while in the host-guest phase and pressure was increased again until the peaks of interest disappeared.

Both experiments at Diamond Light Source made use of a Perkin-Elmer detector for recording diffraction images, requiring some additional corrections during the data analysis. The analysis of data collected during these experiments was performed using x-rays of wavelength $\lambda_{EE8105} = 0.415301$ Å and $\lambda_{EE12996} = 0.415666$ Å.

Powder diffraction profiles from each of the observed phases of Bi_4Te_3 are shown in figure 7.2. All profiles were recorded on pressure increase, apart from the profile from the host-guest phase which was obtained at 8.19 GPa on pressure release from the cubic phase. Weak, unidentified peaks are also present in most of the diffraction profiles; these are indicated in the inset of figure 7.2. The

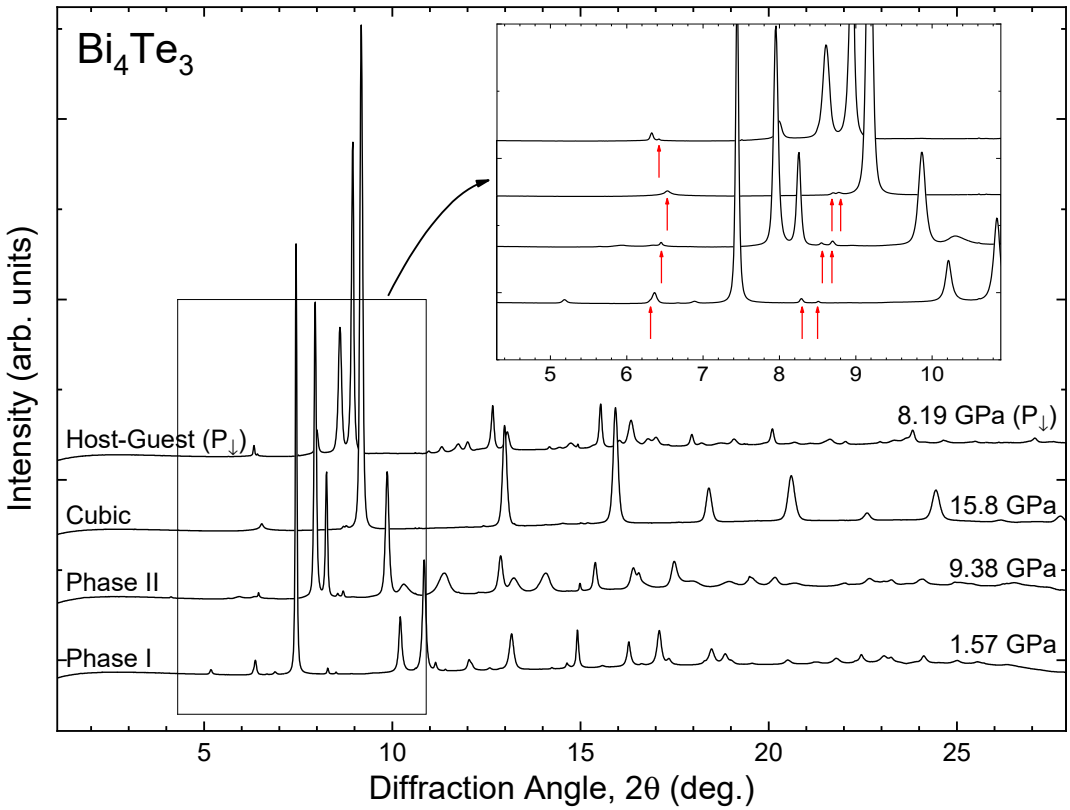

Figure 7.2 *Powder diffraction profiles of Bi_4Te_3 illustrating the observed phases on initial pressure increase (I, II and cubic) along with a profile from the host-guest phase obtained on pressure release from the cubic phase. All profiles are from experiment hc1335. The inset indicates the observed unidentified peaks that are discussed in section 7.1.1.*

unidentified peak just below 6.5° is visible in all of the diffraction profiles of the Bi_4Te_3 structural phases discussed in this work. It lies very close to the position of reflections in phase I and the cubic phase, in particular.

7.1.1 Unidentified Peaks in Bi_4Te_3 Data

As indicated in figure 7.2, there are several weak peaks present in the hc1335 Bi_4Te_3 diffraction profiles which do not belong to any of the Bi_4Te_3 structural phases described here. These same peaks are also observed in the EE8105 and EE12996 Bi_4Te_3 data. The source of these peaks remains unidentified, but certain potential sources can be ruled out.

Observed from ambient pressure up to the highest pressures attained here, these peaks can be seen to move to higher diffraction angles as the sample pressure is

increased, and to lower diffraction angles on pressure decrease. The peak positions change at a similar rate to the peaks from the main sample phases, suggesting that the material responsible for the unidentified peaks compresses at a similar rate. The pressure dependence of the unidentified peaks confirms that they are not due to some external source (such as material on the outside of the diamond anvil cell, or some piece of experimental apparatus) and are coming from within the sample chamber.

These peaks are observed in Bi_4Te_3 data collected during three different experiments, using separate loadings of different diamond anvil cells. This, along with their pressure dependence, also rules out the possibility of some systematic experimental error (such as a detector defect). All samples of powdered Bi_4Te_3 measured in these experiments were taken from the same parent sample. This suggests that if a contaminant is present in these samples, it was likely introduced at some stage in the preparation of the parent sample. The fact that these peaks are observed in data from separate DAC loadings means it is unlikely that a contaminant was introduced while the sample was loaded into the DAC.

By looking at the recorded diffraction images we see that the unidentified peaks are due to highly textured diffraction in the measured images, as illustrated in figure 7.3. This is in contrast to the smooth powder rings of the sample main phase, suggesting a clear distinction between the two, such that these weak peaks are not associated with the structures discussed here. In support of this conclusion is the fact that the unidentified peaks are observed, unchanged, over all phase transitions studied here. If these peaks were associated with any of the discussed structures, it would be expected that these peaks would change or disappear once the sample had fully transformed to a different structure.

The raw diffraction images show these peaks to be associated with measured intensity that is comprised of short arcs arranged around the common centre, the beam centre. This suggests that the source of these peaks is polycrystalline or powder-like, rather than a single crystal which would produce sharp, approximately circular spots on the measured image.

There are instances when these peaks are close to predicted reflection positions in some of the structures, such as the peaks near 5° and 8.5° in phase I, and the (100) reflection of the cubic phase which exhibits the B2 (CsCl) structure type. Each case can be confirmed as an overlap of distinct, separate peaks, as illustrated for the cubic phase of Bi_4Te_3 (see section 7.5).

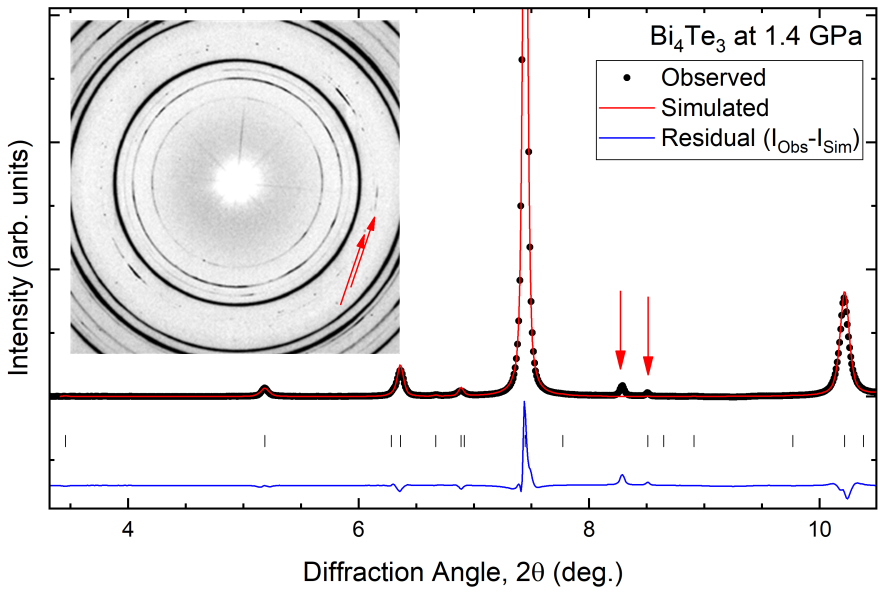

Figure 7.3 *Illustration of the unidentified peaks present in Bi_4Te_3 diffraction profiles, with the associated textured intensity in the raw diffraction images. Example shown is from experiment hc1335 at 1.37 GPa, while the sample is in phase I.*

By comparing the positions of the unidentified peaks at ambient pressure to peak positions predicted using structures reported in the the Inorganic Crystal Structure Database (ICSD), several potential contaminants can be ruled out. These include: Bi [126], Te [127], Fe [128, 129], W [130] and Al [129]. The close spacing of the unidentified peaks does typically rule out most cubic structures. Several oxides of bismuth and tellurium were also considered as a potential source of the unidentified peaks but none was found to exhibit diffraction peaks in agreement with the observed unidentified peaks.

Similar weak peaks are also observed in the diffraction profiles of BiTe and Bi_4Te_5, suggesting that there is some minority phase that is common to the tellurium-rich Bi-Te compositions. These weak, unidentified peaks appear at similar positions in these other compounds and exhibit the same behaviour as a function of pressure to those in Bi_4Te_3.

7.2 Phase I: Ambient Conditions Structure

The ambient-pressure (phase I) structure of Bi_4Te_3 follows the structural trends of the infinitely adaptive $(Bi_2)_m(Bi_2Te_3)_n$ series [24]. Phase I of Bi_4Te_3 consists of three Bi_2 blocks and three Bi_2Te_3 blocks, stacked alternately along the c-axis.

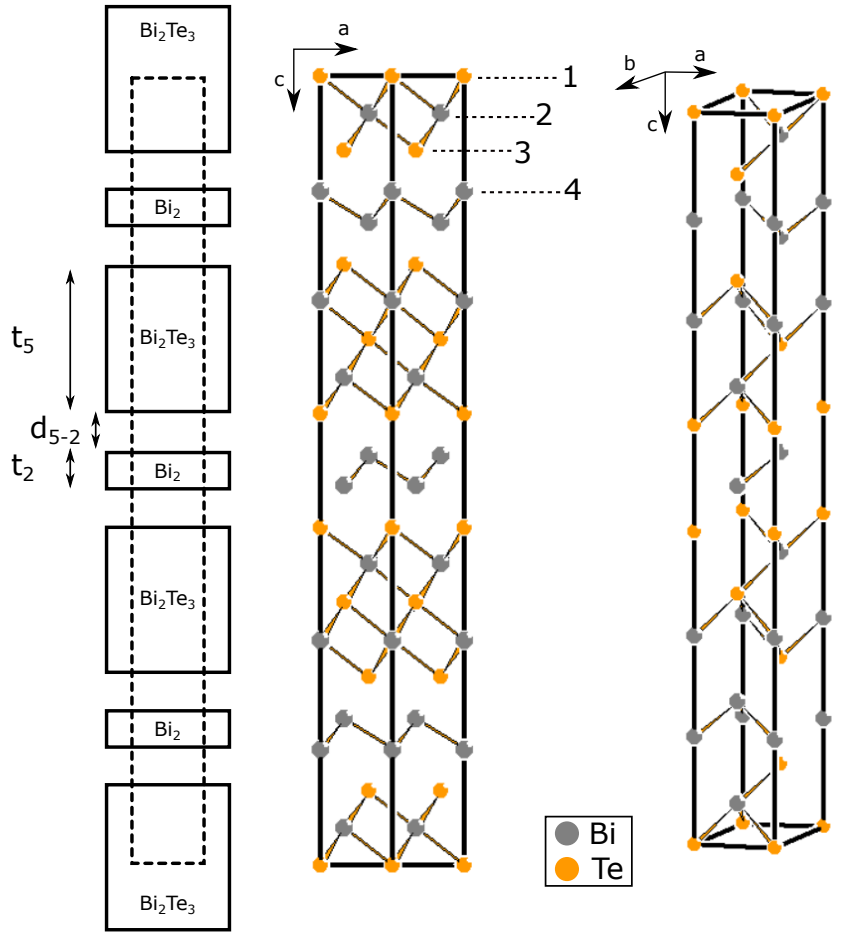

Figure 7.4 *Illustration of the ambient-pressure structure (phase I) of Bi_4Te_3 indicating the numbered atomic positions, the two-atom and five-atom layers, and the thicknesses of and distances between these layers. All such distances are equivalent to those indicated in the figure.*

The unit cell contains three formula units and can be described by the trigonal *R-3m* space group. The 21 atoms in the unit cell are located across four Wyckoff sites: 3*a* (0, 0, 0), 6*c* (2/3, 1/3, z_2), 6*c* (1/3, 2/3, z_3), and 6*c* (0, 0, z_4). There are three free atomic coordinates (z_2, z_3 & z_4), with the rest (z_1 and all x,y coordinates) fixed by symmetry.

These atomic z coordinates, along with the unit cell length along the same direction (i.e. the c lattice parameter) can be used to determine the thickness of the two-atom (t_2) and five-atom (t_5) layers, along with the distance (d_{5-2}) between them as follows:

$$t_5 = 2z_3c \tag{7.1}$$

$$t_2 = c\left[\frac{1}{3} - 2z_4\right] \tag{7.2}$$

$$d_{5-2} = c[z_4 - z_3] \tag{7.3}$$

The phase-I structure has been reported previously in a single-crystal x-ray diffraction study by Yamana *et al.* in 1979 [60]. Yamana *et al.* used an idealised model of the structure, where all two-atom layers had the composition Bi_2 and all five-atom layers had the composition Bi_2Te_3. This model therefore assumed all atomic sites had fixed occupancies with each site occupied by either Bi or Te, with no mixed occupancies or exchange between sites. This idealised model is depicted in figure 7.4. The lattice parameters of the phase-I structure have also been reported by Bos *et al.* in 2007, determined by electron diffraction and le Bail fits to x-ray powder diffraction data [24].

The previously published idealised structure was used as a starting point for Rietveld refinement of the measured ambient-pressure x-ray powder diffraction profile from experiment EE8105. Atomic site occupation factors (SOFs) were fixed to maintain the idealised layer compositions and anisotropically broadened pseudo-Voigt peak shapes were used. The anisotropic peak broadening (also found in phase I of Bi_2Te) can result from stacking faults and is not surprising to find in this layered structure. This initial refinement produced a reasonable fit to the measured peak positions, with an R-value of $wR_p = 1.30\%$, but some discrepancies in the peak intensities remained. While peaks with large l Miller-index values were well fitted, other peaks were not, indicating some preferred orientation in the sample. This was accounted for in the refinement by the addition of March-Dollase preferred orientation [131, 132] along the (001) direction. This was refined through a single parameter, '*pref1*', and significantly improved the fit, reducing the R-value to $wR_p = 0.72\%$.

Allowing the SOFs to refine (while maintaining overall Bi_4Te_3 stoichiometry) led to further improvement in the fit, with $wR_p = 0.65$ % (a ~ 10 % improvement). This refinement appears to be the best description of the ambient-pressure structure and is presented in figure 7.5. The resulting values of the refined parameters are summarised in table 7.1 which also includes the values determined by Yamana *et al.* for comparison.

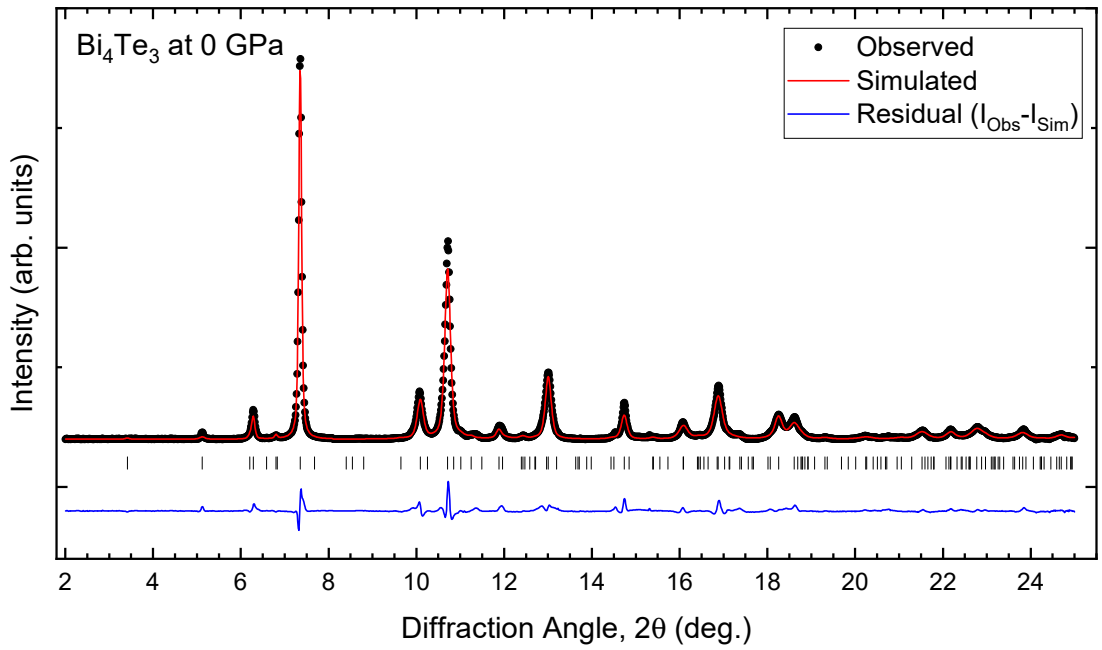

Figure 7.5 *Rietveld refinement of a Bi_4Te_3 XRPD profile at ambient pressure (background subtracted). The refined structure provides a good fit to the measured profile with $wR_p = 0.65\,\%$. The refinement includes the effects of anisotropically broadened peaks and preferred orientation in the powder sample.*

Site	x	y	z	Bi SOF	
1	0	0	0	0.29(3)	
2	2/3	1/3	0.0466(2)	0.941(17)	this work
3	1/3	2/3	0.0904(5)	0.084(10)	
4	0	0	0.1456(2)	0.83(2)	
1	0	0	0	0	
2	2/3	1/3	0.0505(1)	1	Yamana *et al.* [60]
3	1/3	2/3	0.0927(2)	0	
4	0	0	0.1460(1)	1	

Table 7.1 *Refined and previously published atomic parameters for phase I of Bi_4Te_3 at ambient pressure.*

The refined z values are close to those reported by Yamana *et al.* but do not agree within uncertainty. A significant difference between the refinements is the inclusion of variable site occupation factors in this work, which allows the layers to deviate from their idealised compositions. Such exchange of atoms has been reported previously in Bi_2Te [28] and is seen here to significantly improve the fit to the measured Bi_4Te_3 data. In order to quantify the effect such deviations from the idealised structure have on the refined parameters, refinements with fixed

a (Å)	c (Å)	
4.451(1)	41.888(5)	Yamana *et al.* [60]
4.4440(1)	41.922(1)	Bos *et al.* [24]
4.449(2)	41.838(6)	this work

Table 7.2 *Comparison of refined and published lattice parameters of phase I Bi_4Te_3 at ambient conditions.*

SOFs (idealised layers) have been performed on the Bi_4Te_3 data for comparison, both at ambient conditions and at high pressures.

The refined parameters are largely consistent within uncertainty across both models, with the refined SOF models producing larger estimated uncertainties which appear more appropriate given the observed variance in the values with pressure. Comparison of the refined parameters for the ambient-pressure profile show the refined-SOF model to be in better agreement with the values published by Yamana *et al.* and in better agreement with the results from the high-pressure data.

The published and refined lattice parameters are summarised in table 7.2. They show agreement within uncertainty for the a parameter only, but the relative differences are quite similar, with all reported values differing by approximately 0.1%. The differing nature of the measured samples should be noted: a 0.15 mm spherical sample 'cut from aggregates of crystals' in the published work of Yamana *et al.* [60]; a relatively large polycrystalline sample in the work of Bos *et al.* [24]; and a small $\sim 100\ \mu m$ sample of powdered Bi_4Te_3 held in a DAC in this work. Of the three datasets, only the data collected in this work made use of synchrotron radiation.

Table 7.1 shows the refined site occupation factors which indicate some exchange of atoms between the layers. The two-atom layer, which in an idealised model is a Bi_2 layer, is defined by atom 4. As such, the Bi_2 layer becomes approximately 83% Bi, 17% Te and the Bi_2Te_3 layer (40% Bi, 60% Te in the idealised structure) becomes approximately 47% Bi, 53% Te.

A total of 12 high-pressure x-ray powder diffraction profiles were refined for phase I of Bi_4Te_3: 5 from experiment EE8105, 4 from hc1335 and 3 from EE12996. These profiles were recorded at pressures between 1.4–5.3 GPa. The recorded diffraction images were integrated to produce diffraction profiles, and uncertainties on the integrated intensities were estimated as detailed in

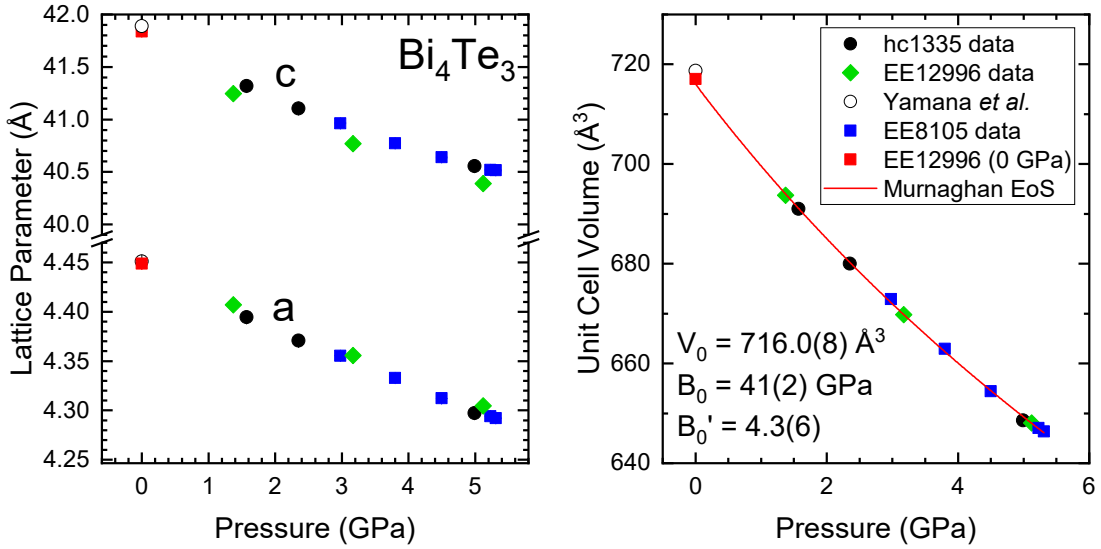

Figure 7.6 *Refined Bi_4Te_3 phase I lattice parameters and unit cell volume. The unit cell volume has been fitted with the Murnaghan equation of state. Lattice parameters have been plotted to same relative vertical scale. Note that the data from experiment EE12996 shows a systematic offset in the c lattice parameter. Error bars are similar to symbol size and are omitted for clarity*

section 3.5.2. These profiles were then refined using Jana2006. It should be noted that, in order to achieve stable refinements with sensible parameters, the isotropic atomic displacement parameters (U_{iso}) were fixed at 0.02 Å^2 for the ambient-pressure refinement and for all refinements performed in this work.

Refinement of these profiles gave stable and largely consistent results. The refined lattice parameters and unit cell volume as a function of pressure are presented in figure 7.6. The lattice parameters show a smooth decrease with increasing pressure, compressing at similar rates. The unit cell volume can be fitted with the Murnaghan equation of state [121] to yield fitted unit cell volume at zero applied pressure, $V_0 = 716.0(8)$ Å^3, bulk modulus, $B_0 = 41(2)$ GPa, and first derivative of the bulk modulus at zero pressure, $B_0' = 4.3(6)$. This is somewhat different from the value of the bulk modulus reported previously by Jeffries *et al.*, which was determined to be ≈52 GPa by fitting their x-ray diffraction data with a Birch-Murnaghan equation of state [3]. Fitting this data with a Birch-Murnaghan equation of state results in values consistent with those of the Murnaghan fit ($B_0 = 39(1)$ GPa and $B_0' = 5.1(3)$).

While refined a values are consistent within uncertainty, the c values show a clear discrepancy between the EE12996 data and the rest. As can be seen in figures 7.6–7.9, there is a clear difference between the EE12996 refinements and the rest, as

seen by systematically offset values and significantly different uncertainties in the refined values. To confirm that this offset was not a result of an error in the initial processing of the data, the integration, processing and refinement of the EE12996 data was checked, along with experimental details and measurement of calibration samples. No sign of error was found, suggesting that the observed differences are real and need to be considered.

The refined Bi_4Te_3 phase-I data was collected over three different experiments: EE8105 (October 2012), hc1335 (July 2014) and EE12996 (February 2016). The EE8105 and EE12996 datasets were collected at the same facility, Diamond Light Source, and the hc1335 dataset was collected at the ESRF. As EE8105 and hc1335 are consistent with one another, there is no further reason to expect that EE12996 is an outlier due to some issue with data collection.

All experiments measured small amounts of powdered Bi_4Te_3 taken from the same parent sample, which was stored securely between experiments. The fact that all measured samples were taken from the same source makes it unlikely that differences in sample composition or texture are to blame, but cannot rule it out entirely. Some natural variation in the measured parameters from these samples may be expected. The systematic offset of the c parameter is similar in scale to the discrepancies between the refined and reported (Yamana *et al.* and Bos *et al.*) c lattice parameters at ambient pressure. Similar differences can be seen in the refined atomic positions (figure 7.7). However, natural variation in the samples does not account for the close agreement between the EE8105 and hc1335 data, which would be expected to differ from one another by a similar margin.

The significant time between experiments does allow the possibility for something to have changed within the parent sample over time, with EE12996 being the most recent experiment. The fact that the measured unit cell volumes are consistent across all three experiments, suggests that the sample has not absorbed moisture, and there is no sign of significant sample contamination in any of the diffraction data. A 'room-temperature annealing' effect may allow the structure to change over time, possibly explaining these differences.

The refined atomic coordinates are shown in figure 7.7. As discussed, the results from experiments EE8105 and hc1335 show consistent values over the pressure range, with the variation in z_3 suggesting a slight underestimation of the uncertainties. At ambient pressure (0 GPa), the positions of atoms 3 and 4 agree

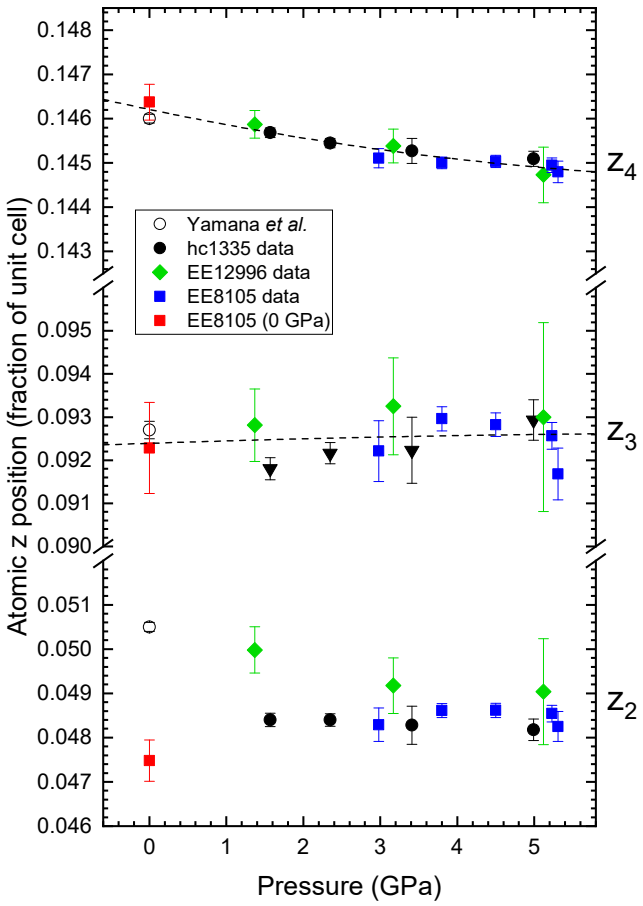

Figure 7.7 *Refined Bi_4Te_3 phase I atomic z positions. Note that the EE12996 data includes substantially larger uncertainties and appear to differ from the other data. Dashed lines are guides to the eye.*

well with those published by Yamana *et al.* The position of atom 2, however, is significantly different from the published value but agrees reasonably well with the observed values in the high-pressure data. As illustrated in figure 7.5, atom 2 lies within the five-atom layer and does not affect the layer thickness or inter-layer distance (see equations 7.1–7.3).

The behaviour of the layers as a function of pressure is shown in figure 7.8. At ambient pressure there is good agreement between the published and refined values, indicating that the inclusion of atomic disorder has little effect on the size of the layers and the distance between them. The EE12996 dataset is consistent with the other data but with significantly larger uncertainties. All datasets show the same trend, with the five-atom layer (t_5) compressing and the distance between the layers (d_{5-2}) reducing as the pressure is increased. The two-atom layer (t_2) is seen to expand slightly on increasing pressure, indicating a strengthening of the interaction between the layers.

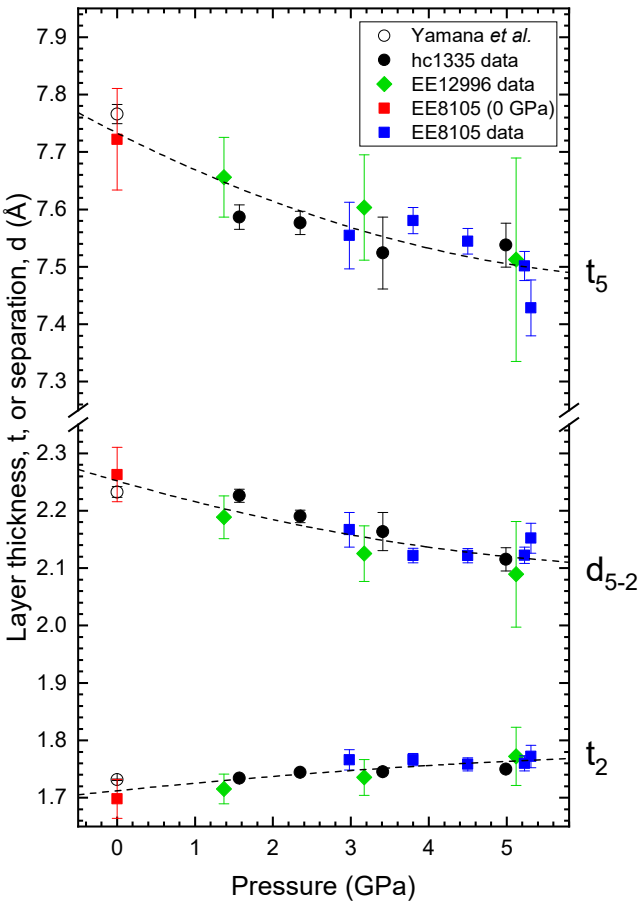

Figure 7.8 *Refined layer thicknesses and inter-layer distance in Bi_4Te_3 phase I, as calculated using equations 7.1–7.3. Dashed lines are guides to the eye.*

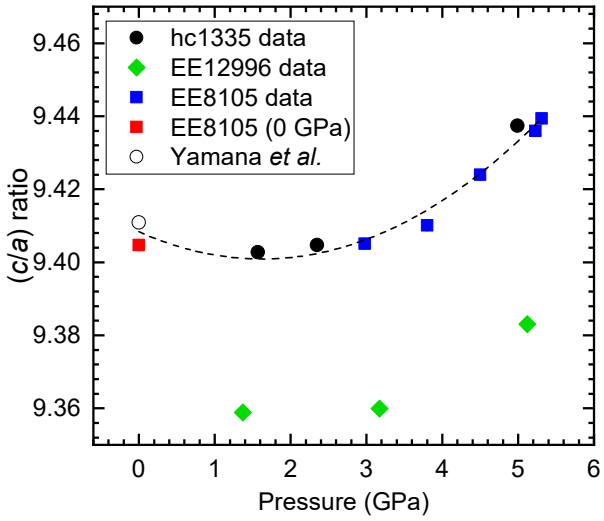

Figure 7.9 *Ratio of refined lattice parameters of Bi_4Te_3 phase I. A shallow minimum is present below approximately 3 GPa. Also note the systematic offset in the EE12996 data, which displays the same pressure behaviour as the other data. Dashed line is a guide to the eye.*

The ratio of the lattice parameters (c/a) is plotted in figure 7.9. It exhibits a clear change in pressure dependence around 3.5 GPa, corresponding to a shallow minimum below approximately 3 GPa. As previously discussed, phase I of Bi_2Te_3 has been established to exhibit a structural anomaly at a few GPa of pressure in what is described in the literature as an 'electronic topological transition'. A minimum in the c/a ratio as a function of pressure has been used as evidence of this transition [47] and such a minimum has also been observed in this work in Bi_2Te-I (see figure 5.20 on page 95).

The atomic site occupation factors (SOFs) were refined, allowing for some exchange of atoms between the layers of the structure. The refined values are shown in figure 7.10. The bismuth occupation factors of the four atomic sites are plotted as a function of pressure, with the idealised values indicated with dashed lines (sites 1 & 3 fully occupied by Bi, and sites 2 & 4 fully occupied by Te, as used in the refinement by Yamana *et al.* [60]). There is clear evidence of exchange of atoms between the constituent layers, with the two-atom layer comprised of approximately 80–90% Bi and 20–10% Te. While the refined SOFs of sites 2 & 3 from all datasets are in agreement, there are differences in the other values. Refinements of the EE12996 data appear to show a structure with more exchange between the layers. This does not appear to be linked to the differences observed in the lattice parameters, as the ambient-pressure refinement from EE8105 exhibits similar SOFs to the EE12996 data, rather than the high-pressure data gathered during experiment EE8105.

Conclusion

The phase-I structure of Bi_4Te_3 has been investigated from ambient pressure to 5.3 GPa through Rietveld refinement of x-ray powder diffraction profiles collected over several experiments. A single ambient-pressure profile was refined and the structure compared to structural details published by Yamana *et al.* [60] and Bos *et al.* [24]. The lattice parameters determined in this work were found to differ slightly ($\sim 0.1\%$) from the published values, which also differ by a similar amount. The refined atomic coordinates could be compared to those determined by Yamana *et al.*; the refined and published positions of atomic sites 3 and 4 (z_3 & z_4) were in agreement, but z_2 was not.

The refined atomic positions and lattice parameters were used to plot the thicknesses of and distances between the constituent layers along the c-axis as

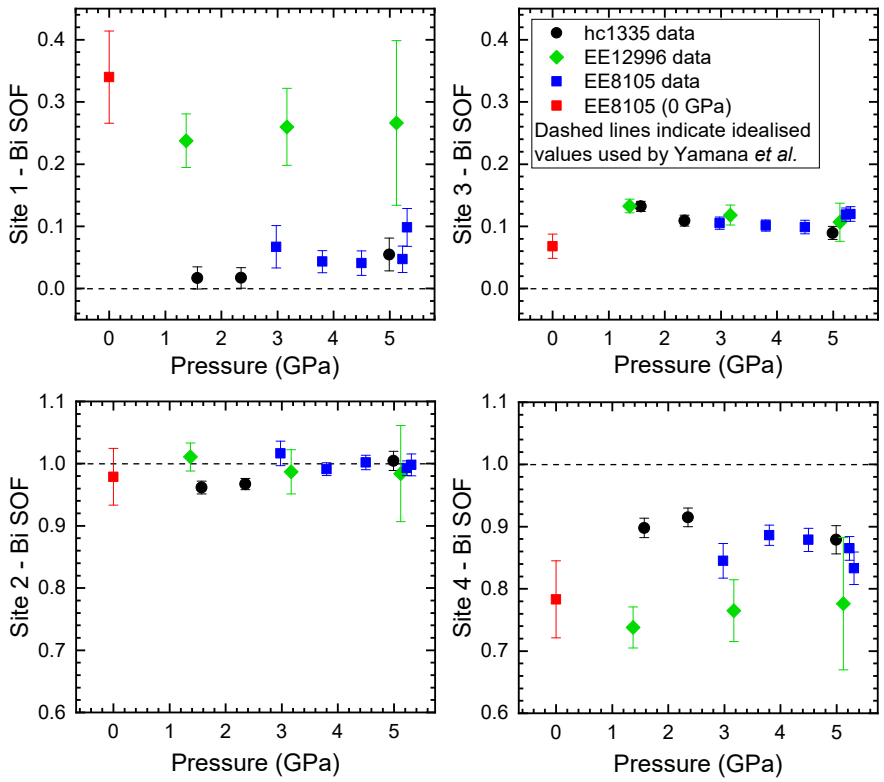

Figure 7.10 *Refined bismuth site occupation factors (SOFs) of phase I of Bi_4Te_3. Dashed lines indicate the idealised values used by Yamana et al. [60].*

a function of pressure. At ambient pressure the refined and published structures described similar layer thicknesses and separations, with the observed differences in atomic coordinates having no effect on these values. On increasing pressure, the thickness of the five-atom layer (t_5) was found to decrease, as was the distance between the layers (d_{5-2}). The thickness of the two-atom layer (t_2) was found to increase slightly as the pressure was increased, signifying an increase in the attraction between the layers as the structure approaches the phase transition.

Some exchange of atoms within the phase-I structure was found, with the two-atom Bi_2 layer in the idealised structure found to contain between approximately 80–90% Bi. The ratio of the lattice parameters, c/a, was found to exhibit a very shallow minimum, with the minimum somewhere below approximately 3 GPa. Such behaviour is similar to that established in Bi_2Te_3 and attributed to an electronic topological transition; it appears that this structural anomaly is a common feature of the Bi-Te series.

Some systematic differences in the refined structural parameters as a function of pressure were found between the EE12996 data and the rest. These differences

were most clear in the lattice parameter ratio (c/a) and the refined site occupation factors. Slight systematic offsets were also observed in the values of the lattice parameters. Checks were made to ensure no systematic errors were made during the processing of the EE12996 data, finding no evidence of error. The systematic offsets in the lattice parameters are on the same relative scale as differences between ambient-pressure values reported by Yamana *et al.* [60] and Bos *et al.* [24], and those determined in this work. The cause of these differences remains unclear.

7.3 Phase II: Unidentified Structure

The first high-pressure phase of Bi_4Te_3 (*phase II*) appears at around 6 GPa on initial pressure increase, overlapping slightly with phase I and persisting to approximately 12 GPa. Figure 7.11 shows the diffraction profile of phase II of Bi_4Te_3 which closely resembles that of phase II of the other Bi-Te compositions investigated here. Like other compositions, phase II of Bi_4Te_3 appears very similar to the first high-pressure phase of Bi_2Te_3, which is also shown in figure 7.11.

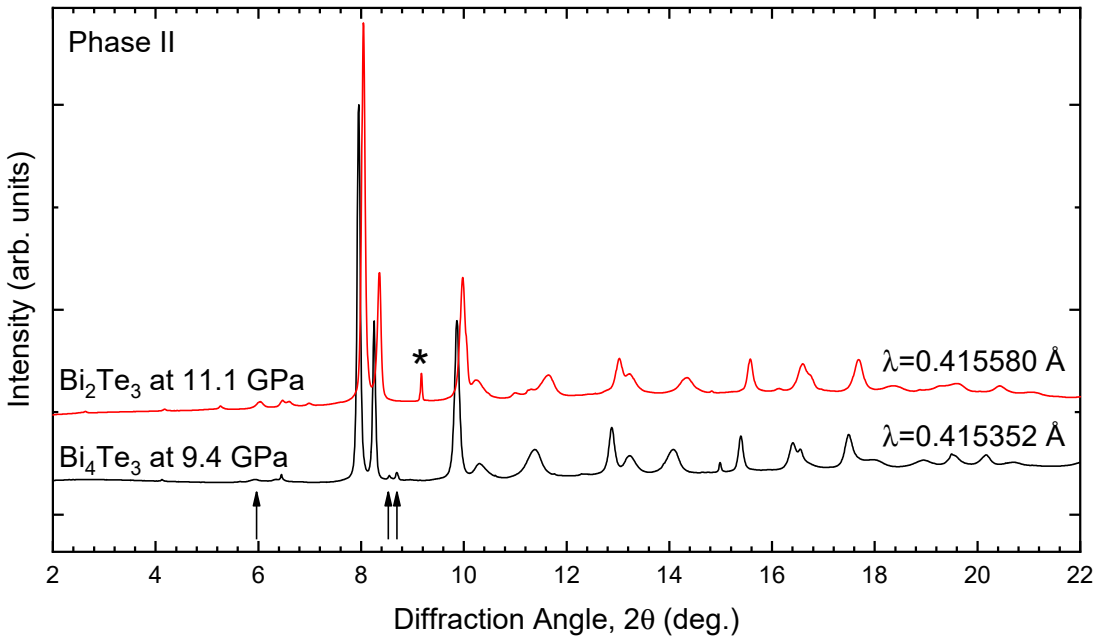

Figure 7.11 *X-ray powder diffraction profiles of Bi_4Te_3 (bottom) and Bi_2Te_3 (top) illustrating the close resemblance between both phases. The presence of weak, unidentified peaks in the Bi_4Te_3 profile are indicated with arrows; these are the same weak peaks discussed in section 7.1.1. The Bi_2Te_3 profile includes a peak (*) due to the solidified nitrogen pressure-transmitting medium.*

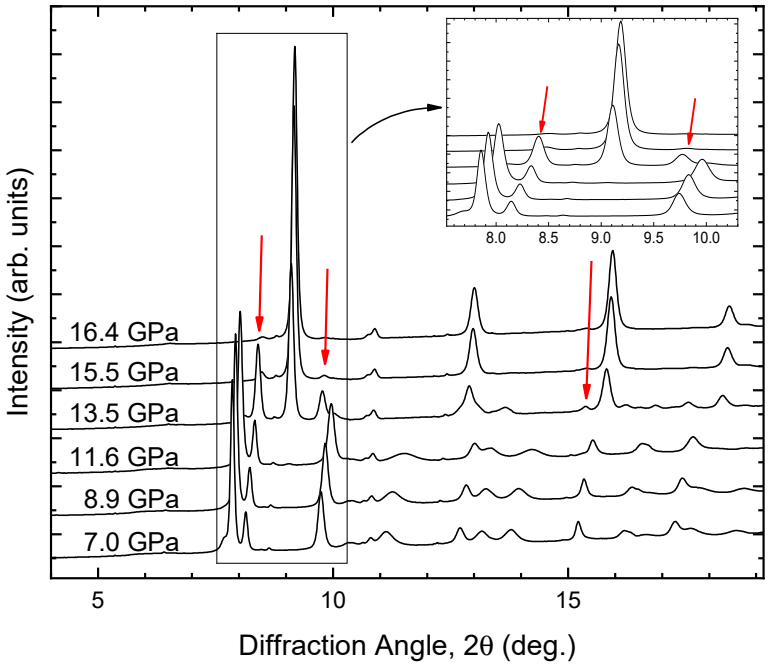

Figure 7.12 *X-ray powder diffraction profiles from Bi_4Te_3 recorded during experiment EE12996 on initial pressure increase. The transition from phase II to the cubic phase can be observed, along with several additional peaks belonging to phase III (indicated by red arrows).*

7.4 Phase III: Observed Peaks

Unique to Bi_4Te_3 is the observation of additional peaks in the diffraction profiles on pressure increase, as the sample is transforming from phase II to the cubic phase. These additional peaks are visible in all Bi_4Te_3 datasets and belong to a phase denoted here as *phase III*. This transition and the visible phase-III peaks are illustrated in figure 7.12.

Figure 7.12 includes a profile at 11.6 GPa where the sample has fully adopted the phase-II structure. The next profile, recorded at 13.5 GPa shows strong peaks from the cubic phase which grow in intensity as the pressure is increased (the sample has fully adopted the cubic structure in the 16.4 GPa profile). The peaks due to phase II are significantly weaker in the 13.5 GPa profile and reduce in intensity as the pressure is further increased. Two additional peaks, not due to the cubic phase or phase II, also appear in the 13.5 GPa profile. These peaks are indicated in the figure and can be seen at 9.8° and 15.4°; they have almost disappeared in the next profile, recorded at 15.5 GPa. A third phase-III peak may be present at 8.4°, overlapped by a peak from the previous phase. The sudden increase in intensity of this peak at 13.5 GPa suggests that a new contribution

may have appeared.

These phase-III peaks appear in similar positions to peaks reported by Jeffries *et al.* in 2011 in high-pressure x-ray powder diffraction data recorded with samples of Bi_4Te_3 [3]. Jeffries *et al.* reported observing two peaks on pressure increase as the majority of the sample transformed from phase II to the cubic phase. These peaks were attributed to a 'Bi_4Te_3-III' phase and were reported to be visible between approximately 11.5–16.5 GPa. These Bi_4Te_3-III peaks coexist with peaks from phase II and the cubic phase in the diffraction profiles.

By estimating the positions of these phase-III peaks in their published XRPD profile recorded at 12.6 GPa (figure 1 of [3]), we can estimate the d-spacings of two peaks observed by Jeffries *et al.* as $d_1 = 2.435$ Å and $d_2 = 1.521$ Å (from $d = \lambda/2\sin\theta$, Bragg's law). A Bi_4Te_3 profile recorded in experiment hc1335 at 12.4 GPa also includes these peaks, and allows for easy comparison with Jeffries *et al.* The two phase-III peaks at 12.4 GPa correspond to d-spacings of $d_1 = 2.447$ Å and $d_2 = 1.536$ Å. These d-spacings are in good agreement with the published observation of phase-III peaks, considering the uncertainty in the values determined from the profile published by Jeffries *et al.*

While unambiguous determination of the structure of this phase is not possible due to the small number of clearly identifiable peaks, a potential structure can be suggested. Bi_2Te_3 adopts a layered R-3m structure at ambient conditions. On increasing pressure, Bi_2Te_3 transforms to a C2/m structure at around 8 GPa, then to a *C2/c* structure above 14 GPa, before finally adopting a body-centred-cubic structure above 14.5 GPa [39, 53]. As members of the Bi-Te series appear to share common structural behaviours under pressure, the reported structures of Bi_2Te_3 may also be found in other Bi-Te compositions.

Phase II of the Bi-Te compositions investigated in this work may be described by the *C2/m* structure proposed for Bi_2Te_3 (however, this is perhaps debatable and is discussed in detail in the final chapter of this thesis; section 10.3). The next high-pressure phase of Bi_2Te_3 was therefore considered as a candidate for the phase III observed in this work. Comparison of peak positions predicted using the *C2/c* structure to the observed phase-III peaks suggests that the *C2/c* structure of Bi_2Te_3 may be a potential candidate. This is, of course, only based on the agreement of a few peak positions and should be considered a starting consideration for future work only.

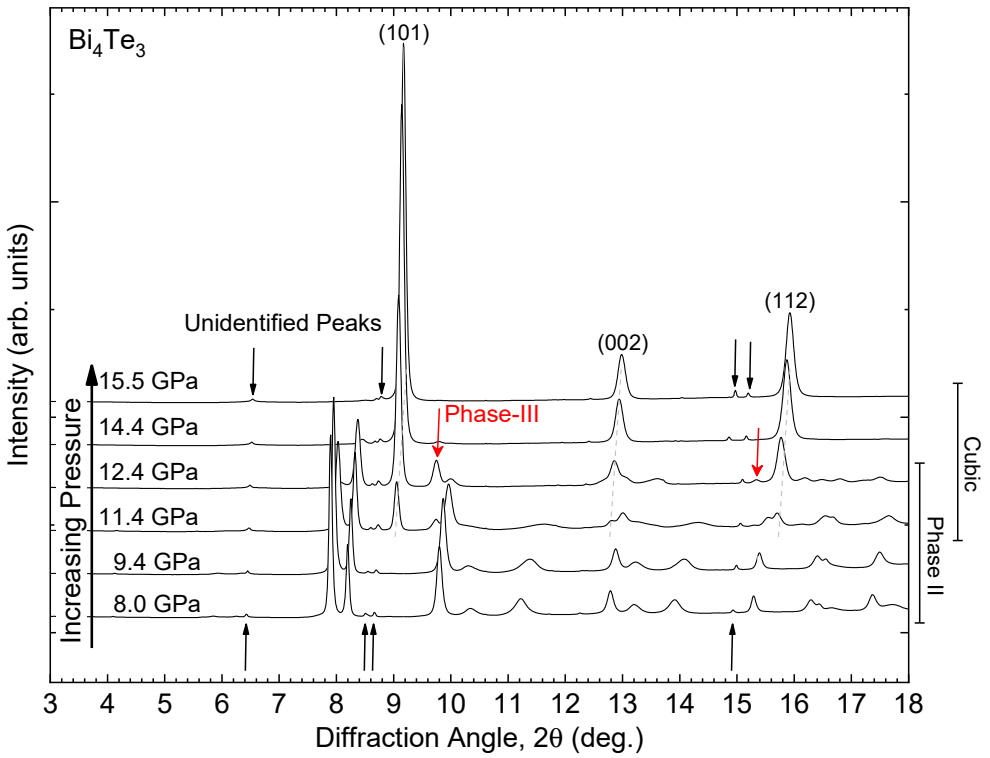

Figure 7.13 *X-ray powder diffraction profiles of Bi_4Te_3 on initial pressure increase (experiment hc1335). The cubic phase (peaks marked with Miller indices) can be seen emerging from phase II, along with a brief appearance of peaks from phase III. Present throughout are unidentified weak peaks, which are indicated near 6.5°, 8.8°, 15° and 15.5°.*

7.5 Phase V: Cubic Structure

The cubic phase of Bi_4Te_3 first appears around 11.4 GPa on initial pressure increase, as the sample is transforming from phase II. Bi_4Te_3 remains in the cubic phase up to the highest pressures recorded here, 18.9 GPa, and then gradually transforms to the host-guest phase on pressure decrease, with an overlap of around 2 GPa. The transition to the cubic phase on initial pressure increase is illustrated in the waterfall plot, figure 7.13. A weak feature at around 6.5° is indicated, which is one of the 'unidentified peaks' that are present throughout the pressure range of the experiment, as discussed in section 7.1.1.

The integrated diffraction profiles from the Bi_4Te_3 cubic phase can be readily indexed with a cubic unit cell, with a body-centred cubic (bcc) structure providing a good fit to the observed profile. As there are only two atoms in the bcc unit cell, the Bi_4Te_3 stoichiometry requires these the two atomic sites to have mixed

chemical occupancy, with each occupied by 57.1% bismuth and 42.9% tellurium on average.

While this chemically-disordered bcc structure provides a good fit to the measured profiles, the weak peak observed at 6.5° lies very close to the expected position of the cubic (001) reflection. The (001) reflection is forbidden in the bcc structure, but does appear when there is some chemical ordering across the two atoms in the unit cell, in a structure resembling the B2 (CsCl) type.

A refined profile from the Bi_4Te_3 cubic phase on initial pressure increase is shown in figure 7.14. This profile is refined with a cubic B2, CsCl-type structure (space group 221) which has two atomic sites of mixed occupancy. While the weak feature at 6.5° is very close to the position of the (001) reflection, careful refinements confirm that this feature is not due to the cubic phase. This peak is poorly fitted when performing le Bail fits to the profile; fixing the lattice parameter to fit this 6.5° peak results in a unacceptable overall fit, with all other peak positions significantly offset. There is also no sign of visible peaks corresponding to other reflections that would indicate ordering within the structure e.g. the (111) and (102) reflections near 11° and 14.5°, as illustrated in figure 7.14. The structure of the cubic phase on initial pressure increase can therefore be confirmed as fully site-disordered bcc. The additional weak features in the profile shown in figure 7.14 are the unidentified peaks present from ambient pressure, as discussed in section 7.1.1.

The cubic phase remains in this bcc structure up to the highest pressures attained here (18.9 GPa). However, on subsequent pressure decrease we see evidence of ordering within the cubic structure around 12 GPa in the diffraction profiles. We can see the (001), (111) and (102) peaks of the B2 CsCl-type structure appear in the profiles, with the (100) peak overlapping with (but clearly distinct from) the unidentified peak near 6.5°. This subtle transition is illustrated in figure 7.15 which shows the changes in the Bi_4Te_3 diffraction profiles as the pressure is decreased. Initially, at high pressures, the profiles (shown in blue) correspond to the site-disordered bcc structure, as discussed previously. On decrease to 10.1 GPa, however, several weak peaks appear in the diffraction profile, as illustrated by the three insets to figure 7.15. These can be indexed as the (001), (111) and (102) reflections of the B2 CsCl-type structure, indicating that some chemical ordering is now present in the cubic structure (profiles shown in black).

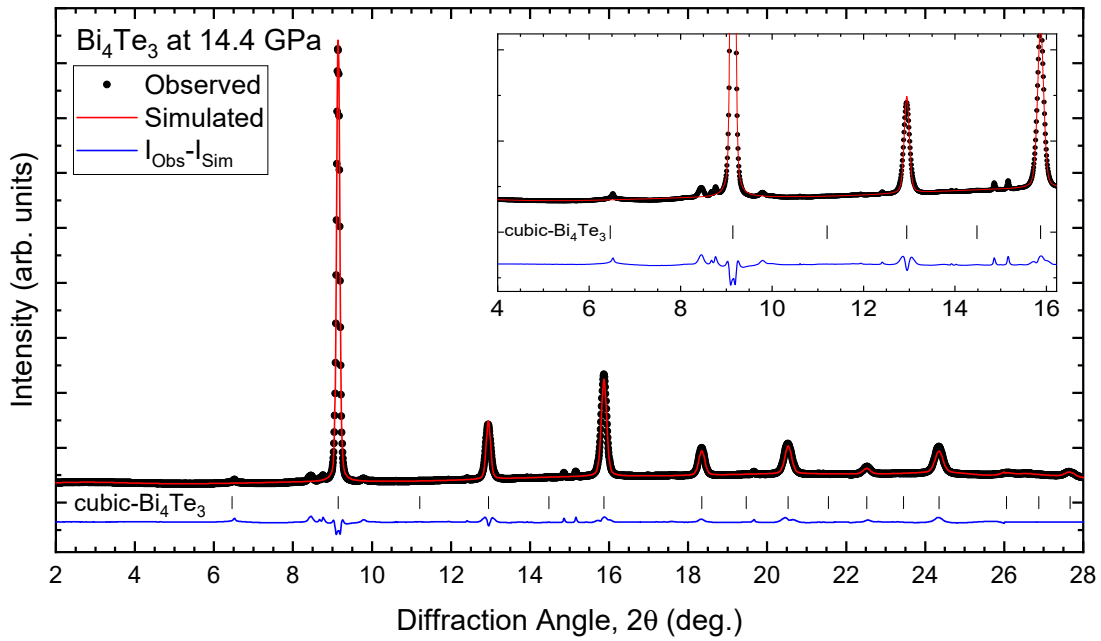

Figure 7.14 *Rietveld refinement of Bi_4Te_3 at 14.4 GPa, $wR_p = 3.51\%$. The refinement model uses the B2 CsCl-type structure (space group 221) with the occupancy of each atomic site constrained to a ratio of 4:3 Bi:Te. This structure is identical to body-centred cubic and, as such, the refinement includes several reflections with zero intensity e.g. (001) at 6.5°.*

On further pressure decrease, the sample gradually transforms to the host-guest phase with the cubic phase still present in its B2 ordered variant (profiles shown in red). Eventually the peaks due to this cubic phase disappear and peaks belonging to phase II appear near 8.2° and 9.8° (profiles shown in green). The weak peaks associated with the (001), (111) and (102) cubic reflections disappear along with the stronger cubic peaks at this pressure; the disappearance of the (001) peak reveals the broad feature that is still present near 6.5°. These transitions confirm there are two peaks that overlap near 6.5° — the broad unidentified peak and the (001) cubic peak. The fact that transitions involving the (001) peak can be seen quite separately from the consistent unidentified peak confirms that we do observe both disordered and ordered variants of the cubic phase.

These partially ordered cubic phase structure refinements were performed using Jana2006 with certain constraints imposed on the refinement in order to maintain the overall sum of site occupation factors (SOFs) on each atomic site. Along with these, two equations were defined to determine the occupation factors of the second atomic site from those of the first, maintaining overall Bi_4Te_3 stoichiometry. As such the refinement required only one refinable SOF.

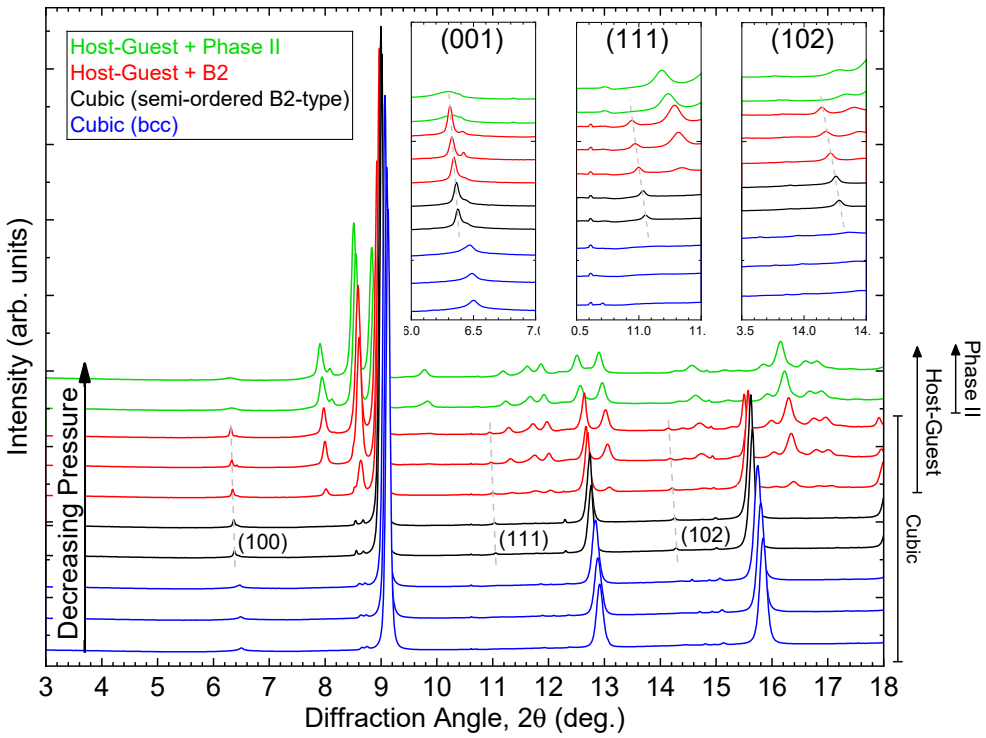

Figure 7.15 *X-ray powder diffraction profiles of Bi_4Te_3 on pressure decrease from the cubic phase. The colours indicate different phases and phase mixtures. Inset plots highlight the weak peaks associated with an ordering of the cubic structure to a partially-ordered B2 CsCl-type structure.*

To illustrate these constraints, consider that the structure has two atomic sites labelled '1' and '2' and each site has two SOFs describing the occupancy by each of the two atom types. As such, we have four SOFs: *Bi1*, *Te1*, *Bi2* and *Te2*. The factor *Bi1* describes the occupation of atomic site 1 by the element bismuth (Bi), and so on. We restrict the refinement such that the expressions $(Bi1 + Te1)$ and $(Bi2 + Te2)$ are each kept constant, maintaining that each site is fully occupied i.e. that the total SOF for each site sums to a value of 1. We then define equations which take into account the SOFs of the fully disordered bcc-type structure, where both sites have a Bi SOF of 0.571 and a Te SOF of 0.429 (i.e. occupied by 57.1% Bi and 42.9% Te, giving Bi_4Te_3 stoichiometry). In the disordered bcc-type structure the sum of the Bi SOFs across both sites is $0.571 \times 2 = 1.142$ and similarly the sum for Te is $0.429 \times 2 = 0.858$. These values allow us to maintain stoichiometry by setting:

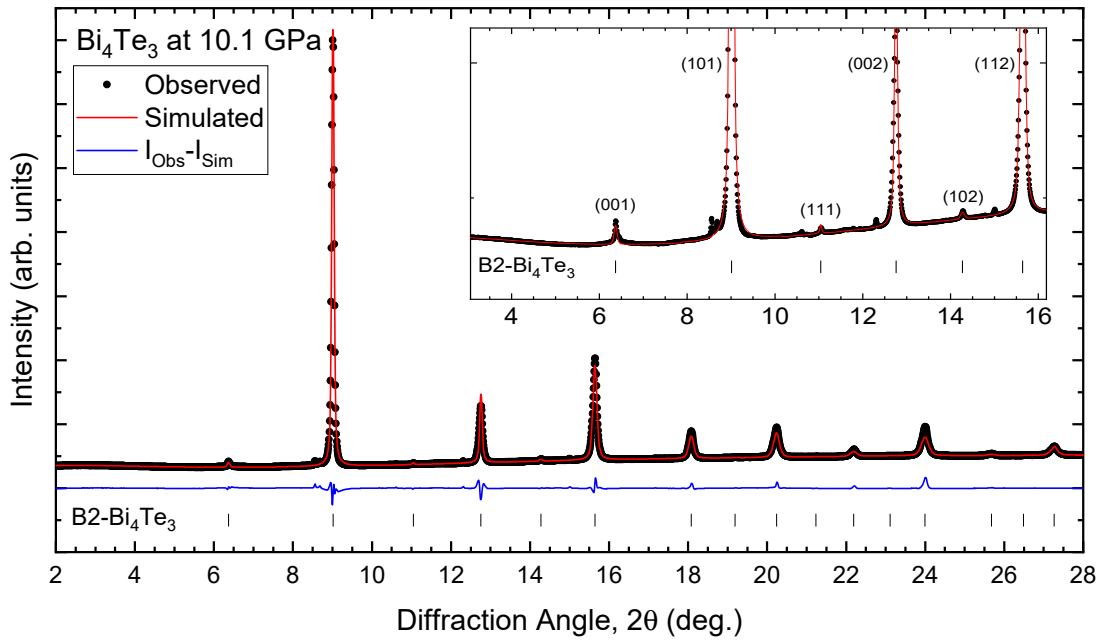

Figure 7.16 *Rietveld refinement of Bi_4Te_3 at 10.1 GPa, $wR_p = 2.73\%$, using the partially-ordered B2 CsCl-type structure. The site at (0,0,0) is occupied by 75.7(3)% Bi, with the rest of the occupancies defined by maintaining an overall ratio of 4:3 Bi:Te.*

$$Bi2 = 1.142 - Bi1$$

$$Te2 = 0.858 - Te1$$

With these four constraints we can refine the atomic occupancies of the partially-ordered CsCl-type structure.

Profiles including these weak peaks refine well using the B2, CsCl-type structure which allows chemical ordering across the two atomic sites. An example refinement of Bi_4Te_3 at 10.1 GPa is shown if figure 7.16. The refinement produces a good fit to the observed profile and reproduces the weak peaks well, resulting in an R-value of $wR_p = 2.73\%$.

The refined lattice parameters and unit cell volumes of the cubic phase (both ordered, B2-type and disordered, bcc-type) are shown in figure 7.17. Both datasets show a clear systematic offset between experiments EE12996 and hc1335, with the data showing very similar pressure dependencies but offset from one another by approximately 0.4 GPa. The results from the hc1335 data show a slightly more dense material. The unit cell volume data from experiment hc1335

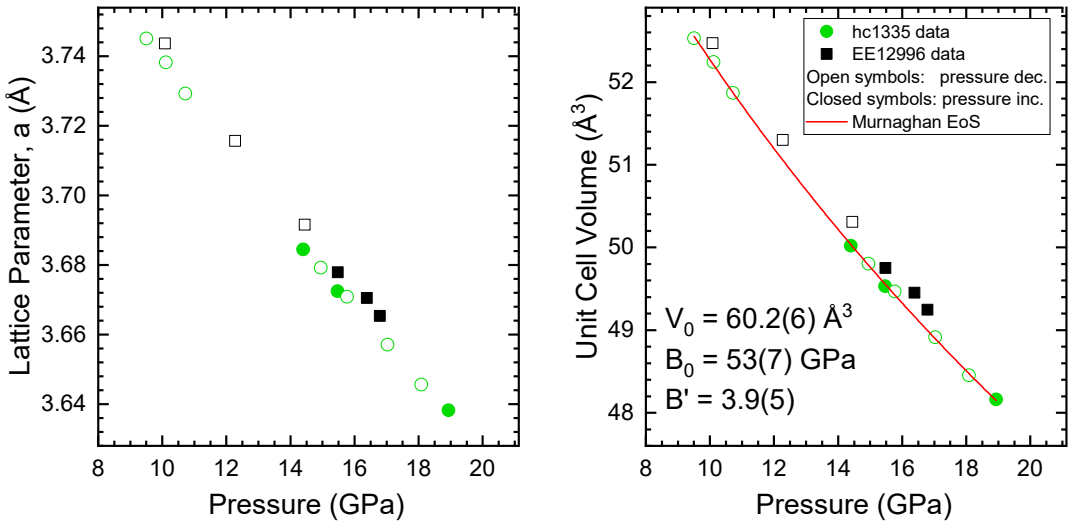

Figure 7.17 *Refined lattice parameter (a) and unit cell volumes for the cubic phase of Bi_4Te_3. Refinements include both the partially-ordered B2-type and disordered bcc-type cubic structures. Unit cell volume data fitted using the Murnaghan equation of state [121].*

is fitted using the Murnaghan equation of state resulting in fitted unit cell volume at zero applied pressure of $V_0 = 60.2(6)$ Å^3, a bulk modulus of $B_0 = 53(7)$ GPa and first derivative of the bulk modulus, $B' = 3.9(5)$. The fit to the EE12996 data is significantly poorer but results in similar values of $V_0 \approx 60$ Å^3, $B_0 \approx 58$ GPa and $B' \approx 3.6$.

The fitted value of the bulk modulus at zero pressure, B_0, of the Bi_4Te_3 cubic phase is much smaller than that reported by Jeffries *et al.*, who reported a bulk modulus of $B_0 \approx 120$ GPa by fitting their measured pressure-volume data with the Birch-Murnaghan equation of state [3].

Refinements of the cubic phase reveal a transition where the structure is seen to order on reduction of pressure below a certain critical pressure which lies between 12.3–14.4 GPa. This transition is evident from the diffraction profiles and can also be seen in the refined site occupation factor as a function of pressure, figure 7.18. At pressures below this transition, the structure appears to order with one site consisting of approximately 75% bismuth and the other site determined by the overall Bi:Te ratio of 4:3. The bismuth occupancy of this site can be seen to increase slightly as the pressure is decreased, until a phase transition to the host-guest phase occurs. This ordered cubic phase was included in the host-guest refinements performed using the custom python Rietveld refinement code. However, the refined SOF values from these fits do not appear to be reliable due

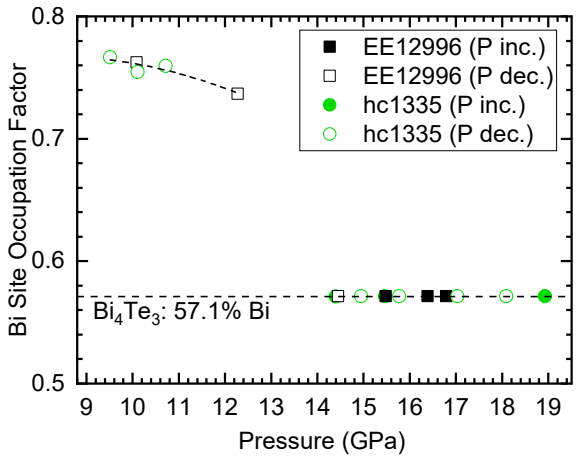

Figure 7.18 *Refined site occupation factor of the cubic-Bi_4Te_3 phase. This single parameter is refined where peaks in the diffraction profiles indicate partial ordering in the cubic structure (below 13 GPa), and is fixed to a value corresponding to a Bi:Te ratio of 4:3 when the profiles indicate a site-disordered bcc structure. Uncertainties similar to symbol size, omitted for clarity. Dashed lines are guides to the eye.*

to the overlap with the host-guest phase and the fact that the cubic phase is a minority phase. All refinements of the cubic phase included with the host-guest phase resulted in one of the cubic atomic sites being essentially fully occupied by bismuth (95–100% Bi occupancy).

Such a 'fully ordered' structure has been observed to occur in cubic Bi-Te compounds at high pressures after gentle thermal annealing. Loa *et al.* have reported observations [12] based on similar data to that which is presented here, with the compositions investigated sourced from the same parent samples used in this work. The observation of such ordering on pressure reduction is not surprising, given the often inverse effects of temperature and pressure — here the reduction in pressure allows the atoms in the structure to rearrange and order, whereas the introduction of thermal energy to the system also allows this process to take place.

7.6 Phase IV: Host-Guest

The host-guest phase of Bi_4Te_3 only appears on pressure release from the cubic phase, with no evidence of any host-guest presence on initial pressure increase. This is in contrast to the other compositions investigated here where the host-

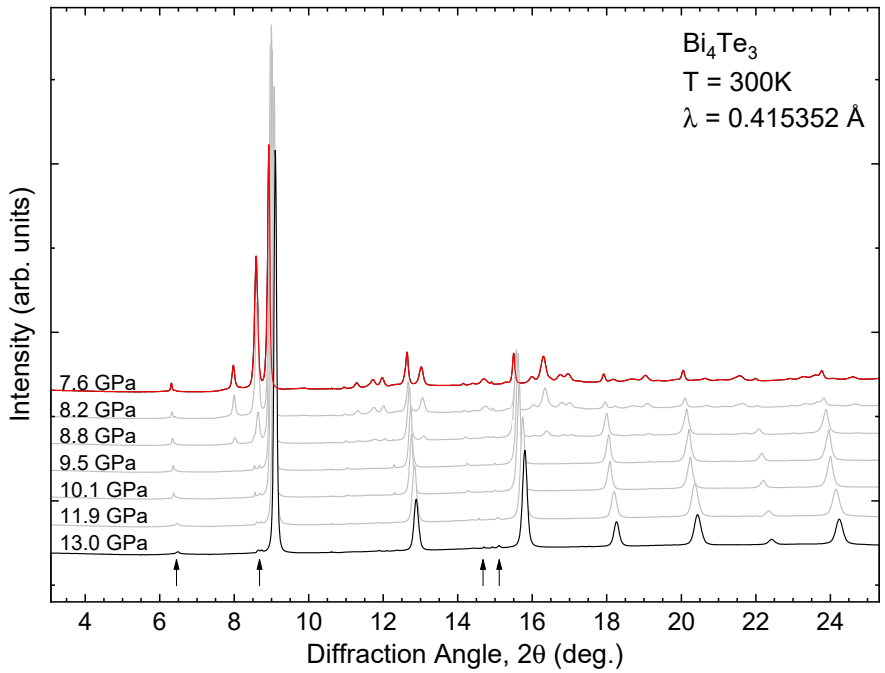

Figure 7.19 *X-ray powder diffraction profiles showing Bi_4Te_3 undergoing a transition from the cubic (black) to the host-guest (red) phase on pressure decrease. Profiles are from experiment hc1335. Weak unidentified 'contaminant' peaks are indicated with arrows in the cubic phase profile.*

guest phase is observed on both pressure increase and decrease: Bi_2Te and Bi_7Te_3.

The transition from the cubic to the host-guest phase in Bi_4Te_3 on pressure decrease is illustrated in the waterfall plot, figure 7.19. The figure shows the sample initially in the cubic phase at 13 GPa; indicated in this profile are the unidentified weak peaks discussed in section 7.1.1. As the pressure is reduced, peaks due to the host-guest phase begin to emerge at 8.8 GPa. The sample then quickly adopts the host-guest structure (7.6 GPa), with a minority remaining in the cubic phase, as can be seen by following the cubic peaks near 13° and 16°.

The structure of the Bi_4Te_3 host-guest phase is the same as that of Bi_2Te and Bi_7Te_3, consisting of two interpenetrating tetragonal substructures, the host and the guest, with the linear guest chains apparently disordered along their lengths (the c-axis direction). Due to this lack of order along the c-axis, the guest-only reflections do not contribute sharp diffraction peaks to the diffraction profile. While the host-guest profiles of Bi_2Te and Bi_7Te_3 exhibit clear diffuse scattering from the disordered guest, with an edge feature that allows for the guest lattice parameter, c_{Guest} to be determined, such a feature is not visible in the host-guest profiles of Bi_4Te_3. This is illustrated in figure 7.20.

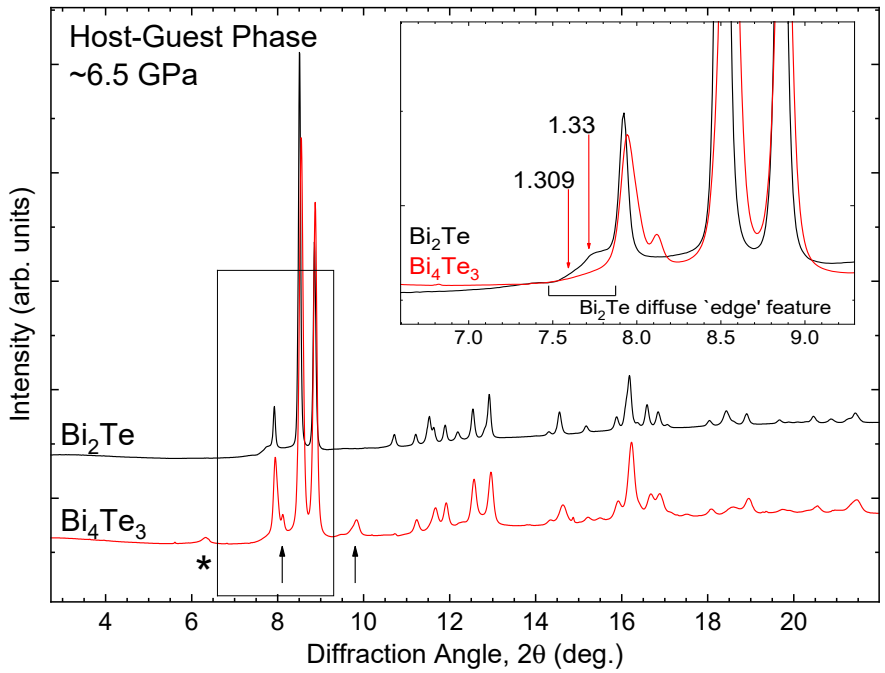

Figure 7.20 *Comparison of Bi_2Te and Bi_4Te_3 host-guest diffraction profiles. Diffuse scattering from the guest is not visible in the Bi_4Te_3 profile. Phase-II (↑) and unidentified (∗) peaks are indicated in the Bi_4Te_3 profile. Inset shows same profiles overlapped. The d-spacings corresponding to c_{Guest} values determined from c_{Host}/c_{Guest} ratios of 1.309 and 1.33 are indicated for the Bi_4Te_3 profile.*

As the value of c_{Guest} could not be determined from the measured Bi_4Te_3 data, an estimate had to be found to provide values that could be used in the Rietveld refinement. While the host lattice parameters can be readily extracted from the host-guest profiles, an estimate of c_{Guest} is required to determine the number of atoms in the unit cell and to refine the site occupation factors. The refinements of the host-guest structures of Bi_2Te and Bi_7Te_3, along with the fitting of the diffuse 'edge features, yielded both the c_{Host} and c_{Guest} lattice parameters for these compounds.

The ratio of these refined parameters, c_{Host}/c_{Guest}, as a function of pressure is plotted in figure 7.21 (a), alongside published values for the host-guest phase of bismuth, Bi-III [32]. These values can be used to estimate a c_{Host}/c_{Guest} value for Bi_4Te_3 by assuming a linear change in this value as a function of composition. Clearly, there are large uncertainties associated with the values determined in this work due to the diffuse nature of the feature used to determine c_{Guest}. Applying a linear fit with zero gradient to the data from each composition (Bi_2Te, Bi_7Te_3 and Bi) yields a representative c_{Host}/c_{Guest} value for each.

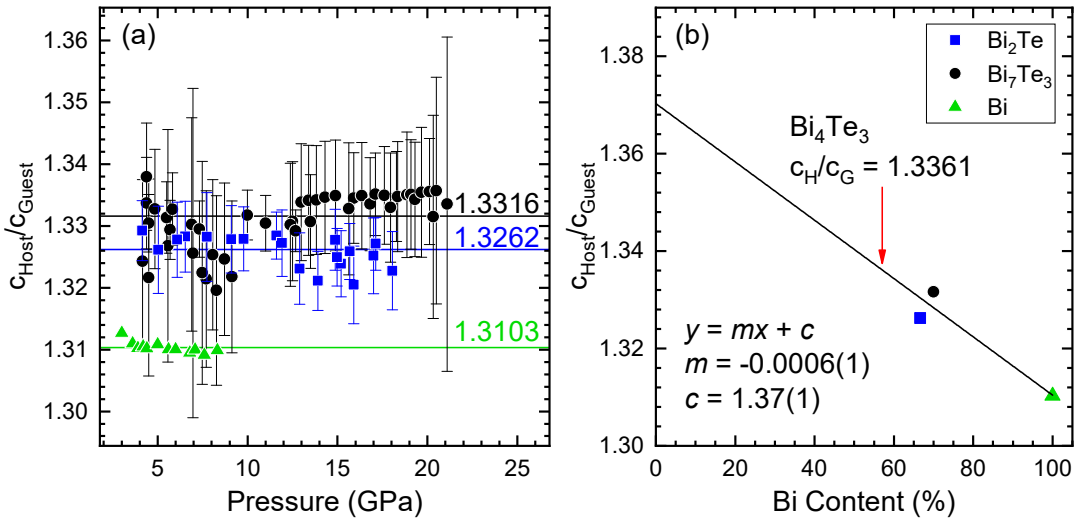

Figure 7.21 *(a) Ratio of refined c-lattice parameters for the host-guest phases of Bi_2Te and Bi_7Te_3, along with published values for Bi-III [32]. Straight lines denote zero-gradient linear fits of to the data, with the resulting value of the c-ratio appended. (b) Fitted c-ratio values plotted as a function of composition. Linear fit used to estimate a value for the c-ratio of Bi_4Te_3 — 1.3361.*

These values are plotted as a function of composition (% Bi content) in figure 7.21 (b). Applying a linear fit allows an estimate for the c_{Host}/c_{Guest} ratio of Bi_4Te_3 to be determined (Bi content 57.1%). The estimated value for Bi_4Te_3 is $c_{Host}/c_{Guest} = 1.3361$. The value of c_{Guest} can now be estimated in the refinements as a function of c_{Host}.

The Bi_4Te_3 host-guest diffraction profiles were refined using the custom Rietveld refinement program described in section 3.5.4. Atomic displacement parameters were fixed (U_{iso} = 0.015 Å^2) in order to avoid unphysically small or negative values. The structural parameters refined in the fit are: the host lattice parameters (a_H and c_H); the host *8h* atomic site coordinate (x); the guest bismuth site occupation factor (SOF); three pseudo-Voigt peak shape parameters (U, W and n); a scaling factor; and a background function (sixth-order Chebyshev polynomial). Where appropriate, peaks from the cubic phase are also included in the refinement as a separate phase.

A total of 28 diffraction patterns of the host-guest phase were recorded at pressures between 5–17 GPa. These patterns were integrated to produce diffraction profiles, and uncertainties on the integrated intensities were estimated as detailed in section 3.5.2. 11 profiles were available for analysis from experiment hc1335, all recorded on pressure decrease from the cubic phase at pressures

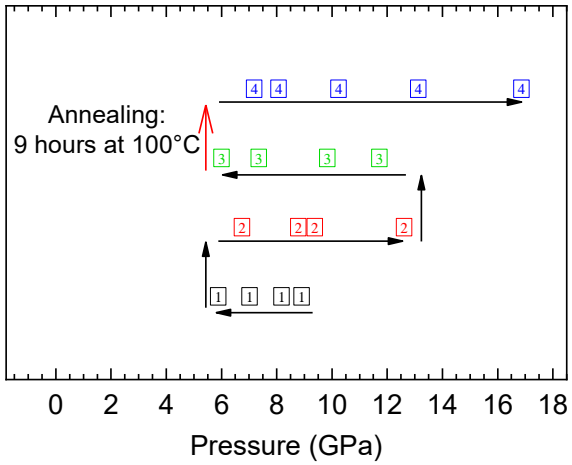

Figure 7.22 *Illustration of the pressures at which Bi_4Te_3 host-guest diffraction data were recorded during experiment EE12996, which included pressure cycling and annealing of the sample.*

between 8.2–4.9 GPa. A total of 17 profiles were available from experiment EE12996 between pressures of 5.9–17 GPa, including pressure cycling and annealing of the sample. As the pressure cycling and the annealing of the sample have been found to have a significant effect on the structural parameters, an understanding of how this was done in the experiment is useful for interpretation of the refinement results. With that in mind, the pressures at which EE12996 host-guest profiles were recorded are illustrated in figure 7.22 and are described in detail below.

The aim of experiment EE12996 was to investigate additional peaks that appear in the host-guest phase as the pressure is reduced past a certain point. These peaks were considered a possible indication of ordering of the guest substructure, but have since been determined to be peaks from phase II, which overlaps with the host-guest phase at lower pressures. After initial pressure increase and subsequent decrease into the host-guest phase, the pressure was reduced to 5.9 GPa until the phase-II peaks appeared. There are 4 profiles recorded on this initial pressure decrease (labelled '1' in figure 7.22). The pressure was then increased to 12.6 GPa, where the phase-II peaks disappeared, with 4 diffraction profiles recorded (labelled '2'). The pressure was decreased once again until the peaks disappeared, with 4 profiles measured down to 6 GPa (labelled '3'). The screws of the diamond anvil cell were then tightened slightly to halt this decrease, resulting a sample pressure of 7 GPa and a diffraction profile of the host-guest phase with the phase-II peaks also present.

At this point, the sample was annealed at 100°C for 9 hours, to investigate

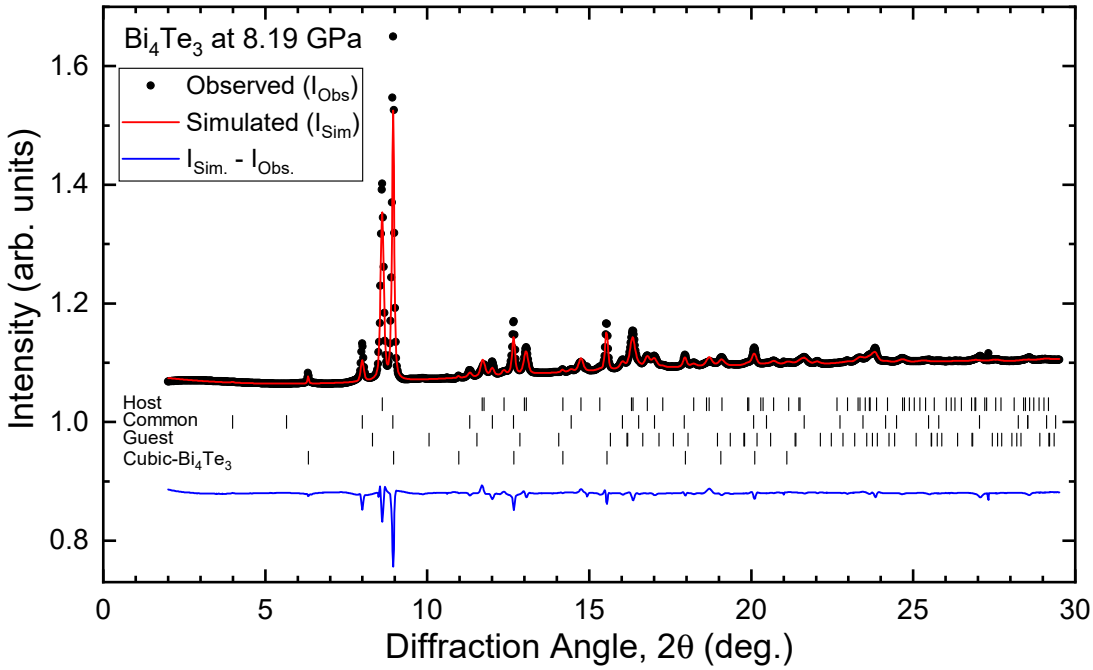

Figure 7.23 *Rietveld refinement of the host-guest phase of Bi_4Te_3 at 8.19 GPa, including peaks from the cubic Bi_4Te_3 phase.*

whether this would have any effect on the additional (phase-II) peaks. During annealing the pressure in the DAC had risen to 7.2 GPa. The pressure was further increased manually until the phase-II peaks had disappeared, with 5 profiles (labelled '4') recorded between 7.2–16.9 GPa, where the experiment was ended. All data analysed here were collected with the sample in the host-guest phase, without transforming to the higher or lower-pressure phase.

An example Rietveld refinement of the host-guest phase is shown in figure 7.23. The simulated profile fits well to the observed, with an R-value of 1.23%, and all observed peaks are accounted for by the *host-guest* and *cubic* phases. The discrepancies between the intensities of the most intense peaks in the simulated and observed profiles (near 9°) can be explained by the weighting used in the refinement. As detailed in section 3.5.2, the refinements make use of uncertainties on the integrated intensities that have been determined from the texture in the recorded diffraction images. These uncertainties better reflect the confidence in the integrated peak intensities, taking into account how smooth and powder-like the Debye-Scherrer ring responsible for each peak is. In this case, the most intense peaks are associated with textured rings and the uncertainties on the intensities of these peaks are accordingly larger. This allows the refinement to prioritise weaker peaks if they arise from more powder-like rings, as these intensities will be more reliable.

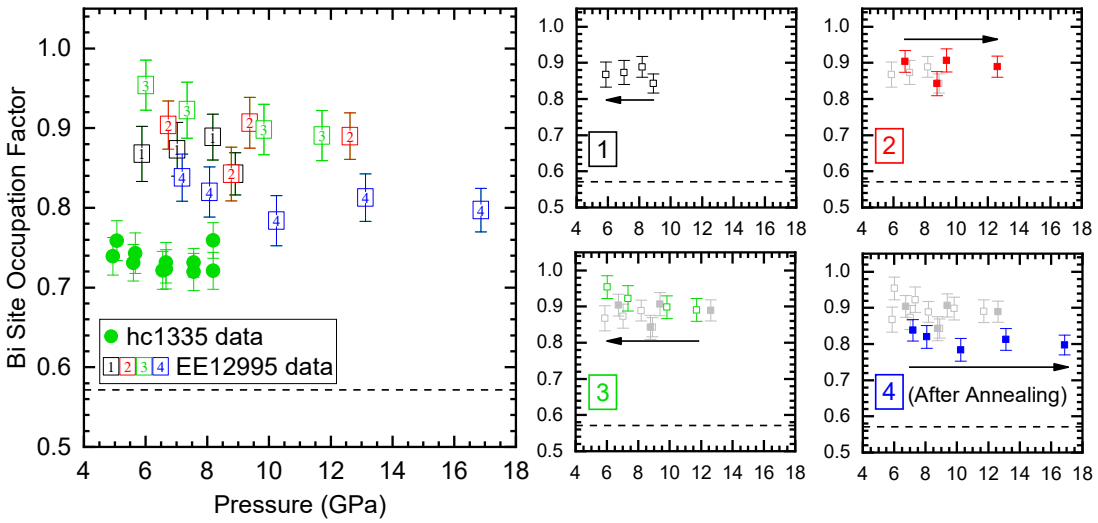

Figure 7.24 *Refined guest bismuth site occupation factors for the host-guest phase of Bi_4Te_3. The four stages of pressure cycling in EE12996 are indicated by the numbered symbols with '1' indicating data from the initial pressure decrease from the cubic phase. Grey symbols indicate data from a previous cycle. Dashed lines indicate a guest Bi SOF of 0.57, corresponding to a fully site-disordered Bi_4Te_3 structure.*

The results of the refinements are presented in figures 7.24–7.26. Clear effects of the pressure cycling and annealing can be seen in the refined structural parameters, particularly in the refined site occupation factors (figure 7.24). The main panel of the figure shows all refined values together, with the pressure cycling indicated by the numbered symbols as in figure 7.22. The refined site occupation factors are also shown being gradually added to a plot in the four subfigures in figure 7.24. The refined SOF values from the initial pressure decrease from the cubic phase are plotted in the top left panel, with symbols labelled '1'. The SOF appears stable at approximately 0.87, indicating guest chains that are composed of 87% bismuth; this is a much higher bismuth content than would be expected if the structure was chemically disordered (57% Bi from the Bi_4Te_3 stoichiometry).

The next panel shows data from the subsequent pressure increase (the previous data included in light grey for reference). The SOF remains stable around a slightly higher value of 0.90. On the subsequent pressure decrease, shown in the next panel labelled '3', the SOF can be seen to rise as the pressure is reduced, to a value of 0.95. Finally, panel '4' shows the refined values on pressure increase after the sample was annealed at 100°C for 9 hours. There is a clear reduction in the value of the SOF to approximately 0.80. Many of these values are within uncertainty of one another, with a typical error of ±0.03 in the refined SOF. This,

combined with the observed spread in the values, suggests that any changes during the pressure cycling (panels 1–3) are slight and cannot be stated with certainty, but there is evidence that pressure cycling has an effect on the chemical ordering in the host-guest structure. The effect of annealing on the structure is far more clear; reducing the amount of bismuth in the guest chains but still at a value significantly higher than 0.57.

Interestingly, the data from experiment hc1335 shows stable values of the SOF at around 0.74 over the entire pressure range. This is further evidence that there is some difference between the samples investigated in the two experiments, as seen in refined parameters across all structural phases. The effect of annealing the EE12996 sample is to reduce the SOF to a value more similar to that of the hc1335 sample.

The pressure-dependence of the two refined host lattice parameters (c_{Host} and a_{Host}) are shown in the main panel of figure 7.25, along with the c_{Host}/a_{Host} ratio and the unit cell volume. The refined lattice parameters show some variation and there are systematic offsets between the hc1335 and EE12996 data. This is more clear in the c_{Host}/a_{Host} ratio plot which shows an offset between the two datasets and the effect of pressure cycling and thermal annealing of the EE12996 sample. Pressure cycling appears to produce consistent values but the ratio is clearly larger after annealing. The hc1335 data produces the largest values, with the annealed sample moving in closer agreement to the hc1335 data. A similar effect was observed in the refined site occupation factor.

The unit cell volumes are largely consistent and can be fitted together using the Murnaghan equation of state. The fit gives values of unit cell volume at zero applied pressure, $V_0 = 332(1)$ Å^2, bulk modulus, $B_0 = 44.8(29)$ GPa, and first derivative of the bulk modulus at zero pressure, $B_0' = 4.0(3)$.

The refined atomic coordinate of the host *8h* Wyckoff site is shown in figure 7.26. All refined data show a similar trend, with the x coordinate decreasing with increasing pressure. This effect is subtle, with a decrease of only $\sim 2\%$ over 10 GPa. While all data exhibit a similar trend, there are systematic offsets in the values, suggesting that this parameter is sensitive to sample history. Interestingly, unlike the other refined parameters, the EE12996 data in closest agreement with that of experiment hc1335 is not the post-annealing data.

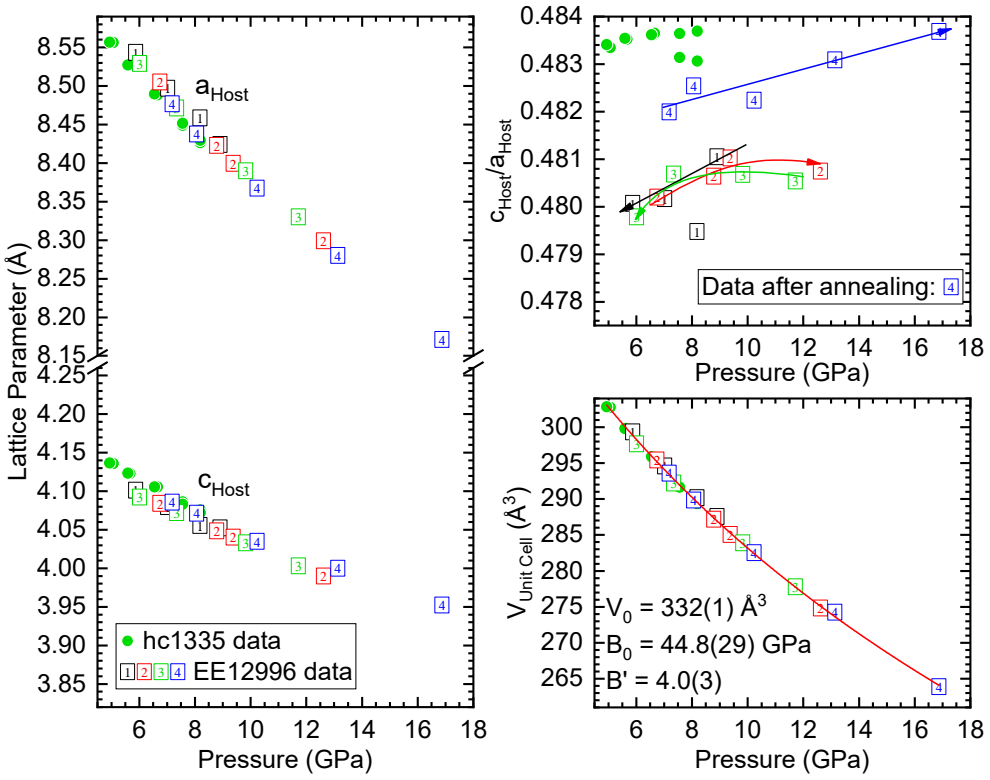

Figure 7.25 *Figures illustrating the refined lattice parameters of the host-guest phase of Bi_4Te_3, their ratio and the derived unit cell volume as a function of pressure. Error bars are smaller then the symbol size and are omitted for clarity. The lattice parameters show a visible discrepancy between the EE12996 and hc1335 data. The refined values agree best in the final cycle of the EE12996 data, after annealing, suggesting that sample history is important in this phase of Bi_4Te_3. All unit cell data has been fitted with the Murnaghan equation of state.*

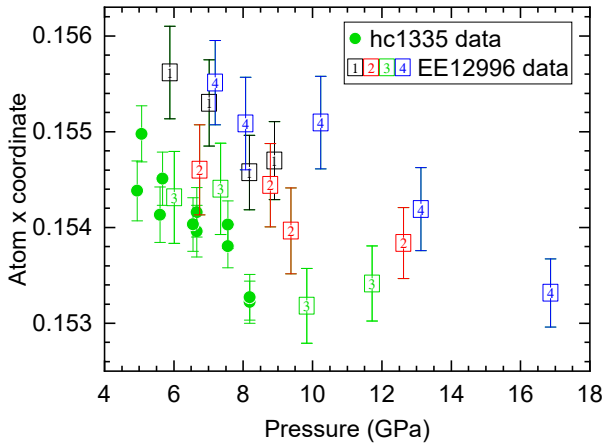

Figure 7.26 *Refined atomic x coordinate of host-guest Bi_4Te_3.*

Conclusion

Bi_4Te_3 is unique in that it adopts the host-guest structure only on decompression from the high-pressure cubic phase. This is in contrast to the other compositions Bi_2Te and Bi_7Te_3, both of which adopt the host-guest phase on compression from phase II, as well as on pressure release from the cubic phase. Another unique feature of Bi_4Te_3 is the lack of clear diffuse scattering from the guest component of the host-guest structure. This edge feature was used to determine c_{Guest} for the other compositions, required for refinement of the site occupation factors.

In order to facilitate refinements of Bi_4Te_3, we have estimated values of c_{Guest} using the results from Bi_2Te and Bi_7Te_3, along with published c-ratio values for Bi-III. The resulting estimate of the c_{Host}/c_{Guest} ratio may not be accurate but the refined parameters are robust to changes in c-ratio, as evidenced by previous refinements using a different c-ratio estimate. This previous estimate (c_{Host}/c_{Guest} = 1.309) was based on published c-ratio values for the host-guest phases of bismuth and antimony. Use of this estimate gave similar results, with the only significant changes found in the refined site occupation factors (SOFs) which were typically larger by an amount comparable to the calculated uncertainty. All observed parameter trends are robust to changes in the c-ratio estimate used.

Pressure cycling and annealing have a clear effect on the Bi_4Te_3 host-guest structure, causing both structural changes and changes in chemical ordering. These effects can be seen in the refined lattice parameters which are robust and unaffected by sample texture; this supports the behaviour observed in the refined values of the SOF and atomic coordinates, which are sensitive to sample texture. It appears that sample history is an important feature in Bi_4Te_3, with annealing and pressure cycling causing clear changes to the structure. The fact that the unit cell volume remains consistent supports the 'rearrangement' of atoms within the structure.

7.7 Phases on Pressure Decrease

There are several phase transitions which occur on pressure decrease in Bi_4Te_3 and these differ slightly from the phases observed on initial pressure increase. X-ray powder diffraction profiles observed on pressure decrease are shown in figure 7.27, where the bottom profile shows the high-pressure cubic phase and profiles plotted

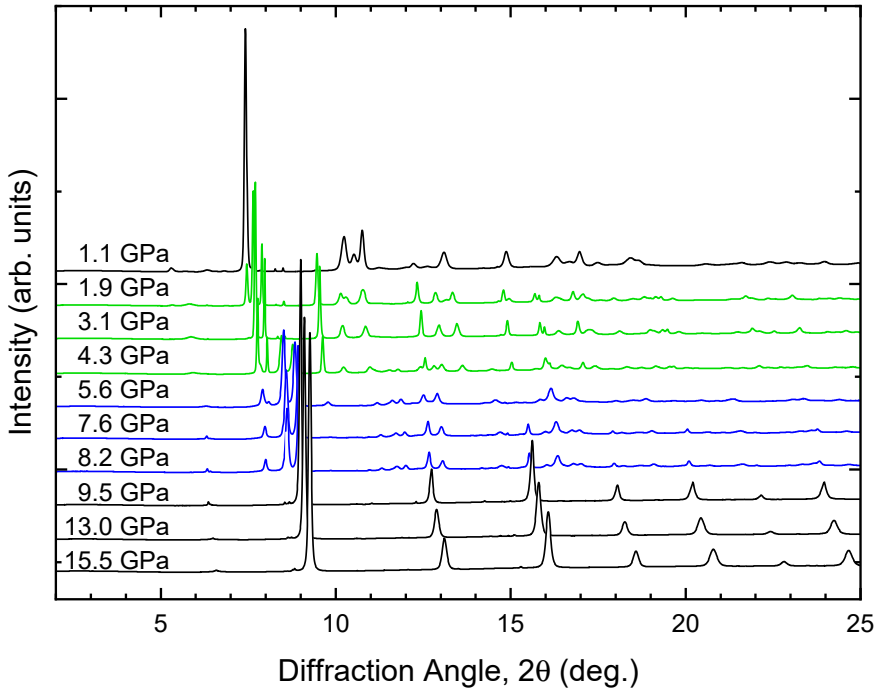

Figure 7.27 *X-ray powder diffraction profiles recorded during experiment hc1335 for a sample of Bi_4Te_3 on pressure decrease from the cubic phase.*

above that are at lower pressures.

As previously discussed, the cubic phase initially adopts a disordered bcc-type structure and transforms to a partially-ordered B2-type structure on pressure decrease. Peaks due to the host-guest phase then appear and there is some overlap between the cubic and host-guest phases. The cubic phase peaks disappear on further reduction in pressure and are replaced with peaks from phase II, which overlaps with the host-guest phase. Finally the sample transforms to phase I.

Unlike on initial pressure increase, the sample adopts a host-guest structure on pressure decrease. Also, no sign of phase-III peaks can be seen in the profiles recorded on pressure reduction.

Chapter 8

BiTe

The remaining compositions that have been investigated in this work are BiTe and Bi_4Te_5. Neither composition adopts the host-guest phase and the data available for these compositions is more limited than that for the previous materials, so these chapters will be more brief than the preceding ones. Once the results for BiTe and Bi_4Te_5 have been presented, the findings of this work as a whole will be discussed, summarising them as a function of composition and in the context of the $(Bi_2)_m(Bi_2Te_3)_n$ series.

This chapter will present the analysis of data collected for BiTe on initial pressure increase and subsequent decrease. While more limited in scope compared to the data available for the preceding compositions, BiTe offers an opportunity to directly compare the 3D and 4D structural models which have been previously used to describe the BiTe phase I structure. This comparison illustrates the subtle failings of the 3D commensurate approximation in comparison to the more appropriate 4D, incommensurately modulated structure. BiTe also appears to adopt phase II and phase III structures similar to those of the other members of the series, however these phases are not studied in detail. Finally data from the cubic phase are analysed, before the phases observed on pressure release are discussed.

8.1 BiTe: Experiment Summary

The composition BiTe was investigated during experiment EE8105 at the Diamond Light Source in October 2012. Collection of diffraction patterns made use of a Perkin-Elmer detector, requiring some additional post-processing of the integrated x-ray diffraction profiles, as detailed in section 3.5.1. A powdered sample of BiTe was loaded into a diamond anvil cell (DAC) with liquid helium as a pressure transmitting medium and a ruby sphere for pressure measurement by the ruby fluorescence technique [83]. The DAC made use of a tungsten (W) gasket and pressure was applied to the cell by means of an external gas membrane. The wavelength of x-rays used in the analysis was $\lambda_{EE8105} = 0.415301$ Å.

Example measured x-ray powder diffraction profiles of BiTe are shown in figure 8.1. BiTe adopts the layered phase-I structure at ambient conditions and transforms to phase II as the pressure is increased. On further increase, the BiTe transforms to the cubic phase, with a few additional peaks from the minority phase III visible as the transition is underway. At the highest pressure attained here, 21.9 GPa, the sample is in the cubic phase. These phases are repeated on subsequent pressure decrease, with the exception of phase III which is not observed.

All recorded diffraction profiles of BiTe included very weak peaks that were not due to any of the main sample phases discussed in this chapter. These weak peaks appear at similar positions to those observed in Bi_4Te_3 and are likely from the same source. As discussed in detail for Bi_4Te_3 in section 7.1.1, these weak peaks do not change over the entire pressure range considered here, except to move to higher/lower diffraction angles with increasing/decreasing pressure. This suggests that the structure responsible for these peaks does not change and is not associated with any of the phases discussed in this work. Details of these peaks will be given in the following sections where appropriate but, as for Bi_4Te_3, the weak peaks observed in the BiTe diffraction profiles remain unidentified.

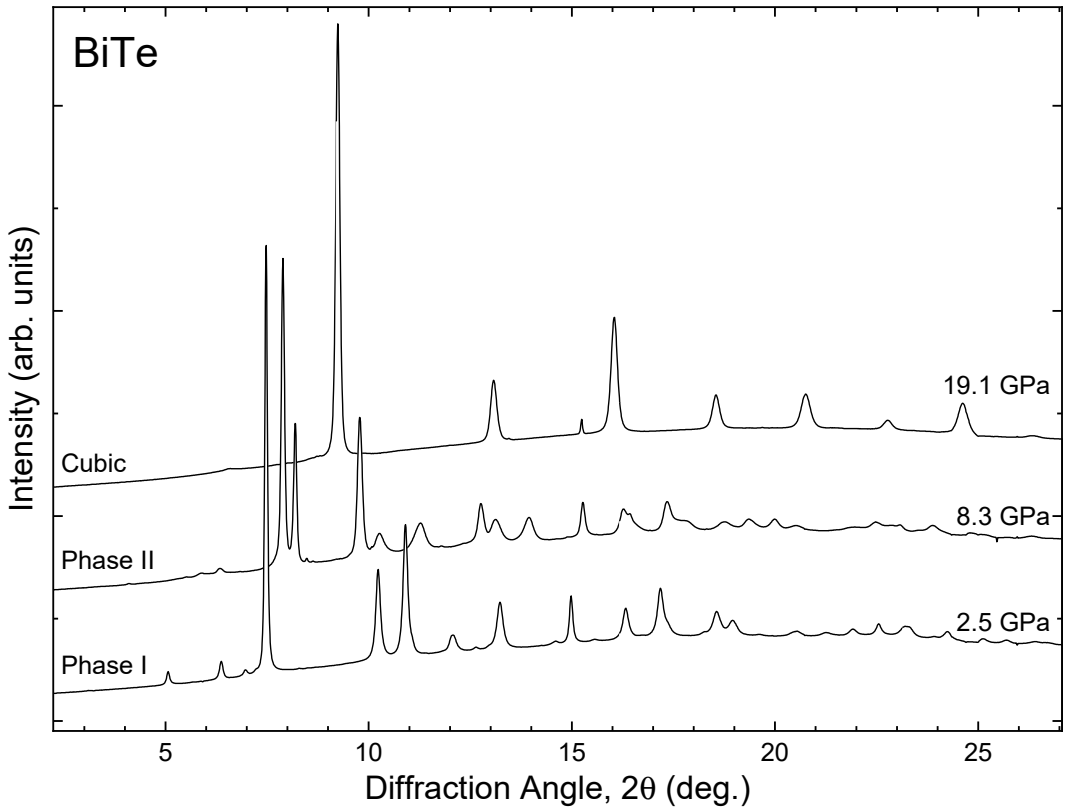

Figure 8.1 *X-ray powder diffraction profiles of BiTe, showing observed structural phases on initial pressure increase.*

8.2 Phase I: Ambient Conditions Structure

The integrated diffraction profiles show the sample to adopt a layered structure at ambient pressure (illustrated in figure 8.2), in keeping with the structural trends in the $(Bi_2)_m(Bi_2Te_3)_n$ series. It is comprised of two five-atom Bi_2Te_3 blocks and one two-atom Bi_2 block stacked alternately along the c axis. The trigonal structure can be described by the space group $P\bar{3}m1$, with six formula units per unit cell and six atomic sites within the structure. In keeping with the existing 3D model published by Yamana *et al.*, these sites are denoted by the labels Te1, Bi1, Te2, Bi2, Te3 and Bi3 [60]. Each site has x, y coordinates that are fixed by symmetry and a free z coordinate (these are listed in table 8.2, on page 166).

Figure 8.2 also shows a schematic view of the structure, illustrating the stacking of the five-atom Bi_2Te_3 and two-atom Bi_2 blocks. The thicknesses (t_5 and t_2) of these blocks, along with the distance between them (d_{5-2} and d_{5-5}) are indicated. These values can be determined from the refined z coordinates of the six atomic sites as in equations 8.1–8.4, where c is the c lattice parameter and z_{Bi1} is the z

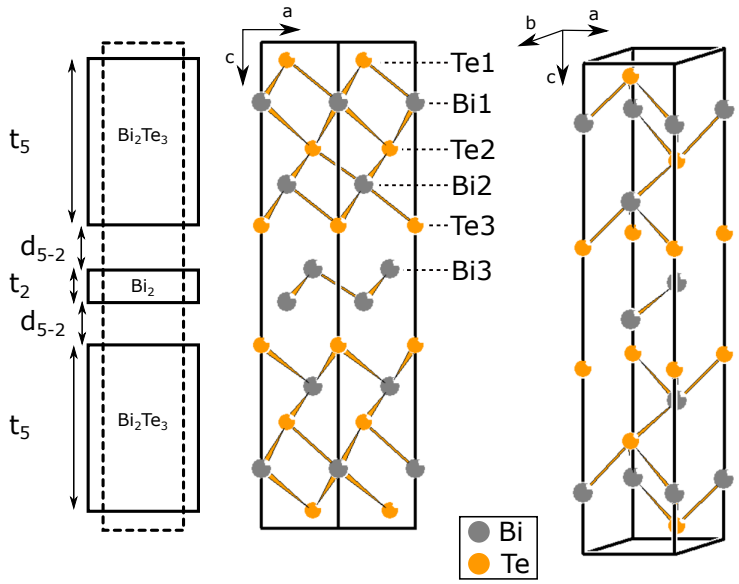

Figure 8.2 *Structure of phase I of BiTe as adopted at ambient conditions. The crystal structure indicates the atoms included in the structural Rietveld refinements and their labels. Also shown is a schematic illustrating the stacking sequence of two Bi_2Te_3 blocks and one Bi_2 block that makes up this structure. Distance between five-atom blocks, d_{5-5}, not shown.*

coordinate of atom Bi1, and so on.

$$t_5 = c\,[z_{Te3} - z_{Te1}] \tag{8.1}$$

$$t_2 = c\,[1 - 2z_{Bi3}] \tag{8.2}$$

$$d_{5-2} = c\,[z_{Bi3} - z_{Te3}] \tag{8.3}$$

$$d_{5-5} = c\,[2z_{Te1}] \tag{8.4}$$

The structure of BiTe under ambient conditions has been previously reported in several works. Yamana *et al.* in 1979 [60] measured x-ray diffraction data and refined the parameters of the structural model illustrated in figure 8.2. They began with the stacking of layers of bismuth and tellurium, as described by Imamov & Semiletov [25], with all atomic layers separated by equal distances. Their structural refinement yielded the z coordinates for all six atomic sites in the structure, along with the a and c lattice parameters. Their refinement assumed no exchange of atoms between the layers, and no vacancies or mixed occupancy of atomic sites. As such, their model represents an idealised structure, with the

compositions of the five- and two-atom blocks as Bi_2Te_3 and Bi_2, respectively.

The model described by Yamana *et al.* follows the 'three-dimensional' (3D) interpretation of the $(Bi_2)_m(Bi_2Te_3)_n$ series which describes the ambient-pressure structures in terms of Bi_2Te_3 and Bi_2 blocks stacked along the c axis [26]. More recent work [24] on the Bi-Te series by Bos *et al.* has, however, suggested that such 'three-dimensional' (3D) structural models do not fully capture the details of certain members of the series. They suggest an alternative description which makes use of a smaller, average unit cell ($a \sim 4.4$ Å and $c \sim 6.0$ Å) which is modulated along the direction of the c axis by a modulation vector, $\vec{q} = \gamma[001]^*$.

By following the approach reported by Lind & Lidin [29] for the $(Bi_2)_m(Bi_2Se_3)_n$ series, they indexed electron diffraction and x-ray powder diffraction (XRPD) data for several members of the Bi-Te series. Lattice constants and modulation vector magnitudes were determined from 'four-dimensional' (4D) le Bail fits to measured XRPD data (with '4D' describing three spatial dimensions plus an additional one dimension describing the modulation).

Bos *et al.* note that members of the series for which the magnitude of the modulation, γ, is rational can be fully described by a 3D structural model. As these structures exhibit a commensurate modulation, the structure can be equivalently described using the 4D modulated model or a commensurate 3D superstructure. This is the case for Bi_2Te_3 ($\gamma = 6/5$), Bi_4Te_3 ($\gamma = 9/7$), Bi_2Te ($\gamma = 4/3$) and Bi ($\gamma = 3/2$). BiTe, however, is reported by Bos *et al.* to be incommensurately modulated ($\gamma = 1.2563(1)$) and, as such, can only be approximated by the 3D structure described above.

In this work, we have analysed our BiTe high-pressure x-ray powder diffraction data using both methods: 3D Rietveld refinements using the layered structural model of Yamana *et al.* [60], and 4D le Bail fits using the modulated substructure as described by Bos *et al.* [24]. The 3D analysis allows us to directly compare the behaviour of the layers in this approximation to the BiTe structure to the structures of Bi_2Te and Bi_4Te_3 (both of which can be fully described with 3D, non-modulated structures). This also allows us to see the deficiencies in this model, and compare it to the more appropriate 4D modulated structure. As our XRPD data was not of sufficient quality to determine the full details of the 4D structure from scratch, we performed le Bail fits to the data to extract the lattice parameters and modulation vector magnitudes (γ), as done by Bos *et al.*

8.2.1 BiTe 3D Rietveld Refinements

X-ray powder diffraction data from BiTe at ambient conditions was recorded with a BiTe sample held within a diamond anvil cell (DAC). No pressure-transmitting medium or pressure calibrant was included, as the DAC was used simply as a sample holder for this single measurement at ambient pressure. Unfortunately, due to a misalignment of the sample, the x-ray beam clipped the edge of the tungsten (W) gasket. This resulted in strong diffraction peaks from the tungsten being present in the BiTe ambient-pressure profile. This profile was refined using Jana 2006 [91] including two structural phases: body-centred cubic (bcc) tungsten and phase I of BiTe.

The BiTe structure model was based on that reported by Yamana *et al.* [60] and is illustrated in figure 8.2. The six free atomic positions are as defined in figure 8.2, with the labels chosen to match the labels used by Yamana *et al.* The occupancies of these atomic sites were initially fixed at their idealised values with no mixed-occupancy sites.

The two-phase refinement fitted well to the observed profile with an R-value of $wR_p = 0.75\%$. The refinement made use of a twelfth-order Chebyshev polynomial background and Pseudo-Voigt peak shapes with widths defined by the anisotropic strain broadening tensor. Inclusion of this anisotropic broadening improved the fit, resulting in an approximate 10% reduction in the R-value when compared to non-anisotropically-broadened peaks. The refined tungsten lattice parameter was $a_W = 3.1650(1)$ Å, in good agreement with literature values [133]. The refined BiTe lattice parameters at ambient pressure are compared to the values reported by Yamana *et al.* in table 8.1.

$a = 4.423(2)$ Å	$c = 24.002(6)$ Å	Yamana *et al.* [60]
$a = 4.4207(6)$ Å	$c = 24.097(6)$ Å	this work

Table 8.1 *Comparison of refined and published lattice parameters of phase I BiTe at ambient conditions.*

The published and refined lattice parameters do show some disagreement, with the a and c values determined in this work 0.05% smaller and 0.4% larger than those reported by Yamana *et al.*, respectively. Such Slight differences are not surprising given the differing nature of the samples studied in each experiment, but the c-lattice parameter values show a greater relative difference. As the

Atom	x	y	z	
Te1	1/3	2/3	0.043(3)	
Bi1	0	0	0.128(2)	
Te2	2/3	1/3	0.224(2)	This work
Bi2	1/3	2/3	0.290(2)	
Te3	0	0	0.373(4)	
Bi3	2/3	1/3	0.464(2)	
Te1	1/3	2/3	0.0552(3)	
Bi1	0	0	0.1242(3)	
Te2	2/3	1/3	0.2149(5)	Yamana *et al.* [60]
Bi2	1/3	2/3	0.2908(3)	
Te3	0	0	0.3687(6)	
Bi3	2/3	1/3	0.4575(3)	

Table 8.2 *Refined atomic positions for the phase-I structure of BiTe at ambient pressure.*

approximated nature of the 3D model of phase-I Bi-Te only appears in the structural details along the c-axis, it is not surprising to find that refinements utilising this approximation struggle to consistently measure the value of c. Use of this approximation does, however, allow us to fully refine the atomic structure of phase I. The refined atomic positions are summarised in table 8.2. All atomic x and y coordinates are defined by symmetry but there are six free z coordinates that are included in the refinement. Again the values refined in this work are in broad agreement with those of Yamana *et al.* but not within uncertainty.

There are 5 high-pressure profiles available (2 at the same pressure) for phase I of BiTe, recorded at pressures ranging from 2.5–5.3 GPa. As the sample was correctly aligned during the high-pressure data collection, these profiles are free from any tungsten peaks. An example refinement is given in figure 8.3, which shows a Rietveld refinement using the 3D model of BiTe at 2.5 GPa. This refinement agrees well with the measured profile, with an R-value of $wR_p = 1.21\%$.

As for the ambient-pressure refinement, all high-pressure refinements make use of Pseudo-Voigt peak shapes with anisotropic strain broadening. The atomic occupancies are fixed at their idealised values and the atomic displacement parameters are also fixed. Attempts were made to refine the site occupation factors, with constraints in place to maintain overall BiTe stoichiometry. These attempts were unsuccessful, as refining the SOFs would lead to several signifi-

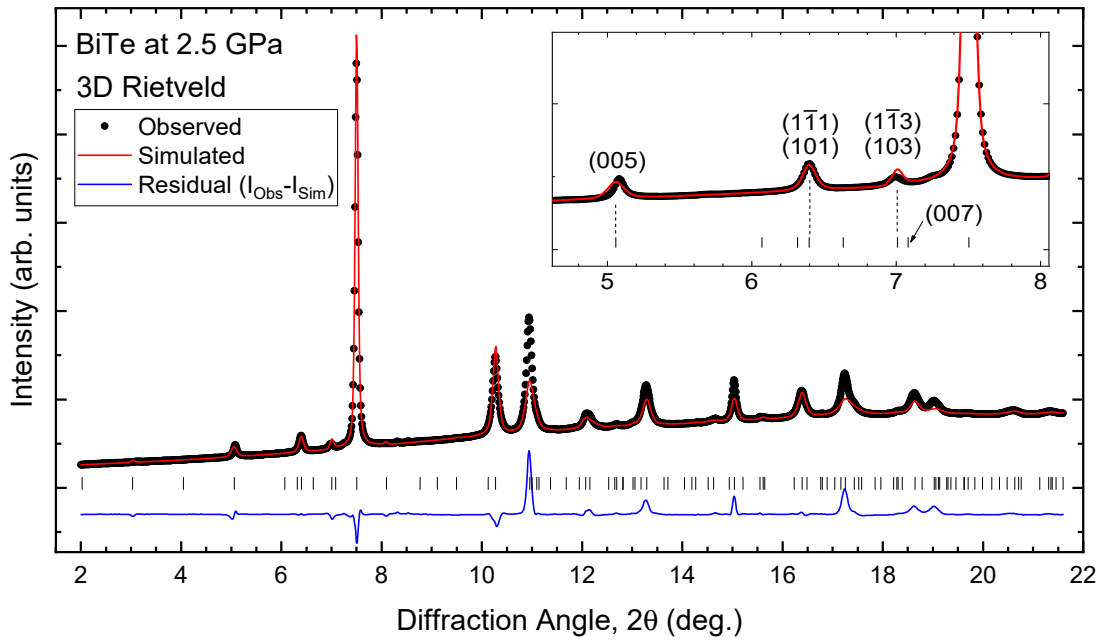

Figure 8.3 *Rietveld refinement of BiTe at 2.5 GPa, where it adopts the phase-I structure. Inset highlights the fit to the weak peaks, with Miller indices indicated. There are subtle misalignments to these observed weak peaks, in particular the (005) reflection, as can be seen in the inset and the sinusoidal feature in the residual at the position of the (005) peak.*

cantly negative atomic occupancies ($\sim -10\%$). Fixing any of these occupancies at zero would allow another to become unphysically negative, all with no significant improvement in the refinement R-value. As such, the Rietveld refinements of BiTe phase I were performed with fixed SOFs, describing idealised layer compositions.

The results of these refinements are presented in figure 8.4, which shows the refined lattice parameters (a & c), unit cell volume and ratio of lattice parameters (c/a) as a function of pressure. The lattice parameters exhibit a smooth decrease with increasing pressure. The differences between the refined and previously reported [60] lattice parameters at ambient pressure, as described in table 8.2, can be clearly seen in the plot. The unit cell volume data is fitted with a Murnaghan equation of state [121], resulting in fitted values for unit cell volume at zero applied pressure, $V_0 = 407.90(29)$ Å^3, bulk modulus at zero pressure, $B_0 = 39.8(8)$ GPa, and first derivative of this bulk modulus, $B_0' = 4.1(3)$.

Figure 8.4 also shows the c/a ratio plotted as a function of pressure which appears to exhibit a minimum below 2.5 GPa. This behaviour is similar to the other members of the $(Bi_2)_m(Bi_2Te_3)_n$ series as seen in this work (in Bi_2Te and Bi_4Te_3) and previously reported in Bi_2Te_3 [47]. All of these observations suggest that this

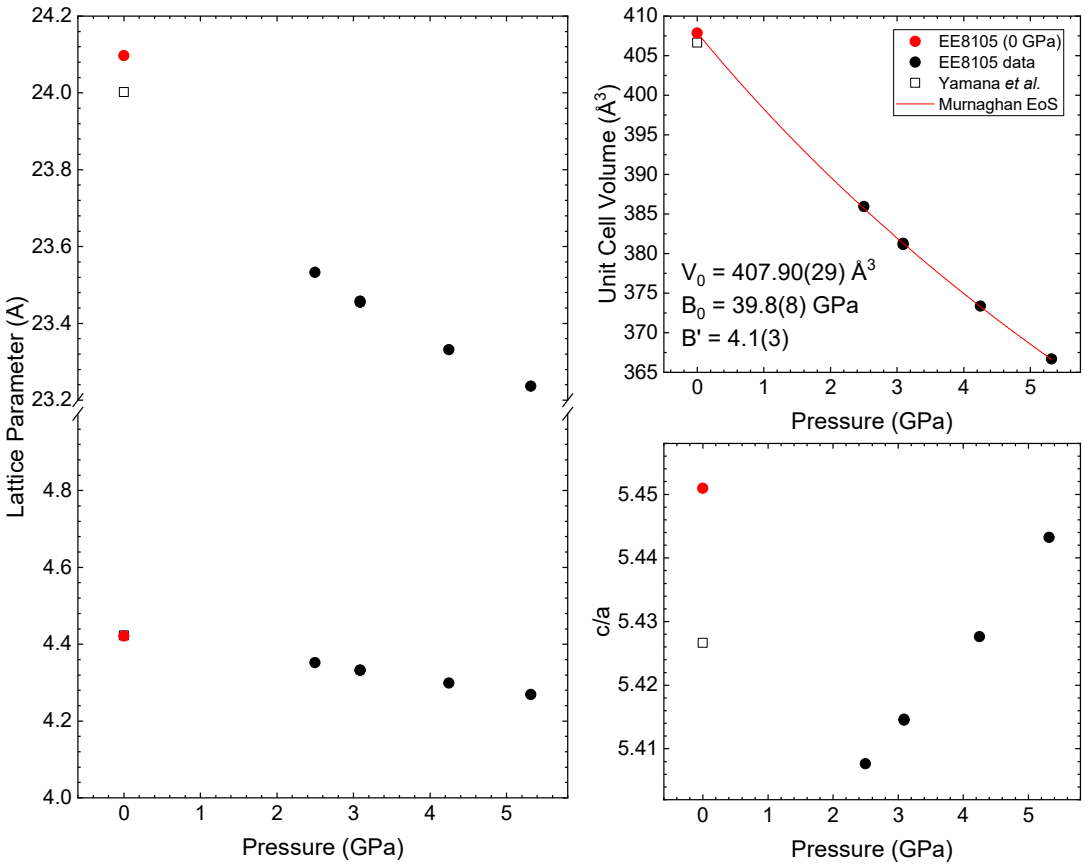

Figure 8.4 *Refined lattice parameters, unit cell volume and lattice parameter ratios for phase I of BiTe under pressure. Error bars have been omitted for clarity where they are on the same scale as the symbol size. Also plotted are previously reported ambient-pressure values [60]; open squares.*

structural anomaly is a common feature of phase I of this series under pressure.

The refined atomic positions (z coordinates) are shown in figure 8.5. The high-pressure data shows consistent values between 2.5–5.3 GPa, with the atomic positions remaining constant over the pressure range. The positions refined from the ambient-pressure profile do show some disagreement with the constant values observed in the high-pressure data, most notably in the coordinates of atoms Bi1, Te2 and Bi3. These differences are on the order of 2-3 times the uncertainties; given the consistency of the values from the high-pressure data such a level of disagreement is surprising. This disagreement may be due to the strong tungsten contaminant peaks present in the ambient-pressure diffraction profile causing slight issues with the Rietveld fit.

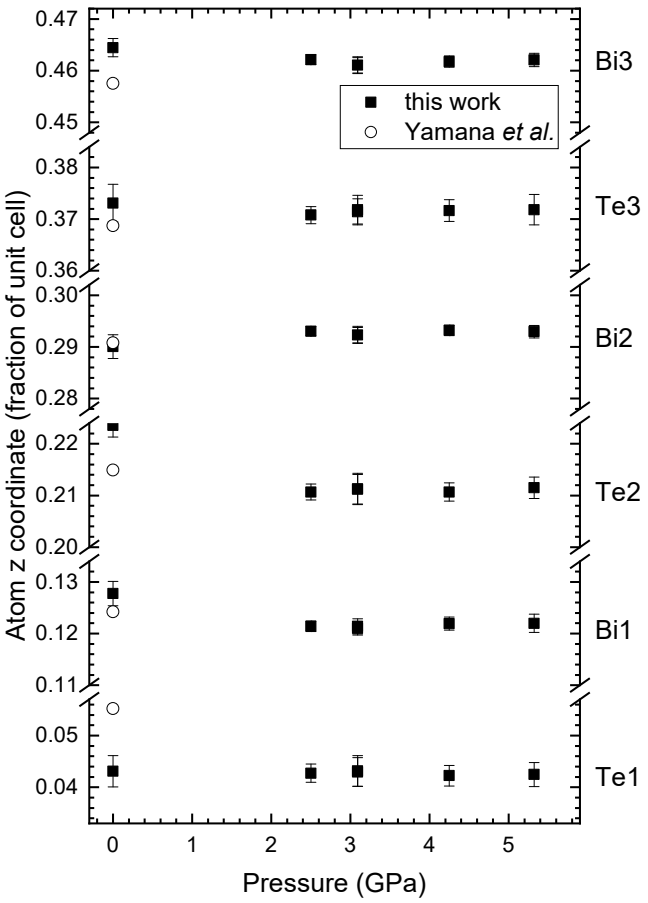

Figure 8.5 *Refined atomic coordinates for phase I of BiTe using th 3D layered model described by Yamana et al. [60]. Published values from Yamana et al. are included for comparison.*

The thicknesses of the two-atom Bi_2 and five-atom Bi_2Te_3 blocks (t_2 and t_5, respectively), the distance between them (d_{5-2}) and the distance between the five-atom layers (d_{5-5}), as calculated using equations 8.1–8.4, are shown in figure 8.6. At ambient conditions, there are significant differences between the refined values and those of the published structure. While the distance between the blocks appears in good agreement, the refined thickness of the five-atom layer is larger by approximately 0.5 Å ($\sim 6\%$), and the refined thickness of the two-atom layer is smaller by approximately 0.35 Å ($\sim 17\%$). The largest difference is in the distance between the five-atom layers, which has a refined value that is 0.57 Å ($\sim$21%) smaller than the published value.

As the pressure is increased, the refined inter-layer distances reduce slightly as the blocks move closer together, with the thickness of the five-atom block simultaneously reducing. The thickness of the two-atom block, however, is observed to increase as the pressure increases. This is likely due to a

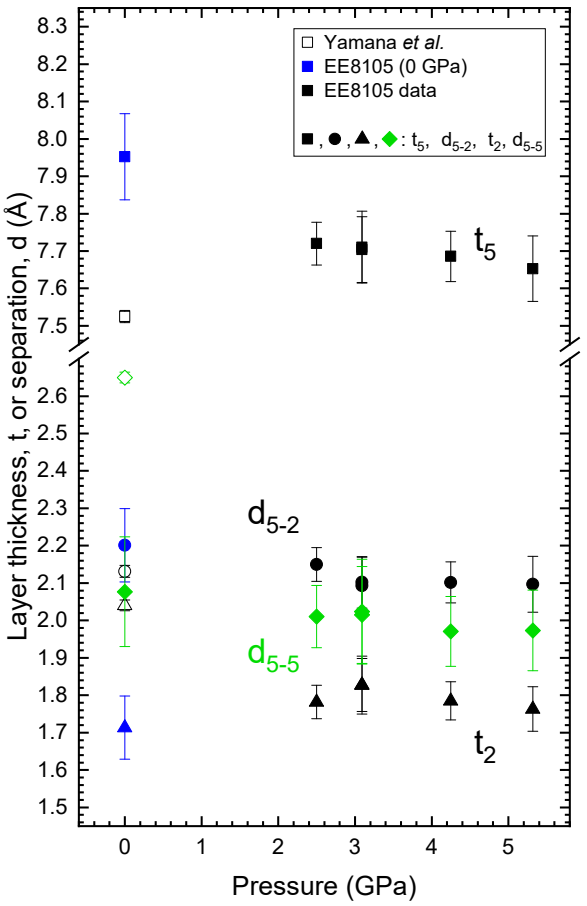

Figure 8.6 *Thicknesses of and distances between the two-atom and five-atom atomic layers in phase I of BiTe as obtained from 3D Rietveld refinements. Atom labels are defined as in figure 8.2 and published values from Yamana et al. at ambient pressure are included for comparison [60]*

strengthening of the interaction between the two-atom layer and the five-atom layers surrounding it which effectively stretches the two-atom layer along the *c*-axis direction. This change in interaction between different layers shows a gradual shift in the structure as BiTe approaches the transition to phase II.

8.2.2 BiTe 4D le Bail Fits

While the 3D model provides a reasonable fit to the observed profile, there are some slight discrepancies that suggest there may be a more appropriate structural description. As illustrated in the inset of figure 8.3, the 3D model fails to correctly fit some of the weak peaks, in particular the (005) reflection. The slight offset between the predicted and measured position of this reflection suggests that the

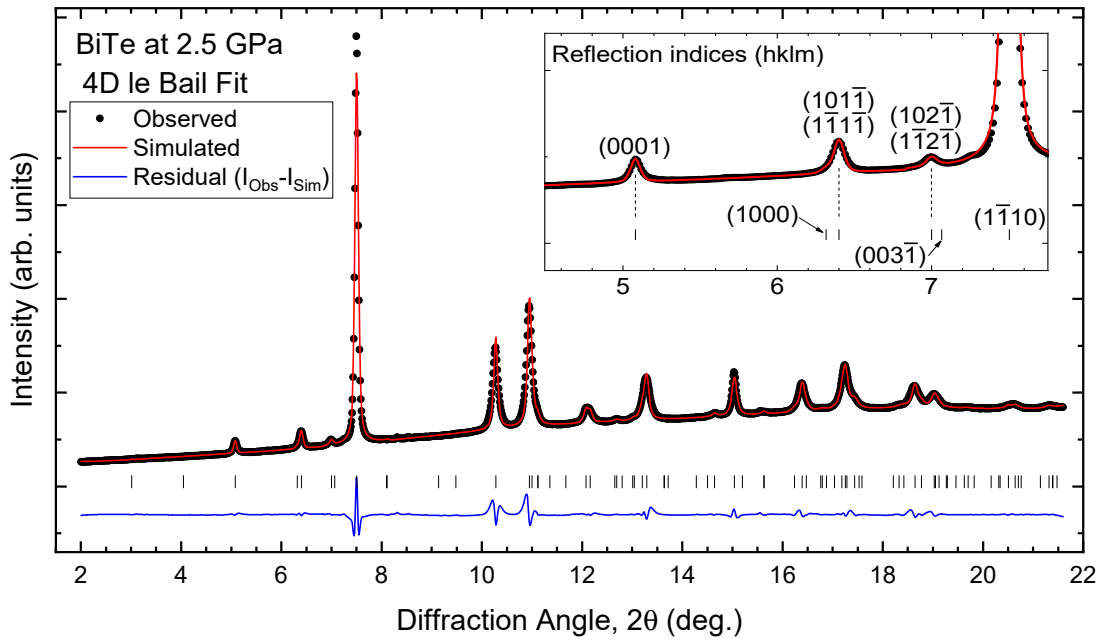

Figure 8.7 *Le Bail fit of BiTe at 2.5 GPa using the modulated structure described by Bos et al. [24]. Inset illustrates the good fit to the weak satellite reflections ($m \neq 0$), which is a significant improvement over the approximated 3D model.*

3D model is not fully describing some aspect of the structure. The fact that this reflection has a large l Miller index and h & k indices of zero, suggests that the feature to be addressed lies along the c axis.

The 3D structural model, with its large aspect ratio and long c axis is essentially a supercell approximation comprised of Bi_2Te_3 and Bi_2 building blocks. This large supercell approximates the true structure, which can be better described with a modulated subcell [24], with the observed weak peaks as satellite reflections resulting from this structural modulation. Such a '4D' modulated structure has been described by Bos *et al.* and is used here to perform le Bail fits to the measured BiTe profiles.

An example le Bail fit to phase I of BiTe at 2.5 GPa is shown in figure 8.7. Overall, the fit is of similar quality to that of the 3D model shown in figure 8.3. However, on closer inspection the finer details of the profile are much better described by the 4D model as illustrated in the inset to the figure. The weak peaks that were slightly offset from the positions predicted by the 3D approximant model are now correctly fitted. This can be seen, in particular, for the weak peak at 5.1° which is poorly fitted by the (005) reflection of the 3D model, but is well fitted by the (0001) satellite reflection of the 4D modulated model.

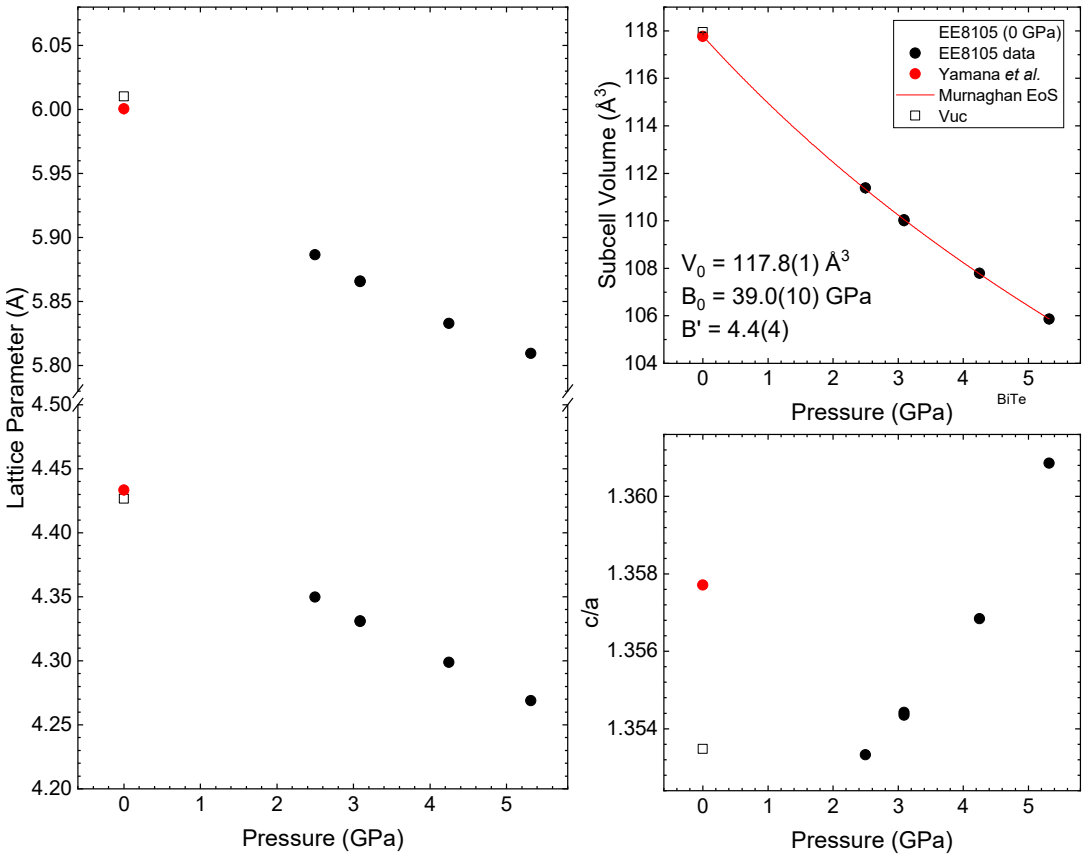

Figure 8.8 *Refined lattice parameters and subcell volume from the 4D le Bail fits using the modulated structure of BiTe. Values reported by Bos et al. at ambient conditions are plotted for comparison.*

As the 4D model has been used to perform le Bail fits to the measured profiles, only the lattice parameters and modulation vector magnitude (γ, from the vector $\vec{q} = \gamma[001]^*$) can be obtained from the data. The refined lattice parameters, volume of the subcell and c/a ratio as a function of pressure are plotted in figure 8.11.

The subcell volume ($a \times a \times c$) can be fitted with the Murnaghan equation of state, giving fitted cell volume at zero applied pressure, $V_0 = 117.8(1)$ Å^3, bulk modulus at zero pressure, $B_0 = 39.0(10)$ GPa, and first derivative of bulk modulus, $B' = 4.4(4)$. These B_0 and B' values agree within uncertainty with those obtained from the 3D model volume data. The c/a ratio appears to exhibit a minimum somewhere below 2.5 GPa, as is the case when using the 3D model approximation. The refined magnitude of the modulation vector, γ, is plotted in figure 8.9. The high-pressure data indicates a constant value over the pressure

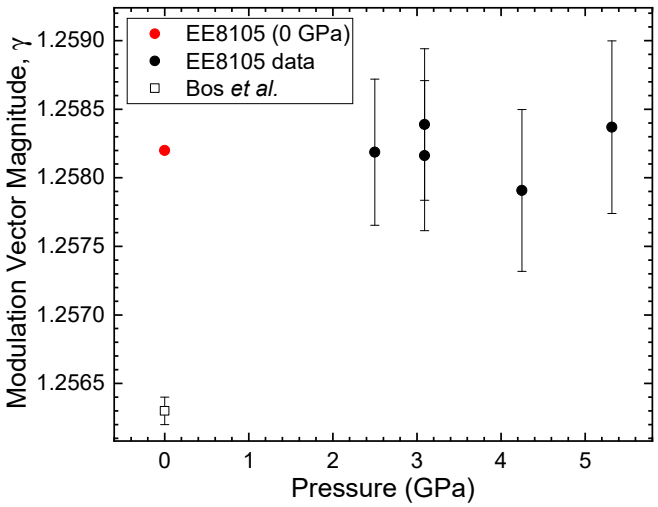

Figure 8.9 *Refined magnitude of the modulation vector, $\vec{q} = \gamma[001]$, for the 4D le Bail fitting of BiTe. Also plotted is the ambient-pressure value reported by Bos et al. [24]. Note that the ambient-pressure (0 GPa) BiTe le Bail fit required the value of γ to be fixed.*

range. The ambient-pressure refinement had this parameter fixed at this value, as free refinement would result in a fit that did not describe the satellite peak properly. This poor fit is likely due to the large tungsten peaks present in the profile throwing the le Bail fit off.

Conclusion

Phase I of BiTe provides an opportunity to directly compare the 3D and 4D structural models. We find that the a lattice parameters obtained from both the 3D Rietveld and 4D le Bail fits agree within uncertainty, as do the values obtained from fitting of the equation of state. Both models result in good fits to the observed data, but the 4D modulated structure fully describes the weak satellite peaks, which the 3D approximation does not. These weak peaks correspond to satellite reflections arising from the modulation of the 4D structure and so the failure of the 3D model to accurately reproduce these peaks is not surprising. As an approximation, the 3D model makes a good attempt to describe these weak peaks through reflections with large l Miller indices, utilising the long c-axis of the approximation. However, there are clear discrepancies in the simulated peak positions, suggesting that a more appropriate description of the structure is indeed possible.

The 4D model is more appropriate and allows for an easier description of the

phase-I structures of the Bi-Te series as a whole [24] but the 3D model can be useful, providing a starting point for electronic structure calculations, for example through density functional theory.

8.3 Phase II: Unidentified Structure

On pressure increase from the ambient-pressure phase, BiTe transforms to its first high-pressure phase (*phase II*) between 6–7 GPa. Peaks due to phase II appear in the diffraction profiles at 6.1 GPa, indicating a brief overlap with phase I. The peaks due to phase I have disappeared in the next recorded profile, at 7.4 GPa. Phase II is then the dominant phase up to around 15 GPa, with ingrowth of the cubic phase starting at around 14 GPa. Phase II of BiTe produces a diffraction profile very similar to that of phase II of all other compositions investigated in this work, suggesting a shared phase-II structure. Figure 8.10 illustrates the similarity between phase II of BiTe and the first high-pressure phase of Bi_2Te_3.

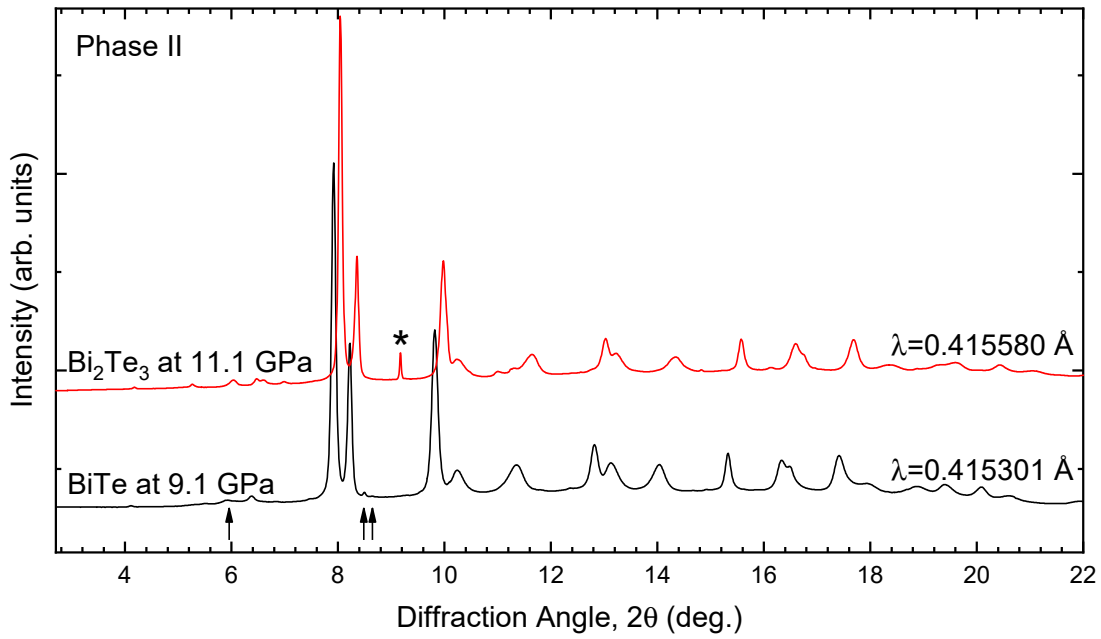

Figure 8.10 *X-ray powder diffraction profiles of BiTe (bottom) and Bi_2Te_3 (top) illustrating the close resemblance between both phases. The presence of weak, unidentified peaks in the BiTe profile are indicated with arrows; these are the same weak peaks as observed in Bi_4Te_3 and discussed in section 7.1.1. The Bi_2Te_3 profile includes a peak (*) due to the solidified nitrogen pressure-transmitting medium.*

8.4 Phase III: Observed Peaks

As in Bi_4Te_3, several new peaks appear in the BiTe diffraction profiles on pressure increase as the sample is transforming from phase II to the cubic phase. These peaks can be identified as phase-III peaks and are only visible in a few profiles over a narrow pressure range. Due to this, the structure of phase III cannot be determined, but the position of the peaks and the pressures at which they appear are consistent with observations of phase-III peaks in Bi_4Te_3, in this work and others [3].

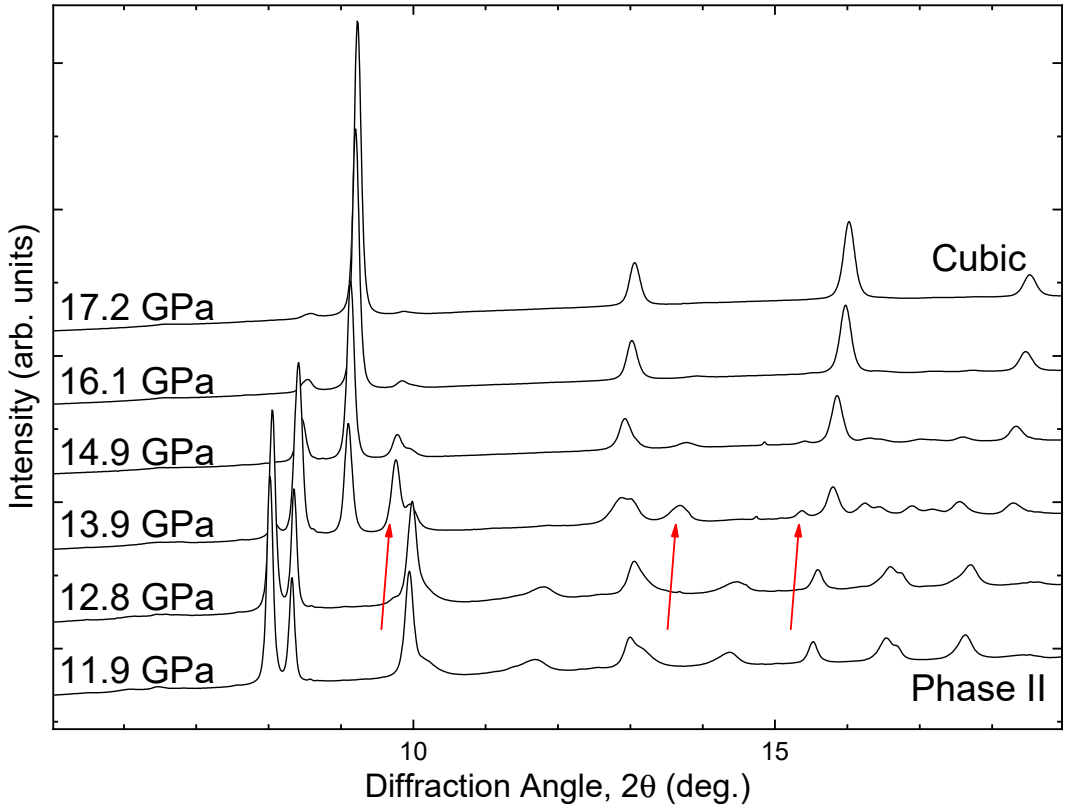

Figure 8.11 *X-ray powder diffraction profiles of BiTe on initial pressure increase showing the transition from phase II to the cubic phase. Peaks identified as 'phase-III' peaks are indicated; these are only briefly visible over a pressure range of a few GPa.*

8.5 Phase V: Cubic Structure

BiTe begins transforming to the cubic phase around 15 GPa on pressure increase and fully adopts this structure above 18 GPa, up to the maximum pressure reached here, 21.9 GPa. The structure of this cubic phase appears to be that of a fully-site disordered body-centred cubic (bcc) structure. There are no signs of any peaks which would indicate any ordering in a B2, CsCl-type structure, such as at the predicted positions of the cubic (001) and (111) which would indicate ordering, as shown in figure 8.12.

The example Rietveld fit shown in figure 8.12 provides a good fit to the observed profile, with an R-value of $wR_p = 2.28\%$. The Rietveld refinements use pseudo-Voigt peak shapes; the residual shows some discrepancies in the fit of the peak shapes, so attempts were made to reduce this. Refinements including peak shapes defined by the anisotropic broadening tensor refined equally well, with the same resulting R-values, but gave no visual improvement to the fit. As this added several refinable parameters, the simpler model of pseudo-Voigt peaks was used.

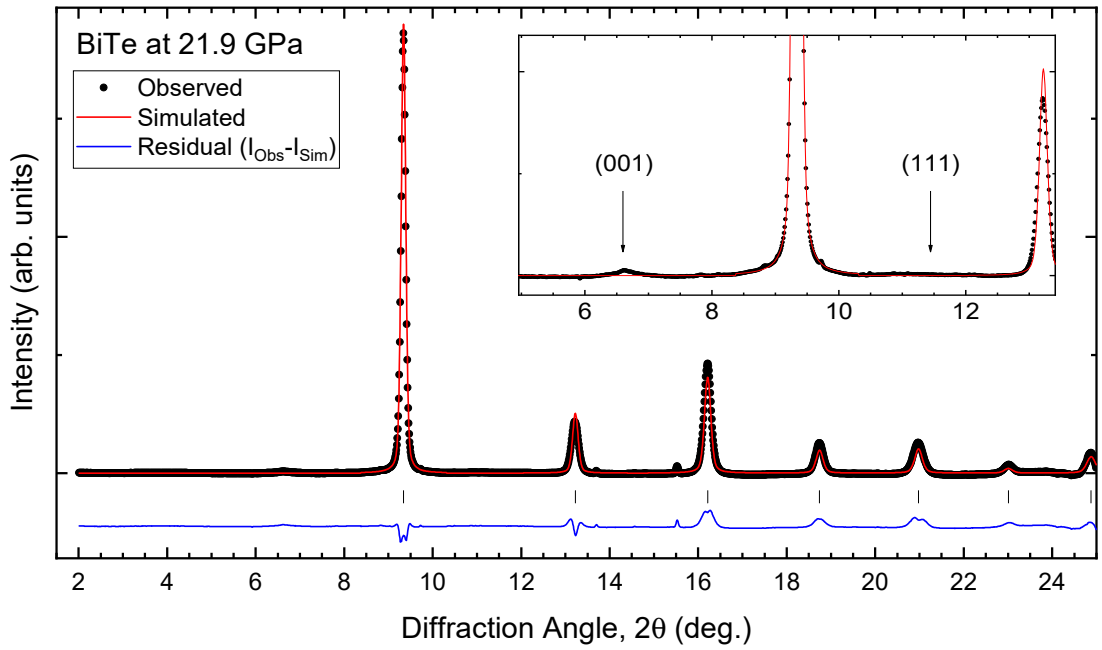

Figure 8.12 *Rietveld refinement of the cubic phase of BiTe at 21.9 GPa. The model used was a fully disordered bcc structure, with the two atoms in the unit cell occupied equally by Bi and Te. Inset shows the lack of peaks at the predicted positions of the (001) and (111) reflections, which would indicate ordering. Note the broad feature at 6.6°; this is an unidentified feature, not associated with the cubic phase.*

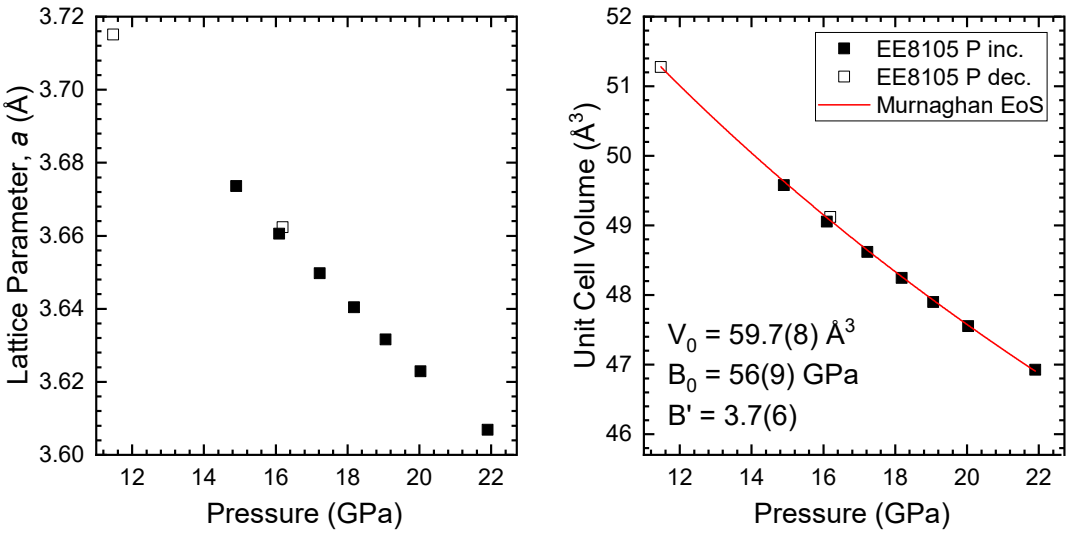

Figure 8.13 *Refined lattice parameter and unit cell volume of the cubic phase of BiTe as a function of pressure. The volume data can be fitted using a Murnaghan equation of state [121]. Error bars are on same scale as symbol size and omitted for clarity.*

A total of 9 cubic-BiTe profiles were available for refinement; 7 on pressure increase and 2 on subsequent decrease. The resulting refined lattice parameter and unit cell volumes are presented in figure 8.13. The plots show good consistency across the pressure range and on both increasing and decreasing pressure runs. Fitting the unit cell volume data with a Murnaghan equation of state [121] results in fitted values of the unit cell volume at zero applied pressure, $V_0 = 59.7(8)$ Å^3, bulk modulus at zero pressure, $B_0 = 56(9)$ GPa, and first derivative of bulk modulus, $B' = 3.7(6)$.

8.6 Phases on Pressure Decrease

On decreasing the pressure from the cubic phase, BiTe goes through several phase transitions, as illustrated in the waterfall plot, figure 8.14. The pressure was changed in larger steps than it was on initial pressure increase, leading to more sudden observed phase transitions and somewhat obscuring the pressures at which the transitions occur. Between 9.2–5.1 GPa the sample transforms from the cubic phase to a mixed phase. The next recorded profile shows the sample to have transformed to what appears to be phase II, with broadening of the diffraction peaks. Finally, at 0.3 GPa, the sample adopts another phase which appears to be an entirely new phase. Unfortunately, this phase was not investigated in detail.

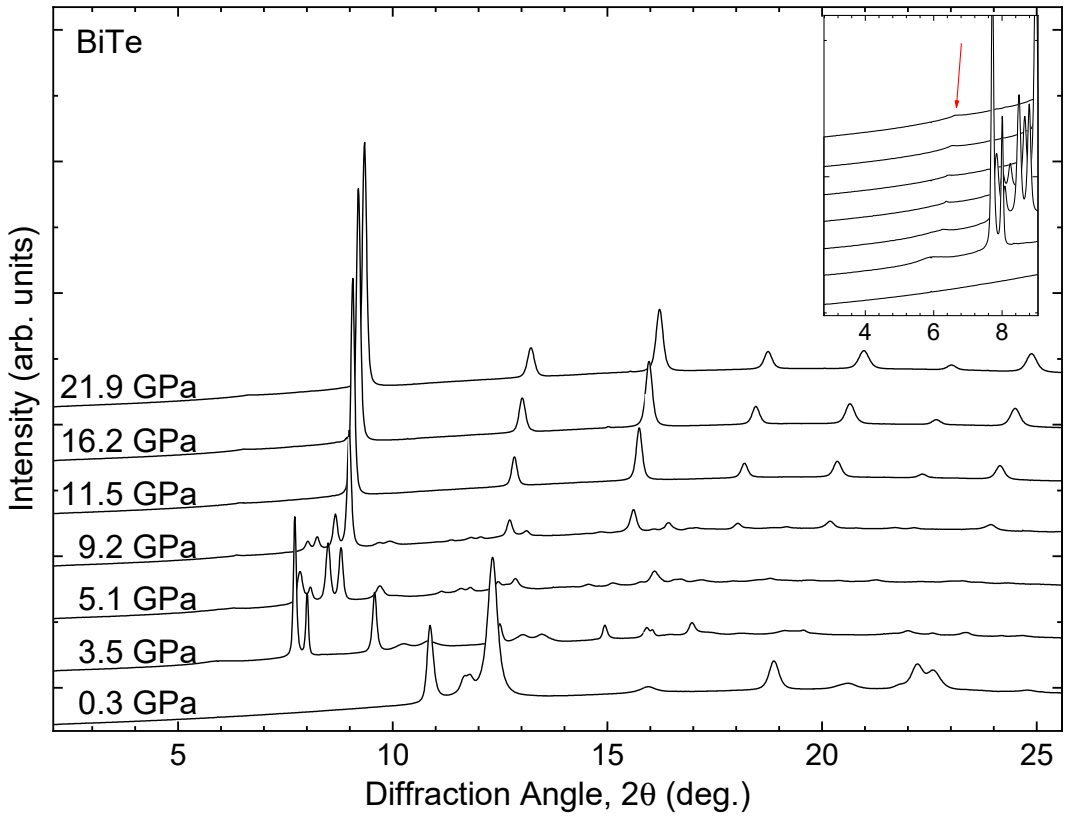

Figure 8.14 *X-ray powder diffraction profiles of BiTe recorded on pressure release. Inset indicates the position of the unidentified broad feature at around 6.5°, which remains consistent across several phase transitions. Note that the sample ends up adopting a new phase at 0.3 GPa.*

The inset in figure 8.14 indicates the position of the broad unidentified feature near 6.5°. This feature does not appear to be associated with the main phases of the sample as it remains consistent throughout several sample phase transitions. This is very similar to the unidentified peak observed in Bi_4Te_3 (see figure 7.2 and section 7.1.1). It is interesting to note that this feature is not present in the profile recorded at 0.3 GPa.

Chapter 9

Bi_4Te_5

The composition Bi_4Te_5 contains approximately 44.4% bismuth and represents the lower end of the stability range of the infinitely adaptive series ($Bi_xTe_{(1-x)}$, $0.44 \leq x \leq 0.7$) [28]. Bi_4Te_5 was investigated over two experiments, EE8105 and hs4718, using x-rays of wavelengths $\lambda_{EE8105} = 0.415301$ Å and $\lambda_{hs4718} = 0.415051$ Å. A single Bi_4Te_5 diffraction image was also recorded during experiment EE8105 (Diamond Light Source, October 2012) at ambient pressure, with the sample held in a diamond anvil cell.

Experiment hs4718 at the ESRF in February 2013, investigated a powdered sample of Bi_4Te_5 loaded in to a Merril-Basset-type diamond anvil cell with helium as a pressure-transmitting medium. X-ray powder diffraction images were recorded from this sample at pressures from 2.8 GPa up to a maximum of 21.2 GPa in approximately 1 GPa steps. No data were recorded on pressure release.

Example XRPD profiles from each of the observed phases are shown in figure 9.1. On pressure increase from ambient conditions, the sample undergoes a transition from the ambient-pressure phase I to the first high-pressure phase, phase II. Peaks from phase II appear in the measured diffraction profiles at 7.1 GPa, with the sample fully transformed from phase I to II by 8.6 GPa. Several peaks from phase III appear at 13 GPa, briefly increasing in intensity as the pressure in increased. The most intense phase-III peak persists up to a pressure of 18 GPa. Peaks due to the cubic phase appear at 15 GPa and grow in intensity, quickly becoming the dominant phase by 16 GPa and persisting up to the highest pressure attained with this sample, 21.2 GPa. Due to a failure of the gasket, no data were recorded

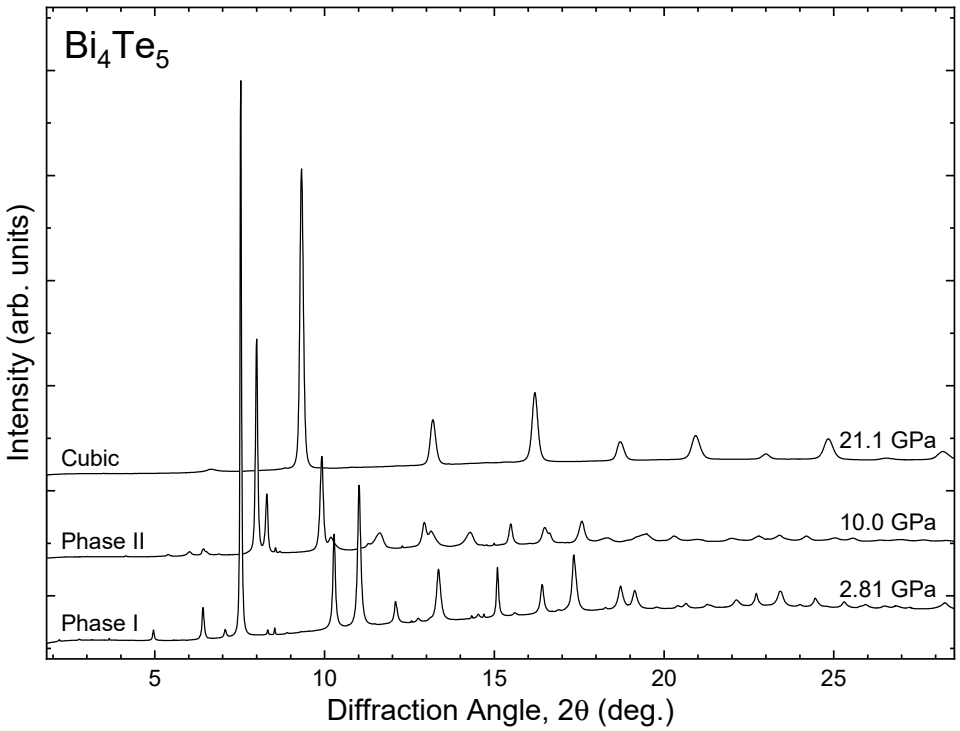

Figure 9.1 *Phases observed in XRPD profiles of Bi_4Te_5 under pressure. Data were recorded on pressure increase only. Several peaks from the unidentified phase III appear on pressurisation as the sample transforms from phase II to the cubic phase.*

on pressure decrease.

As will be illustrated in the following sections where appropriate, weak peaks are present in all of the recorded Bi_4Te_5 diffraction profiles. The positions of these peaks are identical to that of the unidentified peaks observed in Bi_4Te_3 and BiTe, which are described in detail for Bi_4Te_3 in section 7.1.1. As discussed previously, these weak peaks are not associated with the main sample phases investigated here and do not appear to change with pressure, other then moving to higher/lower diffraction angles with increasing/decreasing pressure. These weak peaks remain an unidentified feature of the compositions Bi_4Te_5, Bi_4Te_3 and BiTe.

9.1 Phase I: Ambient Conditions Structure

At ambient conditions Bi_4Te_5 adopts the ambient-pressure structure which can be approximated as a stacking of Bi_2Te_3 and Bi_2 blocks along the *c*-axis, but is better described with an average structure modulated along the *c*-axis by a vector: $\vec{q} =$

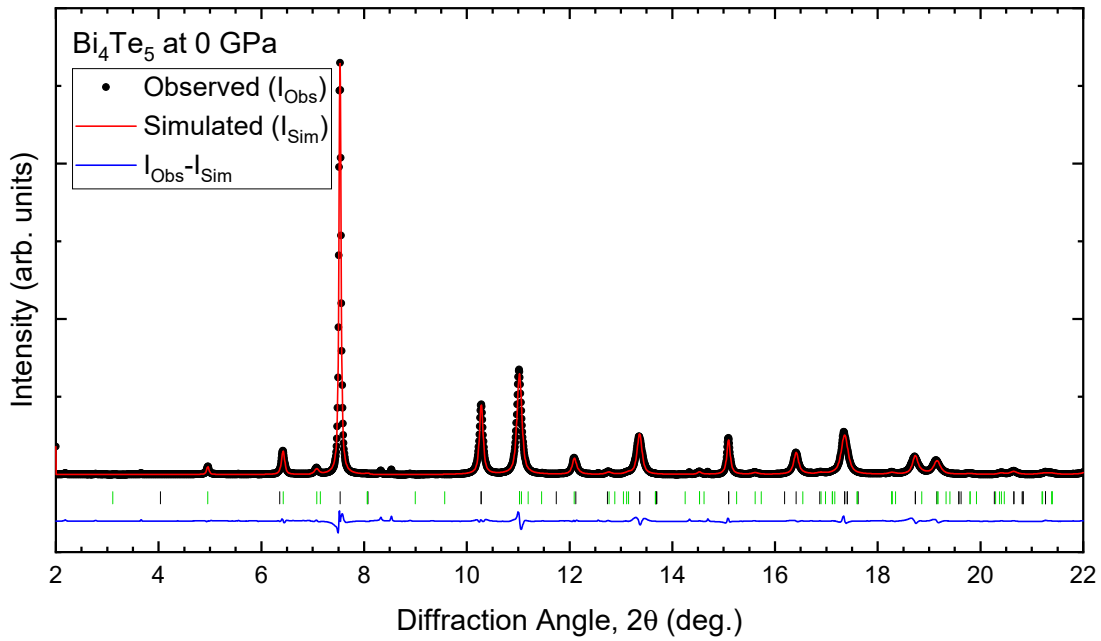

Figure 9.2 *Ambient pressure le Bail fit of Bi_4Te_5, with background Chebyschev polynomial function subtracted. Modulation reflections, (hklm) $m \neq 0$, are shown in green. $wR_p = 0.54\%$.*

$\gamma[001]^*$ [24]. As there is no established model of this averaged structure, and a full structural determination of this four-dimensional (4D) modulated structure is not feasible with the given data, we will restrict the analysis to determination of the lattice parameters and modulation vector magnitude. This can be achieved with a 4D modulated le Bail fit, performed using the refinement software, Jana2006 [91].

The ambient-pressure profile was refined with the use of pseudo-Voigt peak shapes with anisotropic strain broadening. The le Bail fit converged to good agreement with the measured profile, with an R-value of $wR_p = 0.54\%$. This ambient-pressure refinement is shown in figure 9.2. The 4D modulated structure is described by four Miller indices, $(hklm)$. Structure reflections are indicated in the figure by tick marks, with satellite reflections ($m \neq 0$, arising from the modulation of the structure) shown in green.

The structural parameters determined at ambient pressure can be directly compared to those published by Bos *et al.* in their x-ray powder diffraction study of bismuth-tellurides at ambient conditions [24]. The results of their le Bail fit for Bi_4Te_5 are compared to the results from this work in table 9.1. The lattice parameters are in good agreement, showing slight ($\sim 0.1\%$) differences. The magnitude of the modulation vector, γ, agrees within uncertainty.

a (Å)	c (Å)	γ	
4.4154(1)	6.0284(2)	1.2291(1)	Bos *et al.* [24]
4.4113(4)	6.038(1)	1.2293(9)	this work

Table 9.1 *Comparison of refined and published lattice parameters of phase I Bi_4Te_5 at ambient conditions.*

A further 7 diffraction profiles recorded of phase-I Bi_4Te_5 were available for structure refinement by le Bail fitting. All high-pressure fits were performed using anisotropically broadened Pseudo-Voigt peaks, as for the ambient-pressure profile. When fitting these high-pressure profiles, the magnitude of the modulation vector, γ, would refine to values that resulted in poorly-fitted satellite peak positions, in particular the (0001) reflection near 5°. As such, the value of γ was fixed at the ambient-pressure value reported by Bos *et al.*, $\gamma = 1.2291$ [24]. Fixing of this value resulted in well-fitted satellite peak positions and improved overall fits.

The refined lattice parameters, c/a ratio and unit cell volume are shown in figure 9.3. The c/a ratio exhibits a minimum below 3 GPa, in agreement with the structural anomaly seen in phase I of other members of the Bi-Te series. The unit cell volume data can be fitted using a Murnaghan equation of state [121] to yield a fitted unit cell volume at zero applied pressure, $V_0 = 117.2(4)$ Å^3, a bulk modulus at zero pressure, $B_0 = 38(3)$ GPa, and first derivative of this bulk modulus, $B_0' = 5.0(8)$.

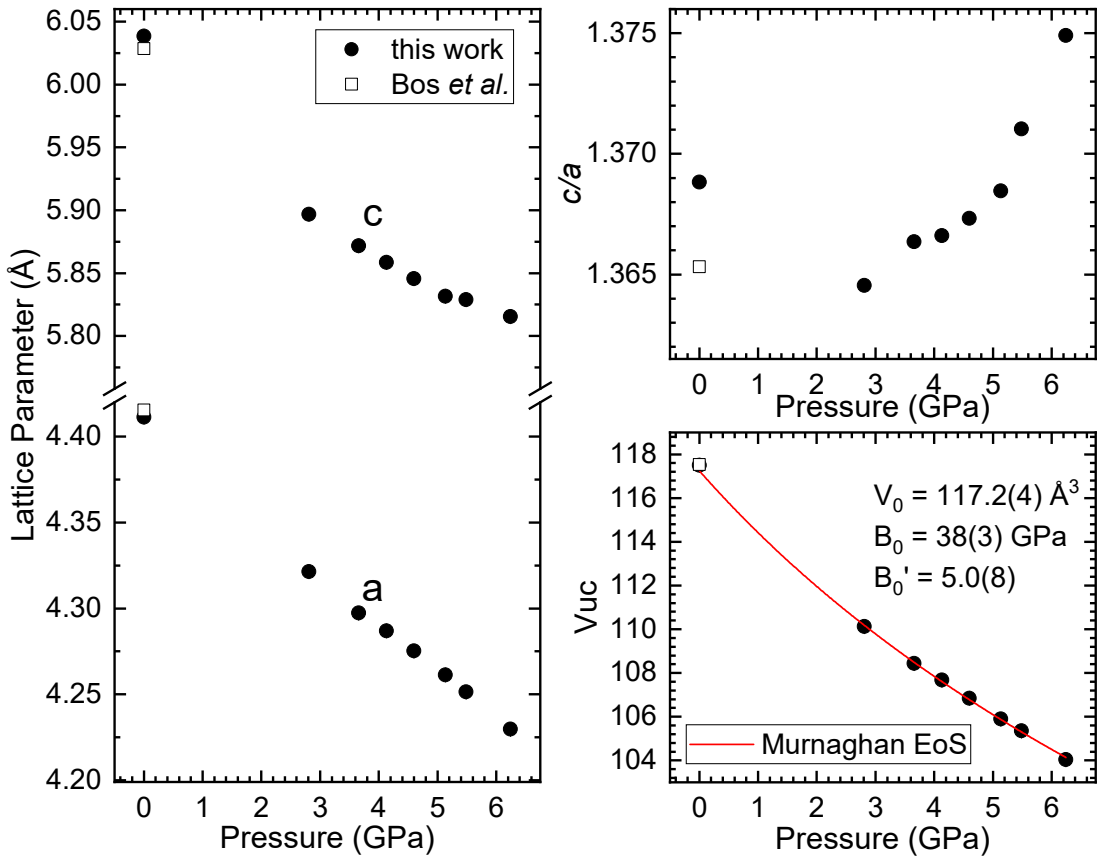

Figure 9.3 *Refined lattice parameters, c/a ratio and unit cell volume of phase I of Bi_4Te_5. Lattice parameters are plotted to same relative scale. Unit cell volume data fitted using a Murnaghan equation of state. Values published by Bos et al. included for comparison [24].*

9.2 Phase II: Unidentified Structure

On pressure increase from the ambient-pressure phase, Bi_4Te_5 adopts a high-pressure phase referred to here as *phase II*. Peaks due to phase II appear in the measured diffraction profiles at around 7.1 GPa. Phase II overlaps with the previous phase I to approximately 8.6 GPa and persists up to around 13 GPa. The diffraction profiles produced by phase II of Bi_4Te_5 are very similar to those from phase II of all other Bi-Te compositions investigated here. Figure 9.4 presents an example profile from phase II of Bi_4Te_5 and compares it with a profile from the first high-pressure phase of Bi_2Te_3. The close resemblance between the two profiles suggests a similar underlying crystal structure.

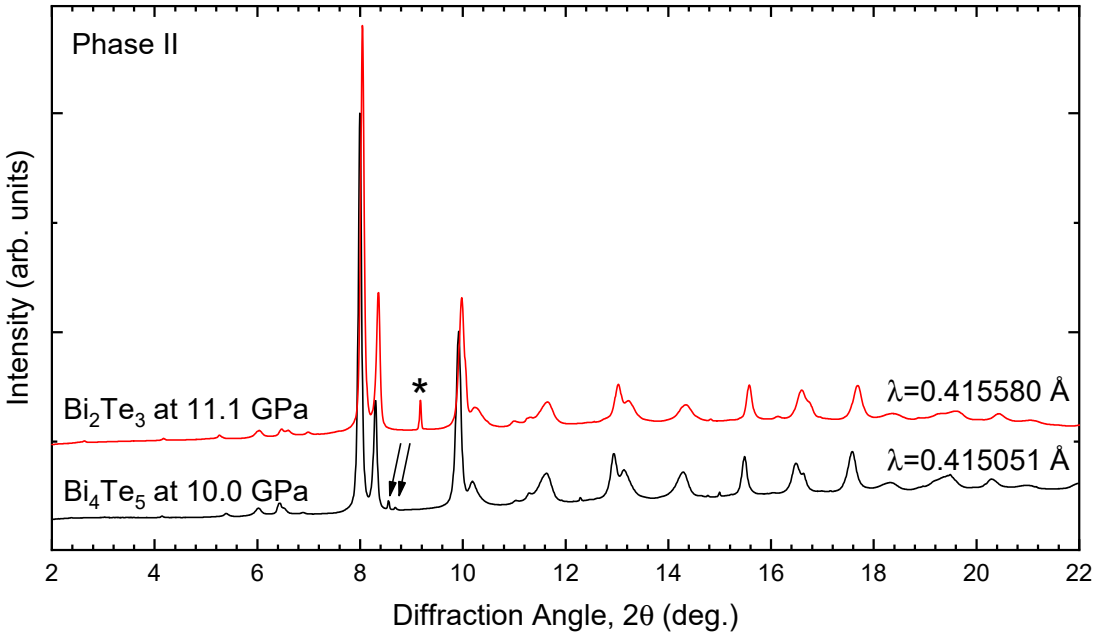

Figure 9.4 *X-ray powder diffraction profiles of Bi_4Te_5 (bottom) and Bi_2Te_3 (top) illustrating the similarity between both phases. The presence of weak, unidentified peaks in the Bi_4Te_5 profile are indicated with arrows; these are the same weak peaks as observed in Bi_4Te_3 and discussed in section 7.1.1. The Bi_2Te_3 profile includes a peak (*) due to the solidified nitrogen pressure-transmitting medium.*

9.3 Phase III: Observed Peaks

As illustrated in figure 9.5, peaks due to the unidentified phase-III structure appear over a pressure range between 13–18 GPa. The scarcity of these peaks makes determination of the phase-III structure impractical, but the positions of the peaks are consistent with the phase III observed in Bi_4Te_3 and BiTe. Phase-III peaks appear in the 13 GPa profile shown in figure 9.5 as indicated by red arrows, with an additional phase-III peak at around 8.5° that can be inferred from the increase in intensity seen at that diffraction angle, where a phase-II peak is present and reducing in intensity from lower pressures.

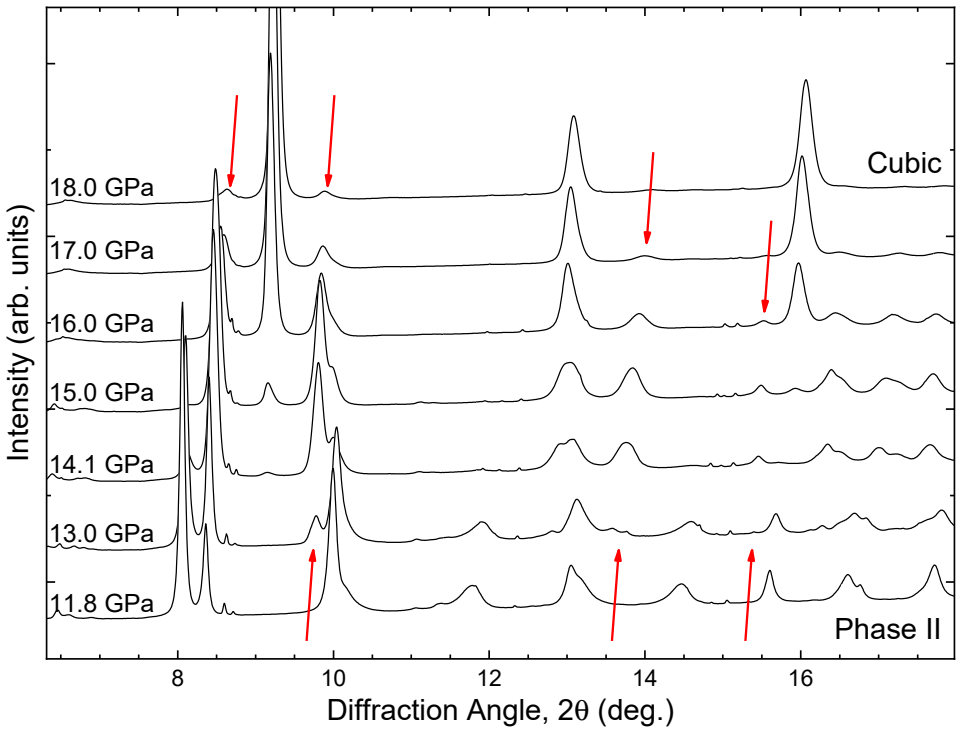

Figure 9.5 *Observed phase-III peaks of Bi_4Te_5 under compression during transition from phase II to the cubic phase. Phase-III peaks are indicated by red arrows. Note the presence of a phase-III peak around 8.5° can be inferred from the increase in intensity of the peak at that positions, which initially includes a phase-II peak i.e. the phase-II peaks have disappeared in the 16 GPa profile, but the peak at 8.5° remains strong.*

9.4 Phase V: Cubic Phase

On pressure increase, peaks belonging to the cubic phase of Bi_4Te_5 first appear at 15 GPa. The cubic phase quickly becomes the dominant phase and is the sole phase present up to 21 GPa, the highest pressure attained in this experiment. The cubic phase can be recognised as the body-centred-cubic structure ($Im\bar{3}m$, space group number 229). Measured diffraction profiles were analysed by Rietveld refinement using Jana2006; an example refinement is shown in figure 9.6. The refinement describes the profile well using anisotropically-broadened pseudo-Voigt peak shapes, resulting in an R-value of $wR_p = 5.65\%$.

Close inspection of the diffraction profiles reveals no evidence of weak peaks that would suggest the structure had undergone ordering in to a B2, CsCl-type structure, as seen in Bi_4Te_3. This is illustrated in the inset of figure 9.6 which indicates the predicted positions of cubic (100), (111) and (210) reflections which,

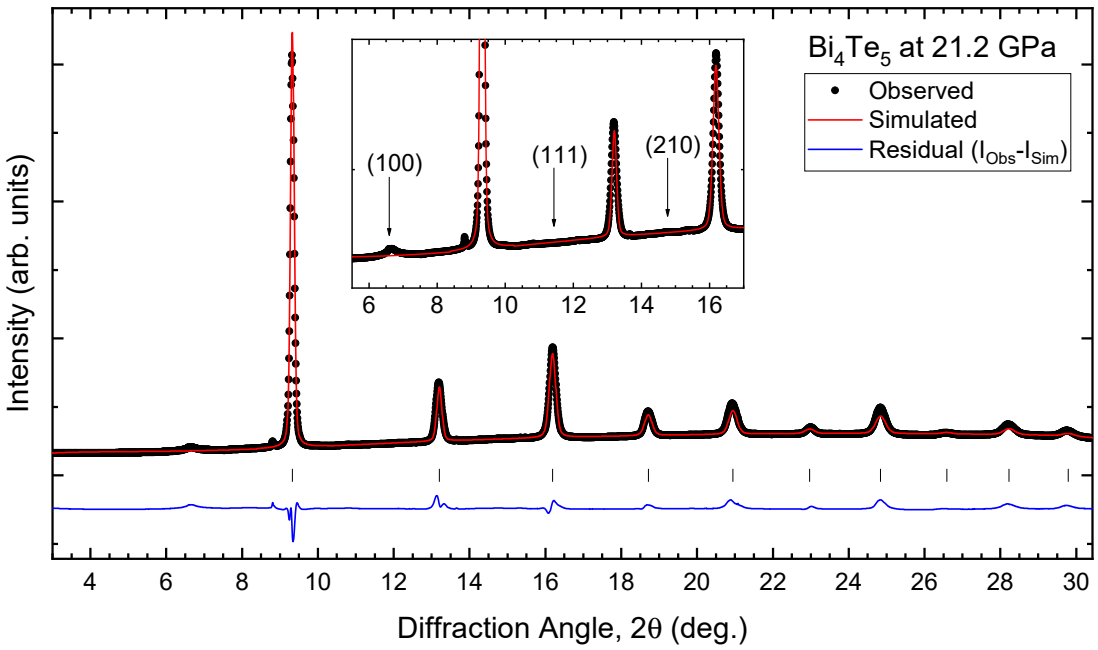

Figure 9.6 *Rietveld refinement of the cubic phase of Bi_4Te_5 at 21.2 GPa. The refinement describes the measured profile well, with an R-value of $wR_p = 5.65\%$. Inset illustrates the lack of B2, CsCl-type reflections which would indicate chemical ordering within the structure. The weak feature near the position of the (100) reflection is an unidentified peak present throughout the entire pressure range which is not associated with the cubic phase.*

if present, would indicate ordering. A weak feature is visible near the predicted position of the (100) reflection, near 6.5°. This feature is one of the unidentified peaks present in the Bi_4Te_5 diffraction profiles throughout the entire pressure range, similar to the unidentified peaks observed in Bi_4Te_3. Another of these unidentified peaks can be seen on the lower-angle side of the (101) cubic peak near 9.5°.

The refined lattice parameters and unit cell volumes of cubic-Bi_4Te_5 are plotted in figure 9.7. Attempts to fit the unit cell volume data were unsuccessful. The reason for this is unclear, but it may be due to the relatively small number of available data points over a small pressure range. Using the fitted equation of state parameters (V_0, B_0 and B_0') from the cubic phase of the closest investigated composition, BiTe, visually acceptable fits to the data can be achieved. By fixing one value at the value determined for BiTe, the fit can be made to converge with this restricted model. Fixing one of the three values at that of BiTe allows the other two values to refine and the fit to the volume data to converge. Performing this fit three times, once with each of the parameters fixed at the value found for

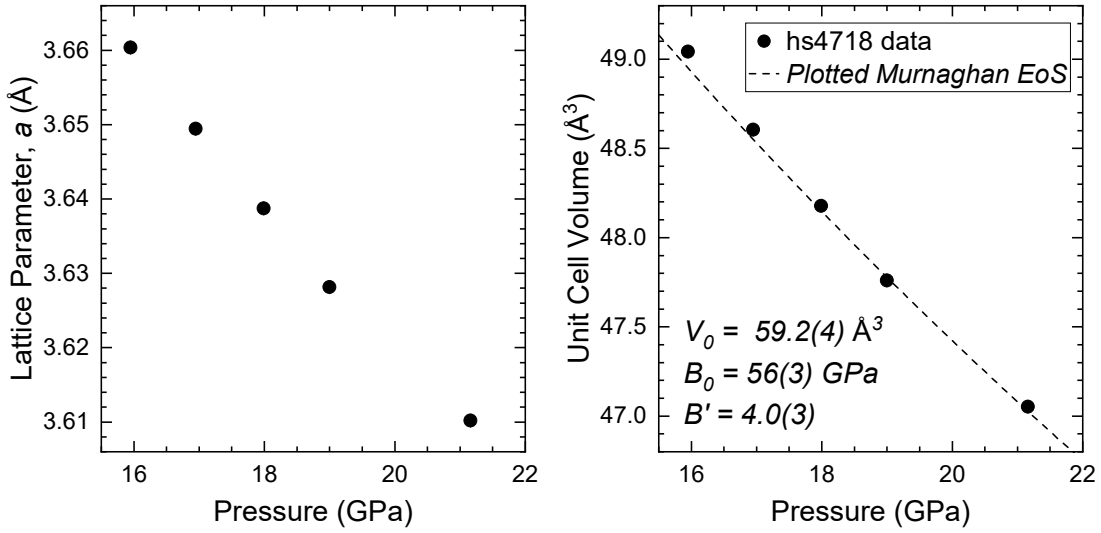

Figure 9.7 *Refined lattice parameter and unit cell volume of the cubic phase of Bi_4Te_5 under pressure. A Murnaghan equation of state [121] has been plotted along with the volume data. The equation of state parameters are representative estimates only and have not been fitted directly to the data — details in text.*

BiTe, gives two fitted values for each parameter. These can be averaged to yield a representative Murnaghan fit with unit cell volume at zero applied pressure, $V_0 = 59.2(4)$ Å^3, bulk modulus at zero pressure, $B_0 = 56(3)$ GPa, and first derivative of this bulk modulus, $B_0' = 4.0(3)$.

Chapter 10

Comparison Across Series

10.1 Overview

In this thesis, the analysis of high-pressure synchrotron x-ray powder diffraction data collected for several members of the $(Bi_2)_m(Bi_2Te_3)_n$ series has been presented. This data was collected over several experiments spread over several years. Each Bi-Te composition investigated was measured during several experiments using a different sample loading each time (these were all taken from the same parent samples). Samples were loaded into diamond anvil cells (DACs) for pressure generation, then x-ray powder diffraction images were recorded and processed in to diffraction profiles. These profiles were then analysed by various methods, primarily Rietveld refinement and le Bail fitting.

The compositions investigated in this work are summarised in table 10.1; they span a range of bismuth contents from 44.4% to 70%. Apart from the end members of the $(Bi_2)_m(Bi_2Te_3)_n$ series, Bi_2Te_3 and elemental Bi, the bismuth-tellurides have not been widely studied under high pressure. The key publications referred to here include comprehensive studies of the ambient-pressure structures of the Bi-Te series by Bos *et al.* [24, 28], and high-pressure structural studies of Bi_2Te [4] and Bi_4Te_3 [3].

Composition:	Bi_4Te_5	BiTe	Bi_4Te_3	Bi_2Te	Bi_7Te_3
% Bi Content:	44.4	50	57.1	66.7	70

Table 10.1 *Summary of compositions investigated in this work.*

In this work, we have observed several different high-pressure structural phases adopted by Bi-Te compounds. Different compositions are found to adopt similar structures and exhibit common structural behaviour under pressure, but differences do exist, indicating that composition plays an important role in the behaviour of these materials under pressure. Members of the $(Bi_2)_m(Bi_2Te_3)_n$ series adopt layered structures at ambient conditions; these structures are related and are referred to here as *phase I*. On pressure increase, all members transform to a new structural phase, *phase II*, which has not been studied in detail here but will be discussed in a following section. On further pressure increase, differences between the compositions begin to emerge. Bi_2Te and Bi_7Te_3 transform to *phase IV* which has a complex host-guest structure, before transforming to *phase V*, with a cubic structure, on further pressure increase. The other compositions (Bi_4Te_5, BiTe and Bi_4Te_3) transform directly to phase V from phase II, and also exhibit an additional minority phase labelled *phase III*. Phase III is transient and only appears as a minority within a window of a few GPa, as the sample transforms from phase II – V. The sparsity of measurable phase-III peaks prevents unambiguous structure determination using the data available in this work.

All compositions adopt the cubic phase V at the highest pressures investigated here. On subsequent pressure release, Bi_2Te and Bi_7Te_3 adopt the same phases as they did on pressure increase, in the same order (ending back in phase I). On pressure decrease, Bi_4Te_3 transforms from the cubic phase V to the host-guest phase IV, before returning to phase I via phase II. BiTe and Bi_4Te_5 adopt the same phases on pressure release as they did on pressure increase, with the exception of the transient phase III. BiTe and Bi_4Te_5 do not adopt the complex host-guest structure at any pressure.

Clearly, the Bi-Te series includes a wealth of information on its behaviour under pressure, adopting several different structures with composition having a strong influence. The following sections will discuss each of the observed structural phases in turn, highlighting some key findings, before summarising and concluding this work.

Figure 10.1 combines the pressure summaries for Bi_7Te_3, Bi_2Te and Bi_4Te_3 into a single plot to the same scale. The available data for BiTe and Bi_4Te_5 are not well-spaced in pressure to provide comparisons which are not potentially misleading.

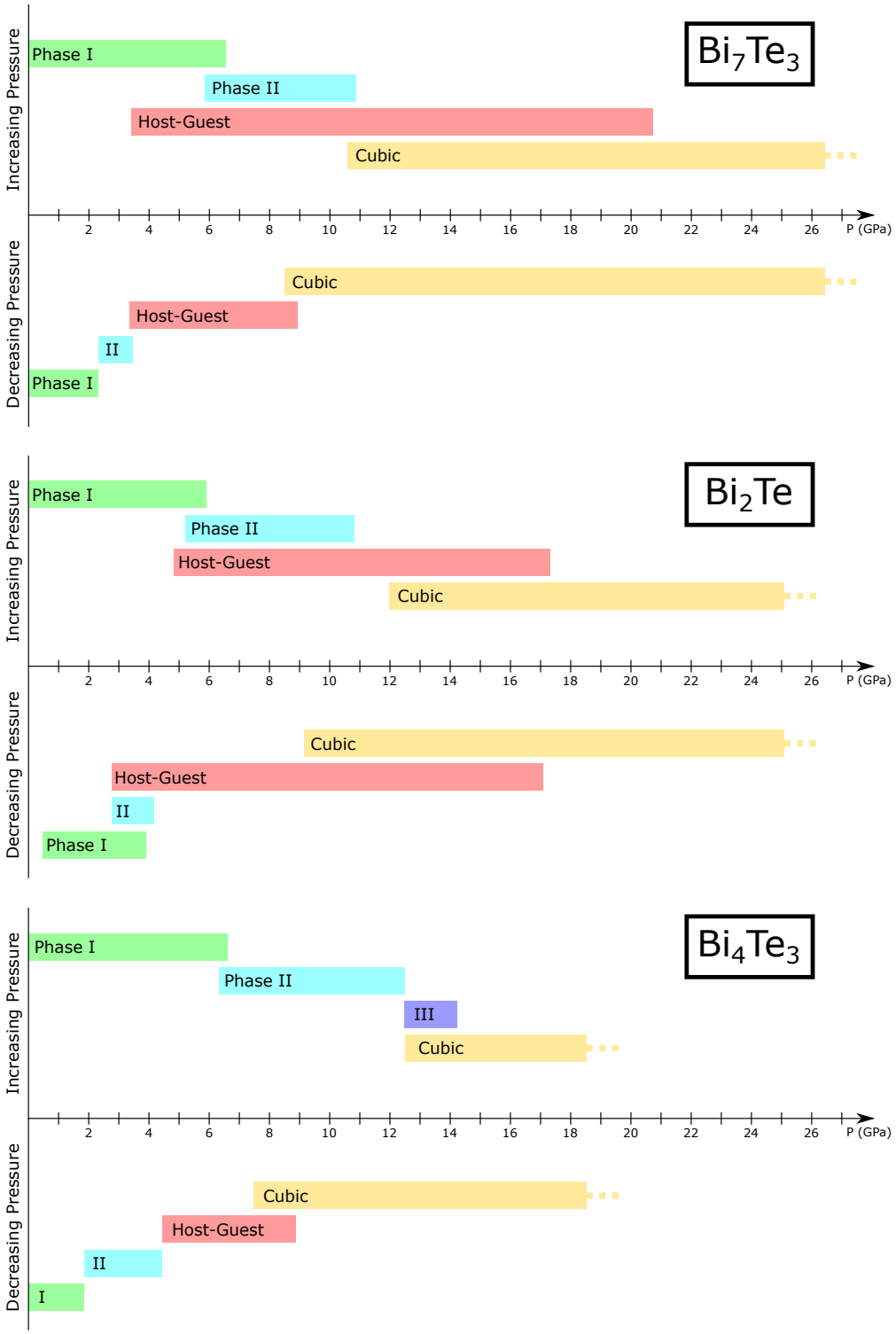

Figure 10.1 *Pressure summary plots for Bi_7Te_3, Bi_2Te and Bi_4Te_3, all plotted to same pressure scale. Labelled, coloured bars represent ranges over which peaks from each phase were clearly identifiable in measured diffraction profiles.*

10.2 Phase I

At ambient pressure, members of the Bi-Te series adopt layered structures comprised of five-atom Bi_2Te_3 and two-atom Bi_2 blocks which are stacked along the *c*-axis. These structures are illustrated in figure 10.2. These three-dimensional (3D) models are, in fact, only an approximation to the actual phase-I structure which is more appropriately described using a four-dimensional (4D) modulated structure [24]. This 4D model consists of an average subcell with a modulation vector applied along the reciprocal *c*-axis: $\vec{q} = \gamma[001]^*$, where γ describes the magnitude of the modulation.

Of the compositions investigated here, Bi_4Te_5, BiTe and Bi_7Te_3 all require description using the 4D modulated model (the 3D models illustrated in figure 10.2 for these compositions are approximations). The other compositions investigated in this work, Bi_2Te and Bi_4Te_3, can be equivalently described by a 3D or 4D structural model, due to the fact that the value of γ is rational (and hence the commensurate modulation can be equivalently described with a supercell in 3D). Analysis of the recorded diffraction profiles was performed using Rietveld

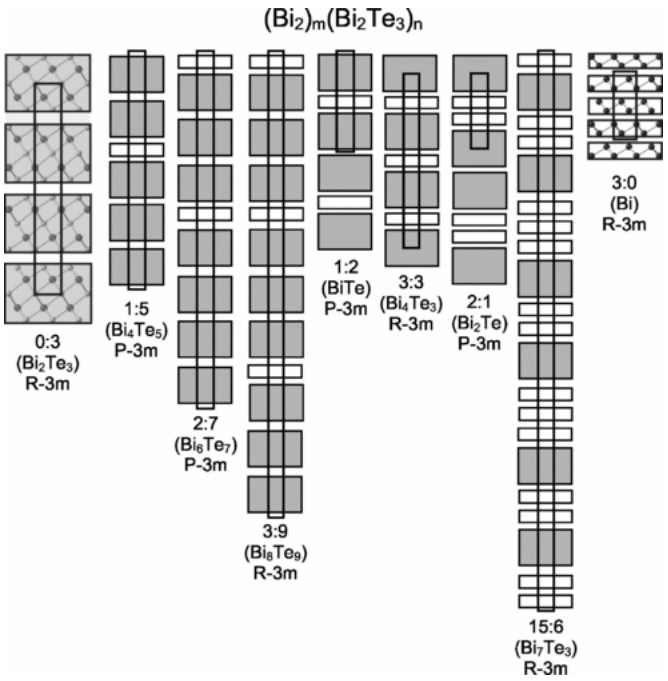

Figure 10.2 *Illustration of the ambient conditions crystal structure of members of the Bi-Te series (figure 1 from [24]). Grey rectangles represent Bi_2Te_3 blocks and white rectangles represent Bi_2 blocks. The end members include positions of the atoms within these blocks.*

structure refinements for the 3D structural models, and le Bail fitting for the 4D modulated structures.

The Rietveld refinements allowed for full determination of the crystal structures, including the positions of atomic sites within the structure and the atomic occupation of these sites. These refinements corroborated the exchange of atom types between the layers reported in phase I of Bi_2Te by Bos *et al.* [28] and also found similar chemical disorder in the structure of Bi_4Te_3. Such deviation from the idealised model of five-atom Bi_2Te_3 and two-atom Bi_2 layers was not found in the BiTe structure. Refinements of BiTe with variable site occupation factors (SOFs) were unstable, requiring the SOFs to be fixed at their idealised values. Therefore it is unclear whether deviations from the idealised layer compositions are purely a feature of the bismuth-rich members of the series, or all members.

The refined structural parameters were found to be robust to this deviation from idealised layer compositions. The refined atomic coordinates and c-lattice parameter were used to determine the thicknesses of the constituent layers and the inter-layer distances as a function of pressure. The thickness of the five-atom and two-atom layers are denoted by t_5 and t_2, respectively, and the distance between these layers is denoted by d_{5-2}. These values are compared as a function of composition by taking the refined values at ambient conditions, as shown in figure 10.3. Figure 10.3 shows the values determined for BiTe, Bi_4Te_3 and Bi_2Te in this work, with published values included where available, including the series end members: Bi [126] and Bi_2Te_3 [118]. As detailed in section 8.2.1, the ambient-pressure data available for BiTe included strong diffraction peaks from the tungsten gasket, leading to refined structural parameters that are somewhat less reliable. The red data points in figure 10.3 indicate values for BiTe that have been extrapolated from the more reliable high-pressure data.

Composition clearly has a significant influence on the phase-I structure. The thickness of the two-atom layer (t_2) decreases with increasing bismuth content and the inter-layer distance (d_{5-2}) increases as the Bi content is increased. The values determined in this work are in good agreement with the previously published values, which support these observations. The published layer thickness values for BiTe (50% Bi) are exceptions to this, differing significantly from both the values determined in this work for BiTe and the overall trends. The published value of t_2 for BiTe is significantly larger than that determined here, but does follow the observed trend. The published value of t_5 for BiTe, however, is a clear outlier.

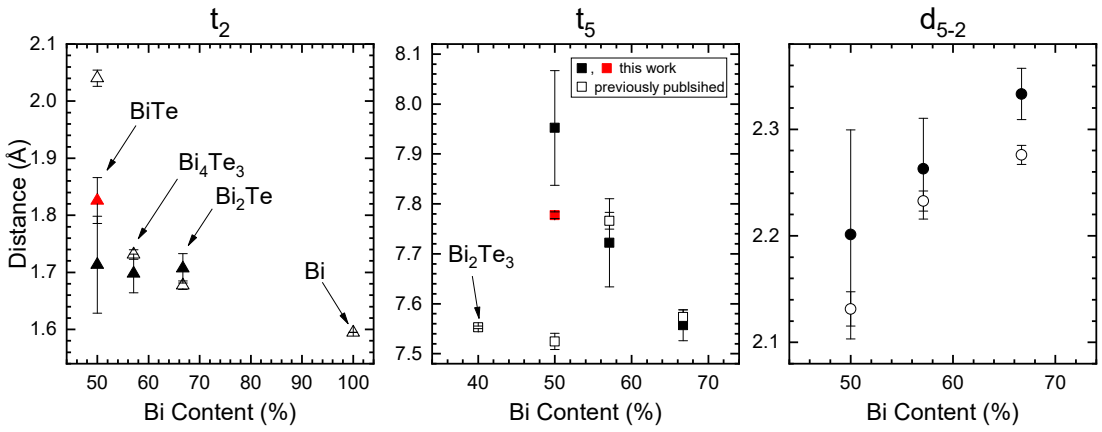

Figure 10.3 *Refined ambient-pressure layer thicknesses and separations. Thickness of five and two-atom layers denoted by t_5 and t_2 and the distance between these layers is denoted by d_{5-2}. Note differing x-axis scales. Red symbols denote BiTe values extrapolated from high-pressure data, due to the unreliability of the BiTe ambient-pressure refinement. Published values are included for comparison: Bi[126], Bi_2Te_3 [118], BiTe & Bi_4Te_3[60], and Bi_2Te [28].*

The thickness of the five-atom layer (t_5) displays a different trend, exhibiting a maximum value around a Bi content of 50%. This non-linear dependence on composition may be surprising, but such effects have been previously reported in phase I of the Bi-Te series. In their determination of the phase-I structures of several members of the series using the 4D modulated structure, Bos *et al.* have reported approximately linear dependences on composition in the subcell volume and modulation vector magnitude (γ). The refined lattice parameters and their ratio (c/a), however, show two distinct linear regimes as a function of composition. These regimes are separated by a clear 'change in structural character' at a Bi content of 0.47%.

The cause of this change is unclear. It may be a purely structural effect, due to the mismatch between the Bi_2Te_3 and Bi_2 block lattice parameters introducing strain to the structure as the composition is changed (by the addition or removal of blocks). Or it may be an electronically-driven change, where the electronic interactions between the blocks changes at this particular composition. Further theoretical consideration would be required to determine the cause of this change, with band-structure calculations potentially useful. Further investigation of the behaviour of the layers as a function of composition is not feasible. Compositions which would give data points that would elaborate on the observed t_5 trend — Bi_4Te_5 (44% Bi), Bi_6Te_7 (46% Bi) and Bi_8Te_9 (47% Bi) — cannot be accurately described using the 3D structural model. As such, the structural description in

terms of stacked layers would only serve as an approximation.

The refined layer thicknesses and distances as a function of pressure for the compositions BiTe, Bi_4Te_3 and Bi_2Te are summarised in figure 10.4. The refined values are very similar across all three compositions and show similar behaviour under pressure. The inter-layer distance, d_{5-2}, shows that the layers move closer to one another as the pressure is increased. The thickness of the five-atom layer is found to decrease with increasing pressure for both BiTe and Bi_4Te_3, but is observed to increase in the case of Bi_2Te. The thickness of the two-atom layer is observed to increase as the pressure is increased in all three compositions.

The observed increase in t_2 as the structures are compressed indicates a strengthening of the inter-layer bonding as the layers are brought closer together. This strengthening of the interaction between layers results in the two-atom layer being stretched and expanding as the material approaches the phase transition. This effect is also observed in the five-atom layer of Bi_2Te (i.e. the Bi-rich composition), but not in BiTe or Bi_4Te_3. This observation illustrates the effect that composition has on the structural behaviour of these materials under pressure.

All compositions showed a subtle structural anomaly between 2–3 GPa which appeared as a minimum in the ratio of the lattice parameters (c/a) as a function of pressure. These observations are summarised in figure 10.5 which shows the refined c/a ratios for all compositions. The data include parabolic fits as guides to the eye. Note the varying degrees of systematic offsets that exist between datasets from different experiments, most noticeably in Bi_2Te. There is no clear dependence on composition to this feature, with the pressures at which the minima occur only broadly indicated as between approximately 2–3 GPa.

This structural anomaly has been well-established in Bi_2Te_3 and attributed to an 'electronic topological transition'. This work represents the first systematic confirmation that all members of the Bi-Te series exhibit this same structural anomaly as a function of pressure. This anomaly in phase I appears to be a common feature of the series, adding to the properties shared by members of the series.

An attempt was made to analyse these features more closely using a method described in work by Polian *et al.* [47] (details in section 5.3, page 94). Unfortunately, this method proved unable to provide a more accurate analysis and is subject to large uncertainties even with high-quality data [39]. Therefore,

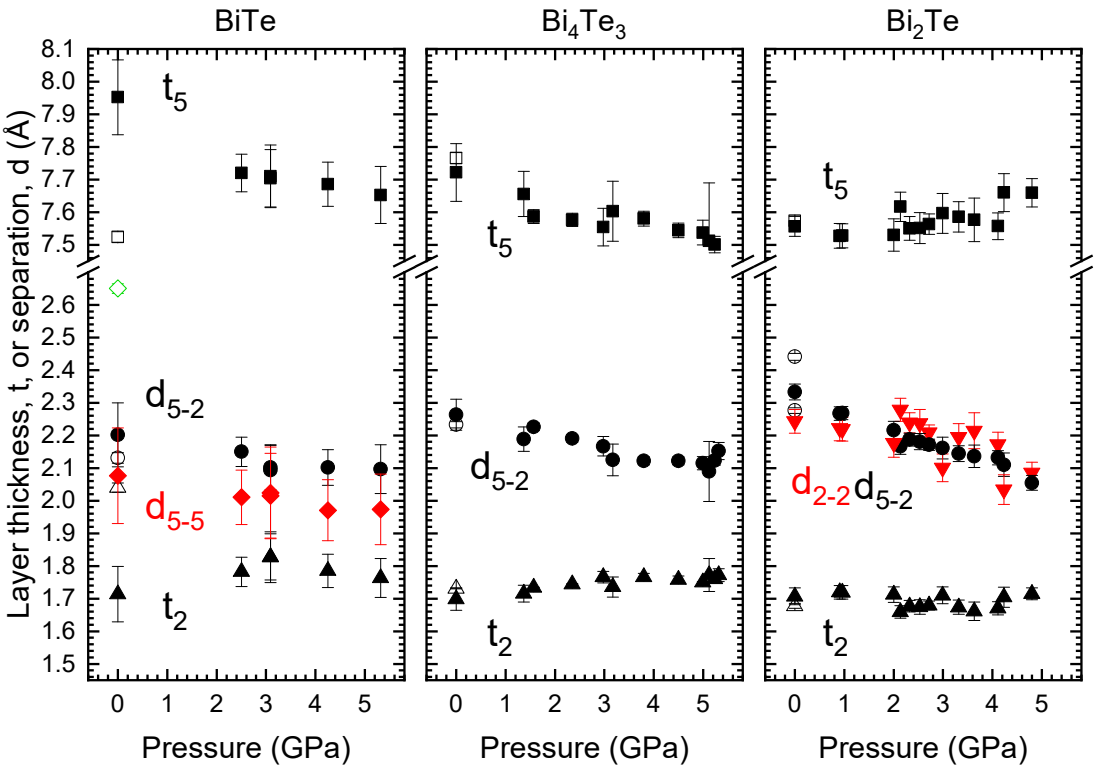

Figure 10.4 *Refined layer thicknesses and separations for BiTe, Bi_4Te_3 and Bi_2Te as a function of pressure. These describe the five-atom and two-atom layers which form the phase-I structures. Thickness of five and two-atom layers denoted by t_5 and t_2. Distances between these layers are labelled with d_{2-2}, d_{5-2} and d_{5-5}; with d_{5-2} the distance between a five-atom and two-atom layer. This simplified plot does not distinguish between data gathered during different experiments. Published values included for comparison [24, 60].*

the observed minimum in the c/a ratio is the most accurate indication of an anomaly occurring within phase I obtainable from the x-ray powder diffraction data. Collection of high-quality single-crystal data may allow further study of the nature of this anomaly, especially if combined with electronic structure calculations to understand underlying electronic changes taking place. However, such calculations may be complicated by the chemical disorder present in these structures.

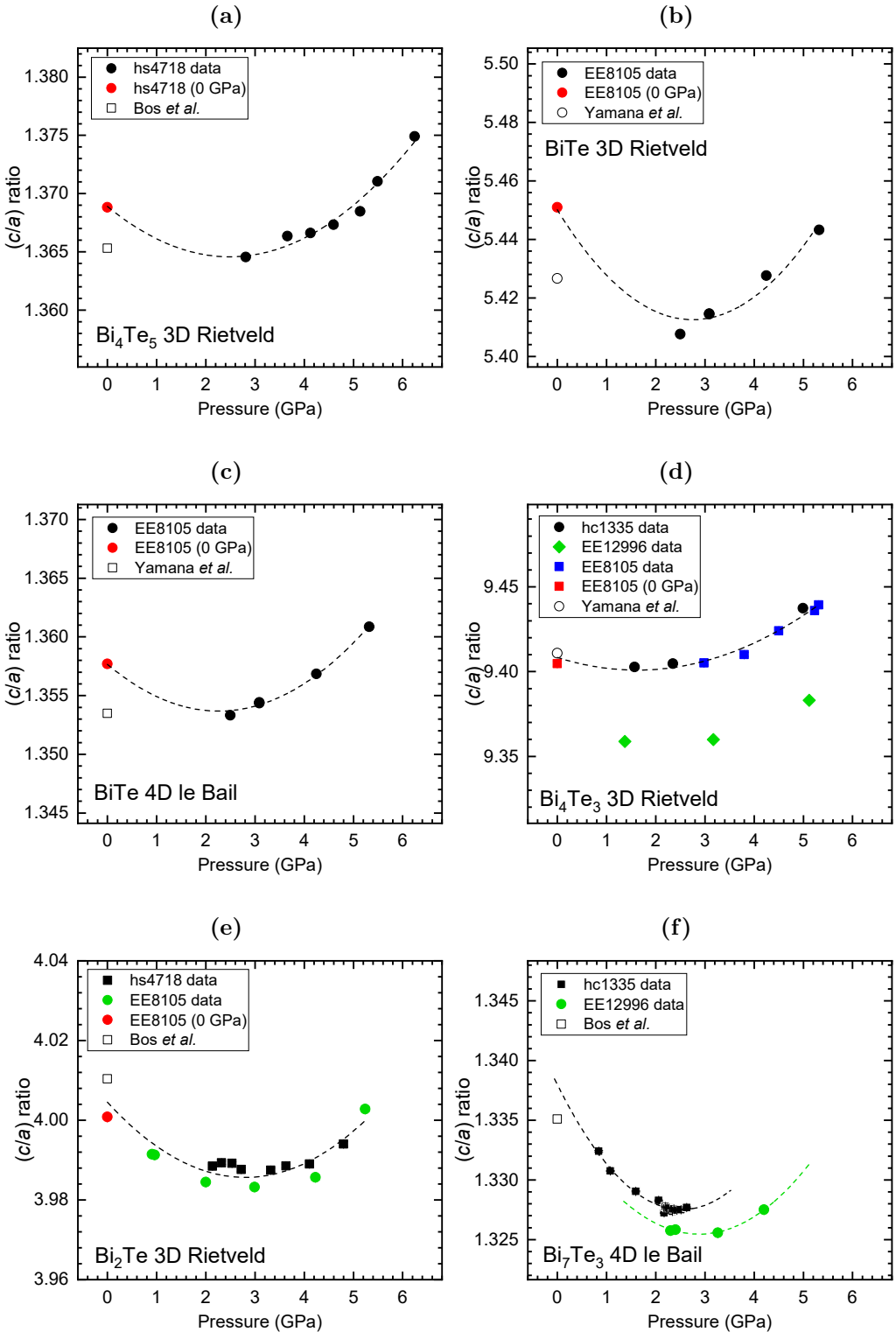

Figure 10.5 *Ratio of refined lattice parameters (c/a) for (a) Bi_4Te_5, (b) BiTe (3D model), (c) BiTe (4D model), (d) Bi_4Te_3, (e) Bi_2Te and (f) Bi_7Te_3. Published values are included where available [24, 60]. Data from this work are fitted with simple parabola as a guide to the eye. All data plotted to a relative scale of ±1% of the value at ambient conditions, as determined in this work (except Bi_7Te_3, where the published value was used).*

10.3 Phase II

All Bi-Te compositions adopt similar layered structures at ambient conditions, collectively referred to as phase I, which produce very similar diffraction profiles. On pressure increase, the first phase transformation in the Bi-Te series is to *phase II*. All Bi-Te compositions exhibit similar diffraction profiles after this transition, leading to the conclusion that the phase-II structures are likely very similar. Phase II has been observed in all compositions investigated in this work, and XRPD diffraction profiles indicative of phase II have been published in high-pressure studies of Bi_2Te_3 [118], Bi_2Te [4] and Bi_4Te_3 [3]. From the observed diffraction profiles, all compositions adopt the phase-II structure as the first high-pressure phase.

As discussed in section 2.4.1, the currently accepted structural model of phase II is only fully defined for Bi_2Te_3. It was first proposed by Zhu *et al.* in 2011 who analysed synchrotron XRPD data using a particle swarm optimisation (PSO) algorithm as a crystal structure prediction tool [110]. They proposed a layered monoclinic sevenfold *C2/m* structure for phase II of Bi_2Te_3 (referred to as β-Bi_2Te_3 by Zhu *et al.*). They performed Rietveld refinements with this structure using high-pressure x-ray powder diffraction data, reporting excellent fits to the measured data. However, in this work, observations based on measured Bi_2Te_3 diffraction data and measured diffraction patterns of phase II of other Bi-Te compositions suggest that the *C2/m* structure may not be the most appropriate model of phase II.

The proposed *C2/m* structure for phase II of Bi_2Te_3 has been indirectly supported by subsequent Raman measurements (see section 2.4.1). However, it should be noted that these measurements confirm that the *C2/m* is compatible with the Raman observations, rather than directly confirming this structure in particular, leaving the possibility of a better description of the structure open.

The PSO algorithm was also applied to the high-pressure phase of Bi_2Te_3 which has since been confirmed as having the body-centred cubic (bcc) structure. The PSO algorithm incorrectly assigned a compact monoclinic *C2/m* structure for this phase, rather than the simple bcc structure. Zhu *et al.* suggest that this is a result of the PSO technique's inability to deal with chemical disorder within the structure. As the bcc structure has only two atoms in the unit cell, the Bi_4Te_3 stoichiometry requires the atomic sites to be of mixed occupancy. It is

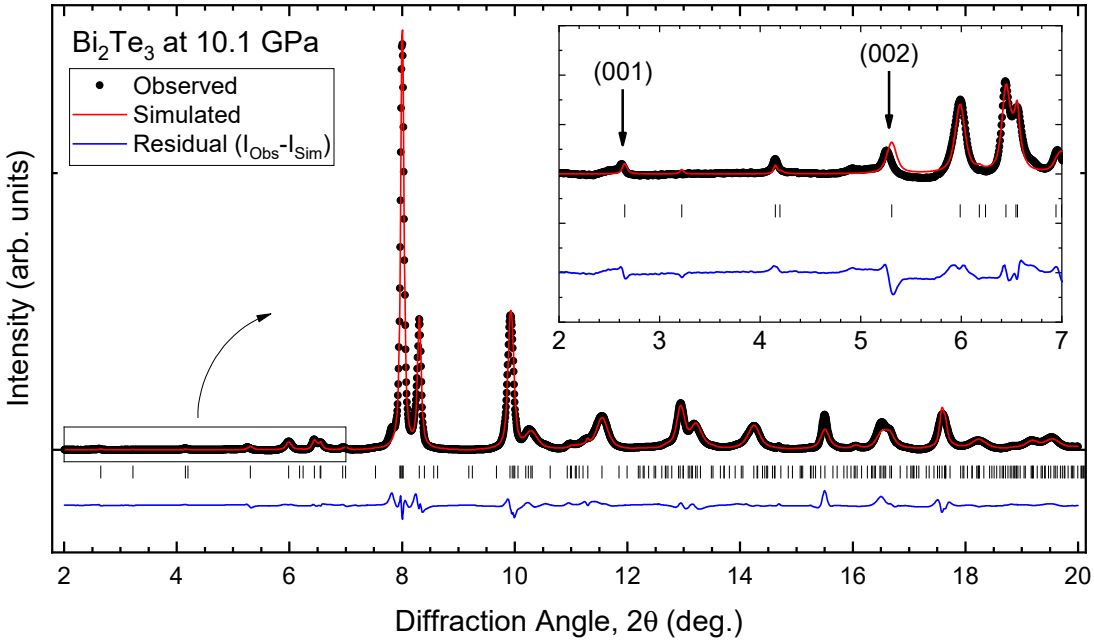

Figure 10.6 *Rietveld refinement of Bi_2Te_3 at 10.1 GPa using the C2/m structure proposed by Zhu et al. [110]. $wR_p = 3.69\%$. The inset shows enlarged low-angle section, illustrating the poorly-reproduced peak positions of the (001) and (002) peaks. Wavelength of x-rays used: $\lambda = 0.415580$ Å.*

possible that a similar situation may have arisen in the prediction of the phase-II structure, the proposed *C2/m* structure masking a simpler or more appropriate structural description.

Some high-pressure x-ray powder diffraction data of Bi_2Te_3 was available from an experiment at the ESRF in June of 2011. The sample was measured at high pressures with the use of a diamond anvil cell and the recorded x-ray diffraction patterns were processed to produce XRPD profiles. Profiles belonging to phase II of Bi_2Te_3 were then used in Rietveld refinement of the *C2/m* structure. An example refinement is shown in figure 10.6. The refined structure provides a reasonably good fit to the measured profile, with an R-value of $wR_p = 3.69\%$. However, there are some aspects which may suggest that this model based on the *C2/m* structure is not fully describing the true Bi_2Te_3 phase-II structure.

The inset of figure 10.6 highlights the failure of the model to reproduce the peak positions of the (001) and (002) reflections, in a discrepancy that is reminiscent of the subtle disagreements observed in phase I of BiTe when refined using the 3D approximated model (see figure 8.3 on page 167). Offsets are also visible between the simulated and measured positions of the peaks near 10°. Further to this, the

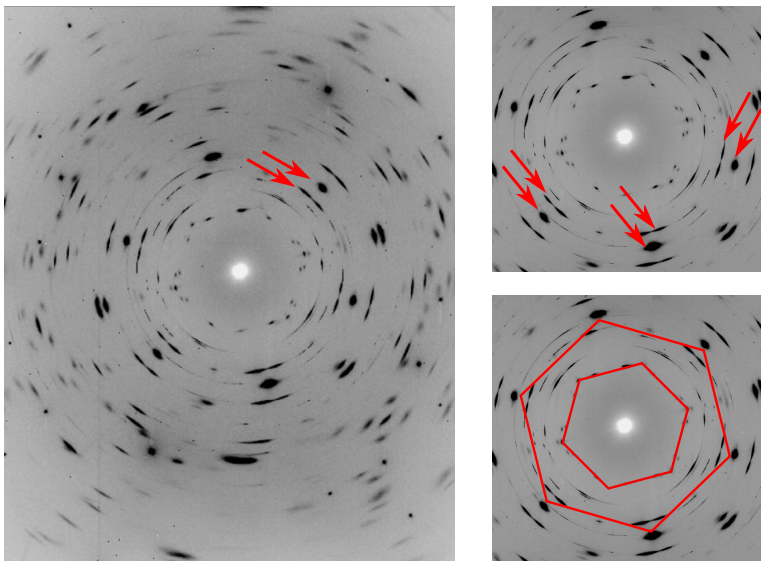

Figure 10.7 *Main panel, left: X-ray diffraction pattern measured from a pseudo-single crystal sample of Bi_4Te_3 at 9.8 GPa, with the sample in phase II. Subfigures show enlarged view of same diffraction pattern. Arrows indicate examples of the broad and sharp diffraction features. Annotations to subfigure illustrate the hexagonal symmetry of the pattern.*

inclusion of many predicted reflections which are found to have zero intensity in the measured profile may suggest that this model is overly complex.

Diffraction data were available for samples of Bi_2Te_3 and Bi_4Te_3 which were polycrystalline but comprised of a small number of crystallites, with some large enough to produce a 'pseudo-single-crystal' diffraction pattern. These pseudo-single-crystal patterns were recorded as diffraction images; an example, Bi_4Te_3 in phase II at 9.8 GPa, is shown in figure 10.7. While clearly not of sufficient quality for single-crystal analysis, this sample of phase-II Bi_4Te_3 did illustrate a number of interesting features, most striking of which is the hexagonal symmetry of the pattern. The annotations in figure 10.7 highlight the hexagonal feature at the centre, as well as the hexagonal symmetry in the diffraction features. These features, indicated by arrows in the main panel, form a pattern of one broad diffraction spot surrounded by two pairs of much sharper, arc-like reflections. Close inspection of the diffraction image reveals what appears to be two classes of reflections, distinguished by their breadth.

In an attempt to find possible alternative structures for phase II, the pseudo-single-crystal diffraction pattern of Bi_4Te_3 was manually processed for reflection indexing. This was done using Fit2D [95, 96] to select individual measured

reflections and to integrate the data in order to determine the corresponding *d*-spacing. The resulting *d*-spacings were then analysed with the use of the software suite *CRYSFIRE* [101] which provides a single interface to utilise several indexing programs including *Dicvol06* [102] and *Treor90* [103]. The *d*-spacings could be grouped together based on the breadths and positions of the corresponding reflections in the diffraction pattern, in an attempt to determine whether the two distinct classes of reflections belonged to distinct structures. These indexing attempts were unsuccessful and unable to yield likely solutions for the measured phase-II reflections.

Further work on this phase would require single-crystal diffraction data in order to unambiguously determine the structure of phase II of the Bi-Te series. Even with the proposed *C2/m* structural model, single-crystal data is likely required for a full structural solution of phase II for the other compositions in the Bi-Te series.

10.4 Phase III

On initial pressure increase, Bi_4Te_3, BiTe and Bi_4Te_5 exbibit several peaks in the diffraction profiles that appear to belong to a distinct structural phase — phase III. The phase appears as the majority of the sample transforms from phase II to the cubic phase and is visible over a narrow pressure range of a few GPa. The observed phase-III peaks have been discussed in the chapters pertaining to each composition and have been discussed in detail for Bi_4Te_3 (section 7.4). These peaks appear at similar positions in each of the three compositions which strongly suggests that these peaks arise from similar structures.

This phase does not seem to be energetically favourable, as it appears only briefly as a minority phase within the sample. It is interesting that this phase does not appear in the high-bismuth-content compositions (Bi_2Te and Bi_7Te_3); another indication of the strong influence of composition on the pressure behaviour of the Bi-Te series.

The compositions in which phase-III appears also exhibit weak peaks that are present in the diffraction profiles throughout the entire pressure range studied here. These weak, unidentified peaks do move to higher(lower) diffraction angles with increasing(decreasing) pressure but remain largely unchanged despite the

significant structural transitions occurring in the Bi-Te sample. The identity of these weak peaks has not been determined, but several likely sources of a minority contaminant have been ruled out (as discussed in section 7.1.1). Further investigation into the structure of phase III may need to consider whether these weak peaks are in some way related, but there is no evidence that they are directly linked and they do not arise from the same source.

10.5 Phase IV - Host-Guest

The complex, semi-disordered host-guest structures of Bi_4Te_3, Bi_2Te and Bi_7Te_3 have been refined with the use of custom Rietveld refinement software. These structures were found to be similar to that of Bi-III [15], comprised of a host framework enclosing linear guest chains. The lack of *guest*-only diffraction peaks in the measured profiles indicates that the guest chains are disordered, with the positions of guest chains in adjacent channels uncorrelated (or, that the guest chains are disordered along their lengths). Determination of the exact nature of this disorder could be achieved with single-crystal x-ray diffraction measurements which would record the diffuse scattering arising from the disordered guest. As discussed in section 2.5.1, the form of this diffuse scattering provides information on the nature of the disorder, and measurements of the chain-chain correlation lengths would be possible [16, 74].

As the guest c-lattice parameter could only be determined from the positions of *guest*-only diffraction peaks, their absence prohibited full structural refinement based on the measured diffraction peaks. Diffuse diffraction features were visible in the Bi_2Te and Bi_7Te_3 XRPD profiles in the form of an 'edge' feature (a rise in intensity in the form of a smooth step) which led to an area of raised, flat intensity at higher diffraction angles. These diffuse features were identified as due to the disordered guest, as confirmed with simulations of the XRPD profiles of semi-disordered host-guest supercells and as have been reported in similar host-guest systems [114, 115]. The position of this edge feature was used to directly estimate the guest c-lattice parameter from the measured diffraction profiles of Bi_2Te and Bi_7Te_3.

The host-guest phase of Bi_4Te_3 also produces no sharp *guest*-only diffraction peaks but does not produce a visible diffuse scattering feature. Therefore, the guest c-lattice parameter was estimated as a fixed fraction of the host c-lattice

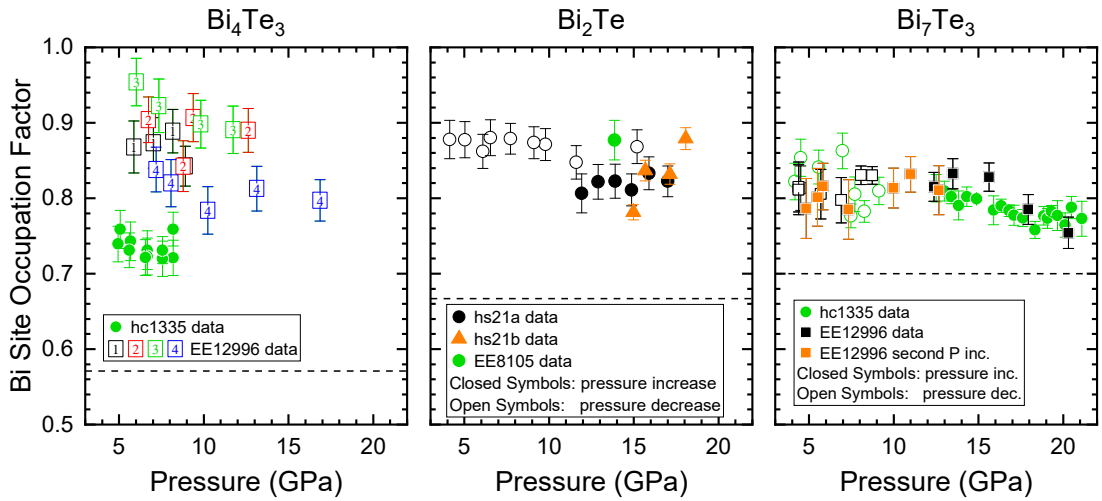

Figure 10.8 *Refined guest bismuth site occupation factors for the host-guest phases of Bi_4Te_3, Bi_2Te and Bi_7Te_3. A value of 1 corresponds to a guest substructure that is fully occupied by bismuth. Dashed lines indicate the value expected for a fully-site disordered structure, such that the guest would be occupied on average by a stoichiometric mix of Bi and Te.*

parameter. The ratio, c_{Host}/c_{Guest}, was estimated for Bi_4Te_3 by considering the measured values for Bi_2Te and Bi_7Te_3, along with the published values for Bi-III. Assuming a linear variation in c_{Host}/c_{Guest} as a function of composition, an estimate for Bi_4Te_3 was determined and used in the Rietveld refinements. While this value may only be a rough estimate, the resulting structural parameters from the Rietveld refinements were found to be robust to changes in the c_{Host}/c_{Guest} value used.

Rietveld refinements have yielded full structural details of these structures, including atomic site occupation factors (SOFs). The refined SOFs reveal partial chemical ordering within the host-guest structures, with the guest substructure consisting of a bismuth-tellurium mix with a majority of bismuth. These guest bismuth SOFs are summarised in figure 10.8. The refinement results show the structures of all three compositions to be partially ordered, with the guest containing significantly more bismuth than would be expected for a fully-site disordered alloy based on the chemical composition.

Similar host-guest structures have been reported at high pressures in Bi-Sb compounds [19]. These structures are similar to the host-guest structure of bismuth, and show no evidence of the structural disorder observed here for the Bi-Te compounds. The Bi-Sb host-guest phases were found to be rather unstable, decomposing into Sb-rich phases with the ambient-pressure structure and Bi-

rich phases with the Bi-III structure. The Bi-Sb host-guest structures were determined to be fully site-disordered alloys, showing no evidence of chemical ordering between the host and guest substructures. This combined with the fact that other examples of this host-guest structure are found in elements, makes the formation of this host-guest structure with two atom types that are distinct enough to produce ordering interesting. These are intriguing structures which include both structural disorder and chemical ordering, meriting further study.

10.6 Phase V - Cubic

All members of the Bi-Te series adopt a cubic phase at high pressures. This phase has a fully site-disordered body-centred cubic (bcc) structure, with the atomic sites occupied by a stoichiometric ratio of Bi and Te. The cubic phase has been observed to order on gentle annealing in to a B2, CsCl-type structure, with one atomic site fully occupied by the majority atom type (Bi or Te) and the second site occupied by a mix which maintains overall stoichiometry [12].

In this work, the cubic phase has been observed in all Bi-Te compositions and has been found to adopt the bcc structure. An ordering of this cubic phase was observed in Bi_4Te_3 on pressure decrease, with weak peaks indicating a change to B2, CsCl-type structure at the low-pressure end of the cubic phase stability range.

10.7 Conclusions and Future Work

In this thesis, several members of the $(Bi_2)_m(Bi_2Te_3)_n$ series have been investigated by means of high-pressure x-ray powder diffraction. Compositions spanning Bi_xTe_{1-x}, $0.44 \leq x \leq 0.70$ were investigated at pressures up to 25 GPa. Analysis of the recorded diffraction data revealed a number of structural phases and pressure-induced phase transitions. Analysis focused on three structural phases in particular: the layered structure of phase I, as found at ambient conditions; a complex semi-disordered host-guest phase; and a high-pressure cubic phase.

We have found significant similarities in the pressure-induced phases of bismuth-tellurides, in keeping with their definition as an infinitely adaptive series at ambient conditions. The chemical composition of samples has been found to have

a significant influence on these structures, with entire structural phases accessible only by certain compositions. The behaviour of several structural phases as a function of pressure have been investigated in detail. One such phase, the complex host-guest phase, has been found to include structural disorder within its guest component and chemical ordering across both substructures.

This work may form the basis of future investigations into the bismuth-telluride series. The structural details presented here may enable further study through electronic structure calculations (in the framework of density functional theory, for example), while the results and observations of this work suggest a number of avenues for further investigation.

The layered phase-I structures of the Bi_xTe_{1-x} series could be further explored through electronic structure calculations, utilising the structural parameters determined in this work. Such calculations may elucidate how these structures form at ambient conditions, and to what degree the observed structural 'change in nature' at $x = 0.47$ is an electronic or structure-driven change. In this work, the structural anomaly which occurs between 2-3 GPa has been confirmed as a common feature of the Bi-Te series. Electronic structure calculations may reveal more details about this anomaly and how it might affect the physical properties of these materials. Additional structural details could be revealed through single-crystal x-ray diffraction (SC-XRD) studies; remaining in the stability range of phase I should ensure that such single-crystal samples survive under pressure.

The remaining question as to the true structure of phase II may also be addressed through SC-XRD. Any structural studies should consider whether the proposed monoclinic *C2/m* structure [110] can accurately account for the measured diffraction data and evaluate possible alternative structures. Alternative structures may include incommensurately modulated structures similar to *C2/m*, and structures of related materials (e.g. Bi-Se, Sb-Se, Bi-Sb and elemental Te) should also be considered.

SC-XRD studies of the Bi-Te host-guest phase may also be of interest. The nature of the disorder in the guest chains could be explored; whether this disorder is inter-chain, intra-chain or a combination. Maintaining a good-quality single-crystal sample on pressurisation to the host-guest phase is unlikely, due to the preceding phase transitions. However, pressure-cycling of large powder grains or crystallisation from the melted state may yield usable samples at high pressures. If SC-XRD is not feasible, high-pressure, low-temperature x-ray

powder diffraction may allow the ordering of the guest chains on temperature decrease to be observed, as has been previously demonstrated in lithium-boride [116] and potassium [17].

Appendix A

Experiment Details: Observed Phase Transitions

This appendix details the observed changes to the x-ray powder diffraction profiles as a function of pressure in all experiments. While an overview of each has been provided in the main body of the thesis, details of the nature of the observed phase transitions may prove useful in consideration of the results. Here the pressures at which phase transitions were observed, the growth and decay of visible peaks, and the overlaps in pressure ranges of all phases will be described. Due to the number of individual samples investigated in this work, inclusion of such details in the main text was not prudent.

A summary of the samples investigated and their labels is given in table 4.3 on page 62.

A.1 Bi_2Te Observations

X-ray powder diffraction (XRPD) data were collected during experiment hs4718 at the ESRF on two samples labelled *hs21a* and *hs21b*.

XRPD images were recorded for sample *hs21a* from 2.1 GPa to a maximal value of 17 GPa where, on further increase of the applied membrane pressure, the gasket hole became unstable and the pressure reduced to 15 GPa. From here, the pressure was reduced to a final pressure of 0.5 GPa. On pressure increase,

phase I is the only observed phase up to 5.5 GPa at which point peaks from phase II appear and grow in intensity to around 8.6 GPa. These phase-II peaks then reduce, disappearing by 13 GPa. Very faint peaks belonging to the host-guest phase appear alongside the phase-II peaks at 5.5 GPa; these grow continuously with the host-guest becoming the dominant phase by around 10 GPa. Peaks from the cubic phase are present as a minority phase from 12 GPa up to the maximum pressure attained.

On subsequent pressure decrease, the *hs21a* profiles include peaks from the cubic and host-guest phases down to 9.1 GPa and 2.7 GPa, respectively. Phase-II peaks reappear at 4.1 GPa and are present down to a pressure of 2.7 GPa, below which the sample fully adopts the ambient-pressure layered structure — phase I.

Sample *hs21b* was checked for quality and composition at 0.5 GPa then XRPD images were recorded at high pressure from 15 GPa up to a final pressure of 20.2 GPa. Consistent with *hs21a*, the integrated high-pressure profiles showed the sample to be initially in the host-guest phase with peaks from the cubic phase also present. These peaks were observed to grow in intensity as the pressure was increased, with the sample fully adopting the high-pressure cubic structure from 19.7 GPa (still with the most intense host-guest peaks weakly present). No diffraction data for this sample were recorded on pressure release.

The recorded diffraction data from experiment EE8105 show transitions consistent with those observed in hs4718. Sample *MB-V6* starts as pure phase I, with very weak peaks from the host-guest phase appearing at 4.2 GPa, followed by the appearance of phase-II peaks at 5.2 GPa. The sample fully transforms to phase II by 6.3 GPa with the host-guest peaks still weakly present. The host-guest phase becomes dominant between 8–9.5 GPa and data collection ends with the sample adopting the host-guest structure but with phase II still present as a minority phase. Sample *MB-V3* starts in a mixed phase at 4.5 GPa: primarily phase II with host-guest peaks weakly present. As the pressure is increased, the host-guest phase becomes dominant by 11 GPa with a single pure host-guest phase profile recorded at 13.9 GPa. No further diffraction patterns were recorded while the pressure was increased to 25 GPa. A single diffraction pattern was measured at this pressure showing the sample to have fully adopted the cubic structure. The sample was then annealed and measured once more afterwards at 14.8 GPa.

A.2 Bi_7Te_3 Observations

X-ray powder diffraction data were collected for two samples of Bi_7Te_3, labelled *hc73* and *EE73*, during two experiments: hc1335 at the ESRF and EE12996 at Diamond Light Source.

A.2.1 hc1335 Bi_7Te_3

Sample *hc73* was taken up in pressure from a starting point of 0.9 GPa to a maximum pressure of 25.9 GPa in steps smaller than 1 GPa. Below 3.5 GPa the sample was found to adopt the ambient-pressure layered structure of phase I. The diffraction peaks in the profile appeared split, suggesting the presence of a contaminant. Upon increasing pressure, new peaks began to appear which were eventually identified as the two main peaks from the host-guest phase (see figure 6.1); these were very subtle at around 3.5 GPa, steadily growing in intensity as the pressure was increased.

Around 6 GPa, peaks belonging to phase II were observed. The phase-I peaks reduced in intensity as phase II became the dominant phase, with the phase-I peaks absent by 7.5 GPa. The peaks due to the host-guest phase grew steadily while the phase-II peaks reduced in intensity, with the host-guest phase overtaking phase II as the majority phase around 10.3 GPa. Around the same pressure, new peaks were observed which could be identified as the cubic phase of Bi_7Te_3 with the body-centred cubic (bcc) structure.

The phase-II peaks disappear entirely around 12.5 GPa, leaving the host-guest as the main phase with strong peaks from the cubic phase and some contaminant peaks. The host-guest phase remains dominant up to around 20 GPa, after which the cubic phase quickly becomes the dominant phase. The cubic phase is observed with only contaminant peaks from around 22 GPa up to the maximum pressure attained, 25.9 GPa.

On subsequent pressure decrease the cubic phase remains visible down to 8.3 GPa. The host-guest phase returns as the dominant phase around 10 GPa (this phase transition occurred during a pressure reduction). The host-guest phase is the sole phase down to 3.5 GPa, where phase II reappears. Both host-guest and phase II coexist with phase I at 2.3 GPa, with the sample returning to phase I on reaching

ambient pressure.

A.2.2 EE12996 Bi_7Te_3

After observation of interesting structural phases in the experiment hc1335, experiment EE12996 aimed to further investigate some of these aspects through thermal annealing and pressure-cycling. The main point of interest was the host-guest phase where a possible order–disorder transition on pressure increase was observed. This transition was based on the appearance of a few peaks in the diffraction profiles, however, the observed peaks (which occurred at positions close to where guest-only peaks would be expected) have since been identified as strong peaks from phase II which overlap with the pressure-range of the host-guest phase.

The diffraction profiles of sample *EE73* exhibit similar pressure behaviour to sample *hc73*, transforming to the same structural phases at similar pressures. The diffraction pattern of sample *EE73* was first measured at 2.4 GPa and pressure was increased in large, ~ 1.5 GPa, steps to a maximum of 26.4 GPa (the highest pressure reached with samples of Bi_7Te_3 in this work). The sample is initially in phase I, which is quickly joined by a small minority of the host-guest phase from 3.3 GPa onwards, as evidenced by the two most intense host-guest peaks being weakly present in the low-pressure profiles. Phase II is present also from 5.6 GPa, and the phase-I peaks disappear by around 6.9 GPa. The balance between the phase-II and host-guest peaks gradually shifts, until the host-guest phase becomes dominant around 10 GPa, with the phase-II peaks fully dissipating by 12.3 GPa.

From around 11 GPa onwards, peaks from the cubic phase of Bi_7Te_3 are present, gradually increasing in intensity until the sample has fully adopted the cubic structure by 22.5 GPa. This phase persists up to the maximum pressure studied, then down to around 8.7 GPa on subsequent pressure release. On decreasing the pressure, the sample transformed suddenly to the host-guest phase during a significant pressure reduction from 10.5–8.7 GPa.

The additional peaks of interest appeared while the sample was mostly in the host-guest phase, at 6.9 GPa. The sample was then annealed at this pressure at a temperature of 100°C for 20.5 hours, after which the pressure had reduced to 5.7 GPa but no visible change in the diffraction pattern was observed. The pressure was further reduced to 4.4 GPa, then increased again until the peaks of

interest disappeared, around 11 GPa. The experiment ended with the sample at 12.7 GPa, in the host-guest phase.

A.3 Bi_4Te_3 Observations

Data were collected for the composition Bi_4Te_3 over three separate experiments: EE8105 and EE12996 at Diamond Light Source, and hc1335 at the ESRF. One sample from each experiment was investigated at high pressures; these samples are labelled *EE43* from experiment EE8105, *hc43* from experiment hc1335 and *EE43b* from experiment EE12996.

A.4 EE8105 Bi_4Te_3

A single measurement of Bi_4Te_3 at ambient pressure was collected during experiment EE8105. A sample of Bi_4Te_3 was held in a Merril-Basset-type diamond anvil cell as a sample holder, with no pressure-transmitting medium. The diffraction image from this sample was recorded, providing a diffraction profile for Bi_4Te_3 at ambient pressure. This profile showed the sample to be in phase I — the layered structure.

Another sample of Bi_4Te_3 (taken from the same batch of powder as the sample investigated at ambient pressure) was then loaded with helium into a DAC for high-pressure measurements. The diffraction pattern from this sample (*EE43*) was first recorded at a pressure of 3 GPa and then the pressure was increased in approximately 1 GPa steps. The diffraction profiles show the sample to adopt the phase-I structure up to 5.2 GPa, where peaks from phase II appear alongside those from phase I. The phase-I peaks quickly reduce in intensity, with phase II becoming the sole phase at 6.8 GPa. The cubic phase starts to appear at 11.7 GPa, along with several other peaks that are visible between 11.7–13.6 GPa. These additional peaks are due to *phase III*, the structure of which could not be unambiguously determined due to the small number of visible phase-III peaks. The cubic phase is then the sole phase present as the pressure is increased up to 14.5 GPa. At this point, due to the gasket hole becoming unstable, the pressure increase was halted.

The pressure was then reduced in larger (2–4 GPa) steps. The sample remains

in the cubic phase down to 10.5 GPa, then is seen to adopt the host-guest phase in the next recorded profile at 6.8 GPa. The next profile at 4.8 GPa shows the host-guest phase mixed with phase II and the next, at 2.8 GPa, shows a mixture of phase II and phase I. The final recorded profile at ambient pressure shows that phase I has been recovered but with substantial broadening of the diffraction profile.

A.4.1 hc1335 Bi_4Te_3

Sample *hc43* initially adopts the layered structure of phase I. This is the sole phase up to a pressure of 5.5 GPa, where peaks from phase II start to appear. The sample transforms gradually from phase I to II, with the phase-I peaks no longer visible at 6.3 GPa. Phase II is recorded as the sole phase until several new peaks appear at 11.4 GPa. These peaks are due to the high-pressure cubic phase and a few peaks are due to an additional phase — *phase III*. These phase-III peaks are only present in a few diffraction profiles in a narrow pressure range between 11.4–12.4 GPa. The high-pressure cubic phase is then the only phase present up to the maximum pressure attained, 18.1 GPa.

The pressure was then decreased in approximately 1 GPa steps. The sample remains in the cubic phase down to 9.5 GPa, where peaks due to the host-guest phase start to appear. These peaks gradually increase in intensity as the host-guest phase becomes dominant (by around 8 GPa), with peaks due to the cubic phase still visible down to 6.5 GPa. At 6.5 GPa, with the majority of the sample in the host-guest phase, peaks due to phase II appear. At 4.3 GPa the sample suddenly adopts the phase-II structure, with the most intense host-guest peaks still visible. Phase II is the sole phase between 3.9–3.1 GPa. Peaks due to phase I appear at around 1.9 GPa and the sample fully transforms to phase I by 1.2 GPa, which was then recovered to ambient pressure.

A.4.2 EE12996 Bi_4Te_3

As mentioned previously, experiment EE12996 sought to investigate the possibility of a phase transition occurring within the host-guest phase. This was based on the appearance of peaks in the host-guest diffraction profiles on pressure decrease which were suspected to indicate an ordering of the guest substructure. This

possibility has since been discounted and the source of these additional peaks identified as phase II overlapping with the host-guest phase (see discussion on page 71).

As these 'peaks of interest' were observed within the host-guest phase, sample *EE43b* was taken quickly up in pressure (∼2 GPa steps). The sample initially adopted the phase-I structure, transforming suddenly to phase II at 7 GPa. Peaks from the minority phase III were visible in two profiles recorded at 13.5 GPa and 15.5 GPa. The majority of the sample was observed to transform to the cubic phase at 13.5 GPa, fully adopting this structure at 16.4 GPa and remaining in the cubic phase up to 16.8 GPa.

On subsequent pressure decrease from 16.8 GPa, the sample was taken quickly to the host-guest phase in ∼2 GPa steps, with the step size reduced to approximately 1 GPa within the stability range of the host-guest phase. On pressure reduction, the sample transforms to the host-guest phase at 8.6 GPa with peaks from the cubic phase still present. The peaks from the minority cubic phase remain visible down to 7 GPa, where they disappear and peaks due to phase II appear. The pressure was further reduced to 5.9 GPa, then increased again to observe whether this pressure cycling has any impact on the (phase-II) peaks of interest.

The pressure was increased from 5.9 GPa until these peaks disappeared between 10.2–12.6 GPa. The pressure was decreased again and the (phase-II) peaks of interest reappeared at 7.4 GPa. Pressure decrease was continued to 5.8 GPa. The pressure was then increased slightly to 7 GPa and the sample annealed in an oven at 100°C for 9 hours.

After annealing, the pressure was found to have risen slightly to 7.2 GPa. The pressure was once again increased in larger steps of approximately 2.5 GPa to a final pressure of 16.9 GPa (the maximum pressure attained with this sample). The sample remained in the host-guest phase throughout this pressure increase, with the additional phase-II peaks disappearing between 13.1–16.9 GPa.

A.5 BiTe Observations

A single sample of BiTe was investigated at high pressures during experiment EE8105 at Diamond Light Source. Initial measurements of a BiTe sample at ambient pressure were taken and then a sample was loaded in to a diamond anvil

cell for measurements under pressure in a single increase/decrease pressure run. Diffraction data were collected at pressures from 2.5 GPa up to a maximum of 21.9 GPa in approximately 1 GPa steps, then on subsequent pressure decrease back to ambient conditions.

At ambient conditions, BiTe adopts the expected phase I layered structure, in keeping with the structural trends of the $(Bi_2)_m(Bi_2Te_3)_n$ series. This is the sole phase present in the diffraction profiles up to 6.1 GPa, when peaks from the next phase, phase II, appear. The transition is quick, with the phase-I peaks almost entirely gone in the next profile, recorded at 7.4 GPa. Phase II is the sole phase up to 13.8 GPa, where strong peaks from the cubic phase appear. These peaks grow steadily in intensity as the phase-II peaks reduce, with the cubic phase becoming dominant around 15 GPa and the phase-II peaks entirely gone by 18.2 GPa.

The sample remains entirely in the cubic phase up to the maximum pressure attained, 21.9 GPa. The subsequent pressure reduction is performed in larger, $\sim$ 2–5 GPa, steps. The cubic phase is the only phase present down to 9.2 GPa. At 9.2 GPa, peaks from phase II appear alongside the cubic-phase peaks. This mixed-phase region continues down to 3.5 GPa, where the sample fully adopts the phase-II structure. Finally, as the gas membrane is removed and the pressure fully released from the cell, the diffraction profile shows the sample to have returned to phase I, although with significantly broadened peaks, indicating a degradation in sample quality.

A.6 Bi_4Te_5 Observations

As only a small amount of data were collected for Bi_4Te_5, the details of the observed phase transitions are included in the main chapter text on page 179.

Bibliography

[1] G Jeffrey Snyder and Eric S Toberer. Complex thermoelectric materials. *Nature materials*, 7(2):105–114, 2008.

[2] MA Il'ina and ES Itskevich. Superconductivity of bismuth telluride. *Sov. Phys.-Solid State (Engl. Transl.);(United States)*, 13(8), 1972.

[3] JR Jeffries, AL Lima Sharma, PA Sharma, CD Spataru, SK McCall, JD Sugar, ST Weir, and YK Vohra. Distinct superconducting states in the pressure-induced metallic structures of the nominal semimetal Bi_4Te_3. *Physical Review B*, 84(9):092505, 2011.

[4] Ryan L Stillwell, Zsolt Jenei, Samuel T Weir, Yogesh K Vohra, and Jason R Jeffries. Superconducting Bi_2Te: Pressure-induced universality in the $(Bi_2)_m(Bi_2Te_3)_n$ series. *Physical Review B*, 93(9):094511, 2016.

[5] Liang Fu and Charles L Kane. Topological insulators with inversion symmetry. *Physical Review B*, 76(4):045302, 2007.

[6] YL Chen, James G Analytis, J-H Chu, ZK Liu, S-K Mo, Xiao-Liang Qi, HJ Zhang, DH Lu, Xi Dai, Zhong Fang, et al. Experimental realization of a three-dimensional topological insulator, Bi_2Te_3. *Science*, 325(5937):178–181, 2009.

[7] Sergey V Ovsyannikov, Vladimir V Shchennikov, Grigoriy V Vorontsov, Andrey Y Manakov, Anna Y Likhacheva, and Vladimir A Kulbachinskii. Giant improvement of thermoelectric power factor of Bi_2Te_3 under pressure. *Journal of Applied Physics*, 104(5):053713, 2008.

[8] SV Ovsyannikov, Yu A Grigor'eva, GV Vorontsov, LN Luk'yanova, VA Kutasov, and VV Shchennikov. Thermoelectric properties of p-$Bi_{2-x}Sb_xTe_3$ solid solutions under pressure. *Physics of the Solid State*, 54(2):261–266, 2012.

[9] Leo Merrill and William A Bassett. Miniature diamond anvil pressure cell for single crystal x-ray diffraction studies. *Review of Scientific Instruments*, 45(2):290–294, 1974.

[10] H.M. Rietveld. A profile refinement method for nuclear and magnetic structures. *Journal of applied Crystallography*, 2(2):65–71, 1969.

[11] Armel Le Bail. Whole powder pattern decomposition methods and applications: A retrospection. *Powder Diffraction*, 20(4):316–326, 2005.

[12] I Loa, J-WG Bos, Ruth Amy Downie, and K Syassen. Atomic ordering in cubic bismuth telluride alloy phases at high pressure. *Physical Review B*, 93(22):224109, 2016.

[13] MI McMahon, S Rekhi, and RJ Nelmes. Pressure dependent incommensuration in Rb-IV. *Physical review letters*, 87(5):055501, 2001.

[14] MI McMahon, RJ Nelmes, U Schwarz, and K Syassen. Composite incommensurate K-III and a commensurate form: Study of a high-pressure phase of potassium. *Physical Review B*, 74(14):140102, 2006.

[15] MI McMahon, O Degtyareva, and RJ Nelmes. Ba-IV-type incommensurate crystal structure in group-V metals. *Physical review letters*, 85(23):4896, 2000.

[16] MI McMahon and RJ Nelmes. Chain "melting" in the composite Rb-IV structure. *Physical review letters*, 93(5):055501, 2004.

[17] Emma E McBride, Keith A Munro, Graham W Stinton, Rachel J Husband, Richard Briggs, H-P Liermann, and Malcolm I McMahon. One-dimensional chain melting in incommensurate potassium. *Physical Review B*, 91(14):144111, 2015.

[18] Victor Naden Robinson, Hongxiang Zong, Graeme J Ackland, Gavin Woolman, and Andreas Hermann. On the chain-melted phase of matter. *Proceedings of the National Academy of Sciences*, 116(21):10297–10302, 2019.

[19] Ulrich Häussermann, Olga Degtyareva, AS Mikhaylushkin, Karin Söderberg, SI Simak, MI McMahon, RJ Nelmes, and Rolf Norrestam. $Bi_{1-x}Sb_x$ under high pressure: Effect of alloying on the incommensurate Bi-III type composite structure. *Physical Review B*, 69(13):134203, 2004.

[20] T. J. Seebeck. Über die magnetische polarisation der metalle und erze durch temperatur differenz. *Annalen der Physik*, 82(2):133–160, 1826.

[21] HJ Goldsmid and RW Douglas. The use of semiconductors in thermoelectric refrigeration. *British Journal of Applied Physics*, 5(11):386, 1954.

[22] DM Slack, Glen A ed. Rowe. CRC Handbook of Thermoelectrics. *CRC, Boca Raton, FL*, pages 407–440, 1995.

[23] MA Ilina and ES Itskevich. Superconductivity of bismuth telluride. *Fizika Tverdogo Tela*, 13(8):2496–2499, 1971.

[24] JWG Bos, HW Zandbergen, M-H Lee, NP Ong, and RJ Cava. Structures and thermoelectric properties of the infinitely adaptive series $(Bi_2)_m(Bi_2Te_3)_n$. *Physical Review B*, 75(19):195203, 2007.

[25] RM Imamov and SA Semiletov. Crystal Structure of the Phases in the Systems Bi-Se, Bi-Te and Sb-Te. *Sov Phys Crystallogr*, 15(5):845–850, 1971.

[26] F Hulliger. Physics and chemistry of materials with layered structures. *Structural Chemistry of Layer-type phases*, 5, 1976.

[27] J. Stuart Anderson. On infinitely adaptive structures. *J. Chem. Soc., Dalton Trans.*, pages 1107–1115, 1973.

[28] J-WG Bos, F Faucheux, RA Downie, and A Marcinkova. Phase stability, structures and properties of the $(Bi_2)_m(Bi_2Te_3)_n$ natural superlattices. *Journal of Solid State Chemistry*, 193:13–18, 2012.

[29] Hanna Lind and Sven Lidin. A general structure model for Bi–Se phases using a superspace formalism. *Solid state sciences*, 5(1):47–57, 2003.

[30] W Klement Jr, A Jayaraman, and GC Kennedy. Phase diagrams of arsenic, antimony, and bismuth at pressures up to 70 kbars. *Physical Review*, 131(2):632, 1963.

[31] Wanaruk Chaimayo, Lars F Lundegaard, Ingo Loa, Graham W Stinton, Alistair R Lennie, and Malcolm I McMahon. High-pressure, high-temperature single-crystal study of Bi-IV. *High Pressure Research*, 32(3):442–449, 2012.

[32] O Degtyareva, MI McMahon, and RJ Nelmes. High-pressure structural studies of group-15 elements. *High Pressure Research*, 24(3):319–356, 2004.

[33] Katsutoshi Aoki, Osamu Shimomura, and Shigeru Minomura. Crystal structure of the high-pressure phase of tellurium. *Journal of the Physical Society of Japan*, 48(2):551–556, 1980.

[34] G Parthasarathy and WB Holzapfel. High-pressure structural phase transitions in tellurium. *Physical Review B*, 37(14):8499, 1988.

[35] Yoshinori Ohmasa, Itsuro Yamamoto, Makoto Yao, and Hirohisa Endo. Structure and electronic properties of Te–Se mixtures under high pressure. *Journal of the Physical Society of Japan*, 64(12):4766–4789, 1995.

[36] Masaharu Takumi, Takeshi Masamitsu, and Kiyofumi Nagata. X-ray structural analysis of the high-pressure phase iii of tellurium. *Journal of Physics: Condensed Matter*, 14(44):10609, 2002.

[37] C Hejny and MI McMahon. Large structural modulations in incommensurate Te-III and Se-IV. *Physical review letters*, 91(21):215502, 2003.

[38] C Hejny and MI McMahon. Complex crystal structures of Te-II and Se-III at high pressure. *Physical Review B*, 70(18):184109, 2004.

[39] FJ Manjón, R Vilaplana, O Gomis, E Pérez-González, D Santamaría-Pérez, V Marín-Borrás, A Segura, Jesús González, P Rodríguez-Hernández, A Muñoz, et al. High-pressure studies of topological insulators Bi_2Se_3, Bi_2Te_3, and Sb_2Te_3. *Physica status solidi (b)*, 250(4):669–676, 2013.

[40] Paul W Lange. Ein Vergleich zwischen Bi_2Te_3 und Bi_2Te_2S. *Naturwissenschaften*, 27(8):133–134, 1939.

[41] Seizo Nakajima. The crystal structure of $Bi_2Te_{3-x}Se_x$. *Journal of Physics and Chemistry of Solids*, 24(3):479–485, 1963.

[42] JR Wiese and L Muldawer. Lattice constants of Bi_2Te_3-Bi_2Se_3 solid solution alloys. *Journal of Physics and Chemistry of Solids*, 15(1-2):13–16, 1960.

[43] Y Feutelais, B Legendre, N Rodier, and V Agafonov. A study of the phases in the bismuth-tellurium system. *Materials research bulletin*, 28(6):591–596, 1993.

[44] LF Vereshchagin, E Ya Atabaeva, and NA Bendeliani. Investigation of the Bi_2Te_3 phase diagram at high temperatures and pressures. *SOV PHYS SOLID STATE*, 13(8):2051–2053, 1972.

[45] N Sakai, T Kajiwara, K Takemura, S Minomura, and Y Fujii. Pressure-induced phase transition in Sb_2Te_3. *Solid State Communications*, 40(12):1045–1047, 1981.

[46] W Kullmann, J Geurts, W Richter, N Lehner, H Rauh, U Steigenberger, G Eichhorn, and R Geick. Effect of hydrostatic and uniaxial pressure on structural properties and Raman active lattice vibrations in Bi_2Te_3. *physica status solidi (b)*, 125(1):131–138, 1984.

[47] Alain Polian, Michel Gauthier, Sergio Michielon Souza, Daniela Menegon Trichês, Joao Cardoso de Lima, and Tarciso Antonio Grandi. Two-dimensional pressure-induced electronic topological transition in Bi_2Te_3. *Physical Review B*, 83(11):113106, 2011.

[48] A Nakayama, M Einaga, Y Tanabe, S Nakano, F Ishikawa, and Yuh Yamada. Structural phase transition in Bi_2Te_3 under high pressure. *High Pressure Research*, 29(2):245–249, 2009.

[49] MK Jacobsen, RS Kumar, AL Cornelius, SV Sinogeiken, and MF Nico. High pressure x-ray diffraction studies of $Bi_{2-x}Sb_xTe_3$ (x= 0, 1, 2). In *AIP Conference Proceedings*, volume 955, pages 171–174. AIP, 2007.

[50] IM Lifshitz et al. Anomalies of electron characteristics of a metal in the high pressure region. *Sov. Phys. JETP*, 11(5):1130–1135, 1960.

[51] Mari Einaga, Ayako Ohmura, Atsuko Nakayama, Fumihiro Ishikawa, Yuh Yamada, and Satoshi Nakano. Pressure-induced phase transition of Bi_2Te_3 to a bcc structure. *Physical Review B*, 83(9):092102, 2011.

[52] Yanchao Wang, Jian Lv, Li Zhu, and Yanming Ma. Crystal structure prediction via particle-swarm optimization. *Phys. Rev. B*, 82:094116, Sep 2010.

[53] SJ Zhang, JL Zhang, XH Yu, J Zhu, PP Kong, SM Feng, QQ Liu, LX Yang, XC Wang, LZ Cao, et al. The comprehensive phase evolution for Bi_2Te_3 topological compound as function of pressure. *Journal of Applied Physics*, 111(11):112630, 2012.

[54] Rosario Vilaplana, D. Santamaría-Pérez, O. Gomis, F. J. Manjón, J. González, A. Segura, A. Muñoz, P. Rodríguez-Hernández, E. Pérez-González, V. Marín-Borrás, V. Muñoz Sanjose, C. Drasar, and V. Kucek. Structural and vibrational study of Bi_2Se_3 under high pressure. *Physical Review B*, 84(18):184110, 2011.

[55] SM Souza, CM Poffo, DM Triches, JC De Lima, TA Grandi, A Polian, and Michel Gauthier. High pressure monoclinic phases of Sb_2Te_3. *Physica B: Condensed Matter*, 407(18):3781–3789, 2012.

[56] R Vilaplana, O Gomis, FJ Manjón, A Segura, E Pérez-González, P Rodríguez-Hernández, A Muñoz, J González, V Marín-Borrás, V Muñoz-Sanjosé, et al. High-pressure vibrational and optical study of Bi_2Te_3. *Physical Review B*, 84(10):104112, 2011.

[57] O Gomis, R Vilaplana, FJ Manjón, P Rodríguez-Hernández, E Pérez-González, A Muñoz, V Kucek, and C Drasar. Lattice dynamics of Sb_2Te_3 at high pressures. *Physical Review B*, 84(17):174305, 2011.

[58] Gopal K Pradhan, Achintya Bera, Pradeep Kumar, DVS Muthu, and AK Sood. Raman signatures of pressure induced electronic topological and structural transitions in Bi_2Te_3. *Solid State Communications*, 152(4):284–287, 2012.

[59] Jinggeng Zhao, Haozhe Liu, Lars Ehm, Zhiqiang Chen, Stanislav Sinogeikin, Yusheng Zhao, and Genda Gu. Pressure-induced disordered substitution alloy in Sb_2Te_3. *Inorganic chemistry*, 50(22):11291–11293, 2011.

[60] KAZUO Yamana, KUNIAKI Kihara, and TAKEO Matsumoto. Bismuth tellurides: BiTe and Bi_4Te_3. *Acta Crystallographica Section B: Structural Crystallography and Crystal Chemistry*, 35(1):147–149, 1979.

[61] S Klotz, JC Chervin, P Munsch, and G Le Marchand. Hydrostatic limits of 11 pressure transmitting media. *Journal of Physics D: Applied Physics*, 42(7):075413, 2009.

[62] RM Brugger, RB Bennion, and TG Worlton. The crystal structure of bismuth-II at 26 kbar. *Physics Letters A*, 24(13):714–717, 1967.

[63] JH Chen, H Iwasaki, and T Ktkegawa. Crystal structure of the high pressure phases of bismuth Bi-II and Bi-III' by high energy synchrotron x-ray diffraction. *High pressure research*, 15(3):143–158, 1996.

[64] RJ Nelmes, DR Allan, MI McMahon, and SA Belmonte. Self-hosting incommensurate structure of barium IV. *Physical Review Letters*, 83(20):4081, 1999.

[65] MI McMahon, LF Lundegaard, C Hejny, S Falconi, and RJ Nelmes. Different incommensurate composite crystal structure for Sc-II. *Physical Review B*, 73(13):134102, 2006.

[66] H Iwasaki. Comment on "bcc arsenic at 111 GPa: An x-ray structural study". *Physical Review B*, 55(21):14645, 1997.

[67] MI McMahon, T Bovornratanaraks, DR Allan, SA Belmonte, and RJ Nelmes. Observation of the incommensurate barium-IV structure in strontium phase V. *Physical Review B*, 61(5):3135, 2000.

[68] O Degtyareva, MI McMahon, and RJ Nelmes. Pressure-induced incommensurate-to-incommensurate phase transition in antimony. *Physical Review B*, 70(18):184119, 2004.

[69] LF Lundegaard, E Gregoryanz, MI McMahon, C Guillaume, I Loa, and RJ Nelmes. Single-crystal studies of incommensurate Na to 1.5 Mbar. *Physical Review B*, 79(6):064105, 2009.

[70] Ingo Loa, RJ Nelmes, LF Lundegaard, and MI McMahon. Extraordinarily complex crystal structure with mesoscopic patterning in barium at high pressure. *Nature materials*, 11(7):627, 2012.

[71] R Briggs, MG Gorman, AL Coleman, RS McWilliams, EE McBride, D McGonegle, JS Wark, L Peacock, S Rothman, SG Macleod, et al. Ultrafast x-ray diffraction studies of the phase transitions and equation of state of scandium shock compressed to 82 GPa. *Physical review letters*, 118(2):025501, 2017.

[72] VJ Emery and G Shirane. One-dimensional fluctuations and the chain-ordering transformation in $Hg_{3-\delta}AsF_6$. In *Molecular Metals*, pages 455–469. Springer, 1979.

[73] LF Lundegaard, GW Stinton, M Zelazny, CL Guillaume, JE Proctor, I Loa, E Gregoryanz, RJ Nelmes, and MI McMahon. Observation of a reentrant phase transition in incommensurate potassium. *Physical Review B*, 88(5):054106, 2013.

[74] EE McBride, O Narygina, GW Stinton, and MI McMahon. Melting of potassium to 22 GPa. In *Journal of Physics: Conference Series*, volume 377, page 012040. IOP Publishing, 2012.

[75] Sergey V Ovsyannikov and Vladimir V Shchennikov. Pressure-tuned colossal improvement of thermoelectric efficiency of PbTe. *Applied physics letters*, 90(12):122103, 2007.

[76] David Michael Rowe. *CRC handbook of thermoelectrics*. CRC press, 1995.

[77] MK Jacobsen, SV Sinogeikin, RS Kumar, and AL Cornelius. High pressure transport characteristics of Bi_2te_3, sb_2te_3, and $BiSbTe_3$. *Journal of Physics and Chemistry of Solids*, 73(9):1154–1158, 2012.

[78] Wilfredo Ibarra-Hernandez, Matthieu J Verstraete, and Jean-Yves Raty. Effect of hydrostatic pressure on the thermoelectric properties of Bi_2Te_3. *Physical Review B*, 90(24):245204, 2014.

[79] Chao Zhang, Liling Sun, Zhaoyu Chen, Xingjiang Zhou, Qi Wu, Wei Yi, Jing Guo, Xiaoli Dong, and Zhongxian Zhao. Phase diagram of a pressure-induced superconducting state and its relation to the Hall coefficient of Bi_2Te_3 single crystals. *Physical Review B*, 83(14):140504, 2011.

[80] Fang Yang, Lin Miao, ZF Wang, Meng-Yu Yao, Fengfeng Zhu, YR Song, Mei-Xiao Wang, Jin-Peng Xu, Alexei V Fedorov, Z Sun, et al. Spatial and energy distribution of topological edge states in single Bi (111) bilayer. *Physical review letters*, 109(1):016801, 2012.

[81] Omar Concepción, Miguel Galván-Arellano, Vicente Torres-Costa, Aurelio Climent-Font, Daniel Bahena, Miguel Manso Silvan, Arturo Escobosa, and Osvaldo De Melo. Controlling the Epitaxial Growth of Bi_2Te_3, BiTe, and Bi_4Te_3 Pure Phases by Physical Vapor Transport. *Inorganic chemistry*, 57(16):10090–10099, 2018.

[82] Markus Eschbach, Martin Lanius, Chengwang Niu, Ewa Młyńczak, Pika Gospodarič, Jens Kellner, Peter Schüffelgen, Mathias Gehlmann, Sven Döring, Elmar Neumann, et al. Bi_1Te_1 is a dual topological insulator. *Nature communications*, 8:14976, 2017.

[83] Richard A Forman, Gasper J Piermarini, J Dean Barnett, and Stanley Block. Pressure measurement made by the utilization of ruby sharp-line luminescence. *Science*, 176(4032):284–285, 1972.

[84] HK Mao, J-A Xu, and PM Bell. Calibration of the ruby pressure gauge to 800 kbar under quasi-hydrostatic conditions. *Journal of Geophysical Research: Solid Earth*, 91(B5):4673–4676, 1986.

[85] JD Barnett, S Block, and GJ Piermarini. An optical fluorescence system for quantitative pressure measurement in the diamond-anvil cell. *Review of scientific instruments*, 44(1):1–9, 1973.

[86] Hans Wonderatschek and Ulrich Müller. *International Tables for Crystallography: Volume A1: Symmetry Relations Between Space Groups*. Springer, 2004.

[87] Max von Laue. Concerning the detection of x-ray interferences. *Nobel lecture*, 13, 1915.

[88] Charles Kittel, Paul McEuen, and Paul McEuen. *Introduction to solid state physics*, volume 8. Wiley New York, 1996.

[89] Bertram Eugene Warren. *X-ray Diffraction*. Courier Corporation, 1990.

[90] W. Clegg, R. Cooper, J. A.K. Howard, S. Moggach, L. Palatinus, S. Parsons, H. J. Shepherd, P. Wood, and D. Yufit. Lecture notes of The 16th BCA/CCG Intensive Teaching School in X-Ray Structure Analysis, March 2017.

[91] Václav Petříček, Michal Dušek, and Lukáš Palatinus. Crystallographic computing system JANA2006: general features. *Zeitschrift für Kristallographie-Crystalline Materials*, 229(5):345–352, 2014.

[92] PJ Brown, AG Fox, EN Maslen, MA O'Keefe, and BTM Willis. Intensity of diffracted intensities. In *International Tables for Crystallography Volume C: Mathematical, physical and chemical tables*, pages 554–595. Springer, 2004.

[93] JM Cowley. Scattering factors for the diffraction of electrons by crystalline solids. *International Tables for Crystallography*, 100:223–245, 1992.

[94] Harry J Lipkin. Physics of Debye-Waller Factors. *arXiv preprint cond-mat/0405023*, 2004.

[95] AP Hammersley, A Thompson, SO Svensson, K Brown, L Claustre, A Freund, A Gonzalez, S McSweeney, and JP Moy. ESRF internal report, 1997.

[96] AP Hammersley, SO Svensson, M Hanfland, AN Fitch, and D Hausermann. Two-dimensional detector software: from real detector to idealised image or two-theta scan. *International Journal of High Pressure Research*, 14(4-6):235–248, 1996.

[97] Bernard Dennis Cullity and Stuart R Stock. *Elements of X-ray Diffraction*. Pearson, 2001.

[98] H Lipson, I Langford, and H Hu. Trigonometric intensity factors. In *International Tables for Crystallography Volume C: Mathematical, physical and chemical tables*, pages 596–598. Springer, 2006.

[99] AP Hammersley. FIT2D: a multi-purpose data reduction, analysis and visualization program. *Journal of Applied Crystallography*, 49(2):646–652, 2016.

[100] Ingo Loa. private communication, 2019.

[101] R Shirley. The Crysfire 2002 system for automatic powder indexing: user's manual. *The Lattice, England*, 2002.

[102] Ali Boultif and Daniel Louër. Powder pattern indexing with the dichotomy method. *Journal of Applied Crystallography*, 37(5):724–731, 2004.

[103] Per-Erik Werner. Trial-and-error computer methods for the indexing of unknown powder patterns. *Zeitschrift für Kristallographie-Crystalline Materials*, 120(1-6):375–387, 1964.

[104] Bob van Laar and Henk Schenk. The development of powder profile refinement at the Reactor Centre Netherlands at Petten. *Acta Crystallographica Section A: Foundations and Advances*, 74(2):88–92, 2018.

[105] Robert Alan Young. *The Rietveld method*, volume 5. International union of crystallography, 1993.

[106] VACLAV Petricek, KAREL Maly, Ph Coppens, Xianhui Bu, I Cisarova, and A Frost-Jensen. The description and analysis of composite crystals. *Acta Crystallographica Section A: Foundations of Crystallography*, 47(3):210–216, 1991.

[107] W. Kraus and G. Nolze. POWDER CELL– a program for the representation and manipulation of crystal structures and calculation of the resulting x-ray powder patterns. *Journal of Applied Crystallography*, 29(3):301–303, 1996.

[108] Allen C Larson and Robert B Von Dreele. GSAS. *Report lAUR*, pages 86–748, 1994.

[109] Matthew Newville, Till Stensitzki, Daniel B Allen, Michal Rawlik, Antonino Ingargiola, and Andrew Nelson. LMFIT: Non-linear least-square minimization and curve-fitting for python. *Astrophysics Source Code Library*, 2016.

[110] Li Zhu, Hui Wang, Yanchao Wang, Jian Lv, Yanmei Ma, Qiliang Cui, Yanming Ma, and Guangtian Zou. Substitutional alloy of Bi and Te at high pressure. *Physical Review Letters*, 106(14):145501, 2011.

[111] Lukas Palatinus and Gervais Chapuis. SUPERFLIP–a computer program for the solution of crystal structures by charge flipping in arbitrary dimensions. *Journal of Applied Crystallography*, 40(4):786–790, 2007.

[112] U Schwarz, A Grzechnik, K Syassen, I Loa, and M Hanfland. Rubidium-IV: A high pressure phase with complex crystal structure. *Physical review letters*, 83(20):4085, 1999.

[113] Malcolm I McMahon and Richard J Nelmes. High-pressure structures and phase transformations in elemental metals. *Chemical Society Reviews*, 35(10):943–963, 2006.

[114] Michael Wörle and Reinhard Nesper. Infinite, linear, unbranched borynide chains in LiB_x—isoelectronic to polyyne and polycumulene. *Angewandte Chemie*, 112(13):2439–2443, 2000.

[115] C-E Chen, Y Schlesinger, and AJ Heeger. X-ray scattering by one-dimensional chains: powder diffraction. *Physical Review B*, 25(4):2472, 1982.

[116] Michael Wörle, Reinhard Nesper, and Tapan K Chatterji. LiB_x ($0.82 < x \leq 1.0$)–an incommensurate composite structure below 150 K. *Zeitschrift für anorganische und allgemeine Chemie*, 632(10-11):1737–1742, 2006.

[117] VV Atuchin, TA Gavrilova, KA Kokh, NV Kuratieva, NV Pervukhina, and NV Surovtsev. Structural and vibrational properties of PVT grown Bi_2Te_3 microcrystals. *Solid State Communications*, 152(13):1119–1122, 2012.

[118] AN Mansour, W Wong-Ng, Q Huang, W Tang, A Thompson, and J Sharp. Structural characterization of Bi_2Te_3 and Sb_2Te_3 as a function of temperature using neutron powder diffraction and extended X-ray absorption fine structure techniques. *Journal of Applied Physics*, 116(8):083513, 2014.

[119] M Shankar Narayana and N Gopi Krishna. X-ray study of Bi, Sb and $Bi_{1-x}Sb_x$ alloys. *physica status solidi (a)*, 202(14):2731–2736, 2005.

[120] Peter W Stephens. Phenomenological model of anisotropic peak broadening in powder diffraction. *Journal of Applied Crystallography*, 32(2):281–289, 1999.

[121] FD Murnaghan. The compressibility of media under extreme pressures. *Proceedings of the national academy of sciences of the United States of America*, 30(9):244, 1944.

[122] P Larson, VA Greanya, WC Tonjes, Rong Liu, SD Mahanti, and CG Olson. Electronic structure of Bi_2X_3 (X= S, Se, T) compounds: Comparison of theoretical calculations with photoemission studies. *Physical review B*, 65(8):085108, 2002.

[123] Francis Birch. Finite elastic strain of cubic crystals. *Phys. Rev.*, 71:809–824, Jun 1947.

[124] GW Stinton, I Loa, LF Lundegaard, and MI McMahon. The crystal structures of δ and δ^* nitrogen. *The Journal of Chemical Physics*, 131(10):104511, 2009.

[125] Yuichi Akahama, Haruki Kawamura, and Anil K Singh. Equation of state of bismuth to 222 GPa and comparison of gold and platinum pressure scales to 145 GPa. *Journal of applied physics*, 92(10):5892–5897, 2002.

[126] P Cucka and CS Barrett. The crystal structure of Bi and of solid solutions of Pb, Sn, Sb and Te in Bi. *Acta Crystallographica*, 15(9):865–872, 1962.

[127] N Bouad, L Chapon, R-M Marin-Ayral, F Bouree-Vigneron, and J-C Tedenac. Neutron powder diffraction study of strain and crystallite size in

mechanically alloyed PbTe. *Journal of Solid State Chemistry*, 173(1):189–195, 2003.

[128] ME Straumanis and Don C Kim. Lattice constants, thermal expansion coefficients, densities, and perfection of structure of pure iron and of iron loaded with hydrogen. *Z METALLKUNDE*, 60(4):272–277, 1969.

[129] EA Owen and EL Yates. XLI. precision measurements of crystal parameters. *The London, Edinburgh, and Dublin Philosophical Magazine and Journal of Science*, 15(98):472–488, 1933.

[130] W. Parrish. Results of the IUCr precision lattice-parameter project. *Acta Crystallographica*, 13(10):838–850, Oct 1960.

[131] WA Dollase. Correction of intensities for preferred orientation in powder diffractometry: application of the March model. *Journal of Applied Crystallography*, 19(4):267–272, 1986.

[132] Emil Zolotoyabko. Determination of the degree of preferred orientation within the March–Dollase approach. *Journal of applied Crystallography*, 42(3):513–518, 2009.

[133] William Parrish. Results of the IUCr precision lattice-parameter project. *Acta Crystallographica*, 13(10):838–850, 1960.